Enhanced sheet conductivity of Langmuir–Blodgett assembled graphene thin films by chemical doping

2016 2D Mater. 3 015002

(http://iopscience.iop.org/2053-1583/3/1/015002)

IOP Publishing   *2D Mater.* **3** (2016) 015002   doi:10.1088/2053-1583/3/1/015002

2D Materials

CrossMark

RECEIVED
14 August 2015

REVISED
6 November 2015

ACCEPTED FOR PUBLICATION
15 December 2015

PUBLISHED
18 January 2016

PAPER

Enhanced sheet conductivity of Langmuir–Blodgett assembled graphene thin films by chemical doping

Aleksandar Matković[1], **Ivana Milošević**[1], **Marijana Milićević**[1], **Tijana Tomašević-Ilić**[1], **Jelena Pešić**[1], **Milenko Musić**[1], **Marko Spasenović**[1], **Djordje Jovanović**[1], **Borislav Vasić**[1], **Christopher Deeks**[2], **Radmila Panajotović**[1], **Milivoj R Belić**[3] **and Radoš Gajić**[1]

[1] Center for Solid State Physics and New Materials, Institute of Physics, University of Belgrade, Pregrevica 118, 11080 Belgrade, Serbia
[2] Thermo Fisher Scientific, Unit 24, The Birches Industrial Estate, East Grinstead, RH19 1UB, UK
[3] Texas A & M University at Qatar, PO Box 23874 Doha, Qatar

E-mail: amatkovic@ipb.ac.rs

Keywords: graphene, nitric acid doping, Langmuir–Blodgett assembly, enhanced conductivity

Supplementary material for this article is available online

Abstract

We demonstrate a facile fabrication technique for highly conductive and transparent thin graphene films. Sheet conductivity of Langmuir–Blodgett assembled multi-layer graphene films is enhanced through doping with nitric acid, leading to a fivefold improvement while retaining the same transparency as un-doped films. Sheet resistivity of such chemically improved films reaches 10 kΩ/□, with optical transmittance 78% in the visible. When the films are encapsulated, the enhanced sheet conductivity effect is stable in time. In addition, stacking of multiple layers, as well as the dependence of the sheet resistivity upon axial strain have been investigated.

1 Introduction

Graphene has a multitude of potential applications from high-speed electronics, to energy storage and conversion, to use as transparent conductor [1–3]. As graphene technology matures, applications are moving from the lab to the market, and the performance-to-cost ratio is becoming a crucial parameter in technology adoption, raising the importance of scalable and cost effective routes for production of graphene and related materials [4–7].

Transparent conductive electrodes (TCEs) [8] are an exemplary technology for which graphene offers key advantages compared to established standards. The unique properties that graphene TCEs offer are flexibility [9], thermal and chemical stability [10, 11], functionalization [12] and ease of integration with organic semiconductors [13–15]. Therefore, the use of graphene has already been demonstrated in photovoltaic solar cells [11, 16–18], liquid crystal displays [10], touch-screen panels [19], organic light emitting diodes [20, 21] and many others.

Most of these applications currently rely on graphene obtained through chemical vapor deposition (CVD) [22–24]. Although the CVD process produces some of the highest quality graphene films [25], there are several drawbacks of this technique. CVD of graphene requires high growth temperatures, a vacuum environment and transfer from the metallic substrate, during which the costly metal is usually sacrificed [26]. Nonetheless, multiple layers of CVD graphene grown on copper, transferred, stacked [27] and chemically doped [19, 28] have managed to surpass the industry standard [8] for TCEs set by indium–tin–oxide.

A low-cost alternative to CVD is solution-processed synthesis of graphene and related materials, the first experiments of which yielded graphene oxide [29–31]. Solution-processed sheets of reduced graphene oxide are functionalized with hydroxyls and epoxides and cannot be fully reduced to graphene, which limits film conductance. This issue can be overcome by using a non-covalent liquid phase exfoliation (LPE) of graphite in organic solvents with matching surface energy. LPE was first demonstrated for graphene [10, 32, 33], and then adopted for other two-dimensional materials such as boron-nitride, MoS_2, WS_2, WSe_2 and other [7, 34–36]. LPE of graphite results in a dispersion of graphene and multi-layer graphene sheets (GSs) in the solvent. There are many ways

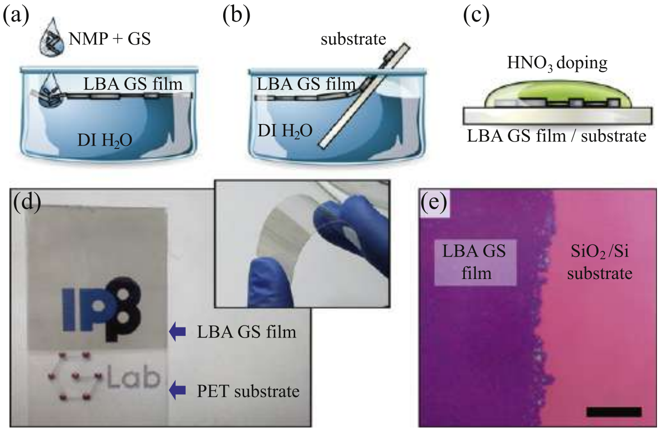

Figure 1. (a)–(c) show schematic representations (out of scale) of a LBA GS film formation, scooping of the film onto a targeted substrate and subsequent chemical doping, respectively. (d) A photograph of a 2 × 2 cm^2 LBA GS film on a PET substrate, demonstrating its transparency in comparison to PET. Inset of (d) shows bending of the sample. (e) Optical microscope image of an edge of a LBA GS film (left) on a SiO_2/Si substrate (right) with 300 nm thick oxide layer. Scale bar in (e) is 20 μm.

to deposit these sheets onto a targeted substrate, for example spray coating [10], ink-jet printing [37–39], vacuum filtration [31, 40], Langmuir–Blodgett assembly (LBA) [41–44], or self-assembly on a liquid–liquid interface [45–47]. Still, the electronic conductance of LPE films is inferior to that of CVD graphene, and any improvement is a step towards industrial applications of solution processed graphene.

We make transparent conductive films of multilayer GSs on flexible polyethylene terephthalate (PET) by LBA on a water–air interface. The sheets adhere strongly to the PET substrate, which allows immersion into other liquids without the risk of the film washing away. We make use of the strong adhesion to chemically dope the graphene in nitric acid for enhanced conductivity, and to stack multiple films on top of each other, opening a gateway to liquid phase assembly of Van der Waals heterostructures [36, 48, 49]. The power of this method is demonstrated by the fivefold reduction in sheet resistivity for a single LBA layer, while maintaining the same optical transparency of the unperturbed films.

We show that LBA GS films can be very effectively p-doped by nitric acid, making them a more suitable low-cost alternative to CVD graphene for various TCE applications. As indicated by the work function measurements and by the measurements of the sheet resistivity under axial strain, chemical doping does not only increase carrier concentration of individual GSs, but also reduces the contact resistance between GSs, which additionally contributes to a larger reduction factor of the sheet resistivity.

2 LBA GS film fabrication and morphological characterization

2.1 Preparation of GS dispersion

As a starting material for the formation of LBA layers, a dispersion of GSs in *N*-methylpyrrolidone (NMP) has been used. The dispersion fabrication process is based on the earlier established protocol [32]. An initial concentration of graphite powder (Sigma Aldrich-332461) was 18 mg ml^{-1} in NMP (Sigma Aldrich-328634). The solution was sonicated in a low-power ultrasonic bath for 14 h, and centrifuged for one hour at 3000 rpm immediately after sonication. The results of this process are GSs in solution, with a concentration of 0.36 mg ml^{-1}. The concentration was determined via UV–VIS spectrophotometry (SUPER SCAN, Varian) [32]. This particular set of LPE parameters was chosen since the resulting dispersion of GSs in NMP was found to be stable for over six months.

2.2 Langmuir–Blodgett assembly

GSs suspended in NMP were used to fabricate transparent and conductive films by LBA at a water–air interface [43]. Since the LPE process introduces a low degree of oxidation and covalent functionalization, resulting GSs have high hydrophobicity, which is very favorable for the formation of LBA layers [41]. Furthermore, driven by the minimization of interfacial energy, LBA produces a close packed structure of GSs [45]. A schematic representation of LBA GS film formation is presented in figure 1(a). Beakers filled with deionized water (18.2 MΩ) with a water–air interface surface-to-water volume ratio of 0.5 cm^{-1} were used for film formation. A 1.5–2 vol% of GS +NMP was added to the interface with a continuous flow rate of 5–10 μl s^{-1}. A closely packed LBA GS film was found to form on the water–air interface with this set of parameters. Formation of the LBA film was found to be self-limiting, meaning that prior to the film formation on the whole given surface, added GSs are fixed at the interface, and after the complete film was formed, any additional GSs fall through the interface to the bottom of the beaker. Only several microliters of the GS+NMP solution are needed to fabricate several square centimeters of film. When scaled up, one liter of GS+NMP solution would be sufficient to produce 150 × 150 m^2 of LBA GS films. Compared to CVD graphene, fabrication cost of these TCEs would be at least three orders of magnitude smaller [4].

2.3 Deposition on a substrate and chemical doping

Interestingly, as proposed by Kim *et al* [43], this process dissolves NMP in the water, effectively removing most of the solvent from the graphene layer. After the film is formed, it is slowly scooped onto the targeted substrate, as schematically presented in figure 1(b). The substrate was either pre-positioned vertically at the edge of the beaker, or was introduced after the LBA film was formed, puncturing the film near the edge of the beaker. Films are then left to dry for several minutes in ambient conditions. After the films were transferred onto the targeted substrates their sheet conductivity was enhanced by chemical doping. This was achieved either by dipping into or covering LBA GS films with a 65% solution of nitric acid in water (see figure 1(c)), followed by quick drying with an air gun.

Our procedure yields quality films on all tested substrates, including SiO_2/Si, quartz, glass and PET. We typically pre-fabricated ~50 nm thick gold electrodes on the substrates prior to GS deposition. Figures 1(d) and (e) show LBA GS films on the PET and SiO_2/Si substrate, respectively. Films fabricated with this method are uniform over the entire substrate area. Up to several square centimeters of uniform LBA GS films on various substrates were fabricated using this technique, with sheet conductivity and optical transparency not varying more than 5% from the mean value over the entire film.

2.4 Film morphology

The morphology of the obtained LBA GS films was characterized with atomic force microscopy (AFM) and scanning electron microscopy (SEM). AFM measurements were carried out on an atomic force microscope, NTEGRA Spectra, in tapping mode. A typical AFM profile of an LBA GS film on a SiO_2/Si substrate is shown in figure 2(a). SiO2/Si was chosen as a substrate for AFM due to its low surface roughness. Figure 2(b) shows a height histogram of a 5 × 5 μm^2 AFM topography image containing a sharp edge of the LBA GS layer (inset). Ten height histograms of sample/substrate edge areas were used to estimate the thickness of LBA GS films. Each histogram had two clearly resolved peaks corresponding to LBA GS film and the substrate. An average film thickness was estimated as a peak-to-peak distance. While the substrate peak is narrow, due to the low roughness of the SiO_2, (left peak in figure 2(b)), the LBA GS film has a much broader height distribution. The sample peak was fitted with a log-normal curve, yielding a mean film thickness (3.4 ± 0.7) nm. This indicates that LBA GS films have an average thickness of ~10 layers.

The lateral profile of graphene flakes was analyzed with a Tescan MIRA3 field-emission gun SEM. A histogram of flake diameter is presented in figure 2(c). The distribution of flake diameters from six 5 × 5 μm^2 SEM images (~2000 flakes) was fitted with a log-normal curve, giving an average flake diameter of 120 nm. Both AFM and SEM images were used to estimate a surface coverage of over 90%.

3 Results and discussion

3.1 Nitric acid doping

The key result of this study is doping of LBA GS films with nitric acid for improved sheet conductivity. Chemical doping of graphene can be accomplished with various liquids, vapors and polymers [10, 16, 17, 19, 28, 50–53]. One of the most efficient p-type chemical dopants of graphite and graphene is nitric acid [19, 28, 52, 54, 55]. Nitric acid has been used to chemically dope CVD graphene, and reduce the sheet resistivity by a factor of two to three [17, 19, 28, 50]. It was also used to chemically dope reduced GO [53]. Nitric acid doping of graphene was found to be very favorable for photovoltaic solar cells, where graphene is used as a top anode [16, 17, 50, 56]. Besides a reduction in sheet resistivity, the doping increases graphene's work function from about 4.5 to 5 eV, making these TCEs more suitable anode electrodes for various types of hybrid solar cells [17, 50, 52, 56, 57]. Recently, nitrogen-doped reduced GO and carbon have been demonstrated to show enhancement in energy storage [58, 59]. In the following sections we discuss the results of doping LBA GS films with nitric acid.

3.2 Nitric acid exposure time

In order to determine optimal conditions for chemical doping, the exposure time of a single layer LBA GS layer to nitric acid was varied between 10 s and 2 h. Figure 3(a) shows the exposure time dependent reduction factor of the sheet resistivity, obtained as the ratio of the sheet resistivity prior and after the doping (R_{ND}/R_D). Even after only 30 s of the exposure, the reduction factor greater than four was achieved, and after several minutes the reduction factor was found to saturate at (5 ± 1). In order to ensure the control over chemical doping, the exposure time of 5 min was chosen as an optimal value in this study.

3.3 Time stability of the enhanced conductivity effect

Considering that nitric acid is volatile and that dopants can be desorbed from the sample, the stability of the sheet resistivity was examined over an extended period of time. Two batches of LBA GS films were prepared,

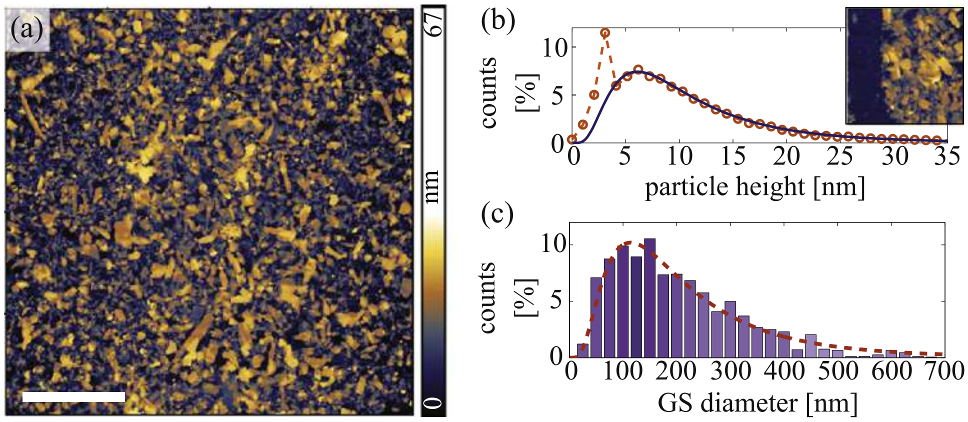

Figure 2. (a) An AFM topography image of a LBA graphene film on a SiO_2/Si substrate. Scale bar is 5 μm. (b) An LBA GS film/substrate height histogram obtained from a 5 × 5 μm^2 AFM topography image (inset), fitted by a log-normal curve (solid line). The height of the film has been estimated to 3.4 nm, indicating an average GS thickness of ten layers. (c) GS diameter histogram obtained from several SEM images. The dashed line in (c) represents a log-normal fit, giving an average GS diameter of 120 nm.

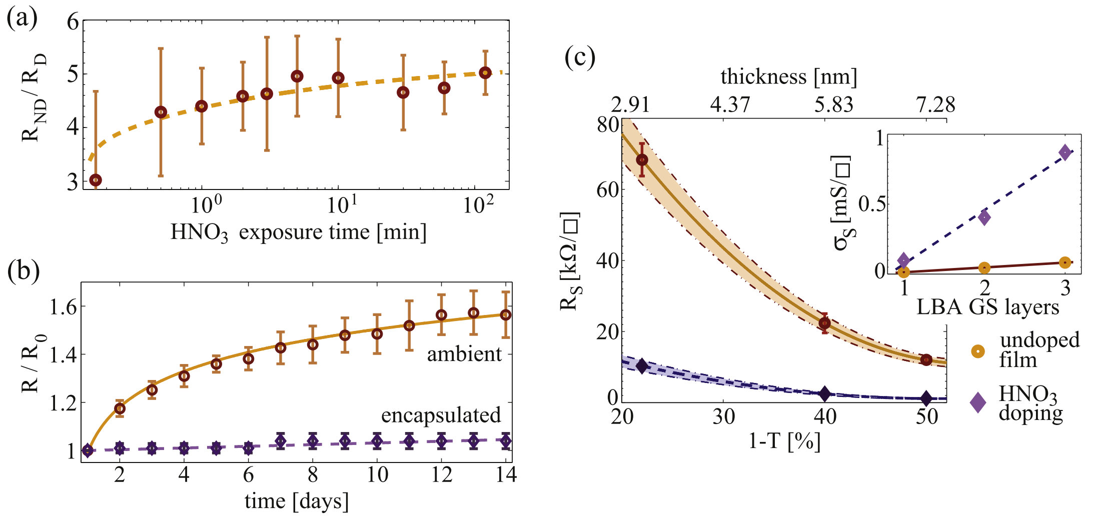

Figure 3. (a) Sheet resistivity reduction factor after chemical doping with varied exposure time. (b) Stability of the doped LBA GS films, comparing encapsulated samples with the ones that were exposed to ambient air. (c) The sheet resistivity (R_S) as a function of the light absorption at 650 nm wavelength. The data for up to three stacked LBA GS layers is shown, both prior (circles) and after (diamonds) the chemical doping, with solid and dashed lines as smooth fits for the undoped and doped samples, respectively. Shaded areas indicate a sample-to-sample variations in both R_S and the light absorption. Inset of (c) shows sheet conductivity as a function of the number of stacked LBA GS layers.

one with the doped LBA GS surface exposed to the ambient conditions, and the other encapsulated (covered with Scotch tape) immediately after chemical doping. Figure 3(b) shows the relative change of sheet resistivity in time as $R(t)/R_0$, where R_0 stands for the initial sheet resistivity. Encapsulated samples show excellent time stability, with less than 5% change in sheet resistivity over two weeks.

3.4 Stacking of multiple LBA GS layers

The excellent adhesion of LBA GS sheets to the PET substrate allows not only for straightforward methods of chemical doping using liquids, but also for reproducible stacking of additional LBA layers. This is a very promising technique for making solution-based GRM heterointerfaces [36], using a simple, one-step, low-cost and high-yield self-assembly process.

Figure 3(c) shows the sheet resistivity (R_S) as a function of optical transmittance of stacked LBA GS layers. After stacking, samples were exposed to nitric acid for 5 min. The lowest sheet resistivity obtained were on the order of 800 Ω/□, albeit at only 50% transmittance. The fact that subsequent doping can affect the entire film could be attributed to intercalation of nitric acid into the LBA GS stacks [28].

The sheet conductivity ($\sigma_S = 1/R_S$) of both doped and undoped samples was found to linearly depend on the number of LBA layers, as shown in the inset of figure 3(c). This indicates that appended LBA layers act as additional transport channels, and that the current is homogenously distributed across the entire film

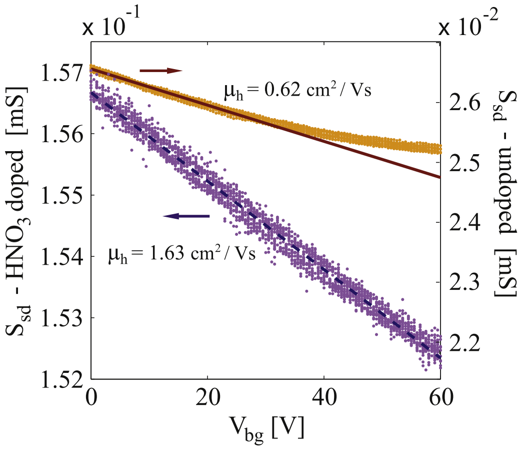

Figure 4. Compared total device conductance S_{sd} of a doped and undoped device, as a function of an applied back-gate voltage V_{bg}. Solid and dashed lines represent linear fits used for estimating hole mobilities of the samples.

when the distance between the electrodes is in the millimeter range [28].

3.5 Sheet resistivity and DC electrical characteristics measurements

The total resistance of each sample was measured in a two-point probe configuration, and the sheet resistivity was obtained by including the sample geometry factors. More details are given in supplementary information. The contact resistance was neglected being a three orders of magnitude smaller than the LBA GS film resistance. Sheet resistivity of as produced LBA GS films on PET was (70 ± 6) kΩ/□ for films with average thickness of 10 graphene layers. The sheet resistivity of the films after the doping was found to be reduced by the factor of five to six, reaching the value of (12 ± 3) kΩ/□. This change is two times larger than that reported for nitric acid doping of CVD graphene [17, 19, 28, 50]. Such a large reduction of sheet resistivity can be attributed to the fact that LPE based films have a large amount of un-functionalized GS edges, thus having more sites available for adsorption of NO_3^- and hydroxyl groups [53].

In order to characterize electrical properties of both undoped and chemically doped LBA GS films, measurements of direct-current (DC) electrical characteristics were carried out at room temperature. Device preparation, schematic representation of the measurement setups and measurements of the current between source (s) and drain (d) electrodes as a function of applied source–drain voltage V_{sd} are given in supplementary information.

Figure 4 shows the dependence of the total conductance (S_{ds}) as a function of back gate voltage (V_{bg}) for several consequent sweeps between 0 and 60 V. The negative slope of $S_{ds}(V_{bg})$ confirms that both undoped and chemically doped LBA GS films have holes as dominant charge carriers. Unintentional p-doping of the sample prior to the exposure to nitric acid is attributed to the remaining water and NMP residue at the interface during film transfer [32]. Conductance function was approximated to be linear, neglecting the deviation of the undoped sample at higher voltages, which is likely due to approaching a charge neutrality point. Using the linear approximation, carrier mobility has been estimated [43, 60] to be 0.6–0.8 cm^2 V^{-1} s^{-1} for the undoped samples, and 1.55–1.75 cm^2 V^{-1} s^{-1} for the samples that were exposed to nitric acid.

3.6 X-ray photoelectron spectroscopy (XPS)

XPS was used to elucidate the mechanisms behind the doping of graphene with HNO_3. Measurements were carried out on a Thermo Scientific Theta Probe XPS system, providing the quantitative elemental analysis. The samples were not encapsulated, and the measurements were carried out at room temperature without *in situ* heating. In addition, angle resolved XPS was used to obtain qualitative information of elemental distribution along the depth of the samples. Experimental details are given in supplementary information. XPS indicated the presence of carbon, oxygen, and nitrogen in the sample (see supplementary information figure S2). Nitrogen 1s core level intensities of undoped LBA GS film on PET imply nitrogen concentrations of ~0.5 at%, which is an indication of intrinsic film doping by residual NMP [32].

Figures 5(a) and (b) show C 1s and O 1s core-level XPS spectra of the pristine and HNO_3-treated graphene films deposited on PET. In figure 5(a) the C 1s band is deconvoluted to reveal peaks corresponding to binding energies of graphene (sp^2) /C–C bonds (284.4 eV), as well as the C–O (288,6 eV) and C=O bonds (289.1 eV). The origin of a small C=O peak in the pristine graphene/PET sample may be from photoelectrons ejected from the PET substrate or from the water molecules trapped between the flakes in the film.

In figure 5(b), the O 1s band peak has been deconvoluted to reveal the C–O (533.6 eV) and C=O (532 eV) bonds. In both C 1s and O 1s bands the chemical modification by HNO_3 is evident through the change in the intensity of C=O peaks. This change is small (oxygen content is reduced from 7.3 to 5.9 at%) and can not solely account for the change in conductivity of graphene films after the treatment with nitric acid. The relative depth plot (see supplementary information figure S3) reveals the change in the elemental distribution across the graphene layer. In pristine graphene films, oxygen atoms are mostly placed closer to the surface layer, while in the acid-treated films the situation is reversed. This can be an indication of the rearrangement in the LBA graphene films on the substrate, with oxygen bonds established between the edges of the graphene flakes deeper in the film. This result is in accordance with the reduction of

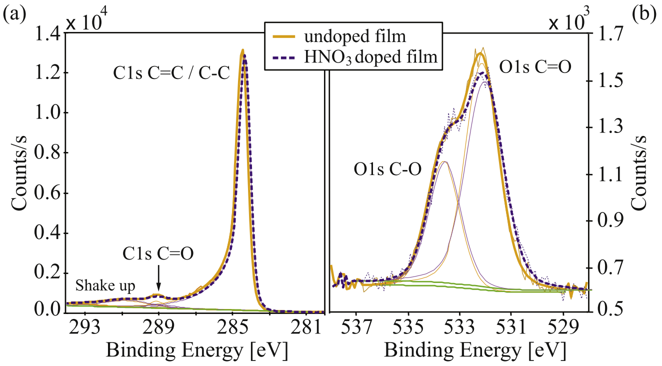

Figure 5. (a) and (b) detailed photoelectron spectra for C 1s and O 1s bands, respectively. Here, solid and dashed lines represent a LBA GS film on PET before and after chemical doping.

the relative intensity of the D- and G-modes in our Raman spectra, corresponding to the GS edges.

The amount of nitrogen in acid-treated films increased from 0.5 to 1 at%. The nature of the measurements could potentially diminish in a small fraction the amount of nitrogen present in the sample. However, the samples were not heated and the nitrogen is incorporated within the film, therefore the change in at% of nitrogen that could arise from these measurements is neglected. In the high-resolution spectrum of N 1s band (see supplementary information figure S3), there is no evidence of the shift in binding energy corresponding to N–O or N–C chemical bonding. Its binding energy (399.8 eV) corresponds to previously reported conjugated nitrogen which does not belong to the graphene molecule [61].

XPS analysis indicates that nitrogen is not incorporated in the honeycomb lattice structure as this would result in n-doping of graphene [51]. The $C{=}O^-$, $C(O)OH^-$, and NO_3^- bonds are changing the carbon atoms hybridization and possibly allowing for the creation of edge-plane like catalytic sites in graphene [52, 62]. Which one of these chemical moieties is the most important factor contributing to the improved conductivity of HNO_3-treated graphene is not clear.

3.7 Transmittance measurements

The effect of chemical doping on optical properties of LBA GS films was investigated with measurements of optical transmittance, using a spectroscopic ellipsometer in photometric mode (SOPRA GES5E IRSE). Figure 6(a) shows the transmittance of a LBA GS film in the visible and UV ranges on quartz. In the UV, the transmittance of graphene is dominated by an exciton-shifted van Hove peak in absorption [63–65]. For this reason the measured data was fitted with a Fano resonant function [65, 66]. Average transmittance of a single LBA GS film at a wavelength of 650 nm was (78 ± 4)%. Considering that each layer of graphene absorbs 2.3% of incident light in the visible part of the spectrum [67] and has a thickness of 0.335 nm, the average film thickness indicated by transmittance measurements is (3.2 ± 0.6) nm, in agreement with AFM measurements.

The transmittance of the doped film at the same wavelength is 74%, which is within the experimental error and the variation between individual samples (figure 6(a), shaded area). While the transmittance decreased only slightly with chemical doping, the sheet resistivity of this sample decreased by a factor of ~ 4.5.

3.8 Raman spectroscopy

Raman spectra of LBA GS films prior to and after nitric acid doping were also investigated. Room temperature measurements of Raman spectra were obtained using a TriVista 557 S&I GmbH Raman spectrometer ($\lambda = 532$ nm). Figure 6(b) shows Raman spectra of a LBA GS film on a glass substrate prior to (solid line) and after (dashed line) chemical doping, compared with graphite powder (dotted-line) before the LPE process. Analogous results were obtained for films on a PET substrate (see supplementary information), however in this case Raman spectra is dominated by PET modes. No significant shifts of any characteristic Raman modes of graphene (graphite) were detected after chemical doping. The only notable change of the Raman spectra due to chemical doping was the reduction of a $I(\mathrm{D})/I(\mathrm{G})$ relative intensity by 25% (see figure 6(b) inset). The relative intensity $I(\mathrm{D})/I(\mathrm{G})$ is indicative of the amount of GS edge scattering [68], hence our results point to a weakening of edge effects in doped films.

3.9 Work function measurements

The work function of a surface holds important information about the electronic structure. Using Kelvin probe force microscopy (KPFM, NTEGRA Spectra), we measured the work function of LBA GS films prior to and after chemical treatment, using the tabulated value of the work function for highly ordered pyrolytic graphite (HOPG) [69, 70] as a reference for

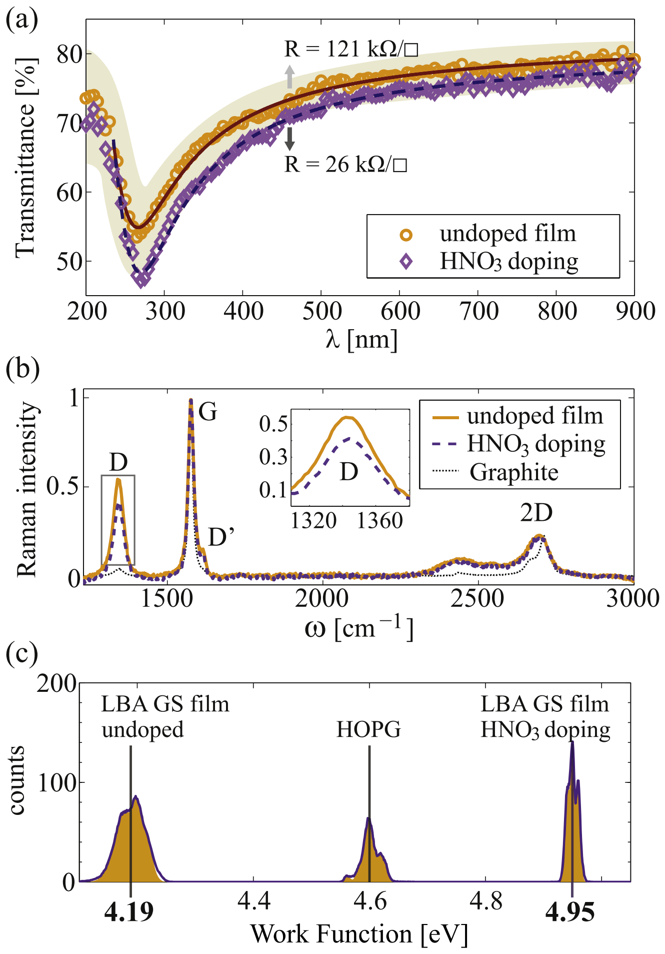

Figure 6. (a) Transmittance of a LBA GS film in the visible and UV ranges on quartz substrate, before (circles) and after (diamonds) chemical doping with HNO_3. Solid and dashed lines represent a Fano resonant function fits. (b) Raman spectra of a LBA GS film, before (solid line) and after (dashed line) chemical doping. Inset of (b) enlarged D modes, showing a reduction of $I(D)/I(G)$ intensity by 25% after chemical doping. (c) KPFM histograms of LAB GS film before (left) and after (right) chemical doping. Positions of the peaks were calibrated with the respect to the measurements of HOPG (middle).

calibrating the AFM tip (details in supplementary information).

As a result, the work function values of (4.19 ± 0.05) eV and (4.95 ± 0.05) eV were obtained for the LBA GS films prior and after chemical doping, respectively. The results are presented in figure 6(c). Undoped films have much lower work function than HOPG, which is expected due to the presence of a large number of GS edges. Furthermore, this confirms that GSs are not functionalized, since in the case of reduced GO or surfactant assisted LPE much higher work functions of the resulting films are obtained [71].

Chemical doping with nitric acid increases the work function by as much as 0.75 eV, a 50% larger increase than in the case of a similar treatment of CVD graphene [17, 50]. An increase of the work function confirms that electrons migrate from GSs [72], resulting in further p-doping and a decrease of the Fermi level with the respect to Dirac point. Adsorption of NO_3^- groups at the sheet edges is also expected to strongly contribute to the increase of the work function.

3.10 Dependence of the sheet resistivity upon axial strain

In addition to chemical doping, the change of the sheet resistivity of LBA GS films on PET substrates was investigated under various bending conditions. The curvature of the substrate was controlled by a micrometer screw in steps of 150 μm, as schematically presented in figure 7(a). The amount of bending is expressed as an axial strain (ϵ) that LBA GS films suffer at the surface of a PET substrate upon bending. Bending radii down to 6 mm were used, giving values of axial strain up to 1.6%. Stretched LBA GS films have shown an increase in the sheet resistivity, significantly larger than in the CVD graphene [9]. Upon axial strain of about 1.5% LBA GS films on PET substrate show an increase of sheet resistivity by as much as 50%. Furthermore, Raman spectra of strained films (given in supplementary information figure S5) did not show any detectable shifts of graphene modes. This indicates that individual GSs are not exhibiting a significant amount of strain. The change in sheet resistivity is attributed to increased separation between individual

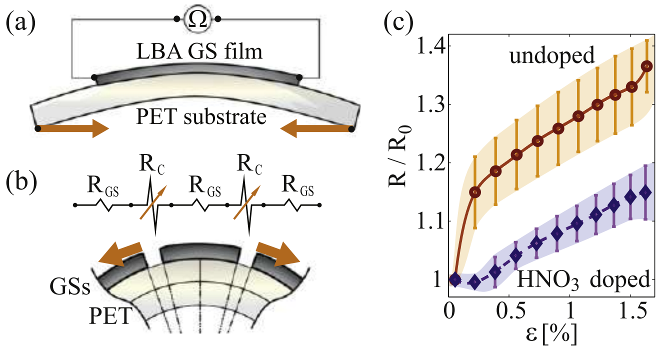

Figure 7. Schematic representations of (a) the bending setup, and (b) how the stretching affects the sheet resistivity components of a LBA GS film. (c) Uniaxial strain dependent relative change in the sheet resistivity of a single LBA GS film, with (diamonds) and without (circles) chemical doping. R_{GS} and R_C stand for the resistance of individual GSs and contact resistance between sheets, respectively.

GSs, which increases the contact resistance between them, as schematically presented in figure 7(b). The relative change in sheet resistivity upon bending reaches 20% larger values in undoped films, as presented in figure 7(c). A large change of resistance upon axial strain opens up a possibility to use LBA GS films in sensing applications as strain gauges, pressure sensors, touch screens or e-skin [73].

Chemically doped samples show a significantly different change in sheet resistivity under small axial strain. For bending radii greater than 30 mm (axial strain less than 0.3%) chemically doped samples show a negligible change in the sheet resistivity. On the other hand, undoped samples show more than 10% change for the same bending conditions. Axial strain of 0.3% would correspond to the separation between individual sheets of 0.36 nm when an averaged sheet diameter of 120 nm is considered. Interestingly, this is well matched with a thermochemical radii of NO_3^- anions. This indicates that NO_3^- groups attached at the edges of GSs provide a contact between the sheets until a high enough axial strain is reached. Afterwards, the sheet resistivity of the doped samples follow a similar trend as the undoped ones. This opens up a possibility to use chemically doped LBA GS films for flexible TCEs, in the cases when small bending radii are not required.

4 Conclusion

In summary, we have shown how the LBA of multilayer GSs produced from the dispersion in NMP and transferred on PET can be used to fabricate transparent and conductive films. An excellent adhesion of these films on PET enables for a straightforward chemical doping and stacking of multiple layers. In particular, p-type chemical doping with nitric acid has been used to reduce sheet resistivity and increase work function of these films, thus making them a more suitable low-cost alternative to CVD graphene for various TCE applications.

The sheet resistivity of deposited LBA GS layers on PET was found to be (70 ± 6) kΩ/□ with the transmittance of 78% at 650 nm wavelength. Upon a short exposure to nitric acid, sheet resistivity was reduced 5–6 fold, reaching the value of (12 ± 3) kΩ/□ with a minor reduction of the visible light transmittance. An increase of the LBA GS film work function by 0.75 eV was found upon chemical doping, yielding a value of 4.95 eV for the doped films. The work function measurements and the dependance of the sheet resistivity upon axial strain both indicate that a large reduction of the sheet resistivity occurs due to adsorption of NO_3^- groups at the edges of GSs. This reduces a contact resistance between the sheets, in addition to an increase of carrier concentration within the sheets.

Acknowledgments

This work is supported by the Serbian MPNTR through Projects ON 171005, III 45018, 451-03-2802-IP/1/167, by Qatar National Research Foundation through Project NPRP 7-665-1-125, and from the proof-of-concept project form the Office of Research and Graduate Studies of TAMUQ.

References

[1] Novoselov K S, Falko V I, Colombo L, Gellert P R, Schwab M G and Kim K 2012 *Nature* **490** 192–200
[2] Ferrari A C *et al* 2014 *Nanoscale* **7** 4598–810
[3] Bonaccorso F, Colombo L, Yu G, Stoller M, Tozzini V, Ferrari A C, Ruoff R S and Pellegrini V 2015 *Science* **347** 1246501
[4] Segal M 2009 *Nat. Nanotechnol.* **4** 612–4
[5] Park S and Ruoff R S 2009 *Nat. Nanotechnol.* **4** 217–24
[6] Britnell L *et al* 2013 *Science* **340** 1311–4
[7] Bonaccorso F, Lombardo A, Hasan T, Sun Z, Colombo L and Ferrari A C 2012 *Mater. Today* **15** 564–89
[8] De S and Coleman J N 2010 *ACS Nano* **4** 2713–20
[9] Kim K S, Zhao Y, Jang H, Lee S Y, Kim J M, Kim K S, Ahn J-H, Kim P, Choi J-Y and Hong B H 2009 *Nature* **457** 706–10
[10] Blake P *et al* 2008 *Nano Lett.* **8** 1704–08
[11] Wang X, Zhi L and Mullen K 2008 *Nano Lett.* **8** 323–7
[12] Wang H-X, Wang Q, Zhou K-G and Zhang H-L 2013 *Small* **9** 1266–83

[13] Pang S, Hernandez Y, Feng X and Mullen K 2011 *Adv. Mater.* **23** 2779–95

[14] Kratzer M, Bayer B C, Kidambi P R, Matković A, Gajić R, Cabrero-Vilatela A, Weatherup R S, Hofmann S and Teichert C 2015 *Appl. Phys. Lett.* **106** 103101

[15] Chhikara M, Pavlica E, Matković A, Beltaos A, Gajić R and Bratina G 2014 *Carbon* **69** 162–8

[16] Miao X, Tongay S, Petterson M K, Berke K, Rinzler A G, Appleton B R and Hebard A F 2012 *Nano Lett.* **12** 2745–50

[17] Wu Y, Zhang X, Jie J, Xie C, Zhang X, Sun B, Wang Y and Gao P 2013 *J. Phys. Chem.* C **117** 11968–76

[18] Park H, Chang S, Zhou X, Kong J, Palacios T and Gradecak S 2014 *Nano Lett.* **14** 5148–54

[19] Bae S *et al* 2010 *Nat. Nanotechnol.* **5** 574–8

[20] Wu J, Agrawal M, Becerril H A, Bao Z, Liu Z, Chen Y and Peumans P 2010 *ACS Nano* **4** 43–8

[21] Han T-H, Lee Y, Choi M-R, Woo S-H, Bae S-H, Hong B H, Ahn J-H and Lee T-W 2012 *Nat. Photon.* **6** 105–10

[22] Coraux J, N'Diaye A T, Busse C and Michely T 2008 *Nano Lett.* **8** 565–70

[23] Reina A, Jia X, Ho J, Nezich D, Son H, Bulovic V, Dresselhaus M S and Kong J 2008 *Nano Lett.* **9** 30–5

[24] Li X *et al* 2009 *Science* **324** 1312–4

[25] Hao Y *et al* 2013 *Science* **342** 720–3

[26] Zaretski A V and Lipomi D J 2015 *Nanoscale* **7** 9963–9

[27] Li X, Zhu Y, Cai W, Borysiak M, Han B, Chen D, Piner R D, Colombo L and Ruoff R S 2009 *Nano Lett.* **9** 4359–63

[28] Kasry A, Kuroda M A, Martyna G J, Tulevski G S and Bol A A 2010 *ACS Nano* **4** 3839–44

[29] Stankovich S, Dikin D A, Dommett G H, Kohlhaas K M, Zimney E J, Stach E A, Piner R D, Nguyen S T and Ruoff R S 2006 *Nature* **442** 282–6

[30] Stankovich S, Dikin D A, Piner R D, Kohlhaas K A, Kleinhammes A, Jia Y, Wu Y, Nguyen S T and Ruoff R S 2007 *Carbon* **45** 1558–65

[31] Eda G, Fanchini G and Chhowalla M 2008 *Nat. Nanotechnol.* **3** 270–4

[32] Hernandez Y *et al* 2008 *Nat. Nanotechnol.* **3** 563–8

[33] Cai M, Thorpe D, Adamson D H and Schniepp H C 2012 *J. Mater. Chem.* **22** 24992–5002

[34] Coleman J N *et al* 2011 *Science* **331** 568–71

[35] Eda G, Yamaguchi H, Voiry D, Fujita T, Chen M and Chhowalla M 2011 *Nano Lett.* **11** 5111–6

[36] Withers F *et al* 2014 *Nano Lett.* **14** 3987–92

[37] Torrisi F *et al* 2012 *ACS Nano* **6** 2992–3006

[38] Secor E B, Prabhumirashi P L, Puntambekar K, Geier M L and Hersam M C 2013 *J. Phys. Chem. Lett.* **4** 1347–51

[39] Del S K, Bornemann R, Bablich A, Schäfer-Eberwein H, Li J, Kowald T, Östling M, Bolívar P H and Lemme M C 2015 *2D Mater.* **2** 011003

[40] Dikin D A, Stankovich S, Zimney E J, Piner R D, Dommett G H, Evmenenko G, Nguyen S T and Ruoff R S 2007 *Nature* **448** 457–60

[41] Li X, Zhang G, Bai X, Sun X, Wang X, Wang E and Dai H 2008 *Nat. Nanotechnol.* **3** 538–42

[42] Zhu Y, Cai W, Piner R D, Velamakanni A and Ruoff R S 2009 *Appl. Phys. Lett.* **95** 103104

[43] Kim H, Mattevi C, Kim H J, Mittal A, Mkhoyan K A, Riman R E and Chhowalla M 2013 *Nanoscale* **5** 12365–74

[44] Yang T, Yang J, Shi L, Mäder E and Zheng Q 2015 *RSC Adv.* **5** 23650–7

[45] Biswas S and Drzal L T 2008 *Nano Lett.* **9** 167–72

[46] Woltornist S J, Oyer A J, Carrillo J-M Y, Dobrynin A V and Adamson D H 2013 *ACS Nano* **7** 7062–6

[47] Salvatierra R V, Domingues S H, Oliveira M M and Zarbin A J 2013 *Carbon* **57** 410–5

[48] Geim A and Grigorieva I 2013 *Nature* **499** 419–25

[49] Yang H, Withers F, Gebremedhn E, Lewis E, Britnell L, Felten A, Palermo V, Haigh S, Beljonne D and Casiraghi C 2014 *2D Mater.* **1** 011012

[50] Lee S, Yeo J-S, Ji Y, Cho C, Kim D-Y, Na S-I, Lee B H and Lee T 2012 *Nanotechnology* **23** 344013

[51] Wei D, Liu Y, Wang Y, Zhang H, Huang L and Yu G 2009 *Nano Lett.* **9** 1752–8

[52] Das S, Sudhagar P, Ito E, Lee D-y, Nagarajan S, Lee S Y, Kang Y S and Choi W 2012 *J. Mater. Chem.* **22** 20490–7

[53] Zheng Q, Ip W H, Lin X, Yousefi N, Yeung K K, Li Z and Kim J-K 2011 *ACS Nano* **5** 6039–51

[54] Dresselhaus M S and Dresselhaus G 2002 *Adv. Phys.* **51** 1–86

[55] Fillaux F, Menu S, Conard J, Fuzellier H, Parker S, Hanon A and Tomkinson J 1999 *Chem. Phys.* **242** 273–81

[56] Lancellotti L, Bobeico E, Capasso A, Della Noce M, Dikonimos T, Lisi N and Delli Veneri P 2014 *2014 Fotonica AEIT Italian Conf. on Photonics Technologies* pp 1–3

[57] Larsen L J, Shearer C J, Ellis A V and Shapter J G 2015 *RSC Adv.* **5** 38851–8

[58] Wang J, Zhou M, Tan G, Chen S, Wu F, Lu J and Amine K 2015 *Nanoscale* **7** 8023–34

[59] Xie X, Su D, Zhang J, Chen S, Mondal A K and Wang G 2015 *Nanoscale* **7** 3164–72

[60] Liang X, Fu Z and Chou S Y 2007 *Nano Lett.* **7** 3840–4

[61] Wu Y, Fang S and Jiang Y 1999 *Solid State Ion.* **120** 117–23

[62] Kudin K N, Ozbas B, Schniepp H C, Prud'Homme R K, Aksay I A and Car R 2008 *Nano Lett.* **8** 36–41

[63] Kravets V G, Grigorenko A N, Nair R R, Blake P, Anissimova S, Novoselov K S and Geim A K 2010 *Phys. Rev.* B **81** 155413

[64] Mak K F, Shan J and Heinz T F 2011 *Phys. Rev. Lett.* **106** 046401

[65] Chae D-H, Utikal T, Weisenburger S, Giessen H, Klitzing K v, Lippitz M and Smet J 2011 *Nano Lett.* **11** 1379–82

[66] Matković A, Beltaos A, Milićević M, Ralević U, Vasić B, Jovanović D and Gajić R 2012 *J. Appl. Phys.* **112** 123523

[67] Nair R R, Blake P, Grigorenko A N, Novoselov K S, Booth T J, Stauber T, Peres N M R and Geim A K 2008 *Science* **320** 1308

[68] Khan U, O'Neill A, Lotya M, De S and Coleman J N 2010 *Small* **6** 864–71

[69] Yu Y-J, Zhao Y, Ryu S, Brus L E, Kim K S and Kim P 2009 *Nano Lett.* **9** 3430–4

[70] Takahashi T, Tokailin H and Sagawa T 1985 *Phys. Rev.* B **32** 8317

[71] Bausi F, Schlierf A, Treossi E, Schwab M G, Palermo V and Cacialli F 2015 *Org. Electron.* **18** 53–60

[72] Giovannetti G, Khomyakov P A, Brocks G, Karpan V M, van den Brink J and Kelly P J 2008 *Phys. Rev. Lett.* **101** 026803

[73] Zang Y, Zhang F, Di C-a and Zhu D 2015 *Mater. Horiz.* **2** 140–56

Opt Quant Electron (2016) 48:319
DOI 10.1007/s11082-016-0591-1

Transparent and conductive films from liquid phase exfoliated graphene

Tijana Tomašević-Ilić[1] · Jelena Pešić[1] · Ivana Milošević[1] · Jasna Vujin[1] · Aleksandar Matković[1] · Marko Spasenović[1] · Radoš Gajić[1]

Received: 5 November 2015 / Accepted: 6 May 2016 / Published online: 14 May 2016

Abstract We describe transparent and conductive films of liquid-phase exfoliated graphene deposited with the Langmuir–Blodgett (LB) method. Graphene sheets (GS) were exfoliated from graphite by ultrasonic treatment in N-Methyl-2-pyrrolidone (NMP) and N, N-dimethylacetamide (DMA) solvents. For comparison, graphene sheets were also exfoliated in a water solution of surfactants. We confirm a higher exfoliation rate for surfactant-based processing compared to NMP and DMA. Furthermore, we demonstrate that our films exfoliated in NMP and DMA, deposited with LB and annealed have a higher optical transmittance and lower sheet resistance compared to films obtained with vacuum filtration, which is a necessary step for GS exfoliated in water solutions. The structural, optical and electrical properties of graphene layers were characterized with scanning electron microscopy, atomic force microscopy, UV/VIS spectrophotometry and sheet resistance measurements. Our facile and reproducible method results in high-quality transparent conductive films with potential applications in flexible and printed electronics and coating technology.

Keywords Graphene · LPE · Langmuir–Blodgett assembly

1 Introduction

Transparent conductors are an essential part of many optical devices. Many of the thin metallic or metal oxide films used as transparent conductors (Granqvist 2007) exhibit nonuniform absorption across the visible spectrum (Phillips et al. 1994), or they are

---

This article is part of the Topical Collection on Advances in the Science of Light.

Guest Edited by Jelena Radovanovic, Milutin Stepic, Mikhail Sumetsky, Mauro Pereira and Dragan Indjin.

✉ Tijana Tomašević-Ilić
ttijana@ipb.ac.rs

[1] Center for Solid State Physics and New Materials, Institute of Physics, University of Belgrade, Pregrevica 118, 11080 Belgrade, Serbia

chemically unstable, or both (Scott et al. 1996; Schlatmann et al. 1996). The experimental discovery of graphene (Novoselov et al. 2004) brought a new alternative to this field. Graphene is a material with high optical transparency, large carrier mobility, good chemical stability, and mechanical strength, making it an excellent choice for transparent electrodes in various optoelectronic devices (Blake et al. 2008).

Although graphene is a natural choice for transparent conductive films (Bonaccorso et al. 2010), the feasibility of its mass production is essential for applications. In order to produce large quantities of graphene Blake et al. (Blake et al. 2008) and Hernandez et al. (2008) developed a method of graphene production using solvent assisted exfoliation (or liquid phase exfoliation, LPE) of bulk graphite, which is simpler and less costly than chemical vapor deposition and returns a higher yield than mechanical exfoliation (Novoselov et al. 2004, 2005). LPE allows the possibility to scale up the synthesis of graphene making it economically available in a large amount, presenting a promising route for large-scale production (Paton et al. 2014).

Numerous research efforts followed up to increase the concentration and quality of the graphene flakes produced. One of the most promising synthesis routes for LPE graphene is non-covalent exfoliation using solvents that have surface energy values comparable to that of graphite (Hernandez et al. 2008). Typically ultrasound assists the separation of graphene flakes from graphite powder in solvent. Exfoliation conditions such as the initial concentration of graphite powder, sonication time (Khan et al. 2010), solvent type (O'Neill et al. 2011; Bourlinos et al. 2009; Hernandez et al. 2010; Lotya et al. 2009; Guardia et al. 2011), and possible filtration (Khan et al. 2011) were tuned in order to optimize the yield and quality of graphene dispersions. These graphene dispersions can be used to form films by various methods, for example spray coating (Blake et al. 2008), vacuum filtration (Hernandez et al. 2008; Lotya et al. 2009) or Langmuir–Blodgett assembly (LBA) (Cote 2009; Kim et al. 2013; Li et al. 2008).

In this study, graphene sheets (GS) were exfoliated from graphite by ultrasonic treatment in organic solvents with high boiling points, N-Methyl-2-pyrrolidone (NMP), N, N-dimethylacetamide (DMA), and for comparison, in a water solution of surfactant, sodium dodecylbenzenesulfonate (SDBS) and Pluronic P-123 (P-123). The graphene dispersions from NMP and DMA were used to form films by controlled deposition of few-layer graphene using the Langmuir–Blodgett (LB) method on a water–air interface. We confirm a higher exfoliation rate for surfactant-based processing, but demonstrate that our films exfoliated in organic solvents with high boiling points and deposited with LB have a higher optical transmittance and lower sheet resistance compared to films obtained with vacuum filtration, which is a necessary step for GS exfoliated in water solutions. The structural, optical and electrical properties of graphene layers were characterized with scanning electron microscopy, atomic force microscopy, UV/VIS spectrophotometry and sheet resistance measurements.

2 Experimental procedure

All chemicals used were purchased from Sigma Aldrich: graphite powder (product number 332461), N-Methyl-2-pyrrolidone (product number 328634), N, N-dimethylacetamide (product number 38840), sodium dodecylbenzenesulfonate (product number 289957) and Pluronic P-123 (product number 435467). The particular graphite powder product was chosen for its large initial flake size, which should result in the largest possible graphene flakes after exfoliation. Stock solutions of SDBS and P-123 of different concentrations were prepared in deionized water (resistivity 18 MΩ) by stirring overnight. A range of graphene dispersions were prepared. A typical sample was prepared by dispersing graphite in the desired solvent using from 30 min to 14 h of sonication in a low power sonic bath. The resulting dispersion was centrifuged for 60 min at 3000 rpm in order to reduce the amount of unexfoliated graphite.

The graphene sheets exfoliated from graphite by ultrasonic treatment in NMP were used to form films at a water–air interface. Beakers filled with deionized water, 10 mL volume, were used for film formation. A 1.5–2 vol% of GS + NMP was added to the interface with a continuous flow rate of 5–10 mL/s (Fig. 1a). This set of parameters provides enough surface pressure for the film to be close-packed. After the film is formed, it is slowly scooped onto the targeted substrate (Fig. 1b), as shown in our previous work (Matković et al. 2016). PET and SiO_2/Si were used as substrates. As it has been shown that annealing decreases sheet resistance due to solvent evaporation (Hernandez et al. 2008; Lotya et al. 2009), some of these deposited films were annealed. Annealing was carried out in a tube furnace at 250 °C in an argon atmosphere for 2 h.

For optical characterization, UV–VIS spectra were taken using a SUPER SCAN Varian spectrophotometer with quartz cuvettes. The resistance of each sample was measured in a two-point probe configuration, and the sheet resistance was obtained by including the sample geometry factors. AFM measurements were taken with an atomic force microscope, NTEGRA Spectra, in tapping mode. SiO_2/Si was chosen as a substrate for AFM due to its low surface roughness. The lateral profile of graphene flakes was analyzed with a Tescan MIRA3 field-emission gun SEM.

3 Results and discussion

We optimized for high graphene concentration and large flake size, tuning exfoliation conditions such as initial graphite concentration, sonication time and solvent type. The Lambert–Beer law was applied to UV–VIS absorption spectra to find graphene concentration. The concentration was estimated from the absorbance at 660 nm by using the extinction coefficient of graphene ($\alpha = 13.90$ mL mg^{-1} m^{-1}) previously determined in surfactant/water solutions (Hernandez et al. 2008; Lotya et al. 2009; Guardia et al. 2011) and ($\alpha = 24.60$ mL mg^{-1} m^{-1}) in NMP and DMA solutions (Hernandez et al. 2008). Figure 2a depicts a higher final concentration for surfactant-based processing for all initial concentrations of graphite powder, from 0.5 to 18 mg mL^{-1}. The most commonly used deposition technique for LPE GS is vacuum filtration. This is a necessary step for GS exfoliated in water solutions. For GS films formed by evaporation of a high boiling point

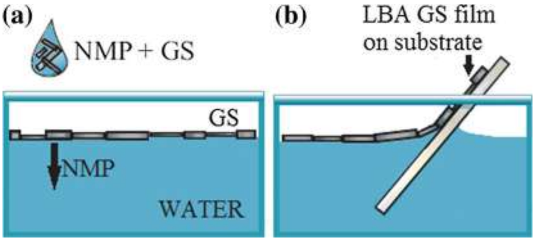

Fig. 1 Schematic representations of **a** LBA GS film formation, **b** scooping of the film onto a targeted substrate

solvent, one of the biggest problems is that graphene flakes aggregate during evaporation (O'Neill et al. 2011) hindering fine control over the film thickness (Hernandez et al. 2008). This can be avoided by depositing with LB, which allows reliable and reproducible thickness control and prevents further agglomeration of graphene flakes during drying (Kim et al. 2013). We chose the dispersion in NMP with the highest graphene concentration (Fig. 2b) for experiments on LB films.

A single LB deposition resulted in films with an average thickness 3.3 nm, as measured with AFM, indicating an average GS thickness of 10 layers (Fig. 3).

Figure 4 shows optical transmittance versus sheet resistance for varying number of LB depositions on PET, compared to graphene film obtained with vacuum filtration of GS exfoliated from the same graphite precursor using the same experimental procedure (Hernandez et al. 2008; Lotya et al. 2009) before and after annealing. The highest transparency for a single LB film deposition prior to annealing was found to be about 83 %, which is between 20 and 40 % higher than the transmittance that can be accomplished with vacuum-filtration. The sheet resistance of one LB film deposition is between 70 and 250 kΩ/sq, 2–5 times lower than sheet resistance achieved with vacuum filtration without annealing. Increasing the graphene film thickness with additional LB depositions led to consistent increases in conductivity, but a decrease in transparency. Our graphene films for three LB depositions prior to annealing have comparable sheet resistance but higher optical transmittance compared to vacuum-filtered films after annealing.

The electrical conductivity is affected by the size and connectivity of the flakes as well as the thickness of the films. Our average GS diameter was is 120 nm, as measured with SEM (Fig. 5). SEM also revealed the presence of pinholes between flakes for a single LB deposition, which probably results in parasitic sheet resistance (Fig. 5a). In order to remove the residual solvent between the overlapping flakes, which may affect transport, we employed thermal annealing. Annealing does not repair the holes and other irreversible defects (Fig. 5b), but it can remove residual solvents, improving the coupling between graphene flakes and hence decreasing sheet resistance. For a single LB deposition, annealing reduced sheet resistance by about six times, without considerably decreasing transparency (Fig. 4). The sheet resistance of a singly deposited film after annealing was found to be between 10 and 20 kΩ/sq, a significant improvement over other published data. After annealing we performed a second LB deposition and achieved sheet resistance of

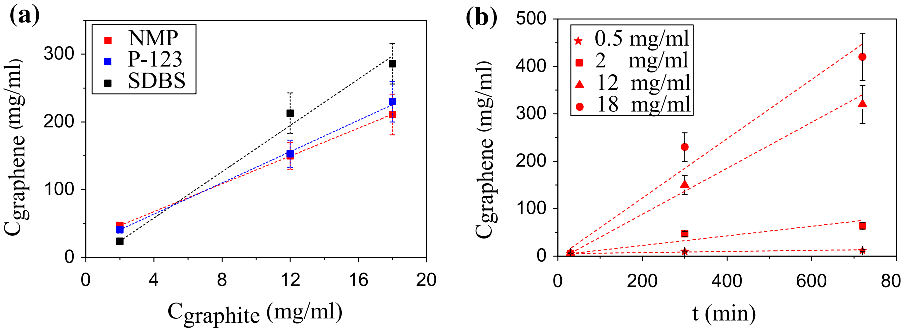

Fig. 2 Concentration of dispersed graphene: **a** in different solutions for different initial graphite concentration and sonication time of 5 h, **b** in NMP for different sonication time and different initial graphite concentration

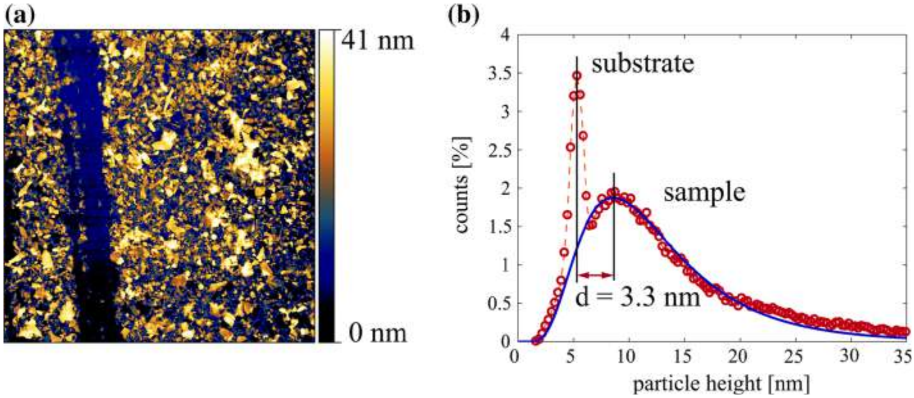

Fig. 3 **a** AFM image of a LB graphene film on a SiO_2/Si substrate, **b** an LB GS film/substrate height histogram fitted with a log-normal curve

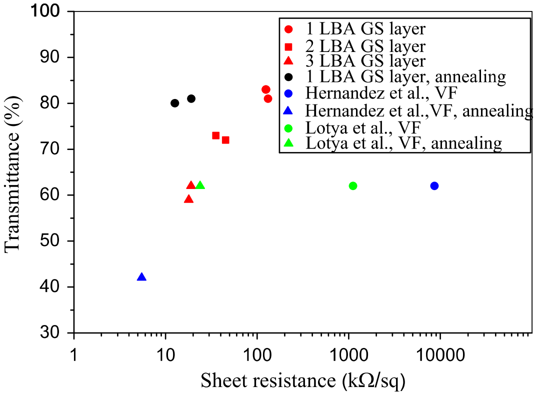

Fig. 4 Optical transmittance versus sheet resistance for varying number of LB deposition of graphene sheets on PET exfoliated in NMP before (*red*) and after annealing (*black*), compared to graphene films obtained with vacuum filtration in the same solvent (*blue*) (Hernandez et al. 2008) and graphene films obtained with vacuum filtration in surfactant/water solutions (*green*) (Lotya et al. 2009) before and after annealing. (Color figure online)

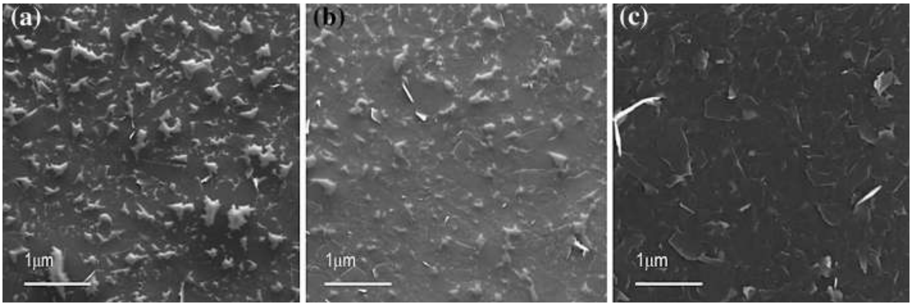

Fig. 5 SEM images of: **a** singly deposited LB film on a glass substrate, **b** the same film after annealing, **c** two LB depositions with an annealing step in between

3 kΩ/sq and a transparency of more than 70 %. Decreased resistance is the result of reduced density of pinholes (Fig. 5c) as well as increased film thickness.

4 Conclusion

In summary, we have shown that Langmuir–Blodgett assembly of multi-layer graphene sheets produced from liquid phase exfoliation of graphite powder in solvents can be used to fabricate transparent and conductive films. The sheet resistance of deposited LBA GS layers was found to be between 15 and 250 kΩ/sq, with transmittance between 60 and 85 %, depending on the number of deposited LBA graphene layers. The conductivity of these LBA films can be further increased by about six times with annealing, without considerably decreasing transparency. Optoelectronic properties of these films are much better compared to graphene films obtained with vacuum filtration of GS exfoliated with the same experimental procedure, which is the most commonly used deposition technique for LPE GS. Ours is a facile, reproducible and low-cost technique for transparent conductive films with potential applications in coating technology.

Acknowledgments This work was funded by the Serbian MPNTR through Projects OI 171005 and Innovation Project 451-03-2802-IP/1/167 and by Qatar National Research Foundation through Projects NPRP 7-665-1-125. The authors would like to express their gratitude to S. Novkovic for technical support with annealing.

References

Blake, P., et al.: Graphene-based liquid crystal device. Nano Lett. **8**, 1704–1708 (2008)

Bonaccorso, F., et al.: Graphene photonics and optoelectronics. Nat. Photonics **4**, 611–622 (2010)

Bourlinos, A.B., et al.: Liquid-phase exfoliation of graphite towards solubilized graphenes. Small **5**, 1841–1845 (2009)

Cote, L.J.: Langmuir–Blodgett assembly of graphite oxide single layers. J. Am. Chem. Soc. **131**, 1043–1049 (2009)

Granqvist, C.G.: Transparent conductors as solar energy materials: a panoramic review. Sol. Energy Mater. Sol. Cells **91**, 1529–1598 (2007)

Guardia, L., et al.: High-throughput production of pristine grapheme in an aqueous dispersion assisted by non-ionic surfactants. Carbon **49**, 1653–1662 (2011)

Hernandez, Y., et al.: High-yield production of graphene by liquid-phase exfoliation of graphite. Nat. Nanotechnol. **3**, 563–568 (2008)

Hernandez, Y., et al.: Measurement of multicomponent solubility parameters for graphene facilitates solvent discovery. Langmuir **26**, 3208–3213 (2010)

Khan, U., et al.: High-concentration solvent exfoliation of graphene. Small **6**, 864–871 (2010)

Khan, U., et al.: Solvent-exfoliated graphene at extremely high concentration. Langmuir **27**, 9077–9082 (2011)

Kim, H.K., et al.: Optoelectronic properties of graphene thin films deposited by a Langmuir–Blodgett assembly. Nanoscale **5**, 12365–12374 (2013)

Li, X., et al.: Highly conducting graphene sheets and Langmuir–Blodgett films. Nat. Nanotechnol. **3**, 538–542 (2008)

Lotya, M., et al.: Liquid phase production of graphene by exfoliation of graphite in surfactant/water solutions. J. Am. Chem. Soc. **131**, 3611–3620 (2009)

Matković, A., et al.: Enhanced sheet conductivity of Langmuir-Blodgett assembled graphene thin films by chemical doping. 2D Mater. **3**(1), 015002 (2016)

Novoselov, K.S., et al.: Electric field effect in atomically thin carbon. Science **306**, 666–669 (2004)

Novoselov, K.S., et al.: Two-dimensional atomic crystals. Natl. Acad. Sci. U.S.A. **102**, 10451–10453 (2005)

O'Neill, A., et al.: Graphene dispersion and exfoliation in low boiling point solvents. J. Phys. Chem. C **115**, 5422–5428 (2011)

Paton, K.R., et al.: Scalable production of large quantities of defect-free few-layer graphene by shear exfoliation in liquids. Nat. Mater. **13**, 624–630 (2014)

Phillips, J.M., et al.: Transparent conducting thin films of GalnO3. Appl. Phys. Lett. **65**, 115–117 (1994)

Schlatmann, A.R., et al.: Indium contamination from the indium–tin–oxide electrode in polymer light emitting diodes. Appl. Phys. Lett. **69**, 1764–1766 (1996)

Scott, J.C., et al.: Degradation and failure of MEH-PPV light-emitting diodes. J. Appl. Phys. **79**, 2745–2751 (1996)

www.nature.com/scientificreports

SCIENTIFIC REPORTS
natureresearch

OPEN

Single-step fabrication and work function engineering of Langmuir-Blodgett assembled few-layer graphene films with Li and Au salts

Ivana R. Milošević[1]✉, Borislav Vasić[1], Aleksandar Matković[2]✉, Jasna Vujin[1], Sonja Aškrabić[3], Markus Kratzer[2], Thomas Griesser[4], Christian Teichert[2] & Radoš Gajić[1]

To implement large-area solution-processed graphene films in low-cost transparent conductor applications, it is necessary to have the control over the work function (WF) of the film. In this study we demonstrate a straightforward single-step chemical approach for modulating the work function of graphene films. In our approach, chemical doping of the film is introduced at the moment of its formation. The films are self-assembled from liquid-phase exfoliated few-layer graphene sheet dispersions by Langmuir-Blodgett technique at the water-air interfaces. To achieve a single-step chemical doping, metal standard solutions are introduced instead of water. Li standard solutions (LiCl, $LiNO_3$, Li_2CO_3) were used as n-dopant, and gold standard solution, $H(AuCl_4)$, as p-dopant. Li based salts decrease the work function, while Au based salts increase the work function of the entire film. The maximal doping in both directions yields a significant range of around 0.7 eV for the work function modulation. In all cases when Li-based salts are introduced, electrical properties of the film deteriorate. Further, lithium nitrate ($LiNO_3$) was selected as the best choice for n-type doping since it provides the largest work function modulation (by 400 meV), and the least influence on the electrical properties of the film.

Graphene, consisting of a single layer carbon arranged in a hexagonal lattice, has attracted extensive interest because of the excellent mechanical and electrical properties associated with its two dimensional structure[1–4]. Chemical vapor deposition (CVD) method has become the most common method for production of large-area graphene films[5]. Still, simple and low-cost methods are needed for mass production especially when considering the cases where high-quality films are not needed for the desired functionality, as in low-power lighting, sensors, transparent heating, and de-icing applications[6]. In that context, liquid-phase exfoliation (LPE) is a perspective way of obtaining large quantities of exfoliated graphite in solution. LPE of graphite results in a dispersion of few-layer graphene sheets (GSs) in the solvent. However, in order to access the full potential of LPE-processed graphene, thin-films needs to be controllably fabricated utilizing techniques capable to introduce self-ordering of GSs[7]. One such example is Langmuir-Blodgett assembly (LBA). Based on surface-tension induced self-assembly of nanoplatelets at the liquid-air interface or the interface of two liquids, LBA is a good method for production of large-scale, highly transparent, thin solution-processed graphene films[8–11].

Excellent electrical conductivity, flexibility and transparency in the visible domain make graphene a natural choice for ultrathin, flexible and transparent electrodes in electronic devices[10,12–19]. Still, a significant work function difference between graphene and frequently employed active layers of photovoltaic and light-emitting diode (LED) devices gives rise to a high contact resistance. Contact resistance can have a significant impact on overall efficiency and performance of the devices[20]. This is of a particular technological relevance considering that any realistic application of graphene based transparent electrode must compete against those based on indium tin

[1]Laboratory for Graphene, other 2D Materials and Ordered Nanostructures of Center for Solid State Physics and New Materials, Institute of Physics, University of Belgrade, Pregrevica 118, 11080, Belgrade, Serbia. [2]Institute of Physics, Montanuniversität Leoben, Franz Josef Str. 18, 8700, Leoben, Austria. [3]Nanostructured Matter Laboratory of Center for Solid State Physics and New Materials, Institute of Physics, University of Belgrade, Pregrevica 118, 11080, Belgrade, Serbia. [4]Institute of Chemistry of Polymeric Materials, Montanuniversität Leoben, Otto-Gloeckel-Straße 2, 8700, Leoben, Austria. ✉e-mail: novovic@ipb.ac.rs; aleksandar.matkovic@unileoben.ac.at

oxide (ITO) or fluorine-doped tin oxide (FTO), which have already gone through decades of interfacial optimization in order to deliver todays' performance[21–23]. Therefore, the understanding of the efficient ways for modulation of the graphene work function is crucial for improving device performances[21,22,24]. In order to enhance the charge injection, the work function of the graphene electrode should be optimized to better match WF of the adjacent layer in order to form an ohmic contact[24].

Recently, the chemical doping has been reported to be an effective method for doping of CVD graphene and tuning its work function by charge transfer between the graphene sheet and metal salts, organic dopants, or metal oxide layers[12,14,21–28]. Such surface charge transfer induced by chemical doping is expected to efficiently control the Fermi level of graphene sheets without introducing substitutional impurities or basal plane reactions, thus, preventing any damage to the carbon networks and not introducing scattering centres that would lower carrier mobility[21]. Kwon *et al*. reported n-type chemical doping of CVD graphene with alkali metal carbonates by soaking in appropriate solutions[23] and alkali metal chlorides by spin-coating of appropriate solutions on the transferred graphene substrates[25]. So far, doping of Langmuir-Blodgett graphene films prepared from LPE dispersions has been done with nitric acid and ozone after the film was formed using the drop-casting method and UV/ozone treatment[9,29]. Chemical doping is especially attractive for LPE-based graphene films since many exposed edges of GSs are expected to enable very efficient functionalization through charge transfer doping. However, the chemical doping with metal salt solutions has not been used to control the work function of LBA graphene films so far. In this work LBA graphene films obtained from LPE dispersion were doped during the process of film formation. Therefore, the formation and doping of the LBA graphene films in our work represent a single-step process. This is a significant improvement compared to previous works where the chemical doping was applied only after the graphene fabrication.

In the present work, we systematically investigated single-step work function modulation (increase and decrease) of the LPE GS films achieved by chemical doping. In particular, using Li standard solutions (LiCl, $LiNO_3$ and Li_2CO_3) as n-dopant, and gold standard solution $H(AuCl_4)$ as p-dopant was investigated. In contrast to previous methods for chemical doping of CVD graphene which can be applied only after the graphene films fabrication, here we described the method for the production and doping of LPE graphene films in a single-step. Single-step work function modulation means doping of the film at the moment of its formation from the LPE graphene dispersion by LBA technique at the air-metal standard solution interface. We have demonstrated tunability of the WF in the range of almost 1 eV, making these metal-salt treated LPE-based graphene electrodes suitable candidates for both electron and hole injection interfaces.

Results and discussion

Morphology of LPE GS films. Fabrication and doping of the GS films is schematically represented in Fig. 1(a): air-metal standard solution interface, introduction of LPE dispersion and formation of the LPE GS film at the interface, scooping of the doped film on the target substrate and finally, obtained doped LPE GS film which is further investigated with different techniques.

Morphology of LPE GS films is depicted in Fig. 1 consisting of both optical (Fig. 1(b1-f1)) and Atomic Force Microscopy (AFM) topographic images (Fig. 1(b2-f2)) for both undoped and metal doped LPE GS films. As can be seen from AFM images, the doping process does not change morphology of LPE films, except that the doped films contain more agglomerates (visible as bright particle-like domains). The following values for the surface roughness were obtained by AFM measurements averaged on ten $50 \times 50\,\mu m^2$ areas: (a) 11.9 ± 1.5 nm for undoped LPE GS film, (b) 11.5 ± 3.5 nm for Li_2CO_3 doped, (c) 13.3 ± 2 nm for $H(AuCl_4)$ doped, (d) 13.7 ± 1.6 nm for LiCl doped, and (e) 13.8 ± 1.2 nm for $LiNO_3$ doped LPE GS films. Therefore, the surface roughness sligtly increases by around 2 nm after the doping, while for Li_2CO_3 doped LPE GS film is practically the same as for the undoped film. Still, optical images recorded on larger scale depict formation of agglomerates in doped films which could degraded their optical (leading to an increased scattering and/or absorption of incoming lights on these clusters) and electrical properties (due to enhanced scattering of charge carriers).

The observed formation of the agglomerates is most likely not an inherent property of the particular metal-salt doping. Overcoming this would likely require further optimization of the LBA process. However, as a benchmark the LBA process in this study was optimized for an undoped film and was left unchanged for all of the metal-salt doped films.

Transmittance measurements. Using the different doping metal standard solution during LBA of graphene films was found to result in different transparency. In the UV region, the transmittance of graphene is dominated by an exciton-shifted van Hove peak in absorption[9,30]. Transmittance at 550 nm was 82% for undoped and 80%, 76%, 74%, 68% for $H(AuCl_4)$, LiCl, $LiNO_3$, Li_2CO_3 doped LPE GS films, respectively (Fig. 2). It can be seen that transmittance decreases for doped LPE GS films. Metal salts decrease the transmittance of the graphene films regardless the type of the present metal (gold or lithium). The degree of the transmittance decrease was related to not only the metal cations but also the anions. Different lithium salts decrease transmittance in different amounts. Transmittance decrease of 14% was the highest for the LPE GS film doped with lithium carbonate (Li_2CO_3). Similar results of the transmittance decrease for metal doped CVD graphene films were obtained in studies of Kwon *et al.*[22,23,25]. Transmittance decrease could be a consequence of the metal particles adsorption and agglomeration on doped films after the solvent evaporation process. Changes in the thickness of LPE GS films with doping could not be excluded because LBA process in this study was optimized for an undoped film and was left unchanged for all of the metal-salt doped films.

Raman measurements. Raman spectra for undoped and $H(AuCl_4)$, LiCl, $LiNO_3$, Li_2CO_3 doped LPE GS films are given in Fig. 3(a). The four basic graphene/graphite peaks D (~1348 cm^{-1}), G (~1579 cm^{-1}), D' (1614

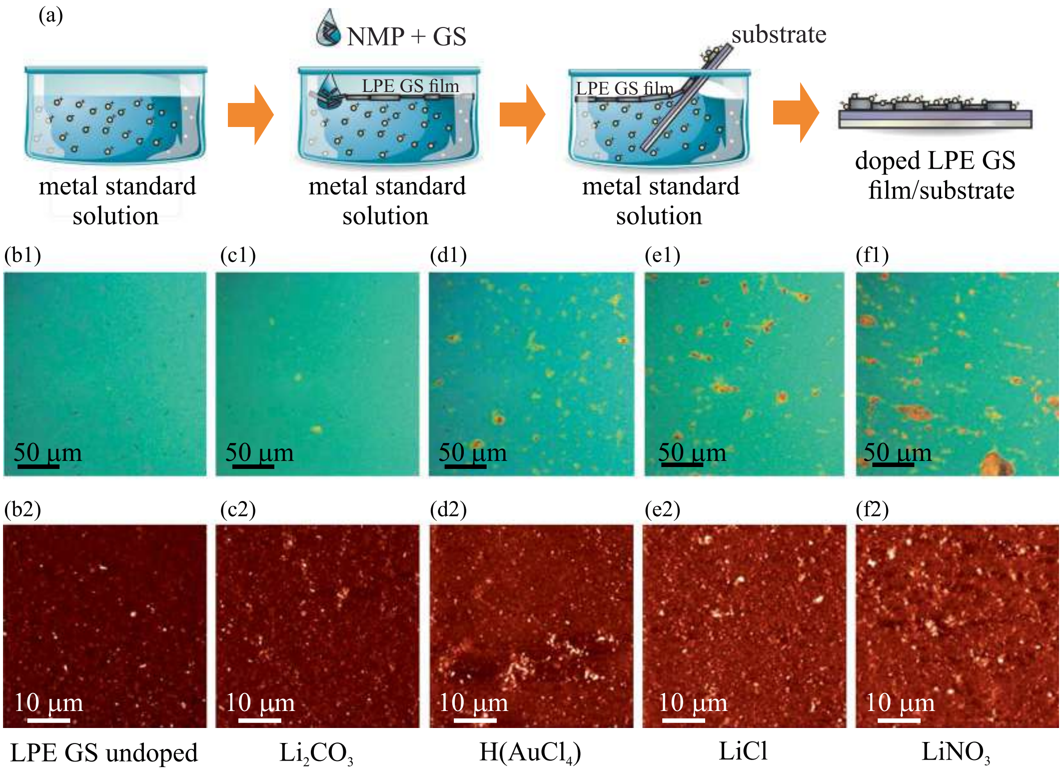

Figure 1. (**a**) Schematic representation of the LPE GS film formation and its doping in the single-step process. (**b1**–**f1**) Optical images are shown in the top row, whereas (**b2**–**f2**) AFM topographic images are shown in the bottom row for the following cases: (**b**) undoped LPE GS film, and (**c**) Li_2CO_3, (**d**) $H(AuCl_4)$, (**e**) LiCl, (**f**) $LiNO_3$ doped LPE GS films. z-scale in all AFM images is 100 nm.

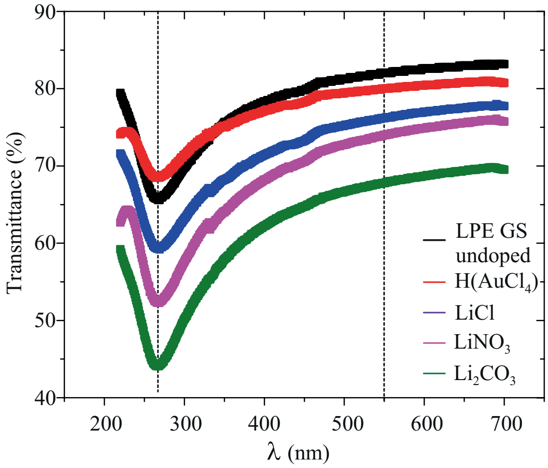

Figure 2. Transmittance spectra of undoped and $H(AuCl_4)$, LiCl, $LiNO_3$, Li_2CO_3 doped LPE GS films.

cm^{-1}) and 2D (2700 cm^{-1}) are observed for all the samples. No significant shifts of any characteristic Raman peaks of graphene were detected after chemical doping (Fig. 3(a)).

The change of the full weight at half-maximum (FWHM) of the Raman modes after doping with metal standard solutions was negligible Fig. 3(b). The only notably change of the Raman spectra was the increase of the intensity ratio of D to G peaks, I(D)/I(G) (Fig. 3(c)). The quantity of defects has been shown to be related to the ratio between the D and G peaks, I(D)/I(G); the larger the ratio, the larger the defect density[31]. We observe increase of the defect density with $H(AuCl_4)$, LiCl, $LiNO_3$, Li_2CO_3 doping in relation to the undoped film and the amount of the increase expressed in percent was 37%, 24%, 29% and 21%, respectively.

All self-assembled films suffer from a large defect density that often leads to a high sheet resistance of deposited film. Therefore, the nature and density of defects in any thin film transparent conductor is important, especially when chemical treatment was used to enhance films' performance. The intensity ratio between the D and

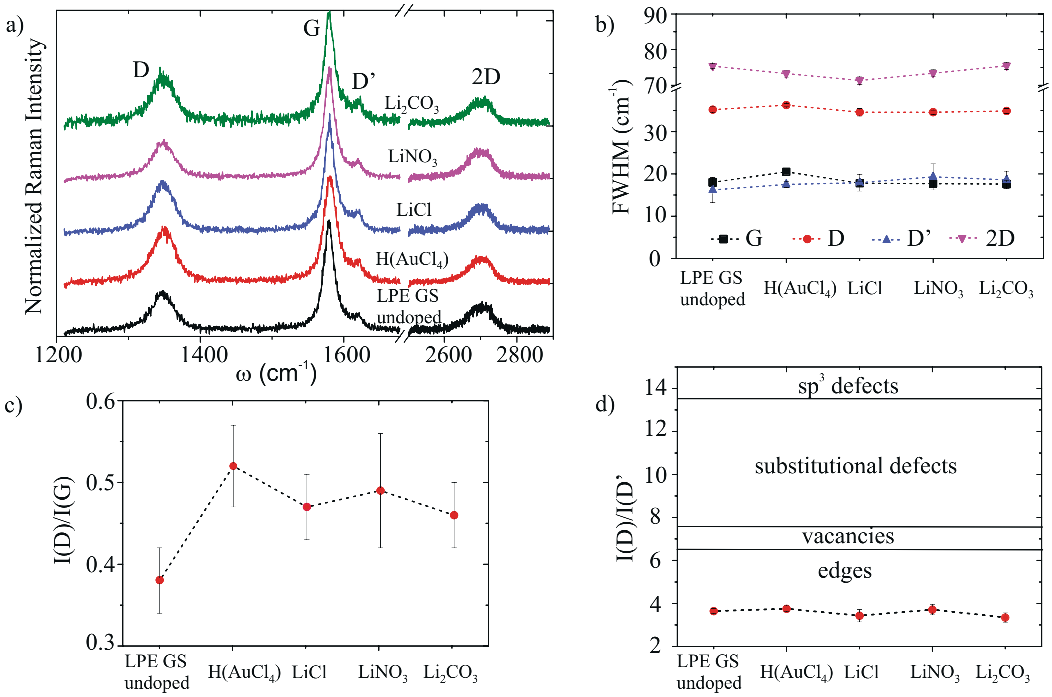

Figure 3. (**a**) Raman spectra of the undoped LPE GS film and films doped with Li and Au salts, (**b**) FWHM of the four basic Raman peaks (**c**)The intensity ratio of D to G peak for different doping metal salts, I(D)/I(G), (**d**) The intensity ratio of D to D' peak, I(D)/I(D'), for different doping metal salts. We refer to peak intensity as the height of the peaks as proposed by Eckmann *et al.*[32].

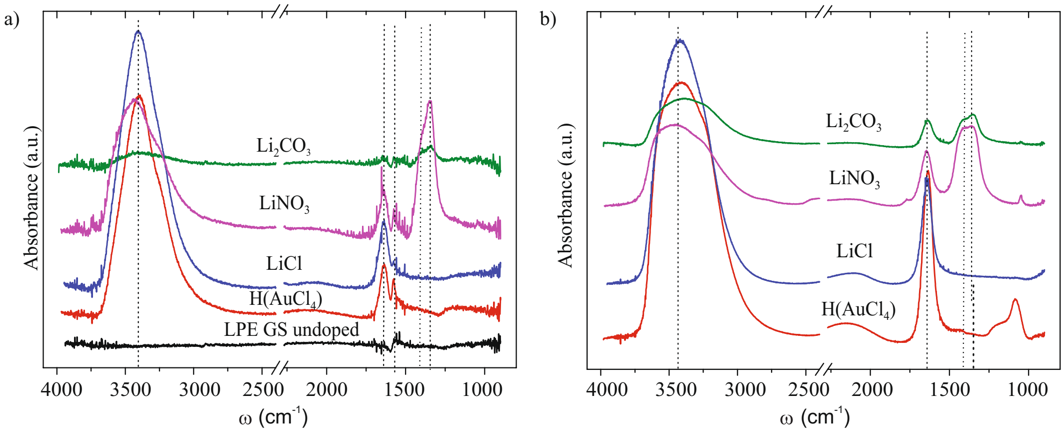

Figure 4. FT-IR spectra of (**a**) undoped and $H(AuCl_4)$, LiCl, $LiNO_3$, Li_2CO_3 LPE GS doped films, (**b**) metal standard solutions (0.1 mg/mL) used for doping processes.

D' peak can be used to get information on the nature of defects in graphene[32,33]. I(D)/I(D') was calculated, and the obtained results were presented in Fig. 3(d). Topological defects (like pentagon-heptagon pairs), boundaries, vacancies, substitutional impurities and sp^3 defects are possible defects in graphene[31]. Studies reporting a ratio of 3.5 for boundaries, 7 for vacancies, 13 for sp^3 and values in-between those for vacancies and sp^3 for substitutional impurities can be found in the literature[31,32,34]. From Fig. 3(d) it can be observed that the D to D' intensity peak ratio is nearly constant in our samples regardless of the doping solution, and the value of the ratio indicates that the edges are the dominant type of defects in our LPE GS films.

Fourier transform infrared absorbance (FT-IR) measurements. FT-IR spectra of undoped and LiCl, $LiNO_3$, Li_2CO_3, $H(AuCl_4)$ doped LPE GS films, as well as FT-IR spectra of corresponding metal standard solutions are shown in Fig. 4.

For the undoped LPE GS film FT-IR spectra is simple. It can be seen only a small peak assignable to C=C skeletal vibration[35–37] of the graphene basal planes at ~1560 cm^{-1}. This peak can also be seen in FT-IR spectra for

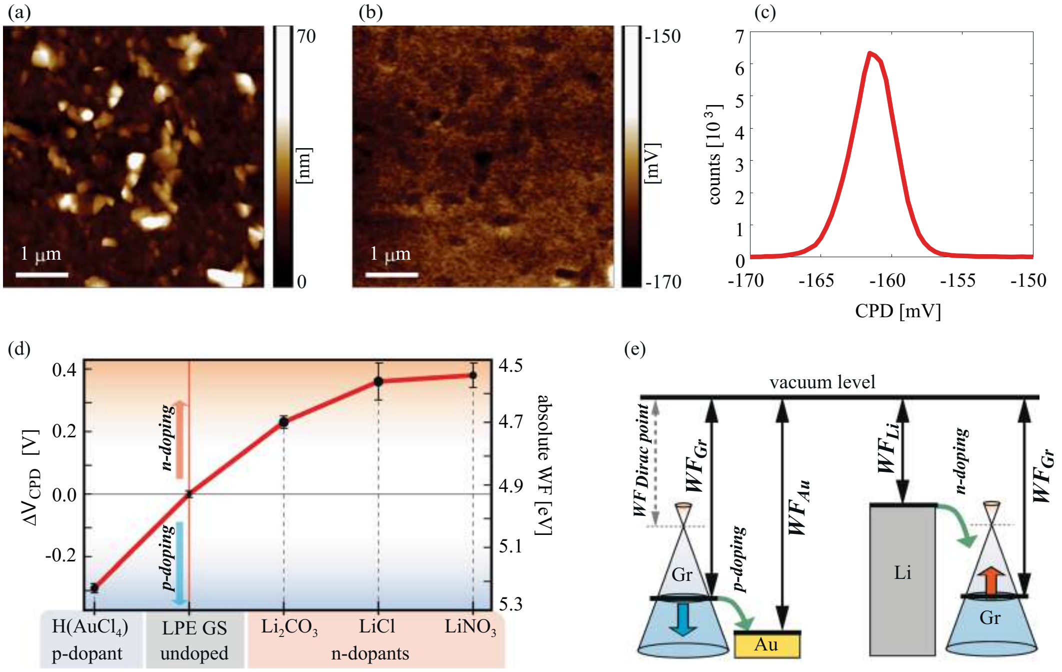

Figure 5. (**a**) AFM topography, (**b**) CPD map measured by KPFM, and (**c**) histogram of (**b**) shown for $H(AuCl_4)$ doped LPE GS film as an example. (**d**) Change in WF for doped LPE GS films for different dopants, in comparison to the undoped LPE GS film. Solid red line in (**d**) is only a guide for the eye. (**e**) Schematic representation of the work functions prior to the interaction (equal vacuum levels) for Au-based salt/graphene and Li-based salt/graphene. The green arrows indicate direction of electron flow showing that in the case of Li (Au) based salts, electrons are transferred to (from) graphene.

all investigated doped films at the same wavenumber indicating that graphene basal planes were not interrupt by doping. The strong peak at around ~3400 cm^{-1} and another, smaller one, near ~1630 cm^{-1} can be seen in all doped LPE GS films (Fig. (4a)) and corresponding metal standard solutions (Fig. (4b)). They are attributed to the water molecules and are assignable to the O-H stretching vibrations (~3400 cm^{-1}) and H-O-H bending mode (~1630 cm^{-1})[38,39]. In the case of FT-IR spectra for LPE GS film doped with $LiNO_3$ the peak at ~1340 cm^{-1} and ~1390 cm^{-1} are assignable to the vibration mode of the NO_3^- ions and asymmetric stretch of O-NO_2, respectively[38,40]. Similar vibration modes can be observed in the case of FT-IR spectra for LPE GS film doped with Li_2CO_3 and can be assigned to the vibration mode of the CO_3^- ions (1340 cm^{-1}) and asymmetric stretch of O-CO_2 (~1390 cm^{-1})[41]. The same vibrational modes could be seen for $LiNO_3$ and Li_2CO_3 standard solutions (Fig. (4b)).

From the observed FT-IR results (Fig. 4(a)) it is clear that additional peaks appear with LPE GS film chemical doping. These additional peaks match with vibrational modes of the anions in solution (Fig. 4(b)). Considering that no new peaks are visible in the given spectra (which would indicate the formation of chemical bonds) the present peaks could be a consequence of the metal salts adsorption to the graphene lattice during the doping. In order to understand Li and Au doping mechanisms XPS measurements were performed and they are presented in separate section.

Work function modulation. Results for the work function dependent on the different metal standard solution used in the LBA process are summarized in Fig. 5. The top row depicts an example with the topography (Fig. 5(a)), corresponding contact potential difference (CPD) map measured by Kelvin probe force Microscopy-KPFM (Fig. 5(b)), and the histogram of the CPD distribution measured on $H(AuCl_4)$ doped graphene film (Fig. 5(c)). The histogram is characterized with a single peak, which is used for the averaging and calculation of the absolute value of work function. The same procedure was done for all considered films. More details about the measurements of CPD and WF calculations are given in Supplementary information in Supplementary Figs. S3-S5. As a result, the values of the absolute work function are presented in Fig. 5(d) for both, doped and undoped LPE GS films. As can be seen, n-doping of graphene films is achieved by Li-based salts, whereas Au-based salt leads to p-doping.

The change of the WF due to the doping can be explained according to the schematic presentation in Fig. 5(e), illustrating that Li (Au) as a lower (higher) work function material compared to GS films. Therefore, presence of Li-based salts into the graphene film results in a reduction of the work function of the entire film. This behavior can be interpreted as an increase in the Fermi level of GSs – compared to the value for the undoped films – indicating predominantly a charge transfer from Li-based salts to graphene (n-doping), as expected when considering that Li has lower WF than graphene (graphite). In contrast to Li-based salts, the Au-based salt shows an opposite trend for the relative change of the work function. This indicates charge transfer from graphene to

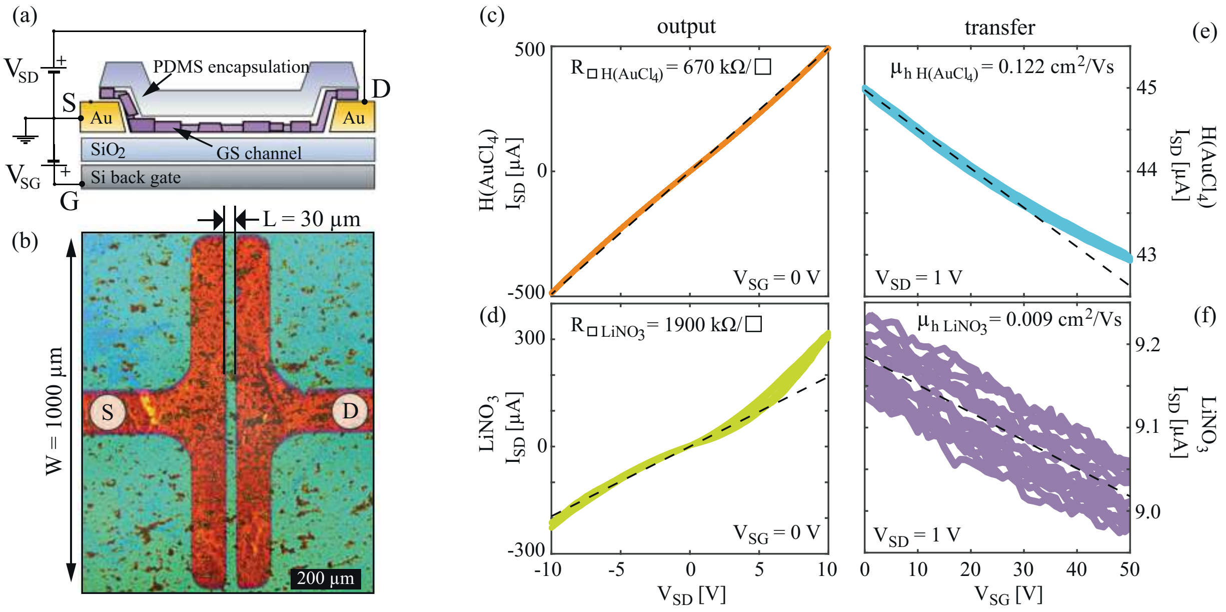

Figure 6. (**a**) Schematic cross-section of the bottom-contacted back-gated FET devices, also indicating electrical connections. (**b**) Optical microscopy image of one of the devices, without PDMS capping (for clarity). LBA GS film covers the entire sample surface. (**c,d**) Output curves of $H(AuCl_4)$ and $LiNO_3$ doped samples, and (**e,f**) transfer curves of $H(AuCl_4)$ and $LiNO_3$ doped samples, respectively. Dashed lines represent least squares linear fits (to selected regions) that were used to extract sheet resistance and linear mobility.

Au-based salt and a relative reduction of the Fermi level in GSs (p-doping). It is also worth mentioning that poly-crystalline nature of LPE based GS films, large amount of sheet edges and presence of the residual solvent (NMP) results in p-doped films[9], as was also observed in the electrical measurements presented in the following subsection. Therefore, WF values are lower for the LPE-based films by at least 200 meV, than for the pristine exfoliated single-crystals[42]. p-type doping is also reflected on the WF of the reference samples (undoped LPE GS), and therefore on the whole accessible range for the WF modulation by this method. This was also highlighted in Fig. 5(e), where the $WF_{Dirac\ point}$ depicts the case of undoped graphene[42].

According to Fig. 5(d), the maximal doping in both directions is similar, around 0.3–0.4 eV, finally providing a significant range of around 0.7 eV for the work function modulation of LPE GS films. The achieved range was obtained for 0.1 mg/mL concentration of dopants. For smaller concentrations (one order of magnitude lower, 0.01 mg/mL), the observed changes in CPD were in the order of 10 mV. On the other hand, for higher concentrations (for one order of magnitude higher, 1 mg/mL) gave rise to the problems related to the formation of continuous, large-area LPE GS films, and were therefore excluded from this study. The reported shift of the Fermi level is very similar to the other (comparable) systems in the literature. WF values change of 0.3 eV in our experiment (chemical doping by Au ions) are the same order of magnitude as in Kwon *et al.* manuscripts for gold-chloride (WF change of 0.6 eV[21], 0.6 eV[22], 0.4 eV[25]). Compared with Kwon *et al.* alkali carbonate[23] and chloride[25] graphene chemical doping data (0.4 eV and 0.3–0.4 eV, respectively) WF values change for Li in our manuscript (0.2 eV and 0.4 eV) are in the same order of magnitude. Compared with literature data the same effect can be achieved but advantages of our approach is fast and simple solution-based method for one-step fabrication and WF control of large-area graphene films.

Sheet resistance. The schematic cross-section of the devices used for the electrical characterization is shown in Fig. 6(a), also indicating electrical connections. An optical microscopy image for one of the devices without PDMS encapsulation (for clarity) is shown in Fig. 6(b) illustrating source (S) and drain (D) contact geometries. One characteristic set of transport and output curves for $H(AuCl_4)$ and $LiNO_3$ doped film is presented in Fig. 6(c–f). Here linear fits were used to extract sheet resistances and apparent linear hole mobilities. Transfer curves for all four salt-treatments and for the reference LPE GS film are presented in the Supplementary information (Supplementary Fig. S1).

In the cases of a reference (undoped) and $H(AuCl)_4$ doped LPE GS samples, output curves barely deviate from a perfect linear behavior in a rather large bias range, indicating that the contact resistance is negligible in comparison to the channel. This is in contrast to all samples doped with Li-based salts, where a significant deviation from the linear output curves were observed at higher bias, indicating non-negligible contact resistance. This can be attributed to large WF differences with Au bottom contacts in the case of Li-based salt doping of the films. Furthermore, while $H(AuCl_4)$ doping enhances electrical performance of the films, a significant increase of the resistivity and reduction of the mobility was observed in the case of all Li-based salt dopings.

The slope of the transfer curves indicates that holes are the majority carriers for all samples, including both the undoped (reference) and all metal salt doped films. Linear fits to the transfer curves were used to estimate

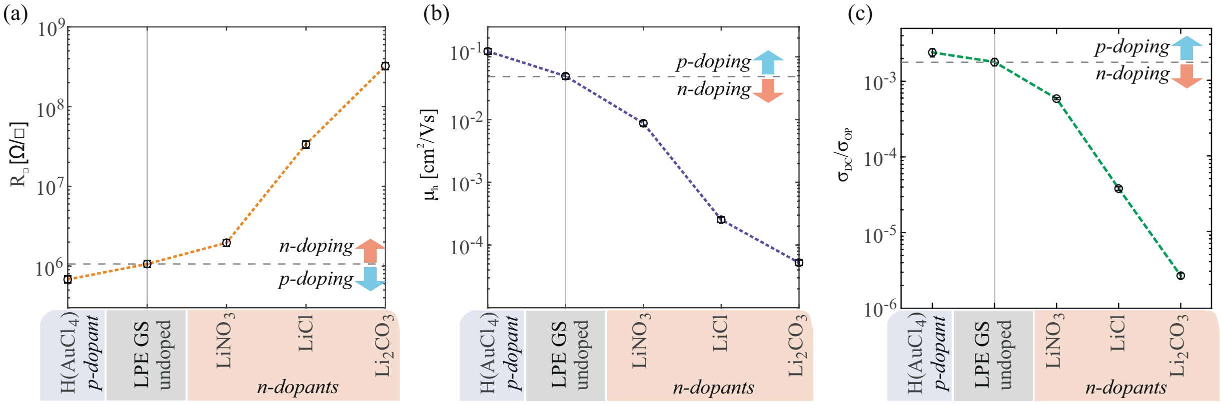

Figure 7. The dependence of the electrical properties of LBA graphene films on the type of metal standard solution based doping; (**a**) sheet resistance, and (**b**) apparent linear hole mobility, and (**c**) direct current conductivity to optical conductivity ratio (σ_{DC}/σ_{OP}). Dashed lines in (**a**–**c**) serve only as a guide for the eye.

apparent hole mobility of the devices. While the type of majority carriers was not affected by the doping, a significant (over one order of magnitude) suppression of the field-effect was observed for Li salt dopings of the films.

Figure 7 summarizes electrical properties obtained for all of the measured devices as a function of the different metal based doping.

The results indicate that anions also play a significant role. In the case of Li-based salts, a large variation of the electrical properties was obtained by the different choice of the anion species. Nonetheless, the experiments point out that metal cations dictate the direction of the WF shift (see Fig. 5), as is apparent in the case of H(AuCl$_4$) and LiCl where only cation species is varied. Our results of metal based doping of LPE graphene films demonstrate a tradeoff between enhancement of the electrical performance and modulation of the WF. Similar results were obtained for CVD doping with Li and Au salts[23,25]. Of a particular technological relevance is large reduction of the WF of graphene. While many methods for chemical modulation of graphene result in p-type doping[43–46], stable and simple n-type doping is much harder to achieve[47–49]. For an efficient electron injection, a significant reduction of graphene's WF is required. As pointed out by WF measurements and electrical characterization, LiNO$_3$ is the best choice from the tested Li-based salts with respect to both the largest WF reduction (by 400 meV) and least deterioration of the electrical properties of the films with ~2–3 times increase in sheet resistance compared to the reference (undoped LPE GS).

In contrast, doping of LPE GS films by HNO$_3$ vapor results in an increase of the apparent mobility[9]. However, using a LiNO$_3$ solution reduces the mobility by one order of magnitude. Therefore, Li$^+$ cations – and not anions – are likely responsible for the deterioration of the electrical properties upon n-doping. An increase of sheet resistance was observed in doping of CVD graphene with alkali metal carbonates and chlorides[23,25]. There, a significant increase in the sheet resistance was related to the combination of carbon atoms and dopant metals because electron donation occurred[23,25]. Also, Chen *et al.* observed that the mobility of the charge carriers decreases with the increase of the potassium doping concentration which they attributed to additional scattering caused by ionized potassium atoms[49,50]. It is most likely that Li$^+$ cations are acting as scattering centers for the carriers, or provide traps at the boundaries between neighbouring GSs and effectively increase contact resistance between the overlapping GSs.

Finally, considering that the main potential application of these LPE GS films lies in transparent electrodes, direct current conductivity to optical conductivity ratio (σ_{DC}/σ_{OP}) is presented in Fig. 7(c) for all metal standard solution doping cases and for the reference (undoped). σ_{DC}/σ_{OP} is a parameter frequently reported in order to characterize the relative performance of the films in terms of transparency and sheet resistance[11,33,51]. The higher the ratio the better the quality of transparent electrodes[33]. Compared to the changes in the electrical properties (Fig. 7(a)) the changes in the optical properties (Fig. 2) are minor. Therefore, the dependence of the σ_{DC}/σ_{OP} on the type of the metal-ion doping clearly follows the trend set by $1/R_\square$.

X-ray Photoemission Spectroscopy (XPS) measurements. In order to understand Au and Li ion doping mechanisms XPS measurements were performed. C 1 s, Au 4 f and Li 1 s core-level XPS spectra are shown in Fig. 8. N 1 s, Cl 2p and O 1 s spectra are presented as Supplementary Fig. S2. The C 1 s peak of undoped and LiCl, LiNO$_3$, Li$_2$CO$_3$, H(AuCl$_4$) doped LPE GS films is shown on Fig. 8(a). The C 1 s peak is deconvoluted using Gaussian profile into 4 components for undoped and doped films: C=C/C–C in aromatic rings (284.5 eV); C–C sp^3 (285.4 eV); C–O (286.6 eV) and C=O (289 eV)[23,52]. In the case of Li$_2$CO$_3$ we can see a small additional peak at 289.2–291.0 eV[53] which can be assigned to carbonate. Detected oxygen peak (C=O) is likely due to the residual of NMP and oxygen functionalized edges (C–O) on graphene[54,55]. The C=C/C–C peak was shifted to a lower binding energy by about 0.16, 0.48, 0.10 and 0.83 eV for H(AuCl$_4$), LiCl, LiNO$_3$ and Li$_2$CO$_3$ doping process, respectively. The C=C/C–C peak shifts in present work are a consequence of doping by different metal standard solutions. Kwon *et al.* have shown that degree of doping was related to the electronegativity of the anion in the Au complex where anions with a high electronegativity and high bond strength are adequate for use as a p-type

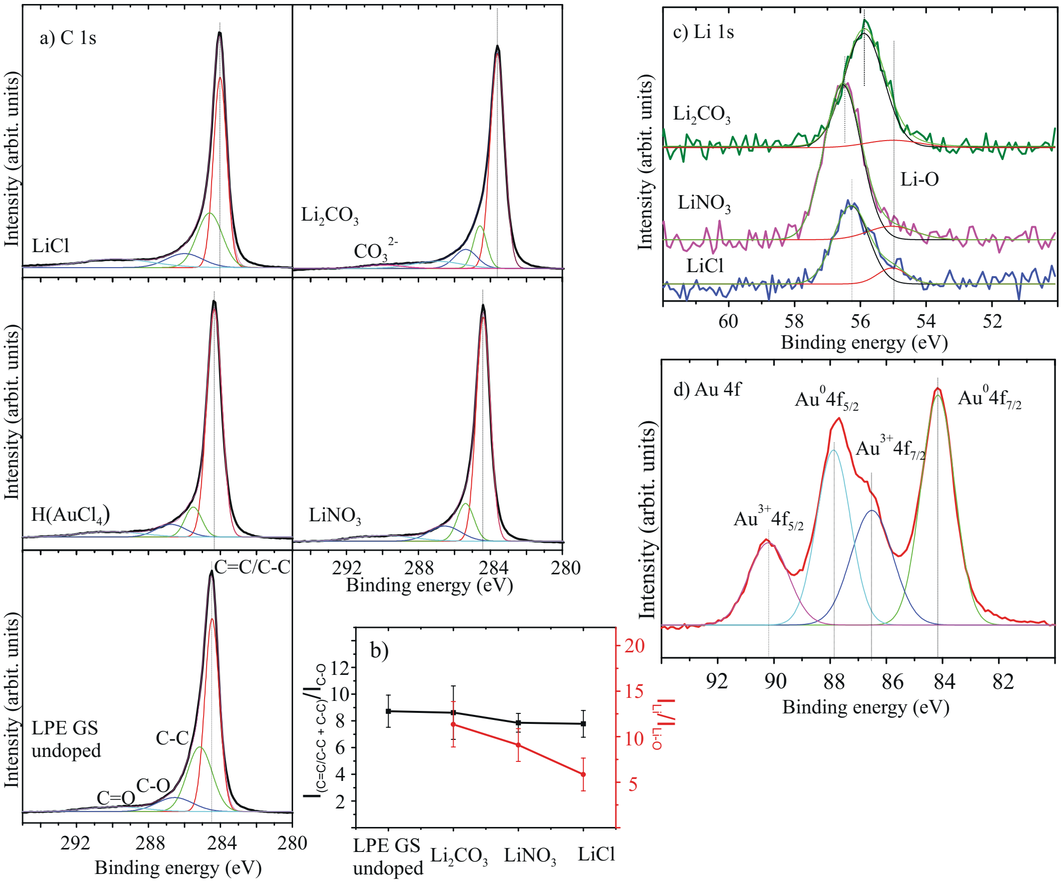

Figure 8. (**a**) XPS C 1 s spectra of undoped and H($AuCl_4$), LiCl, $LiNO_3$, Li_2CO_3 doped LPE GS films. C=C/C–C in aromatic rings (284.5 eV); C–C sp^3 (285.4 eV); C–O (286.6 eV) and C=O (289 eV) were considered. For Li_2CO_3 a small additional peak at 289.2–291.0 eV can be assigned to carbonate. (**b**) Peak intensity ratio for the sum of C=C/C-C and C-C peaks intensities, and the intensity of C-O, $I_{(C=C/C\text{-}C+C\text{-}C)}/I_{(C\text{-}O)}$ (black line) and the ratio of Li 1 s intensity from Li salts to Li-O intensity, $I_{Li}/I_{Li\text{-}O}$ (red line). (**c**) XPS Li 1 s spectra for different Li compounds and for Li–O. (**d**) The Au 4 f peak in the XPS data of H($AuCl_4$).

dopant in graphene[21]. Thus, different shifts of C=C/C–C peak for different metal-salt doping materials could be also a consequence of anions influence on graphene films.

Figure 8(c) show the Li 1 s core-level XPS spectra. Literature values for Li 1 s core-level for different Li compounds are: LiCl (56.2 eV), Li_2CO_3 (55.5 eV) and $LiNO_3$ (55.8 eV)[56] and they correspond well to the values obtained in this work. Li 1 s peak at 55.0 eV is assigned to Li–O bond[57]. Vijayakumar and Jianzhi have shown that lithium ion tends to bind with the oxygen rather than the carbon on graphene surface, and interacts by forming Li-O ionic bond[58]. Also Kwon *et al.* have proposed that C–O–X complexes can be formed during doping treatment and can act as an additional dipole to further reduce the value of WF[23–25,59]. The intensity ratio between sum of the intensities of C=C/C-C and C-C peaks, and the intensity of C-O ($I_{(C=C/C\text{-}C+C\text{-}C)}/I_{(C\text{-}O)}$) is shown in Fig. 8(b). Also, the ratio of Li 1 s intensity from Li salts to Li-O intensity ($I_{Li}/I_{Li\text{-}O}$) can be seen in Fig. 8(b). In both cases, intensity ratios decrease for Li_2CO_3, $LiNO_3$, LiCl, respectively and this implies increased formation of C–O and Li–O bonds. Increased number of Li-O bonds follow the increasing trend of C–O bonds, which is in correlation with the WF change (Fig. (5d)). The above mentioned results strongly suggest that the mechanism of n-type doped LPE GS films with lithium-salts could be explained with formation of Li complexes (C–O–Li).

Figure 8(d) show the Au 4 f peak of gold-chloride doped LPE GS film. The peak is composed of metal (Au^0) and metal ion (Au^{3+}). The peaks at 84.2 eV and 87.9 eV are assigned to neutral Au (Au^0 $4f_{7/2}$ and Au^0 $4f_{5/2}$, respectively), and the peaks at 86.5 eV and 90.2 eV are assigned to Au ion (Au^{3+} $4f_{7/2}$ and Au^{3+} $4f_{5/2}$, respectively). Au ions (Au^{3+}) have positive reduction potential and have tendency to spontaneously accept charges from other materials (graphene) and reduce to Au^0 [21,22,25,60]. Therefore, the mechanism of p-doped LPE GS film can be explained as spontaneous electron transfer from graphene film to Au^{3+}, resulting in depletion of electrons in the graphene networks, thus increasing the WF of doped graphene.

Conclusion

We demonstrate a straightforward single-step method for forming and doping of LPE GS films by metal standard solutions through charge transfer processes. Chemical doping of graphene allows to modulate its WF in a very large range, and therefore potentially enables to use the same electrode material for both, the injection and for the extraction of the electrons. n-doping of graphene films is achieved by Li-based salts, whereas Au-based salt leads to p-doping. Furthermore, solution-processed graphene films are in particular suited for the chemical modulations, since a large number of the sheet edges opens up many adsorption sites and enhances the doping effects when compared to many other types of graphene.

The morphology of the LPE GS films does not change with the doping process, except that doped films contain agglomerates. FT-IR measurements point out that graphene basal planes stay chemically unchanged with metal doping and the charge transfer process is enabled with adsorption of the metal salts. Li-based salts decrease the WF, while Au-based salts increase the WF of the entire film. The maximal doping in both directions gives a significant range of around 0.7 eV for the work function modulation. Changing the dopant (Au or Li based salts) significantly affects the electrical properties of the films. In the case of the Li-based salts doping of the film, a significant suppression of the field-effect mobility and the increase of the sheet resistance was observed. This indicates that adsorbed Li-anions act as scattering centers for the charges. XPS data indicated that different mechanisms exist in the case of Au and Li doping. For Au ions spontaneous charge transfer occurred from graphene, thus increasing WF. In the case of Li doping, potential adsorption sites are a large number of the sheet edges where C-O bonds are preferential sites for lithium ions and for forming of C-O-Li complexes. In all cases graphene films are p-type, which is in accordance with KPFM measurements. Also, tradeoff between Li complex which reduce the value of WF and anion which increase the value of WF could be a reason of such a doping.

Metal salts charge transfer doping – which happens with this single-step method – provides a facile and effective method to tune the WF of LPE graphene therefore extending the potential use of these materials in low-cost transparent electrode applications.

Methods

Preparation of GS dispersion and doping solutions.

A dispersion of GS in N-methyl-2-pyrrolidone (NMP, Sigma Aldrich, product no. 328634) has been used. GS dispersion was prepared from graphite powder (Sigma Aldrich, product no. 332461) of initial concentration 18 mg/mL. The solution was sonicated in a low-power ultrasonic bath for 14 h. The resulting dispersion was centrifuged for 60 min at 3000 rpm immediately after the sonication.

Stock standard solutions used in our work for n-doping are 1 mg/mL LiCl, $LiNO_3$ and Li_2CO_3 and for p-doping is 1 mg/mL gold standard solution (Merck, $H(AuCl_4)$, product no. 170216). Lithium standard solutions were prepared from originated Li salts (LiCl, $LiNO_3$ and Li_2CO_3, Merck, product no. 105679, 105653 and 105680, respectively). By appropriate dilution of the stock solution with deionized water we obtained 0.1 mg/mL metal water solution which is then used in doping process.

Deposition on a substrate and doping of LPE GS films.

GS dispersion in NMP was used to fabricate transparent and conductive films by LBA technique at a water-air interface, like in our previous work[9,29,61]. A small amount of GS dispersion was added to the water-air interface and after the film was formed it was slowly scooped onto the target substrate. Applying the same process of fabricating the GS films and using the appropriate metal standard solution instead of water, chemical doping was achieved. As substrates SiO_2/Si wafer were used for electrical and WF measurements, while quartz and CaF_2 substrates were chosen for optical and FT-IR spectroscopy, respectively.

Characterization of undoped and doped LPE GS films.

The Morphology of LPE GS films was studied by optical and atomic force microscopy (AFM). Topographic AFM measurements were done by NTEGRA Prima AFM system and NSG01 probes with a typical tip radius of around 10 nm. The surface roughness of LPE GS films was calculated as a root-mean square of the height distribution and averaged on ten $50 \times 50\ \mu m^2$ areas.

Kelvin probe force microscopy (KPFM) – established almost three decades ago[62] and in the meantime frequently applied to graphene[42,63–65] – was employed in order to characterize changes in the electrical surface potential and corresponding Fermi level shifts due to doping. For this purpose, we measured the contact potential difference (CPD) between AFM tip and the sample surface[66] by using Pt covered NSG01/Pt probes with a typical tip curvature radius of 35 nm. In the first pass of KPFM, the sample topography was measured in tapping AFM mode. In the second pass, the probe was lifted by 20 nm, and moved along the trajectory measured in the first pass. Simultaneously, the sum of AC and DC voltage was applied between the sample and the probe. The AC voltage excites AFM probe oscillations during its movement, while the CPD between AFM tip and the sample surface in every point is then equal to the value of variable DC voltage which cancels the AFM probe oscillations. For all samples, the CPD was measured on five $5 \times 5\ \mu m^2$ areas, and then averaged. In order to obtain the absolute value of the work function, the following procedure was applied[42]. The CPD is equal to the work function difference between AFM tip (WF_t) and sample (WF_s), $CPD = WF_t - WF_s$. The calibration of the WF_t was done by a standard procedure consisting of KPFM measurements on a freshly cleaved HOPG with a well known work function of 4.6 eV[42]. Finally, the sample work function was calculated as $WF_s = WF_t - CPD$, where CPD is measured by KPFM for all, undoped and doped LPE GS films.

The effect of chemical doping on optical properties of LBA GS films was investigated with measurements of optical transmittance, using UV-VIS spectrophotometer (Beckman Coulter DU 720 UV-VIS Spectrophotometer).

Electrical measurements were performed under ambient conditions in a standard field-effect device configuration with Si substrate acting as a back gate electrode, using Keithley 2636 A SYSTEM SourceMeter. Devices were based on bottom-contact gold pads defined by a shadow mask with $L/W = 30\ \mu m/1000\ \mu m$, and SiO_2 as a gate dielectric with thickness of 285 nm. Graphene films were deposited using the same LBA method as described above. The top surface of the devices was encapsulated by polydimethylsiloxane (PDMS) films (GelPak X4) to ensure stable performance and minimize any adsorption/desorption during electrical measurements that could occur from the surroundings (e.g. water vapor). Electrical characterization was performed on several devices of each doping with metal standard solution, and for undoped films as a reference. For each device ten subsequent forward and backward transfer and output curves were measured, using low sweeping rate (~0.005–1 Hz per point in a voltage sweep) to minimize parasitic capacitance. Sheet resistance and apparent linear field-effect mobility were extracted using fits to output and transfer curves, respectively. For the output measurements source-drain bias was varied in a range between −10 V and +10 V, with the gate electrode grounded. For transfer measurements, the gate voltage was varied between 0 V and 50 V, with source-drain bias at 1 V in all cases except for Li_2CO_3 where due to a very weak field-effect (very low mobility) 10 V bias was used.

The room-temperature micro-Raman spectra of undoped and metal salt doped LPE GS films were collected using Tri Vista 557 triple spectrometer coupled to the liquid nitrogen-cooled CCD detector. Nd:YAG laser line of 532 nm was used for the excitation and 50 magnification objective was used for focusing the beam onto the sample. Low laser power (less than 1 mW) was applied to prevent the thermal degradation of the sample. Each LPE GS film sample was measured at eight different positions.

Fourier transform infrared absorbance spectra (FT-IR spectra) of undoped and metal salt doped LPE GS films were measured over a range of 400–4000 cm^{-1} with Nicolet Nexus 470 FT-IR spectrometer. Standard solutions which were used for the preparation of doped films were measured too and they were prepared by drop casting method on the CaF_2 substrate.

XPS spectra were recorded using a Thermo Scientific instrument (K-Alpha spectrometer, Thermo Fisher Scientific, Waltham, USA) equipped with a monochromatic Al Kα X-ray source (1486.6 eV). High-resolution scans were performed with a pass energy of 50 eV and a step size of 0.1 eV. All analyses were performed at room temperature.

Data availability

The datasets obtained and analysed during the current study that are not included in this article are available from the corresponding authors on reasonable request.

Received: 17 June 2019; Accepted: 28 April 2020;

References

1. Geim, A. K. Graphene: Status and prospects. *Science* **324**, 1530–1534 (2009).
2. Geim, A. K. & Novoselov, K. S. The rise of graphene. *Nat. Mater.* **6**, 183–191 (2007).
3. Novoselov, K. S. *et al*. Room-temperature quantum hall effect in graphene. *Science* **315**, 1379–1379 (2007).
4. Bonaccorso, F., Sun, Z., Hasan, T. & Ferrari, A. C. Graphene photonics and optoelectronics. *Nat. Photonics* **4**, 611–622 (2010).
5. Kwon, K. C., Kim, B. J., Lee, J. L. & Kim, S. Y. Role of ionic chlorine in the thermal degradation of metal chloride-doped graphene sheets. *J. Mater. Chem. C* **1**, 253–259 (2013).
6. Ferrari, A. C. *et al*. Science and technology roadmap for graphene, related two-dimensional crystals, and hybrid systems. *Nanoscale* **7**, 4598–4810 (2015).
7. Backes, C. *et al*. Guidelines for exfoliation, characterization and processing of layered materials produced by liquid exfoliation. *Chem. Mater.* **29**, 243–255 (2017).
8. Li, X. *et al*. Highly conducting graphene sheets and Langmuir-Blodgett films. *Nat. Nanotechnol.* **3**, 538–542 (2008).
9. Matković, A. *et al*. Enhanced sheet conductivity of Langmuir-Blodgett assembled graphene thin films by chemical doping. *2D Mater* **3**, 015002 (2016).
10. Lee, S. K. *et al*. All graphene-based thin film transistors on flexible plastic substrates. *Nano Lett.* **12**, 3472–3476 (2012).
11. Zheng, Q. *et al*. Transparent conductive films consisting of ultralarge graphene sheets produced by Langmuir-Blodgett assembly. *ACS Nano* **5**, 6039–6051 (2011).
12. Park, J. *et al*. Work-function engineering of graphene electrodes by self-assembled monolayers for high-performance organic field-effect transistors. *J. Phys. Chem. Lett.* **2**, 841–845 (2011).
13. Tong, S. W., Wang, Y., Zheng, Y., Ng, M. F. & Loh, K. P. Graphene intermediate layer in tandem organic photovoltaic cells. *Adv. Funct. Mater.* **21**, 4430–4435 (2011).
14. Wang, Y., Tong, S. W., Xu, X. F., Özyilmaz, B. & Loh, K. P. Interface engineering of layer-by-layer stacked graphene anodes for high-performance organic solar cells. *Adv. Mater.* **23**, 1514–1518 (2011).
15. Wu, J. *et al*. Organic light-emitting diodes on solution-processed graphene transparent electrodes. *ACS Nano* **4**, 43–48 (2010).
16. Wang, X., Zhi, L. & Mullen, K. Transparent, conductive graphene electrodes for dye-sensitized solar cells. *Nano Lett.* **8**, 323–327 (2008).
17. Alfano, B. *et al*. Modulating the sensing properties of graphene through an eco-friendly metal-decoration process. *Sensors Actuators, B Chem.* **222**, 1032–1042 (2016).
18. Lynch, P., Khan, U., Harvey, A., Ahmed, I. & Coleman, J. N. Graphene-MoS2 nanosheet composites as electrodes for dye sensitised solar cells. *Mater. Res. Express* **3**, 035007 (2016).
19. Mosciatti, T. *et al*. A multifunctional polymer-graphene thin-film transistor with tunable transport regimes. *ACS Nano* **9**, 2357–2367 (2015).
20. Giubileo, F. & Di Bartolomeo, A. The role of contact resistance in graphene field-effect devices. *Prog. Surf. Sci.* **92**, 143–175 (2017).
21. Kwon, K. C., Kim, B. J., Lee, J. L. & Kim, S. Y. Effect of anions in Au complexes on doping and degradation of graphene. *J. Mater. Chem. C* **1**, 2463–2469 (2013).
22. Kwon, K. C., Choi, K. S. & Kim, S. Y. Increased work function in few-layer graphene sheets via metal chloride doping. *Adv. Funct. Mater.* **22**, 4724–4731 (2012).
23. Kwon, K. C., Choi, K. S., Kim, B. J., Lee, J. L. & Kim, S. Y. Work-function decrease of graphene sheet using alkali metal carbonates. *J. Phys. Chem. C* **116**, 26586–26591 (2012).
24. Huang, J. H., Fang, J. H., Liu, C. C. & Chu, C. W. Effective work function modulation of graphene/carbon nanotube composite films as transparent cathodes for organic optoelectronics. *ACS Nano* **5**, 6262–6271 (2011).
25. Kwon, K. C., Choi, K. S., Kim, C. & Kim, S. Y. Role of metal cations in alkali metal chloride doped graphene. *J. Phys. Chem. C* **118**, 8187–8193 (2014).
26. Wang, X., Xu, J. B., Xie, W. & Du, J. Quantitative analysis of graphene doping by organic molecular charge transfer. *J. Phys. Chem. C* **115**, 7596–7602 (2011).
27. Shin, H. J. *et al*. Control of electronic structure of graphene by various dopants and their effects on a nanogenerator. *J. Am. Chem. Soc.* **132**, 15603–15609 (2010).
28. Shi, Y. *et al*. Work function engineering of graphene electrode via chemical doping. *ACS Nano* **4**, 2689–2694 (2010).

29. Tomašević-Ilić, T. *et al*. Reducing sheet resistance of self-assembled transparent graphene films by defect patching and doping with UV/ozone treatment. *Appl. Surf. Sci.* **458**, 446–453 (2018).
30. Matković, A. *et al*. Spectroscopic imaging ellipsometry and Fano resonance modeling of graphene. *J. Appl. Phys.* **112**, 123523 (2012).
31. Bracamonte, M. V., Lacconi, G. I., Urreta, S. E. & Foa Torres, L. E. F. F. On the nature of defects in liquid-phase exfoliated graphene. *J. Phys. Chem. C* **118**, 15455–15459 (2014).
32. Eckmann, A. *et al*. Probing the nature of defects in graphene by Raman spectroscopy. *Nano Lett.* **12**, 3925–3930 (2012).
33. Rytel, K. *et al*. Ultrasonication-induced sp3 hybridization defects in Langmuir-Schaefer layers of turbostratic graphene. *Phys. Chem. Chem. Phys.* **20**, 12777–12784 (2018).
34. Eckmann, A., Felten, A., Verzhbitskiy, I., Davey, R. & Casiraghi, C. Raman study on defective graphene: Effect of the excitation energy, type, and amount of defects. *Phys. Rev. B - Condens. Matter Mater. Phys.* **88**, 035426 (2013).
35. Drewniak, S. *et al*. Studies of reduced graphene oxide and graphite oxide in the aspect of their possible application in gas sensors. *Sensors* **16**, 103 (2016).
36. Kim, W. J., Basavaraja, C., Thinh, P. X. & Huh, D. S. Structural characterization and DC conductivity of honeycomb-patterned poly(ε-caprolactone)/gold nanoparticle-reduced graphite oxide composite films. *Mater. Lett.* **90**, 14–18 (2013).
37. Ţucureanu, V., Matei, A. & Avram, A. M. FTIR spectroscopy for carbon family study. *Crit. Rev. Anal. Chem.* **46**, 502–520 (2016).
38. Wu, X. *et al*. One-step freezing temperature crystallization of layered rare-earth hydroxide (Ln2(OH)5NO3·nH2O) nanosheets for a wide spectrum of Ln (Ln = Pr-Er, and Y), anion exchange with fluorine and sulfate, and microscopic coordination probed via photoluminescence. *J. Mater. Chem. C* **3**, 3428–3437 (2015).
39. Nakamoto, K. Infrared and Raman Spectra of Inorganic and Coordination Compounds. Part A: Theory and Applications in Inorganic Chemistry; Part B: Application in Coordination, Organometallic, and Bioinorganic Chemistry, 5th Edition (Nakamoto, Kazuo). *John Wiley and Sons* (John Wiley and Sons, 2009).
40. Geng, F. *et al*. New layered rare-earth hydroxides with anion-exchange properties. *Chem. Eur. J.* **14**, 9255–9260 (2008).
41. Lefèvre, G. *In situ* Fourier-transform infrared spectroscopy studies of inorganic ions adsorption on metal oxides and hydroxides. *Adv. Colloid Interface Sci.* **107**, 109–123 (2004).
42. Yu, Y. *et al*. Tuning the graphene work function by electric field effect. *Nano Lett.* **9**, 3430–3434 (2009).
43. Levesque, P. L. *et al*. Probing charge transfer at surfaces using graphene transistors. *Nano Lett.* **11**, 132–137 (2011).
44. Kuruvila, A. *et al*. Organic light emitting diodes with environmentally and thermally stable doped graphene electrodes. *J. Mater. Chem. C* **2**, 6940–6945 (2014).
45. Meyer, J. *et al*. Metal oxide induced charge transfer doping and band alignment of graphene electrodes for efficient organic light emitting diodes. *Sci. Rep* **4**, 5380 (2014).
46. Matković, A. *et al*. Probing charge transfer between molecular semiconductors and graphene. *Sci. Rep* **7**, 9544 (2017).
47. Sanders, S. *et al*. Engineering high charge transfer n-doping of graphene electrodes and its application to organic electronics. *Nanoscale* **7**, 13135–13142 (2015).
48. Han, K. S. *et al*. A non-destructive n-doping method for graphene with precise control of electronic properties via atomic layer deposition. *Nanoscale* **8**, 5000–5005 (2016).
49. Chen, J. H. *et al*. Charged-impurity scattering in graphene. *Nat. Phys.* **4**, 377–381 (2008).
50. Pinto, H. & Markevich, A. Electronic and electrochemical doping of graphene by surface adsorbates. *Beilstein J. Nanotechnol* **5**, 1842–1848 (2014).
51. De, S. & Coleman, J. N. Are there fundamental limitations on the sheet resistance and transmittance of thin graphene films? *ACS Nano* **4**, 2713–2720 (2010).
52. Benayad, A. *et al*. Controlling work function of reduced graphite oxide with Au-ion concentration. *Chem. Phys. Lett.* **475**, 91–95 (2009).
53. López, G. P., Castner, D. G. & Ratner, B. D. XPS O 1s binding energies for polymers containing hydroxyl, ether, ketone and ester groups. *Surf. Interface Anal.* **17**, 267–272 (1991).
54. Hernandez, Y. *et al*. High-yield production of graphene by liquid-phase exfoliation of graphite. *Nat. Nanotechnol* **3**, 563–568 (2008).
55. Kim, H. *et al*. Optoelectronic properties of graphene thin films deposited by a Langmuir-Blodgett assembly. *Nanoscale* **5**, 12365–12374 (2013).
56. Naumkin, A. V., Kraut-Vass, A., Gaarenstroom, S. W. & Powell, C. J. NIST X-ray photoelectron spectroscopy database. Available at: https://srdata.nist.gov/xps/EngElmSrchQuery.aspx?EType=PE&CSOpt=Retri_ex_dat&Elm=Li. (2019).
57. Moulder, J. F., Stickle, W. F., Sobol, P. E. & Bomben, K. D. *Hanbook of X-ray photoelectron spectroscopy*. *Reference book of standard spectra for indentification and interpretation of XPS data* (Perkin-Elmer Corporation, Physical Electronic division, 1992).
58. Vijayakumar, M. & Jianzhi, H. Exploring the interaction between lithium ion and defective graphene surface using dispersion corrected DFT studies. *ECS Trans* **53**, 23–32 (2013).
59. Pickett, W. E. Negative electron affinity and low work function surface: Cesium on oxygenated diamond (100). *Phys. Rev. Lett.* **73**, 1664–1667 (1994).
60. Syu, J. Y. *et al*. Wide-range work-function tuning of active graphene transparent electrodes via hole doping. *RSC Adv.* **6**, 32746–32756 (2016).
61. Tomašević-Ilić, T. *et al*. Transparent and conductive films from liquid phase exfoliated graphene. *Opt. Quantum Electron.* **48**, 319 (2016).
62. Nonnenmacher, M., O'Boyle, M. P. & Wickramasinghe, H. K. Kelvin probe force microscopy. *Appl. Phys. Lett.* **58**, 2921–2923 (1991).
63. Vasić, B. *et al*. Atomic force microscopy based manipulation of graphene using dynamic plowing lithography. *Nanotechnology* **24**, 015303 (2013).
64. Vasić, B. *et al*. Low-friction, wear-resistant, and electrically homogeneous multilayer graphene grown by chemical vapor deposition on molybdenum. *Appl. Surf. Sci*. **509**, 144792 (2020).
65. Panchal, V., Pearce, R., Yakimova, R., Tzalenchuk, A. & Kazakova, O. Standardization of surface potential measurements of graphene domains. *Sci. Rep* **3**, 2597 (2013).
66. Udum, Y. *et al*. Inverted bulk-heterojunction solar cell with cross-linked hole-blocking layer. *Org. Electron.* **15**, 997–1001 (2014).

Acknowledgements

This work has been supported from the Serbian MPNTR through projects OI 171005, OI 171032, 451-03-02141/2017-09/32 and with support from the Lise Meitner fellowship by Austrian Science Fund (FWF): M 2323-N36. We further acknowledge support by the Austrian Academic Exchange Service (OeAD) via the project SRB 13/2018.

Author contributions

I.M. devised the concept of LPE GS films doping with metal standard solutions in the single-step method. I.M. and J.V. prepared LPE dispersions and fabricated undoped and doped LPE GS films on different substrates. B.V. did AFM and KPFM measurements, A.M. performed electrical measurements, I.M. and J.V. did FTIR measurements, S.A. and I.M. performed Raman measurements and I.M., T.G, M.K., S.A. and J.V. performed and processed XPS measurements. C.T. and R.G. oversaw the study. I.M., A.M. and B.V. wrote the manuscript. All authors discussed and analysed the results and reviewed the manuscript.

Competing interests

The authors declare no competing interests.

Additional information

Supplementary information is available for this paper at https://doi.org/10.1038/s41598-020-65379-1.

Correspondence and requests for materials should be addressed to I.R.M. or A.M.

remote sensing

MDPI

Article

Quiet Ionospheric D-Region (QIonDR) Model Based on VLF/LF Observations

Aleksandra Nina [1,*], Giovanni Nico [2,3], Srđan T. Mitrović [4], Vladimir M. Čadež [5], Ivana R. Milošević [1], Milan Radovanović [6,7] and Luka Č. Popović [5,8,9]

[1] Institute of Physics Belgrade, University of Belgrade, 11080 Belgrade, Serbia; novovic@ipb.ac.rs
[2] Istituto per le Applicazioni del Calcolo (IAC), Consiglio Nazionale delle Ricerche (CNR), 70126 Bari, Italy; g.nico@ba.iac.cnr.it
[3] Department of Cartography and Geoinformatics, Institute of Earth Sciences, Saint Petersburg State University (SPSU), 199034 Saint Petersburg, Russia; g.nico@spbu.ru
[4] Novelic, 11000 Belgrade, Serbia; mitar027@beotel.net
[5] Astronomical Observatory, 11060 Belgrade, Serbia; vcadez@aob.rs (V.M.Č.); lpopovic@aob.rs (L.Č.P.)
[6] Geographical Institute "Jovan Cvijić" SASA, 11000 Belgrade, Serbia; m.radovanovic@gi.sanu.ac.rs
[7] Institute of Sports, Tourism and Service, South Ural State University, 454080 Chelyabinsk, Russia; milan.georgaf@gmail.com
[8] Department of Astronomy, Faculty of Mathematics, University of Belgrade, 11000 Belgrade, Serbia; lpopovic@matf.bg.ac.rs
[9] Faculty of Science, University of Banja Luka, 78000 Banja Luka, Bosnia and Herzegovina; luka.popovic@pmg.unibl.org
* Correspondence: sandrast@ipb.ac.rs

Abstract: The ionospheric D-region affects propagation of electromagnetic waves including ground-based signals and satellite signals during its intensive disturbances. Consequently, the modeling of electromagnetic propagation in the D-region is important in many technological domains. One of sources of uncertainty in the modeling of the disturbed D-region is the poor knowledge of its parameters in the quiet state at the considered location and time period. We present the Quiet Ionospheric D-Region (QIonDR) model based on data collected in the ionospheric D-region remote sensing by very low/low frequency (VLF/LF) signals and the Long-Wave Propagation Capability (LWPC) numerical model. The QIonDR model provides both Wait's parameters and the electron density in the D-region area of interest at a given daytime interval. The proposed model consists of two steps. In the first step, Wait's parameters are modeled during the quiet midday periods as a function of the daily sunspot number, related to the long-term variations during solar cycle, and the seasonal parameter, providing the seasonal variations. In the second step, the output of the first step is used to model Wait's parameters during the whole daytime. The proposed model is applied to VLF data acquired in Serbia and related to the DHO and ICV signals emitted in Germany and Italy, respectively. As a result, the proposed methodology provides a numerical tool to model the daytime Wait's parameters over the middle and low latitudes and an analytical expression valid over a part of Europe for midday parameters.

Keywords: ionosphere; D-region; VLF/LF signals; remote sensing; quiet conditions; modeling

check for updates

Citation: Nina, A.; Nico, G.; Mitrović, S.T.; Čadež, V.M.; Milošević, I.R.; Radovanović, M.; Popović, L.Č. Quiet Ionospheric D-Region (QIonDR) Model Based on VLF/LF Observations. *Remote Sens.* **2021**, *13*, 483. https://doi.org/10.3390/rs13030483

Academic Editor: Benedikt Soja
Received: 2 December 2020
Accepted: 26 January 2021
Published: 29 January 2021

1. Introduction

The ionosphere is the upper atmospheric layer that, due to its electrical properties, affects the propagation of electromagnetic waves [1,2]. This property is of high significance in many fields that include application of data obtained by different kinds of microwave signals (like the Global Navigation Satellite System (GNSS) [3–8] and Synthetic aperture radar (SAR) interferometry meteorology [9]), and both signal and ionospheric characteristics have influence on changes in signal propagation within this medium. For example, telecommunication signals emitted from the ground are affected by the ionosphere below the signal reflection height, while satellite signals are primarily affected by the F-region due to the largest values of electron density in the altitude domain located in this region.

Research of ionospheric properties is a very complex task because of permanent influences coming from outer space and different terrestrial layers. For this reason, it is of crucial importance to include as many observational data as possible in their modeling. For example, although the unperturbed D-region has not visible influences on satellite signal propagation, the recent results presented in Reference [10] show the importance of inclusion of its effects during intensive disturbances that are not considered in existing models (see, for example, Reference [11–13]).

Application of the specific technique for remote sensing of the ionosphere depends on the altitude domain. In addition, the choice of a particular analysis methodology depends on temporal and spatial characteristics of the collected data. The remote sensing of the lower ionosphere based on the propagation of very low/low frequency (VLF/LF) radio signals is an effective means to collect continuous observations the covering areas. These signals can propagate several thousand kilometres within the Earth-ionosphere waveguide, and the global observational setup is based on numerous worldwide located transmitters, and receivers. The VLF/LF receivers have the possibility of simultaneous monitoring of several signals coming from different directions with time sampling shorter than 1 s. For this reason, the databases collected by a particular receiver contain information that can be used in analyses of local and global, short and long-term variations. Because of these properties, this type of remote sensing is used in studies of how many terrestrial and extraterrestrial phenomena influence the lower ionosphere and, consequently, the propagation of electromagnetic waves which can significantly be affected by the disturbed D-region [14–21].

There are several models for modeling the VLF/LF propagation in the Earth ionosphere waveguide, such as the Long-Wave Propagation Capability (LWPC) program [22], finite-difference time-domain (FDTD) method [23], coupled beams and effective complex impedance model [24], and Modefinder [25]. These models are used in many studies for determination of ionospheric parameters where characteristics of the considered area, the ionospheric state and properties of the analyzed disturbances affect the possibility of applying certain approximations. For example, during quiet conditions or during disturbances that do not affect the horizontal uniformity of the observed D-region it is possible to assume only altitude variations of the ionospheric plasma parameters, while, in the case of local disturbances caused by for example day-night transitions along the propagation path and lightnings, it is necessary to take into account both the vertical and horizontal variations of these parameters. The horizontal uniform ionosphere is analyzed in many papers using the LWPC and Modefinder models [10,26–31]. As an example, some localized perturbations of the ionosphere are considered in Reference [32]. FDTD method was used to model the day-night transitions along the propagation path (see, for example, Reference [23]). Effects of the geomagnetic field and its variations which can induce the need to include gyrotropy and anisotropy into account are most important in analyses of the high-latitude lower ionosphere, while, in the mid-latitude areas, effects of variations in the geomagnetic field should be taken into account during large geophysical disturbances of the Lithosphere-Atmosphere-Ionosphere-Magnetosphere system caused by large magnetic storms, hurricanes, etc. [24]. In this paper, we present a model of the daytime D-region parameters under quiet conditions which is based on data recorded in ionospheric remote sensing by VLF/LF signals and LWPC program that simulates their propagation. The chosen time period, in absence of local intensive geophysical disturbances (induced by, for example, solar terminator, lightnings, and hurricanes) which are followed by significant anisotropy, allows us to assume a horizontally uniform ionosphere. In addition, we consider mid- and low-latitude domains where influence of the magnetic field variations on the considered signals (the presented model is relevant for not too long propagation paths of VLF/LF signals which are reflected at altitudes below 76 km) is not significant under quiet conditions. To calculate the quiet D-region parameters, we also include into the consideration the analysis of disturbances induced by solar X-ray flares during the mid-day period when the indicated approximations are also justified and already used in many previous studies [10,26–31]. This is possible because solar X-ray flares do not cause local disturbances and induce practically horizontally uniform perturbations, especially within not too large areas, during the mid-day period.

Modeling of the solar X-ray flare perturbed D-region based on data obtained in its remote sensing by the VLF/LF signals assumes two approximations: (1) the lower ionosphere is usually considered as a horizontal uniform medium, and (2) the parameters in quiet conditions are considered as known quantity in which values are determined in previous statistical studies that, generally, do not represent the considered periods and areas. As we already said, the first approximation is good for a not too long propagation path of the considered signal and for daytime periods of a few hours around midday (this period depends on the season) in absence of intensive local disturbances. However, the second approximation can significantly affect the modeling, and this task was a subject of several studies which focused attention on the electron density and Wait's parameters (the "sharpness" and signal reflection height). There are several methodologies used in these studies. They are based on the broad-band detection of radio atmospherics in periods of lightning activities and detection of the narrow-band VLF signals. A technique to measure the local mid-latitude daytime D-region parameters from the Earth-ionosphere waveguide mode interference pattern in spectra of radio atmospherics launched by lightning discharges, presented in Reference [33], is limited to periods of lightning activities. In the cases based on the analysis of narrow-band VLF signals, properties of modeling and necessary approximations which affect certainty of its applications strongly depend on geographical location of the considered transmitters and receivers. Namely, if the propagation path of the considered VLF signal is very long, as, for example, in the case of studies based on data recorded by receiver located in New Zealand from which transmitters are more than 10,000 km away [34–36], it is necessary to include changes in Wait's parameters along the length of the path [34,35]. These changes provide additional possibilities for errors in modeling due to necessary approximations and changes in the ionosphere due to periodical and sudden events. Of course, increasing the propagation path length induces more effects of local disturbances which also affect the model certainty. Analyses of more receivers and transmitters can reduce these problems. A procedure for these ionospheric parameters modeling is given in Reference [37], where data for three signals recorded by six receivers are considered. In the mentioned studies, related to the considered areas, there are presented dependencies of the daytime Wait's parameters on zenith angle during the solar maximum and minimum [34,35], on both zenith angle and local time [33], and dependencies of the signal reflection height on zenith angle for different seasons [35]. Expressions which provide dependencies of Wait's parameters on more variables (zenith angle, season, smoothed sunspot number, latitude, and geomagnetic field) is presented in Reference [38]. However, the equations related to calculation of the signal reflection height cannot be applied to the newer sunspot datasets because one of these equations includes the Zürich sunspot number which refers to production of the sunspot number before 1981.

All these problems and the importance of determination of the quiet D-region parameters for many technologies motivate us to develop a model of the D-region which can be applied to shorter signal paths which significantly reduces disadvantages induced by the long distance signal propagation, and that includes the influences of:

- long-term variations (about 11 years) in solar radiations during solar cycle;
- seasonal variations (due to Earth's revolution);
- daytime periodical changes; and
- sudden mid- and short-term influences

on the D-region properties. In other words, the aim of this study is to develop a procedure that will make it possible to take advantage of densely spaced VLF/LF transmitters and receivers, like those in Europe, to accurately model the D-region parameters in the area of interest and for the considered time period.

In this paper, we present the Quiet Ionospheric D-Region (QIonDR) model which provides a procedure for the determination of the D-region plasma parameters in quiet conditions using the VLF/LF observational data for the considered area in mid- and low-latitude domains, and the considered time period. The QIonDR model provides an analysis of the Wait's parameters "sharpness" and signal reflection height. Determination of these parameters is important because knowing them allows computation of the D-region electron density N and, consequently, many other parameters, using different models [28,31,33,34,39,40]. As a result, in this study we also show the modeled electron density. To visualize the QIonDR model output, we apply it to data for the DHO and ICV signals emitted in Germany and Italy, respectively, and recorded in Serbia.

The article is organized as follows. The proposed methodology is presented in Section 2, while the analyses of observations and events are given in Section 3. Application of the QIonDR model on the DHO and ICV signals recorded in Belgrade is shown in Section 4, and conclusions of this study are given in Section 5.

2. Methodology

In this section, we describe a methodology for modeling Wait's parameters β_0 and H'_0 and the electron density N_{e0} in the quiet ionospheric D-region. This methodology is based on data obtained by the VLF/LF remote sensing of this atmospheric layer, using two VLF/LF signals, and the satellite X-ray flux data needed to determine the periods of ionospheric disturbances induced by solar X-ray flares.

To model propagation of the VLF/LF signal, we use the LWPC program. It models characteristics of the chosen signal considering its propagation in the Earth-ionosphere waveguide. Properties of the bottom boundary are based on the Westinghouse Geophysics Laboratory conductivity map [41], while the upper boundary is characterized by a conductivity that may be specified by the user. In this paper, we used Wait's model of the ionosphere [42] which describes the horizontally homogeneous exponential conductivity profile by conductivity parameter ω_r:

$$\omega_\mathrm{r}(h) = \omega_0^2(h)/\nu(h), \tag{1}$$

where $\omega_0(h)$ and $\nu(h)$ are the electron plasma frequency and effective electron-neutral collision frequency, respectively. The first parameter can be obtained from the electron density N_e ($\omega_0^2(h) \approx 3180 N_\mathrm{e}$), while dependency of the collision frequency ν on the altitude h is given by an approximative equation based on experimental data presented in Reference [43,44]:

$$\nu(h) = 1.82 \times 10^{11} e^{-0.15h}, \tag{2}$$

Finally, according to the obtained vertical profiles of ω_r shown in Reference [42], an approximative equation for this parameter is given in the following form:

$$\omega_\mathrm{r}(h) = 2.5 \times 10^5 e^{\beta(h-H')}, \tag{3}$$

where the parameters β and H' are known as Wait's parameters and called "sharpness" and signal reflection height, respectively. These parameters are input parameters in the LWPC program. ω_r is used for calculation of the reflection coefficient (the phase of the reflection coefficient is referred to the level where $\omega_\mathrm{r} = 2.5 \times 10^5\ \mathrm{s}^{-1}$) which is also dependent on the magnetic field. In Reference [42], it is assumed that the geomagnetic field is purely transverse. This approximation is possible because, for arbitrary directions of propagations, it has been indicated that transverse component of the geomagnetic field is most important for reflection of VLF radio waves at highly oblique incidence. Finally, the reflection coefficient is used in a mode theory calculations, which are described in Reference [42]. The output of LWPC program are the modeled amplitude and phase for input parameters and observed signal. Detailed descriptions of the LWPC and Wait's models are given in Reference [22,42], while their application in the QIonDR model is described in detail in this Section.

Figure 1 shows the work-logic of the proposed methodology. It is split in the following two procedures related to the time period of the analysis of ionospheric parameters: (1) the Midday procedure (MDP), and (2) the Daytime procedure (DTP), detailed in Sections 2.1 and 2.2, respectively.

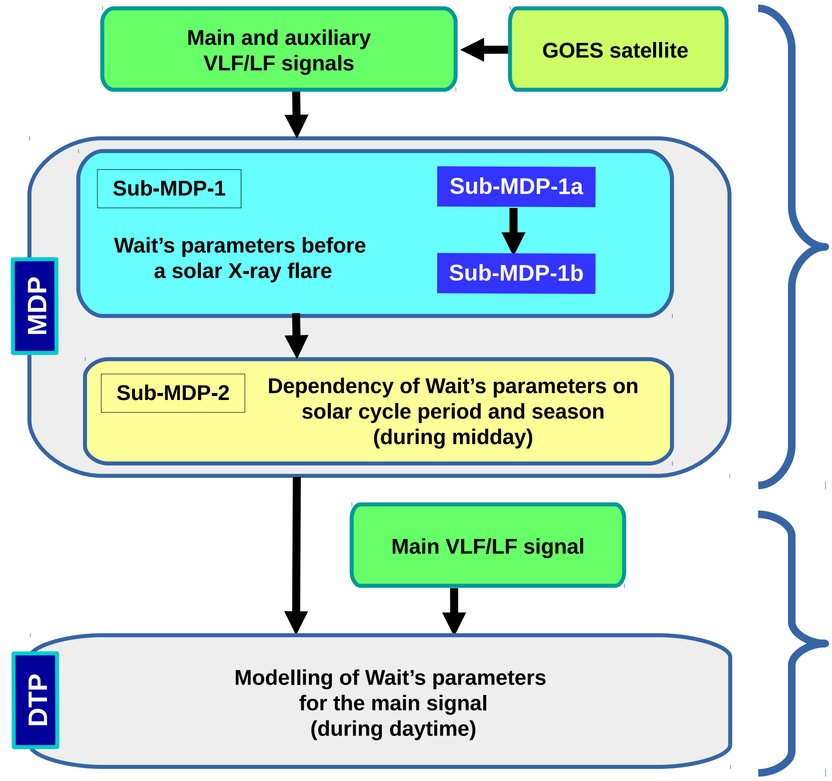

Figure 1. Diagram of the proposed methodology. It consists of two procedures, Midday procedure (MDP) and Daytime procedure (DTP), which are used for the midday and daytime periods. The VLF/LF signals and GOES data are given in input to MDP, which is split in two sub-procedures Sub-MDP-1, to estimate Wait's parameters before a solar X-ray flare, and Sub-MDP-2 to model the dependency of these parameters on the solar cycle period and season at midday. To a finer detail, Sub-MDP-1 is further split in Sub-MDP-1a and Sub-MDP-1b, corresponding to the analyses of a signal s and a disturbed state i of an X-ray flare XF, and determination of Wait's parameters in quiet conditions before a solar X-ray flare XF, respectively. DTP requires as input both the output of MDP and VLF/LF signals to model the daytime evolution of Wait's parameters.

2.1. Midday Periods

First, we analyze the changes in the midday ionospheric parameters induced by solar X-ray flares detected by the GOES satellite which occurred in midday periods. We process the recorded amplitudes and phases of both main and auxiliary VLF/LF signals in order to determine changes of these values at two different times during the solar X-ray flare influence with respect to their values before the disturbance (see Section 2.1.1). These changes are further used as input parameters in MDP (Section 2.1.2) which consists of two sub-procedures, first to determine Wait's parameters before a solar X-ray flare, and second to estimate the dependency of these parameters on the solar cycle period and season at the midday. The first sub-procedure is further split in Sub-MDP-1a and Sub-MDP-1b, corresponding to the analyses of a signal s and a disturbed state i of an X-ray flare XF (XF in general is notation for particular flare; as an example see Table 1), and the determination of Wait's parameters in the quiet conditions before a solar X-ray flare XF, respectively. The output of Sub-MDP-1 consists of Wait's parameters for all considered X-ray flares.

Their values are further fitted in Sub-MDP-2 which provides two functions describing the dependencies of Wait's parameters on the solar sunspot number and season. These two analytical expressions are the output of MDP, and they are used to model the daytime evolution of Wait's parameters in DTP using the amplitude and phase of VLF/LF signals (Section 2.2).

2.1.1. VLF/LF Signal Processing

When an X-ray flare occurs, the main and auxiliary VLF/LF signals are processed, taking both the amplitude and phase, in order to detect changes with respect to their values in quiet conditions before an X-ray flare. Figure 2 shows an example of temporal evolutions of signals' amplitude and phase, where their values in quiet and pertubed conditions are emphasized. These amplitude and phase values are needed in processing steps described in the following:

1. **Determination of the amplitude A_0^{XFs} of signal s in a quiet state before an X-ray flare XF.** To find this value for both VLF/LF signals, we consider three time bins of length Δt_{bin} (in our processing we use $\Delta t_{\mathrm{bin}} = 20$ s) within a time window of a few minutes before the signal perturbation. The amplitude A_0^{XFs} is defined as the minimum of median values of recorded amplitudes in each bin, while the maximal absolute deviation of the recorded amplitudes in the considered bins from the median value is used as a figure for its absolute error $\mathrm{d}A_0^{\mathrm{XFs}}$. In the following, we use "d" for the absolute error and "Δ" to denote the difference between the amplitudes at two different times during the disturbance and quiet state.
2. **Determination of the reference phase $P_{\mathrm{ref}}^{\mathrm{XFs}}$ of a signal s during an X-ray flare XF.** The recorded phase of a VLF/LF signal represents the phase deviation of the considered signal with respect to the phase generated at the receiver. For this reason, the recorded phase has a component of constant slope that should be removed. A linear fit is performed through five points, three before the signal perturbation and two at the end of the considered observation interval, is performed. Phase values at these points are determined in the same way as in the procedure for amplitude estimation as described in point 1). For each time bin Δt, we compute the median value of phase samples. Furthermore, the largest deviation of phase values within each bin is used to estimate the absolute error $\mathrm{d}P_{\mathrm{ref}}^{\mathrm{XFs}}$ of the reference phase.

   It is worth noting that disturbances induced by a solar X-ray flare can last from several tenth of minutes to over one hour. For this reason, quiet conditions can be different before and after disturbances. In addition, it is possible that some sudden events or some technical problem affect at least one signal in a time interval starting after the one used in this study. For instance, in Figure 2, we show a visible increase in the "quiet" visible increase in the "quiet" phase of about 15° and 5° for the DHO and ICV signals, respectively.
3. **Determination of differences in the amplitude ΔA^{XFsi} and phase ΔP^{XFsi} of the signal s during a disturbance induced by a solar X-ray flare XF in state i with respect to quiet conditions.** To avoid any dependence of results on the selection of time, we perform twice the analysis of changes in the signal parameters with respect to the initial, unperturbed state, by selecting two different times which are emphasized by vertical dashed and dotted lines in right panels in Figure 2 displaying time evolutions of the amplitude ($\Delta A^{\mathrm{XFsi}} = A^{\mathrm{XFs}}(t_{\mathrm{i}}) - A_0^{\mathrm{XFs}}$) and phase ($\Delta P^{\mathrm{XFsi}} = P^{\mathrm{XFs}}(t_{\mathrm{i}}) - P_{\mathrm{ref}}^{\mathrm{XFs}}(t)$) changes for both signals during the disturbance induced by the solar X-ray flare occurred on 17 September 2015.

   The absolute errors $\mathrm{d}A^{\mathrm{XFs1}}$ and absolute errors $\mathrm{d}A^{\mathrm{XFs2}}$ of amplitudes A^{XFs1} and A^{XFs2}, and $\mathrm{d}P^{\mathrm{XFs1}}$ and $\mathrm{d}P^{\mathrm{XFs2}}$ of phases P^{XFs1} and P^{XFs2}, respectively, are determined as for the quiet state, i.e.: (1) we calculate A^{XFs1}, A^{XFs2}, P^{XFs1} and P^{XFs2} as median values in two bins of width $\Delta t_{\mathrm{bin}} = 20$ s around times t_1 and t_2; (2) we define absolute errors $\mathrm{d}A^{\mathrm{XFs1}}$ and $\mathrm{d}A^{\mathrm{XFs2}}$, and $\mathrm{d}P^{\mathrm{XFs1}}$ and $\mathrm{d}P^{\mathrm{XFs2}}$ in terms of maximal absolute deviations of the corresponding quantities within the bins. The total absolute errors are obtained as follows:

$$\mathrm{d}(\Delta A^{\mathrm{XFsi}}) = \mathrm{d}A_0^{\mathrm{XFs}} + \mathrm{d}A^{\mathrm{XFsi}}, \tag{4}$$

$$\mathrm{d}(\Delta P^{\mathrm{XFsi}}) = \mathrm{d}P_{\mathrm{ref}}^{\mathrm{XFs}} + \mathrm{d}P^{\mathrm{XFsi}}. \tag{5}$$

where $i = \{1, 2\}$.

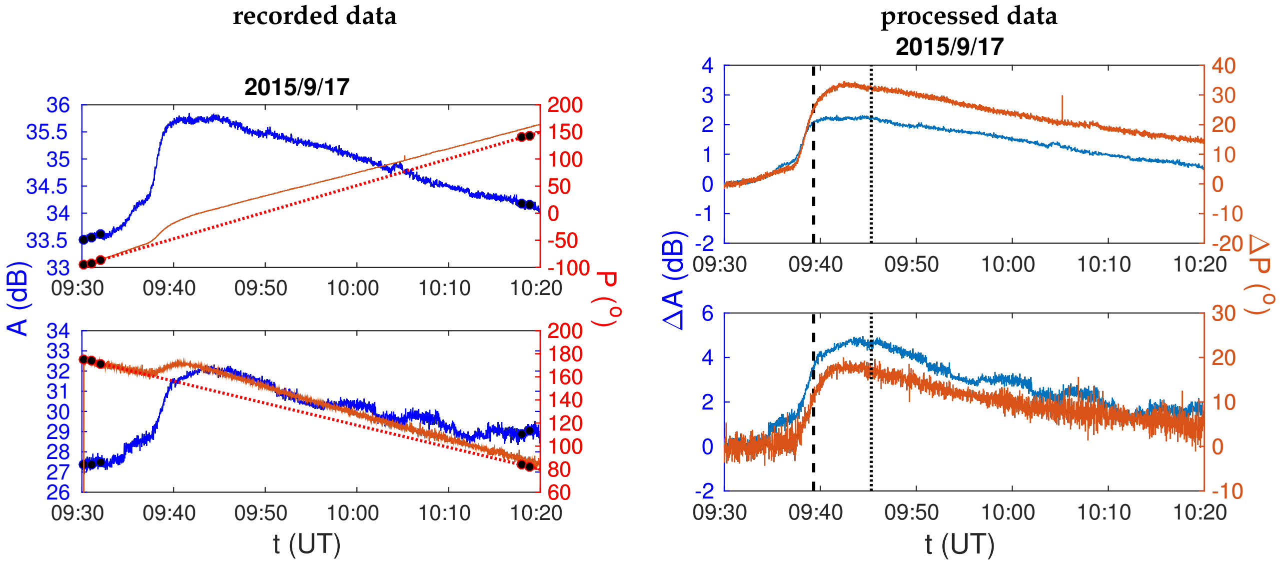

Figure 2. Time evolutions of the recorded amplitude and phase of DHO and ICV signals during the disturbance induced by the solar X-ray flare occurred on 17 September 2015 (left panels), and their deviations from the corresponding values in quiet conditions before the disturbance (right panels). The upper panels refer to the DHO signal, while the ICV signal data are shown in the bottom panels.

As a result of the above processing, the changes in amplitude and phase at the two times during the disturbance are obtained with respect to their values in quiet conditions.

2.1.2. Modeling

As shown in Figure 1, the procedure for modeling Wait's parameters describing the quiet conditions in midday periods (denoted with MDP in Figure 1) is split into two sub-procedures that provides estimations of: (1) their values for a particular event, and (2) their dependencies on the solar cycle period, described in terms of smoothed daily sunspot number σ, and season parameter $\chi = \mathrm{DOY}/365$, where DOY is the day of year. Here, we approximate the tropical year lasting 365 days (instead 365.24255 days).

Sub-MDP-1: Estimation of Wait's parameters in quiet conditions before a solar X-ray flare. As can be seen in Figure 1 this procedure consists of two following sub-procedures:

- **Sub-MDP-1a.** This sub-procedure provides values of Wait's parameters in the quiet ionosphere for which the amplitude $\Delta A_{\mathrm{mod}}^{\mathrm{sqd}}$ and phase $\Delta P_{\mathrm{mod}}^{\mathrm{sqd}}$ changes are similar to the corresponding recorded values, ΔA^{XFsi} and ΔP^{XFsi}, respectively. It is based on determination of changes in two sets of the modeled amplitude $\Delta A_{\mathrm{mod}}^{\mathrm{sqd}} = A_{\mathrm{mod}}^{\mathrm{sd}} - A_{\mathrm{mod}}^{\mathrm{sq}}$ and phase $\Delta P_{\mathrm{mod}}^{\mathrm{sqd}} = P_{\mathrm{mod}}^{\mathrm{sd}} - P_{\mathrm{mod}}^{\mathrm{sq}}$ of the signal s, and their deviations from the corresponding recorded values ΔA^{XFsi} and ΔP^{XFsi} for the signal s and disturbed state i. These sets, representing the modeled quiet and disturbed states, q and d, respectively, are performed in simulations of the considered VLF/LF signal propagation using LWPC numerical model developed by the Space and Naval Warfare Systems Center, San Diego, CA, USA [22]. The input parameters of this numerical model are Wait's parameters "sharpness" and signal reflection height, while the modeled amplitude and phase are its output (see the diagram in Figure 3).

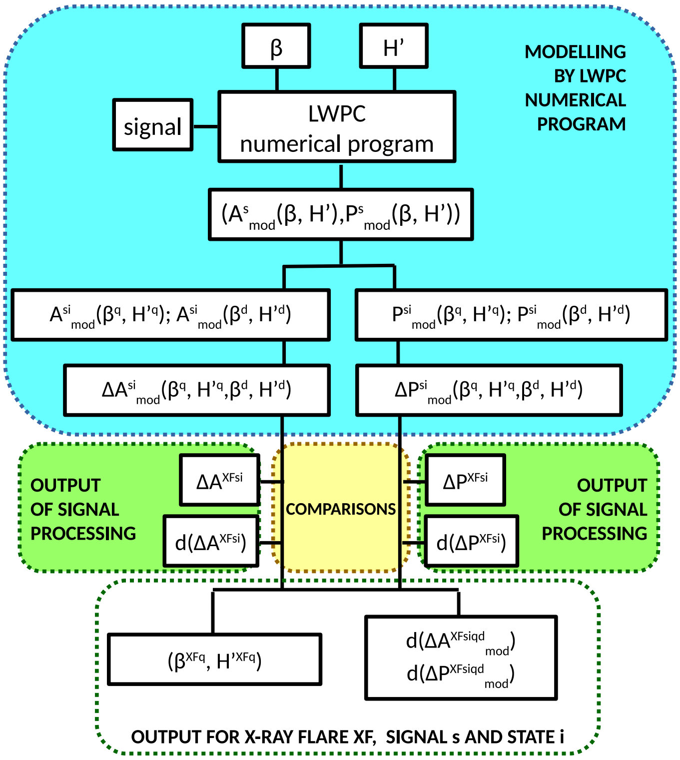

Figure 3. Diagram of sub-procedure MDP-1a.

According to the results presented in literature (see Reference [26,27,31,33–35]), Wait's parameters can be considered within intervals 0.2 km^{-1}–0.6 km^{-1} for β, and 55 km–76 km for H', where the quiet conditions can be described within intervals 0.2 km^{-1}–0.45 km^{-1} for β^{q}, and 68 km–76 km for H'^{q}. To model the parameter values representing a disturbed state d, β^{d} and H'^{d}, given those describing a quiet state q, we use conditions $\beta^{\mathrm{q}} < \beta^{\mathrm{d}}$ and $H'^{\mathrm{q}} > H'^{\mathrm{d}}$ which are based on many studies [26,27,31]. In the following, we use these intervals with steps of 0.01 km^{-1} and 0.1 km, respectively, as input in the LWPC numerical program.

The first output of the Sub-MDP-1a are the pairs of Wait's parameters referring to the quiet state before a solar X-ray flare XF ($\beta^{\mathrm{XFq}}, H'^{\mathrm{XFq}}$) for which the LWPC model can calculate the amplitude and phase differences for both main (m) and auxiliary (a) signals ($s = m, a$) and for both disturbed state ($i = 1, 2$) that satisfy the conditions:

$$\mathrm{d}(\Delta A^{\mathrm{XFsiqd}}_{\mathrm{mod}}) = \mathrm{abs}(\Delta A^{\mathrm{sqd}}_{\mathrm{mod}} - \Delta A^{\mathrm{XFsi}}) < \mathrm{d}(\Delta A^{\mathrm{XFsi}}), \quad \text{and} \tag{6}$$

$$\mathrm{d}(\Delta P^{\mathrm{XFsiqd}}_{\mathrm{mod}}) = \mathrm{abs}(\Delta P^{\mathrm{sqd}}_{\mathrm{mod}} - \Delta P^{\mathrm{XFsi}}) < \mathrm{d}(\Delta P^{\mathrm{XFsi}}), \tag{7}$$

where $\mathrm{d}(\Delta A^{\mathrm{XFsi}})$ and $\mathrm{d}(\Delta P^{\mathrm{XFsi}})$ are the absolute errors in the recorded signal characteristics.

The second output of Sub-MDP-1a are errors in modeling, e.g., the absolute deviations of the modeled changes in the amplitude and phase from their recorded values: $\mathrm{d}(\Delta A^{\mathrm{XFsiqd}}_{\mathrm{mod}})$ and $\mathrm{d}(\Delta P^{\mathrm{XFsiqd}}_{\mathrm{mod}})$. Both outputs are used in Sub-MDP-1b.

- **Sub-MDP-1b.** The goal of this sub-procedure is to find the pair of Wait's parameters ($\beta_0^{\mathrm{XFmidday}}$,$H'^{\mathrm{XFmidday}}_0$), from those ($\beta^{\mathrm{XFq}}, H'^{\mathrm{XFq}}$) extracted in Sub-MDP-1a, which provides the best agreement between the modeled and measured amplitude and phase changes of the VLF/LF signals. To do that, we analyze both the observation and modeling absolute errors, i.e., $\mathrm{d}(\Delta A^{\mathrm{XFsi}})$ and $\mathrm{d}(\Delta P^{\mathrm{XFsi}})$, for observations and $\mathrm{d}(\Delta A^{\mathrm{XFsiqd}}_{\mathrm{mod}})$ and $\mathrm{d}(\Delta P^{\mathrm{XFsiqd}}_{\mathrm{mod}})$ for modeling. These values are used to quantify the observed $w^{\mathrm{XF}}_{\mathrm{obs}}$ and modeled $w^{\mathrm{XFq}}_{\mathrm{mod}}$ weights for each extracted pair of Wait's parameters. Details about the estimations of these weights are provided in Appendix A, while an example of representation of the extracted pairs in the 2D Wait's parameter space is shown in the left panel of Figure 4. Each pair of Wait's parameters is represented as a point. The color of points describes their observation and modeling precisions. To find points (i.e., pairs of Wait's parameters) which best model the amplitude and phase changes, the region around each candidate point is analyzed as follows. The weight of each point, describing the overall observation and modeling precisions, is computed as the product of observed and modeled weights, i.e., $w^{\mathrm{XF}}_{\mathrm{obs}} w^{\mathrm{XFq}}_{\mathrm{mod}}$.

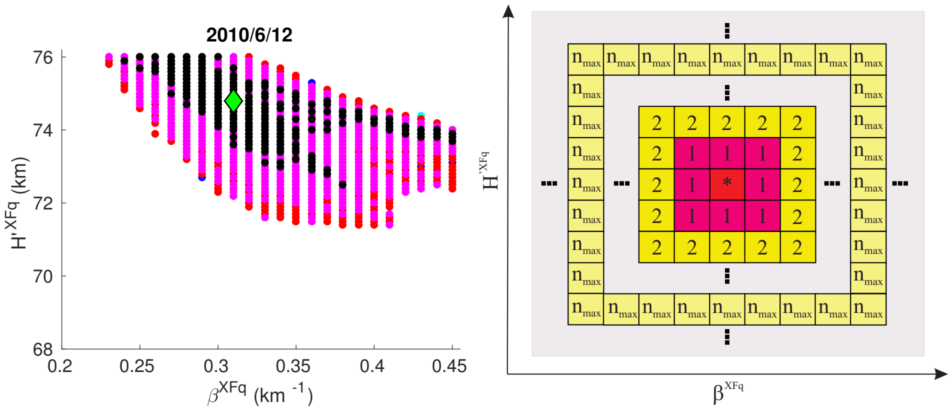

Figure 4. Left panel: Visualization of pairs of Wait's parameters "sharpness" and signal reflection height ($\beta^{\mathrm{XFq}}, H'^{\mathrm{XFq}}$) in quiet state q that satisfy conditions given by Equations (6) and (7) for an X-ray flare XF occurred on 12 June, 2010. The color of each point denotes the category of the corresponding pair. Each category includes pairs having all the four relative errors lower than c·10% (see Equation (A1)). Colors black, magenta, red, blue and cyan indicate the c-values increasing from 1 to 5 in steps of 1. The green diamond indicates the pair ($\beta_0^{\mathrm{XFmidday}}$, H'^{XFmidday}_0) which provides the best agreement of modeled and recorded amplitude and phase changes for the considered X-ray flare. Right panel: Region of Wait's parameter space around the point "*" with the visualization of the neighbor system. The first neighbors ($n = 1$) are colored pink, the second ones ($n = 2$) orange, and the most distant neighbors considered in the procedure ($n = n_{\mathrm{max}}$) are colored yellow.

Furthermore, the weight $w^{\mathrm{XFq}}_{\mathrm{n}}$ is introduced to quantify the influence of each point within the region around the candidate point. This weight is defined as

$$w^{\mathrm{XFq}}_{\mathrm{n}} = \Sigma_{\mathrm{k}} \left\{ \frac{1}{n^{\mathrm{qk}}} w^{\mathrm{XFk}}_{\mathrm{obs}} w^{\mathrm{XFk}}_{\mathrm{mod}} \right\}, \tag{8}$$

where n^{qk} is the distance between the quiet states q and k which refer to pairs ($\beta^{\mathrm{XFq}}, H'^{\mathrm{XFq}}$) and ($\beta^{\mathrm{XFk}}, H'^{\mathrm{XFk}}$), respectively.
The total weight $w^{\mathrm{XFq}}_{\mathrm{tot}}$ for the pair ($\beta^{\mathrm{XFq}}, H'^{\mathrm{XFq}}$) is computed as:

$$w^{\mathrm{XFq}}_{\mathrm{tot}} = w^{\mathrm{XFq}}_{\mathrm{obs}} w^{\mathrm{XFq}}_{\mathrm{mod}} + w^{\mathrm{XFq}}_{\mathrm{n}}. \tag{9}$$

Finally, the pair of Wait's parameters ($\beta_0^{\mathrm{XFmidday}}$, H'^{XFmidday}_0) describing the quiet D-region before a solar X-ray flare XF, which provides the best agreement of the considered modeled and observed amplitude and phase changes, is obtained as the pair with the largest total weight $W_{\rm tot}^{\rm XF} = \max_{\rm q}\{w_{\rm tot}^{\rm XFq}\}$. The estimation errors $[e\beta_{0-}^{\rm XF}, e\beta_{0+}^{\rm XF}]$ and $[eH'^{\rm XF}_{0-}, eH'^{\rm XF}_{0+}]$ of these parameters are obtained from distribution of pairs $(\beta^{\rm XFq}, H'^{\rm XFq})$ which satisfy conditions (6) and (7). For instance, the error for $\beta_0^{\rm XFmidday}$ are computed as follows. For the pair $(\beta_0^{\rm XFmidday}, H'^{\rm XFmidday}_0)$ represented by green diamonds in Figure 4, the interval $[e\beta_{0-}^{\rm XF}, e\beta_{0+}^{\rm XF}]$ is estimated by taking the smaller and larger values of $\beta^{\rm XFq}$ estimates, for the given $H'^{\rm XFmidday}_0$. In the same way, we estimate the error for $H'^{\rm XFmidday}_0$.

Sub-MDP-2: Modeling of Wait's parameters in terms of sunspot number and season. The aim of this subroutine is to model the behaviour of Wait's parameters by fitting the $({\beta_0}^{\rm XFmidday}, H_0'^{\rm XFmidday})$ pair. This requires a deeper understanding of the X-ray influences on the D-region. During quiet conditions, the solar hydrogen Lyα radiation has a dominant influence on ionization processes in the ionospheric D-region (see, for example, Reference [45]). The intensity of this radiation varies periodically during the solar cycle and its variation depends on the sunspot number. Because of that, we use the smoothed daily sunspot number σ to represent the intensity of the incoming solar radiation in the Earth's atmosphere. The intensity of this radiation decreases with the solar zenith angle due to larger attenuations in the atmosphere above the considered locations. Generally, the zenith angle changes are due to seasonal and'daily variations. However, this study focuses on time intervals around middays which allows us to assume that the seasonal changes represent the zenith angle variations. We introduce the seasonal parameter $\chi = \mathrm{DOY}/365$ where DOY is the day of year. This parameter has values between 0 and 1. Some authors report on possible influences of the geomagnetic field on the Wait's parameter [38,46]. However, this is is more pronounced at polar and near polar areas due to shapes of geomagnetic lines that allows charge particle influences on the ionospheric properties. As this study is focused on the low and mid latitude ionosphere, we neglect these effects.

Dependencies of Wait's parameters at midday on solar cycle and seasonal variations can be given as functions:

$$\beta_0^{\rm midday} = f(\sigma, \chi) \tag{10}$$

and

$$H_0'^{\rm midday} = g(\sigma, \chi). \tag{11}$$

These relations are not general and have yet to be determined for the location of interest and the time to which the recorded data refer to.

The knowledge of these functions allow us to calculate the vertical distribution of the Wait's horizontally uniform ionosphere, $N_{\rm e0}(h, \sigma, \chi)$, using the equation given in Reference [34] for different values of σ and χ:

$$N_{\rm e0}^{\rm midday}(\sigma, \chi, h) = 1.43 \cdot 10^{13} e^{-\beta^{\rm midday}(\sigma,\chi) H'^{\rm midday}(\sigma,\chi)} e^{[\beta^{\rm midday}(\sigma,\chi) - 0.15]h}, \tag{12}$$

where $N_{\rm e0}^{\rm midday}$ and $\beta^{\rm midday}$ are given in m^{-3} and km^{-1}, respectively, and $H'^{\rm midday}$ and altitude h are given in km. This equation was used to determine the temporal $(H_0'(t, h))$ and energy $(H_0'(\epsilon, h))$ distributions of the D-region electron density perturbed by a solar X-ray flare (see, for example, Reference [31,47,48]).

2.2. Daytime Variations of Ionospheric Parameters

The determination of the daytime variation of Wait's parameters and electron density is based on the comparison of observational and modeling data as for the analysis of midday variations. However, the DTP procedure considers only one VLF/LF signal, e.g., the main one. The reason for that is that the approximation of a horizontally uniform ionosphere during the entire daytime period (far from the sunrise and sunset) can be used when the size of the observed area corresponds to a relatively short propagation path of the signal.

2.2.1. VLF/LF Signal Processing

The goal of this procedure is to find the amplitude and phase variations relative to their values in the midday period. We consider data recorded during the daytime period, far from the sunrise and sunset. The midday period is estimated from tendency of the amplitude time evolution $A(t)$. Namely, it rises until the midday and decreases afterwards which allows us to assume the period around the amplitude maximum as the midday period. The duration of this period is a few minutes and it depends on the season and possible existence of unperiodical disturbances which should be excluded from the analysis.

To exclude the short-term amplitude picks that do not represent periodic daily variations, the midday amplitude A^{midday} is estimated as the median amplitude value in the midday period.

Similarly to the analysis in Section 2.1.1, the time evolution of the phase is determined by estimating the linear phase trend obtained by interpolation of phase values estimated within time bins in quiet conditions. The midday phase P^{midday} is estimated from the obtained phase evolution P(t) in the same way like for the midday amplitude.

The final step of this processing is the calculation of amplitude and phase deviations from their reference values, i.e., $\Delta A = A - A^{\text{midday}}$ and $\Delta P = P - P^{\text{midday}}$.

2.2.2. Modeling

The modeling of daytime temporal evolution of Wait's parameters is based on comparison of deviation of observational and modeled changes with respect to their midday values. The modeled midday values $A_{\text{mod}}^{\text{midday}}$ and $P_{\text{mod}}^{\text{midday}}$ are obtained from β_0^{midday} and $H_0'^{\text{midday}}$, while the modeled amplitude A_{mod} and phase P_{mod} are outputs of the LWPC program for the given pair of Wait's parameters. Wait's parameters $(\beta(t), H'(t))$ at time t are estimated as those that best satisfy the conditions

$$A - A^{\text{midday}} = A_{\text{mod}} - A_{\text{mod}}^{\text{midday}} \tag{13}$$

and

$$P - P^{\text{midday}} = P_{\text{mod}} - P_{\text{mod}}^{\text{midday}}. \tag{14}$$

Finally, the electron density $N_{e0}(t,\sigma,\chi)$ is obtained from Equation (15):

$$N_{e0}(t,h,\sigma,\chi) = 1.43 \cdot 10^{13} e^{-\beta(t,\sigma,\chi)H'(t,\sigma,\chi)} e^{(\beta(t,\sigma,\chi)-0.15)h}, \tag{15}$$

where the parameters are given in the same units as in Equation (12).

3. Studied Area and Considered Events

To give an example of this model application, we apply it to data recorded in Belgrade in the lower ionosphere observations by the VLF signals emitted in Germany and Italy, while the information of the X-ray flares occurrences was taken from the website https://hesperia.gsfc.nasa.gov/goes/goes_event_listings/. For a better understanding of the presented procedure, we will first describe observations and then (in Section 4) we present the application of the model to the observed data.

3.1. Remote Sensing of Lower Ionosphere

The lower ionosphere observations are performed by two VLF signals of frequencies 23.4 kHz and 20.27 kHz emitted by the DHO transmitter in Germany (Rhauderfehn, 53.08 N, 7.61 E) and the ICV transmitter in Italy (Isola di Tavolara, 40.92 N, 9.73 E), respectively.

Amplitudes and phases of these signals are recorded by the AWESOME (Atmospheric Weather Electromagnetic System for Observation Modeling and Education) receiver [49] located in Belgrade, Serbia, which was a part of the Stanford/AWESOME Collaboration for Global VLF Research (http://waldo.world/narrowband-data/). The locations of the considered transmitters and receiver, as well as the propagation paths, are shown in Figure 5.

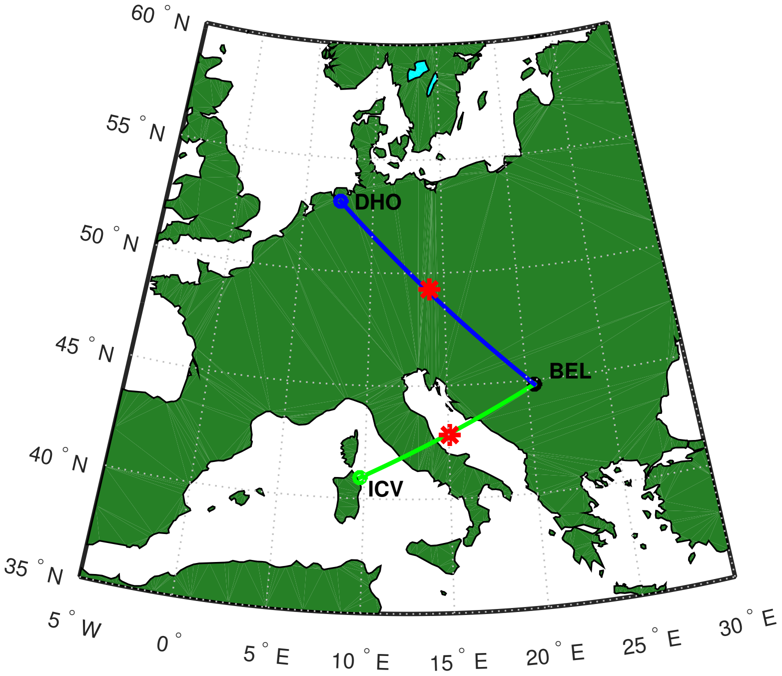

Figure 5. Propagation paths of the main and auxiliary VLF signals emitted by the DHO (Germany) and ICV (Italy) transmitters, respectively, and received in Belgrade (BEL). The stars indicate the locations of the path midpoints.

The best properties of the recorded VLF/LF signals in the Belgrade receiver station are those of the DHO signal. That can be explained by a not too long propagation path and a large emitted power (800 kW). This is why the DHO signal is used in many studies based on data collected by the Belgrade receiver station (see, for example, Reference [10,50]). Although the distance between the Italian transmitter and Belgrade receiver is shorter than the path in the first case, its emitted power is 40 times lower than that of the signal emitted in Germany. For this reason, we rank the DHO and ICV signals as the main and auxiliary ones, respectively.

3.2. Considered X-ray Flares

As one can see in Section 2, the presented model assumes a horizontally uniform Wait's ionosphere [42] for the area where both signals propagate. That assumption requires analyses of the time period when solar influences is similar above the considered part of Europe, e.g., periods around the midday. In addition, modeling of the electron density by the procedure given in Reference [34] is more appropriate for not too intensive flares. For this reason, we consider flares of up to class M5 (like in Reference [10]). Due to absence or insignificant ionospheric disturbances induced by low intensive flares, we consider events of classes larger than C5.0. In our collected database, we find 9 not too intensive events for which the differences in solar zenith angles, $\Delta\theta = \theta_{\mathrm{DHO}} - \theta_{\mathrm{ICV}}$ (calculated using the website https://www.esrl.noaa.gov/gmd/grad/solcalc/azel.html for the latitude/longitude points of the middle propagation paths DHO-BEL (49°16′48″ N, 14°0′0″ E) and ICV-BEL (42°48′36″ N, 15°3′36″ E), obtained in calculations by the program given at the website https://www.gpsvisualizer.com/calculators) satisfy the first mentioned condition. As one can see in Table 1, classes of the considered flares are between C6.1 and M3.2, while differences in the solar zenith angles of the DHO and ICV signal mid-paths, θ_{DHO} and θ_{ICV}, respectively, are lower than 6.4$^{\mathrm{o}}$.

Table 1. Dates, times, and classes of the considered X-ray flares, and zenith angles θ_{DHO} and θ_{ICV} for the latitude/longitude points of the middle propagation paths DHO-BEL and ICV-BEL, respectively. Differences of these angles, $\Delta\theta$, are given in the last column. The positions of the considered VLF signal mid-paths, and corresponding angles θ_{DHO}, θ_{DHO} and $\Delta\theta$ are calculated using tools given at https://www.gpsvisualizer.com/calculators and https://www.esrl.noaa.gov/gmd/grad/solcalc/azel.html, respectively.

Flare XF	Date	Time (UT)	Flare Class	θ_{DHO} ($^{\mathrm{o}}$)	θ_{ICV} ($^{\mathrm{o}}$)	$\Delta\theta$ ($^{\mathrm{o}}$)
F1	5 May 2010	11:37	C8.8	33.79	27.88	5.91
F2	12 June 2010	09:20	C6.1	35.39	31.25	4.14
F3	3 November 2014	11:23	M2.2	64.84	58.61	6.23
F4	15 November 2014	11:40	M3.2	53.57	51.35	2.22
F5	6 January 2015	11:40	C9.7	72.05	65.76	6.29
F6	21 January 2015	11:32	C9.9	69.25	62.88	6.37
F7	29 January 2015	11:32	M2.1	53.07	50.65	2.42
F8	17 Septembere 2015	09:34	M1.1	50.31	44.28	6.03
F9	14 May 2016	11:28	C7.4	37.50	35.31	2.19

4. Results and Discussion

The proposed methodology is applied to data obtained in observations described in Section 3. Here, we present the results of:

1. Modeling the ionospheric parameters in midday periods over the part of Europe included within the location of transmitted signals (Sardinia, Italy, for the ICV signal) and (Lower Saxony, Germany for the DHO signal) and the receiver in Belgrade, Serbia, with respect to the daily smoothed sunspot number and season. This part consists of the following steps:
    - Modeling of pairs of Wait's parameters which satisfy conditions given by Equations (6) and (7) by the LWPC numerical program and determination pair (${\beta_0}^{\mathrm{XF}}$, ${H_0'}^{\mathrm{XF}}$) that provides the best fit of observational data for the considered X-ray flares.
    - Determination of dependencies of the midday Wait's parameters, ${\beta_0}^{\mathrm{midday}}$ and ${H_0'}^{\mathrm{midday}}$, and the electron density, N^{midday}, from parameters that describe the solar activity and Earth's motion: the smoothed daily sunspot number σ, and parameter χ describing seasonal variations.
2. Modeling of daytime variations of ionospheric parameters for a particular day. This procedure consists of:
    - Modeling of time evolutions of Wait's parameters from comparisons of the recorded and modeled amplitude and phase changes with respect to their values in the midday.
    - Modeling of the electron density time evolution for the D-region heights during daytime.

For both analyses, it is necessary to know the modeled amplitude and phase of the considered signals. For this reason, we first present the description of their determination.

4.1. Modeling of the DHO and ICV Signal Amplitudes and Phases by the LWPC Numerical Program

As noticed in Section 2, the LWPC program simulates propagation of the VLF and LF signals from a particular transmitter to a particular receiver of these waves. Wait's parameters, the "sharpness" β and signal reflection height H' are the input values for this program, while the modeled amplitude A_{mod} and phase P_{mod} are its outputs. In this study, we perform analysis for input values of β and H' in domains 0.2 km^{-1}–0.6 km^{-1} and 55 km–76 km, respectively, with corresponding steps of 0.01 km^{-1} and 0.1 km.

Results of modeling by the LWPC program for location of the Belgrade receiver and the DHO and ICV transmitters are shown in Figure 6. Here, it is important to pay attention to the fact that these panels represent the modeled amplitudes and phases (within the domain from $-180°$ to $180°$), while the procedure for comparison of recorded and modeled signal characteristics, described in Section 2.1.2, requires changes of these values in the disturbed with respect to quiet conditions. The dependencies of these changes on the input Wait's parameters have the same distributions as the presented corresponding graphs because they have lower than those modeled by the LWPC program for a constant value of modeled amplitude or phase in quiet conditions.

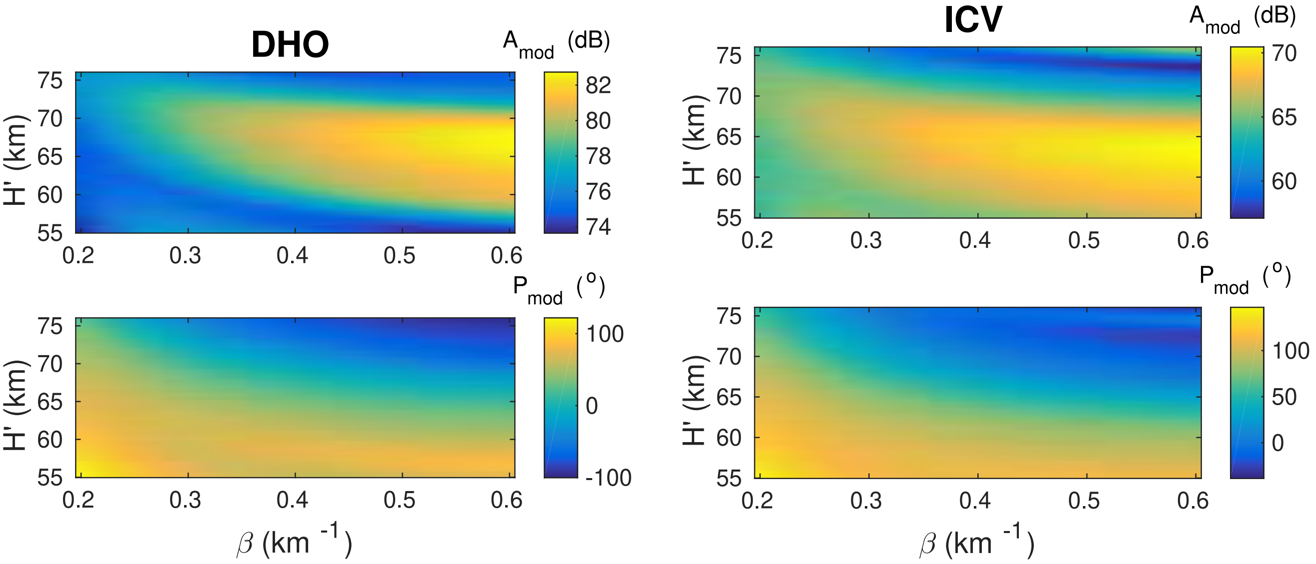

Figure 6. Surface plots of the modeled (by Long-Wave Propagation Capability (LWPC) program) amplitude (upper panels) and phase (lower panels) of the DHO (left panels) and ICV (right panels) signal for receiver located in Belgrade, Serbia, as functions of Wait's parameters β and H'.

As one can see in Figure 6, there is no unique pair of Wait's parameters that produce specific LWPC output values. That is why only one presented panel, even though the modeled amplitude/phase in quiet conditions are given, it cannot be used for determination of the input pair that provides the best fit of the observed data. The fact that it is impossible to determine a unique combination of Wait's parameters from a single value of signal characteristic was noticed by other authors (see, e.g., Reference [36]).

4.2. *Midday Values—Solar Cycle and Seasonal Variations*

The procedure for determination of the considered midday values during the solar cycle and year consists of two parts:

- Determination of pairs $(\beta^{\mathrm{XFq}}, H'^{\mathrm{XFq}})$ which describe quiet states before the considered X-ray flares (Section 4.2.1).
- Determination of dependencies of Wait's parameters and the electron density in midday quiet conditions on σ and χ (Section 4.2.2).

4.2.1. Determination of Pairs $(\beta^{\mathrm{XFq}}, H'^{\mathrm{XFq}})$

Comparison of the recorded and modeled changes in amplitude and phase of the DHO and ICV signals using the procedure described in Section 2.1.2 gives pairs of Wait parameters $(\beta^{\mathrm{XFq}}, H'^{\mathrm{XFq}})$ which satisfy the conditions given by Equations (6) and (7). These values are presented for all considered events in Figure 7. To better visualize the precision in comparisons, we divide the extracted pairs in ten categories depending on relative errors in modeling of both amplitude and phase of the DHO and ICV signals. The category c = 1, 2, 3, ..., 10 indicates that all relative errors defined by Equation (A1) for pairs $(\beta^{\text{XFq}}, H'^{\text{XFq}})$ have values less than $c \cdot 10\%$. The values of $(\beta^{\text{XFq}}, H'^{\text{XFq}})$ which have the largest total weight calculated by Equation (9), e.i. values $(\beta_0^{\text{XFmidday}}, H'^{\text{XFmidday}}_0)$ for a X-ray flare XF, are indicated by green diamonds.

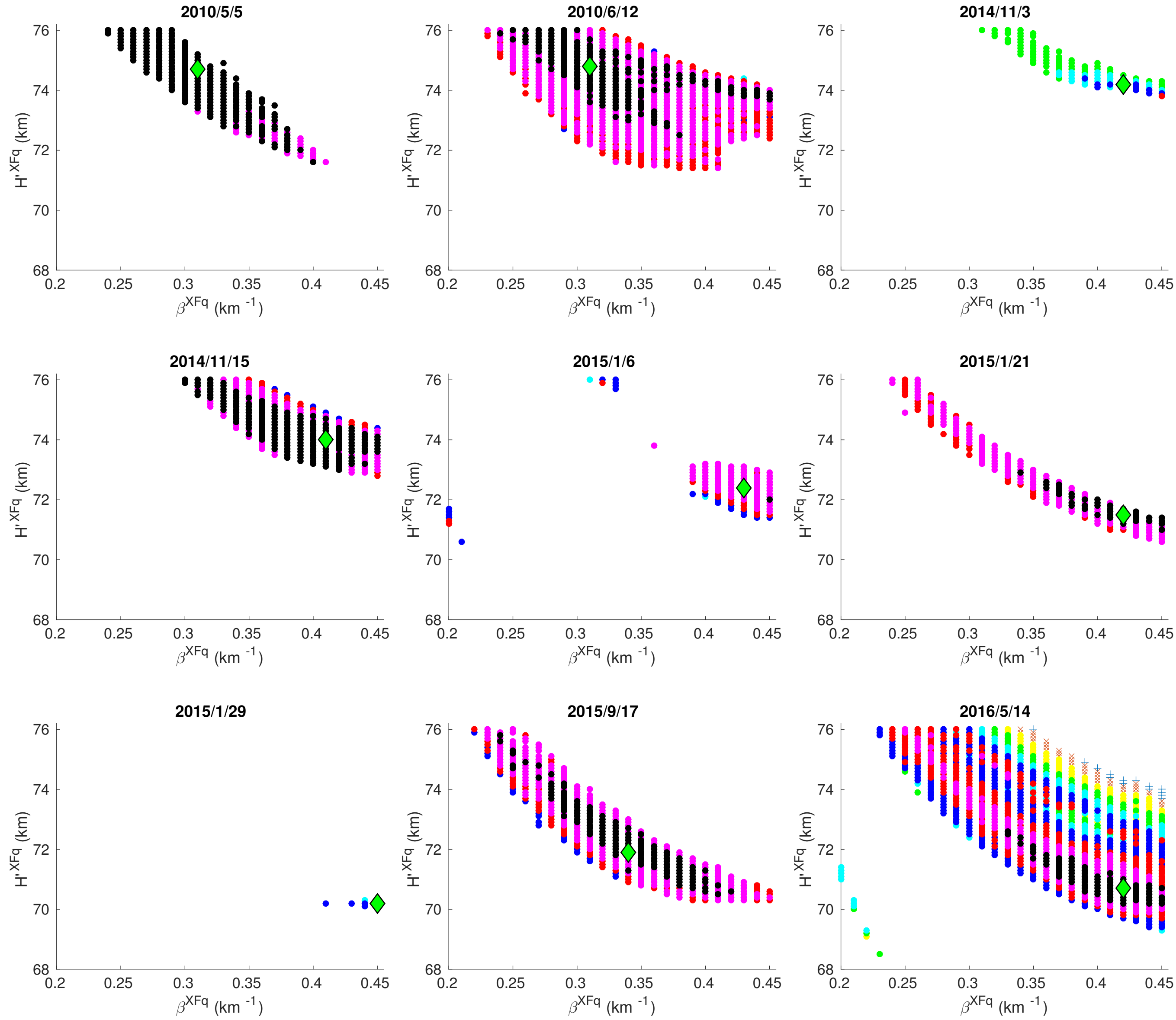

Figure 7. Visualization of pairs of Wait's parameters "sharpness" and signal reflection height $(\beta^{\text{XFq}}, H'^{\text{XFq}})$ in quiet state q that satisfy conditions given by Equations (6) and (7) for an X-ray flare XF that occurred on the date indicated on the corresponding panel (see Table 1). Categories $c = 1, 2, 3..., 10$, describing relative errors defined by Equation (A1), are shown with different scatters: black, magenta, red, blue, cyan, green and yellow filled circles, x, +, and ·, respectively. The pair $(\beta^{\text{XFq}}, H'^{\text{XFq}})$ which has the largest total weight calculated by Equation (9) for a particular event, i.e., value $(\beta_0^{\text{XFmidday}}, H'^{\text{XFmidday}}_0)$ for a X-ray flare XF, is indicated by green diamonds.

According the number of neighbors (see Figure 7) that also satisfy the conditions given by Equations (6) and (7), stability of the obtained pairs ($\beta_0^{\text{XFmidday}}$ and H'^{XFmidday}_0) is good in 8 out of 9 cases. It can be also seen in Table 2 showing the relevant domains with higher $e\beta_{0+}^{\text{XF}}$ and eH'^{XF}_{0+}, and lower $e\beta_{0-}^{\text{XF}}$ and eH'^{XF}_{0-} values of Wait's parameters with respect to $\beta_0^{\text{XFmidday}}$ and H'^{XFmidday}_0 (for fixed other parameter), respectively. Visualization by different scatters shows that 6 cases have the highest precision of modeling for $c = 1$, while the lowest precision occurs for $c = 3$. The weights $W_{\text{tot}}^{\text{XF}}$, calculated by Equation (9) and given in Table 2, show large differences for the considered events (from 1.4 to 154.5).

Table 2. The obtained Wait's parameters "sharpness", $\beta_0^{\text{XFmidday}}$, and signal reflection height, H'^{XFmidday}_0, and domains of their possible deviations going to larger ($e\beta_{0+}^{\text{XF}}$ and eH'^{XF}_{0+}) and lower values ($e\beta_{0-}^{\text{XF}}$ and eH'^{XF}_{0-}) for the considered flares. The last three columns show weights $W_{\text{tot}}^{\text{XF}}$ of the determined pairs of Wait's parameters ($\beta_0^{\text{XFmidday}}$, H'^{XFmidday}_0), smoothed daily sunspot number σ, and seasonal parameter χ.

Flare XF No	$\beta_0^{\text{XFmidday}}$ (km^{-1})	H'^{XFmidday}_0 (km)	$e\beta_{0+}^{\text{XF}}$ (km^{-1})	$e\beta_{0-}^{\text{XF}}$ (km^{-1})	eH'^{XF}_{0+} (km)	eH'^{XF}_{0-} (km)	W_{tot}	σ	χ
F1	0.31	74.7	0.01	0.04	0.5	1.4	104.0	10.7	0.3452
F2	0.31	74.8	0.08	0.06	1.2	2.6	103.5	23.1	0.4493
F3	0.42	74.2	0.03	0.03	0.3	0.2	5.6	100.5	0.8438
F4	0.41	74.0	0.04	0.05	0.9	0.9	154.5	100.1	0.8767
F5	0.43	72.4	0.02	0.03	0.7	0.9	29.7	112.6	0.0164
F6	0.42	71.5	0.01	0.03	0.2	0.5	56.8	87.6	0.0575
F7	0.45	70.2	0.00	0.02	0.1	0.1	1.4	84.8	0.0795
F8	0.34	71.9	0.04	0.04	1.1	1.0	115.9	54.0	0.7151
F9	0.42	70.7	0.03	0.06	3.6	1.0	111.5	68.6	0.3699

4.2.2. Wait's Parameters and Electron Density in Quiet Conditions

The final step in determination of midday Wait's parameters is analysis of their dependencies on daily smoothed solar sunspot number σ and seasonal variations described by parameter χ. To better visualize the difference due to larger solar radiation in the period around the maximum of the solar cycle than in the period around its minimum, we show the relevant points in Figure 8 with a filled and open scatters, respectively. Different seasons are described with blue (winter), green (spring), yellow (summer), and red (autumn) scatters.

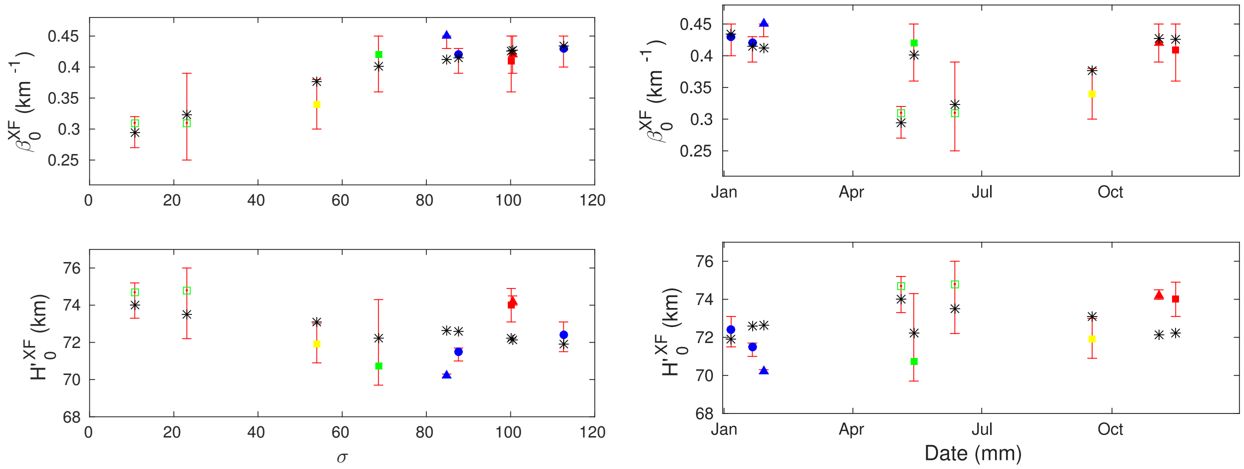

Figure 8. Dependencies of the "sharpness" β (upper panels) and signal reflection height H' on the smoothed daily sunspot number σ (left panels) and season (right panel). The modeled values $\beta_0^{\text{XFmidday}}$ and H'^{XFmidday}_0 are shown as filled (for periods near the solar cycle maximum) and open (for periods near the solar cycle minimum) scatters. Different seasons are described by blue (winter), green (spring), yellow (summer), and red (autumn) scatters. Scatters marked by "*" indicate values obtained from Equations (16) and (17).

Dependencies of the midday Wait's parameters on the solar sunspot number are shown in the left panels of Figure 8. Here, we consider the smoothed sunspot number (over 21 days) and take the value for the period of 20 days before and the considered day from the database given at http://sidc.oma.be/silso/datafiles. The upper panel indicates the increase of the parameter β with σ, while decrease of the signal reflection height with σ is clearly shown in the bottom panel. These tendencies are in agreement with previous studies of Wait's parameters during solar X-ray flares where the increase/decrease of the "sharpness"/signal reflection height with the electron density is reported (see, for example, Reference [31]). In this case, the rise of the D-region electron density is a consequence of the Lyα radiation increase in approaching the solar cycle maximum. In fitting of these dependencies, we assume polynomial functions of the orders 2 and 1, respectively, which is by one order of magnitude larger than in Reference [38] where the dependency of the parameter β is given as a linear function of the sunspot number, while variation of H' with the sunspot number is not suggested. As one can see in the right panels in Figure 8, the seasonal variation is more complex than in the previous case. However, if two scatters related to the solar cycle minimum are excluded we can see approximative sinusoidal shapes in both cases. For this reason, we assume sinusoidal dependencies of Wait's parameters on parameter χ similarly as in Reference [38] but with daily (instead of monthly) changes and additional phase shifts which provide maximum/minimum values of β/H′ for the summer solstice when the expected radiation coming in the considered area reaches its annual maximum.

Tow-dimensional fittings of Wait's parameters yield the following expressions:

$$\beta_0^{\text{midday}} = 0.2635 + 0.002573 \cdot \sigma - 9.024 \cdot 10^{-6}\sigma^2 + 0.005351 \cdot \cos(2\pi(\chi - 0.4712)) \qquad (16)$$

and

$$H_0'^{\text{midday}} = 74.74 - 0.02984 \cdot \sigma + 0.5705 \cdot \cos(2\pi(\chi - 0.4712) + \pi), \qquad (17)$$

which provides good agreement of the computed Wait's parameters with their modeled values given in Table 1. The maximum differences of their values are less than 0.04 km^{-1}, and 2.5 km. These values are in good agreement with those obtained in Reference [51] for the night-time Wait's parameters and they are similar to the maximum "errors" given in Table 2. Wait's parameters are visualized in Figure 9 for β_0 (left panel) and H_0' (right panel). The obtained values lie in domains 0.31 km^{-1}–0.45 km^{-1} and 70.6 km–74.7 km, respectively. An increase/decrease in dependencies of the "sharpness"/reflection height with σ is visible during the whole year. The minimum/maximum values of β_0/H_0' for the same σ are reached during the summer solstice when the solar radiation has the greatest impact on the ionosphere.

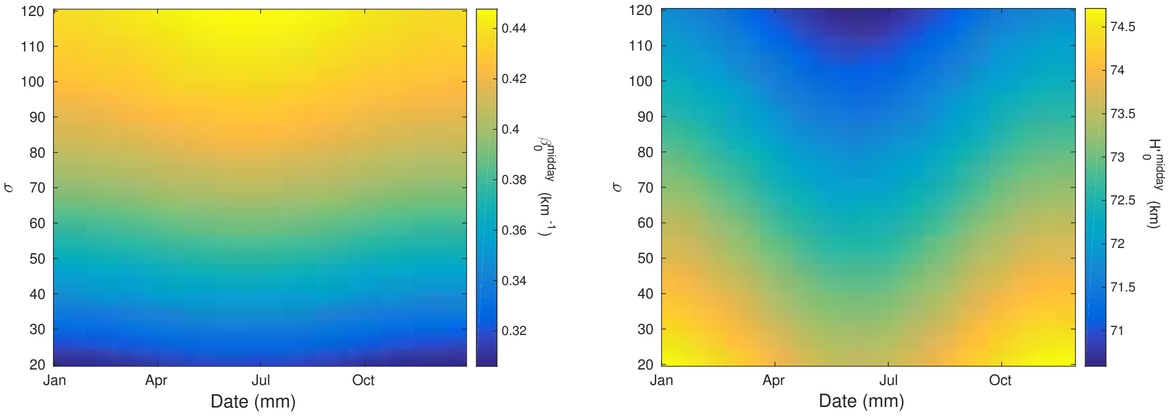

Figure 9. Dependencies of Wait's parameters in the quiet midday ionosphere, the "sharpness" β_0^{midday} (left panel) and signal reflection height $H_0'^{\text{midday}}$ (right panel) on season and smoothed daily sunspot number σ.

Introduction of Equations (16) and (17) in Equation (12) gives the midday electron density from σ and χ at altitude h. These dependencies at 70 km, 75 km, and 80 km are shown in Figure 10.

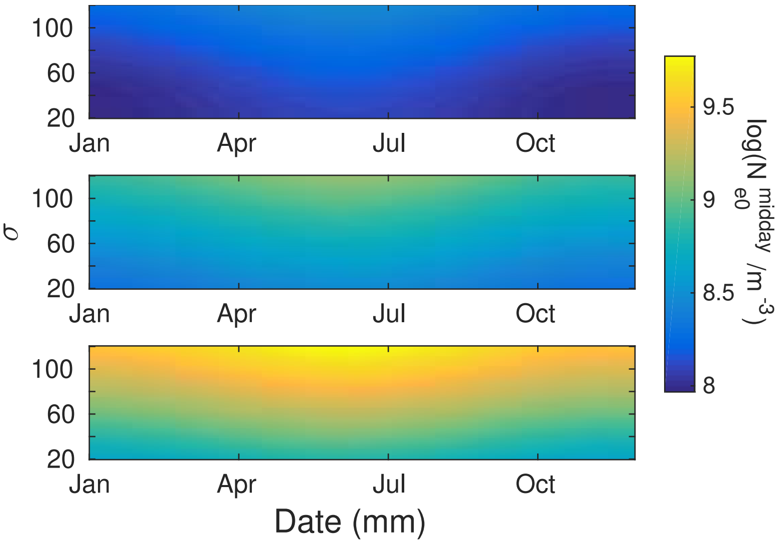

Figure 10. Dependencies of $\log(N_{e0}^{\mathrm{midday}}/1\mathrm{m}^{-3})$ at the altitudes of 70 km (upper panel), 75 km (middle panel), and 80 km (bottom panel) on season and smoothed daily sunspot number σ.

As one can see, variations are more visible at larger heights and can reach values near 10^{10} m^{-3} at 80 km for periods with large number of solar sunspot number. Due to the most intensive influences of solar radiation, the electron density has largest values during the summer solstice.

4.3. Daytime Variations

Knowing the midday Waits parameters allows us to calculate their time evolutions during a quiet day. Here, we present an example using the DHO signal amplitude and phase recorded by the Belgrade VLF receiver on 6 September 2014 (DOY = 250; χ = 0.6849) in which deviations, ΔA and ΔP, from the corresponding midday values are shown in the left panels of Figure 11. We consider a time interval from 9 UT to 15 UT when approximation of a horizontally uniform ionosphere within the medium where the signal propagates. A lack of data between 13 UT and 14 UT is due to a regular pause in the VLF/LF signals monitoring by the AWESOME receiver located in Belgrade.

To obtain the daytime evolution of β and H', we first calculate their midday values. According to the database given at http://sidc.oma.be/silso/datafiles, the mean value of daily sunspot number for 20 days before and for the considered day is σ = 107.1. Introducing these values in Equations (16) and (17) gives the midday Wait's parameters for the analyzed day: $\beta_0^{\mathrm{midday}} = 0.42$ km^{-1} and $H_0'^{\mathrm{midday}} = 72.5$ km. The recorded midday amplitude $A_{\mathrm{mod}}^{\mathrm{midday}} = 30.35$ dB and phase $P_{\mathrm{mod}}^{\mathrm{midday}} = 1.11^{\mathrm{o}}$ are estimated from time evolutions of the corresponding signal characteristics. Finally, the time evolution of Wait's parameters are calculated by the procedure as described in Section 2.2.2 and shown in the right panels of Figure 11. In the considered time period (excluding a short-term peak), these parameters have values within approximative domains 0.36 km^{-1}–0.45 km^{-1} and 71.2 km–74.2 km, respectively. Comparisons of the data obtained by the QIonDR model with those calculated by the LWPC default and IRI (see Reference [52] and references therein; Wait's parameters are calculated from electron density altitude distribution and expression for the electron density given in Reference [34]) models and with data presented in previous studies [27,33,35,53] show the best comparison of the QIonDR modeled amplitude and phase variations with the recorded ones. The QIonDR model fits better than the LWPC default model with data shown in Reference [27,33,35,53] for both Wait's parameters. The IRI model agrees better with the QIonDR ones for H_0', as well as in some periods for β_0.

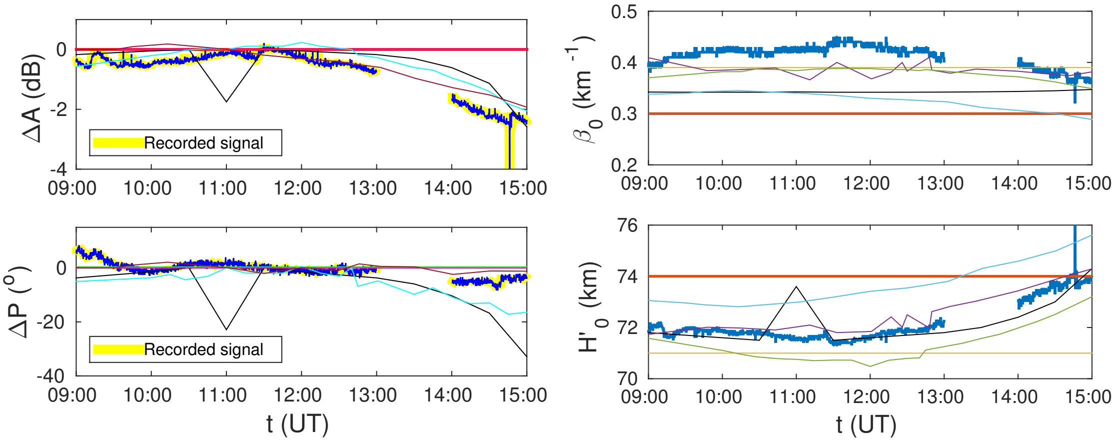

Figure 11. Daytime variations of the amplitude and phase changes (**left panels**) and Wait's parameters (**right panels**) during 6 September 2014 obtained by Quiet Ionospheric D-Region (QIonDR), default Long-Wave Propagation Capability (LWPC), and International Reference Ionosphere (IRI) models and compared with data presented in studies indicated in legend [22,27,33,35,52,53]. The gap between 13 UT and 14 UT is due to the one hour break in data receiving by the Atmospheric Weather Electromagnetic System for Observation Modeling and Education (AWESOME) receiver. ▬ QIonDR; ▬ LWPC default [22]; ▬ IRI [52]; ▬ Thomson et al., 2005 [27]; ▬ Han et al., 2011 [33]; ▬ McRae and Thomson, 2000 [35]; ▬ Thomson et al., 2017 [53].

The daytime variation in the D-region electron density during the considered day, obtained from the calculated Wait's parameters and Equation (15), is shown in Figure 12. The time variation of electron density is more noticeable at higher altitudes while the vertical changes are most pronounced in the midday period. Similarly to the comparison of Wait's parameters, the QIonDR model fits better than the LWPC default model with data shown in Reference [27,33,35,53] for the electron density at 70 km and 80 km. The IRI model agrees better with the QIonDR ones for the electron densities at 70 km.

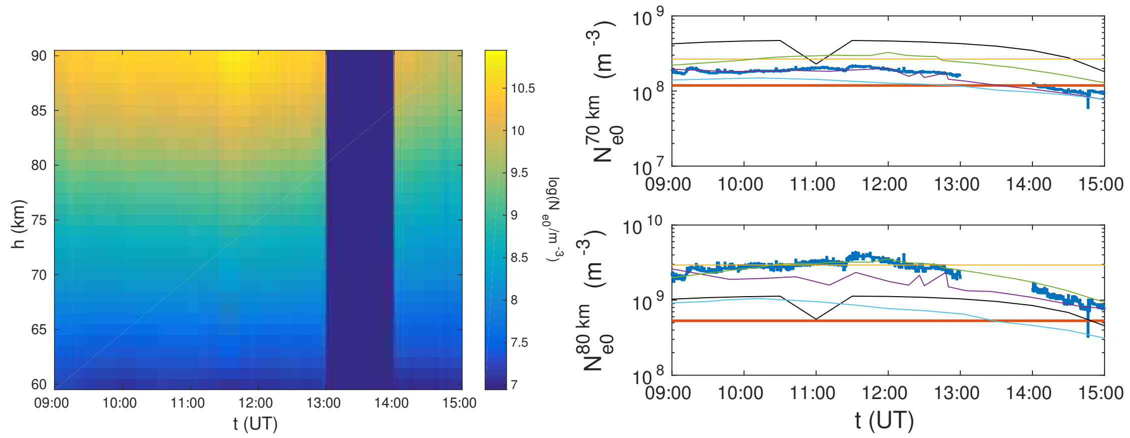

Figure 12. Left panel: Daytime variation of $\log(N_{e0}/1\mathrm{m}^{-3})$ during 6 September 2014 obtained by the Quiet Ionospheric D-Region (QIonDR) model. The gap between 13 UT and 14 UT is due to the one hour break in data receiving by the Atmospheric Weather Electromagnetic System for Observation Modeling and Education (AWESOME) receiver. Right panels: Comparisons of the obtained electron density time evolutions at 70 km (upper panel) and 80 km (bottom panel) with those obtained for Wait's parameters presented in Figure 11. ▬ QIonDR; ▬ LWPC default [22]; ▬ IRI [52]; ▬ Thomson et al., 2005 [27]; ▬ Han et al., 2011 [33]; ▬ McRae and Thomson, 2000 [35]; ▬ Thomson et al., 2017 [53].

A similar analysis is provided also for the D-region disturbed by a solar X-ray flare on 17 September 2015 (signal characteristics for this event are shown in Figure 2). Comparisons of the amplitude and phase changes, as well as time evolutions of Wait's parameters and the electron density for different values of initial Wait's parameters, are shown in Figure 13. In these calculations, we applied the LWPC model for the initial Wait's parameters obtained by the QIonDR, LWPC default, and IRI models, and based on the studies presented in Reference [27,35,53]. In all these cases, the modeled amplitude and phase variations are in very good agreement with the recorded ones. For better visibility, we show only the obtained data for the QIonDR and LWPC default models. As one can see in Figure 13a, they are practically completely fitted with the recorded data except for the end of the observed period when minor deviations are noticeable in the case of LWPC default program for the amplitude changes. Agreement of β is better for QIonDR than for the LWPC default model with data obtained by IRI model and data from Reference [27,35], as well as for data from Reference [53], in some periods. In the cases of H' and electron density time evolutions, the QIonDR better fits with data obtained for initial parameters calculated by the IRI model, used in Reference [27], and, in some periods, for initial parameters given in Reference [35]. In addition, comparison of all parameters is in better agreement for the QIonDR than LWPC default model with data presented in Reference [26,29] for the maximum X-radiation flux of flares of the same or very similar class as the considered one.

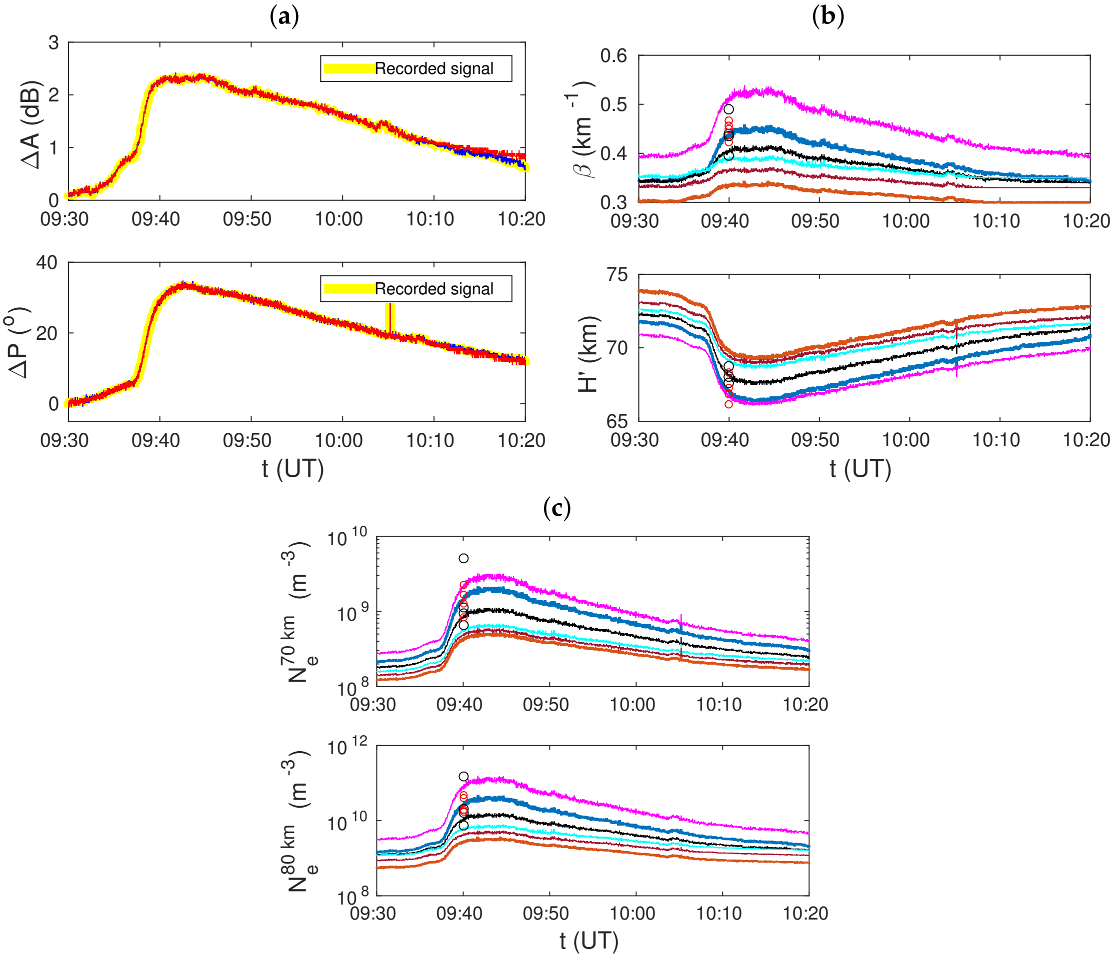
(**a**) (**b**) (**c**)

Figure 13. Comparisons for the D-region disturbed by a solar X-ray flare on 17 September 2015. (**a**) Comparisons of time evolutions of the recorded amplitude (upper panel) and phase (lower panel) changes with their modeled values by the Long-Wave Propagation Capability (LWPC) model for Wait's parameters β_0 and H'_0 determined by the Quiet Ionospheric D-Region (QIonDR) model (blue line) and by default (red line). (**b**) Comparison of time evolutions of Wait's parameters β and H' obtained by the LWPC program for their initial values modeled by the QIonDR, LWPC default and International Reference Ionosphere (IRI) models, and those presented in literature indicated in the legend [22,27,35,52,53]. The values obtained in Reference [26,29] at the moment of maximum X-radiation flux for flares of the same or very similar class as the considered one are shown by scatters. (**c**) Comparison of time evolutions of the electron density at 70 km (upper panel) and 80 km (bottom panel) for Wait's parameters shown in graph (**b**). — QIonDR; — LWPC default [22]; — IRI [52]; — Thomson et al., 2005 [27]; — McRae and Thomson, 2000 [35]; — Thomson et al., 2017 [53]; o Grubor et al., 2008 [29]; o McRae and Thomson, 2004 [26].

5. Conclusions

In this paper, we present a procedure for calculations of the D-region plasma parameters during quiet conditions. The proposed methodology is applied to areas monitored by the VLF/LF radio signals emitted and recorded by relatively closely located transmitters and receivers like, for example, in Europe. It is based on two different VLF/LF signals acquired by one receiver. We applied the proposed methodology to the DHO and ICV signals emitted in Germany and Italy, respectively, and recorded in Serbia. The obtained results of this study are:

- A new procedure for estimation of Wait's parameters and electron density. It is divided in two parts: (1) determination of dependencies of these parameters on the smoothed daily sunspot number and season at midday, and (2) determination of time evolution of these parameters during daytime;
- Estimation of Wait's parameters and electron density over the part of Europe included within the location of the transmitted signals (Sardinia, Italy, for the ICV signal) and (Lower Saxony, Germany for the DHO signal) and the receiver in Belgrade, Serbia. The obtained results show variations in which inclusion in different analyses of more events or time periods will allow more realistic comparisons and statistic studies;
- Analytical expressions for dependencies of Wait's parameters on the smoothed daily sunspot number and seasonal parameter valid over the studied area.

The determination of the "sharpness" β and signal reflection height H' during quiet conditions are needed for calculations of the electron density and other plasma parameters in the D-region during both the quiet and disturbed conditions. As a consequence, a more realistic modeling of the D-region can be attained based on results obtained by the proposed methodology. This could benefit to statistical analyses of the D-region related to different unperturbed conditions subject to daily and seasonal variations, as well as variations during a solar cycle. Furthermore, the most accurate modeling of the D-region based on the results obtained by the proposed methodology could also improve the mitigation of ionospheric propagation artefacts in telecommunication and microwave Earth Observation applications.

Due to approximation of the horizontally uniform ionosphere and neglect of influence of geomagnetic field variations on the VLF/LF signal propagation, application of the presented model is limited to:

- Time periods during quiet conditions or during disturbances that do not affect the assumed horizontal uniformity of the observed D-region (for example, the midday periods during the influence of solar X-ray flares),
- VLF/LF signals in which propagation paths between transmitters and receivers are relatively short, and
- Mid- and low-latitude areas where the spatial variations of the magnetic field are not significant in the given conditions.

In other words, the presented model cannot be used when losses, gyrotropy and anisotropy in the region of 70–90 km can significantly affect the propagation of VLF/LF signals in the waveguide Earth-Ionosphre, in particular in situations of large geophysical disturbances of the Lithosphere-Atmosphere-Ionosphere-Magnetosphere system caused by large magnetic storms, hurricanes, etc.

The proposed methodology can be applied during the daytime period when the solar influence on the ionosphere is the largest. During this period the electron density can significantly rise due to influence of intensive sudden solar phenomena like a solar X-ray flare, which can further importantly affect propagation of the mentioned electromagnetic waves.

It is worth noting that the proposed methodology can be applied only to relatively small areas like the one studied in this paper. For this reason, it is more relevant for Europe characterized by a high density network of VLF/LF transmitters and receivers. Improvements of the receiver and/or transmitter networks in future will make the application of the proposed methodology more interesting in providing a real to near-real-time mapping of the D-region electron density above more regions around the world.

Author Contributions: Conceptualization, A.N.; methodology, A.N.; software, A.N. and S.T.M.; validation, G.N., L.Č.P., V.M.Č., S.T.M., I.R.M., and M.R; formal analysis, A.N., G.N., V.M.Č., and L.Č.P.; investigation, A.N.; resources, A.N.; data curation, A.N. and S.T.M.; writing—original draft preparation, A.N.; writing—review and editing, all authors; visualization, A.N. and I.R.M.; funding acquisition, M.R. and A.N. All authors have read and agree to the published version of the manuscript.

Funding: The authors acknowledge funding provided by the Institute of Physics Belgrade and the Astronomical Observatory (the contract 451-03-68/2020-14/200002) through the grants by the Ministry of Education, Science, and Technological Development of the Republic of Serbia.

Data Availability Statement: Publicly available datasets were analyzed in this study. This data can be found here: https://hesperia.gsfc.nasa.gov/goes/goes_event_listings/; https://www.gpsvisualizer.com/calculators; https://www.esrl.noaa.gov/gmd/grad/solcalc/azel.html; http://sidc.oma.be/silso/datafiles; https://ccmc.gsfc.nasa.gov/modelweb/models/iri2012_vitmo.php.

Acknowledgments: The authors thank Frédéric Clette for help in preparation of our study and anonymous reviewers for very useful suggestions and comments. For visualization of the signal propagation paths, authors use website and for calculations the solar zenith angles website . The used daily sunspot numers can be find at . The data for IRI model can be find at . Requests for the VLF data used for analysis can be directed to the corresponding author.

Conflicts of Interest: The authors declare no conflict of interest.

Sample Availability: The VLF data used for analysis is available from the corresponding author.

Appendix A

In this appendix, we provide details of determination of the observational, $w_{\mathrm{obs}}^{\mathrm{XF}}$, and modeled, $w_{\mathrm{mod}}^{\mathrm{XFq}}$, weights described in Section 2.1.2. Changes in the signal amplitude and phase can differ by more than one order of magnitude. For this reason, and also due to different unit of amplitude and phase measurements, in the following, we introduce relative errors of these changes. The observation and modeling weights are defined as follows:

- **Weight $w_{\mathrm{obs}}^{\mathrm{XF}}$.** The relative errors of the recorded signal amplitude and phase are obtained as a ratio of their absolute errors and the corresponding observed changes:

$$\delta(\Delta A^{\mathrm{XFsi}}) = \frac{\mathrm{d}(\Delta A^{\mathrm{XFsi}})}{\Delta A^{\mathrm{XFsi}}}; \quad \delta(\Delta P^{\mathrm{XFsi}}) = \frac{\mathrm{d}(\Delta P^{\mathrm{XFsi}})}{\Delta P^{\mathrm{XFsi}}}. \tag{A1}$$

The total relative error $\delta_{\mathrm{obstot}}^{\mathrm{XF}}$ of the observed changes related to a solar X-ray flare XF is given by:

$$\delta_{\mathrm{obstot}}^{\mathrm{XF}} = \sum_{\mathrm{s}}\sum_{\mathrm{i}}\left[\delta\left(\Delta A^{\mathrm{XFsi}}\right) + \delta\left(\Delta P^{\mathrm{XFsi}}\right)\right]. \tag{A2}$$

The observational weight for an X-ray flare XF is defined as reciprocal value of the total relative error:

$$w_{\mathrm{obs}}^{\mathrm{XF}} = \frac{1}{\delta_{\mathrm{obstot}}^{\mathrm{XF}}}. \tag{A3}$$

- **Weight $w_{\mathrm{mod}}^{\mathrm{XFq}}$.** This weight is computed for Wait's parameters in a quiet state q for which AT LEAST one corresponding pair $(\beta^{\mathrm{XFd}}, H'^{\mathrm{XFd}})$ is such that Equations (6) and (7) are satisfied for both signals s and both states i. In the case there are more pairs $(\beta^{\mathrm{XFd}}, H'^{\mathrm{XFd}})$ with the quite state q, the relative error $\delta_{\mathrm{modtot}}^{\mathrm{XFq}}$ is defined as:

$$\delta_{\mathrm{modtot}}^{\mathrm{XFq}} = \min_{\mathrm{d}}\left\{\sum_{\mathrm{s}}\sum_{\mathrm{i}}\left[\delta\left(\Delta A_{\mathrm{mod}}^{\mathrm{XFsiqd}}\right) + \delta\left(\Delta P_{\mathrm{mod}}^{\mathrm{XFsiqd}}\right)\right]\right\}. \tag{A4}$$

The modeled weight is calculated as:

$$w_{\mathrm{mod}}^{\mathrm{XFq}} = \frac{1}{\delta_{\mathrm{modtot}}^{\mathrm{XFq}}}. \tag{A5}$$

References

1. Kintner, P.M.; Ledvina, B.M. The ionosphere, radio navigation, and global navigation satellite systems. *Adv. Space Res.* **2005**, *35*, 788–811.
2. Meyer, F. Performance requirements for ionospheric correction of low-frequency SAR data. *IEEE Trans. Geosci. Remote Sens.* **2011**, *49*, 3694–3702.
3. Jakowski, N.; Stankov, S.M.; Klaehn, D. Operational space weather service for GNSS precise positioning. *Ann. Geophys.* **2005**, *23*, 3071–3079.
4. Benevides, P.; Nico, G.; Catalão, J.; Miranda, P.M.A. Bridging InSAR and GPS Tomography: A New Differential Geometrical Constraint. *IEEE Trans. Geosci. Remote Sens.* **2016**, *54*, 697–702.
5. Benevides, P.; Nico, G.; Catalão, J.; Miranda, P.M.A. Analysis of Galileo and GPS Integration for GNSS Tomography. *IEEE Trans. Geosci. Remote Sens.* **2017**, *55*, 1936–1943.
6. Su, K.; Jin, S.; Hoque, M.M. Evaluation of Ionospheric Delay Effects on Multi-GNSS Positioning Performance. *Remote Sens.* **2019**, *11*, 171.
7. Yang, H.; Yang, X.; Zhang, Z.; Sun, B.; Qin, W. Evaluation of the Effect of Higher-Order Ionospheric Delay on GPS Precise Point Positioning Time Transfer. *Remote Sens.* **2020**, *12*, 2129.
8. Farzaneh, S.; Forootan, E. A Least Squares Solution to Regionalize VTEC Estimates for Positioning Applications. *Remote Sens.* **2020**, *12*, 3545.
9. Miranda, P.M.A.; Mateus, P.; Nico, G.; Catalão, J.; Tomé, R.; Nogueira, M. InSAR Meteorology: High-Resolution Geodetic Data Can Increase Atmospheric Predictability. *Geophys. Res. Lett.* **2019**, *46*, 2949–2955,
10. Nina, A.; Nico, G.; Odalović, O.; Čadež, V.; Drakul, M.T.; Radovanović, M.; Č. Popović, L. GNSS and SAR Signal Delay in Perturbed Ionospheric D-Region During Solar X-ray Flares. *IEEE Geosci. Remote Sens. Lett.* **2020**, *17*, 1198–1202.
11. Zhao, J.; Zhou, C. On the optimal height of ionospheric shell for single-site TEC estimation. *GPS Solut.* **2018**, *22*, 48.
12. Nava, B.; Coïsson, P.; Radicella, S. A new version of the NeQuick ionosphere electron density model. *J. Atmos. Solar-Terr. Phys.* **2008**, *70*, 1856–1862.
13. Scherliess, L.; Schunk, R.W.; Sojka, J.J.; Thompson, D.C.; Zhu, L. Utah State University Global Assimilation of Ionospheric Measurements Gauss-Markov Kalman filter model of the ionosphere: Model description and validation. *J. Geophys. Res.-Space* **2006**, *111*, 1–19.
14. Silber, I.; Price, C. On the Use of VLF Narrowband Measurements to Study the Lower Ionosphere and the Mesosphere–Lower Thermosphere. *Surv. Geophys.* **2017**, *38*, 407–441.
15. Nina, A.; Pulinets, S.; Biagi, P.; Nico, G.; Mitrović, S.; Radovanović, M.; Č. Popović, L. Variation in natural short-period ionospheric noise, and acoustic and gravity waves revealed by the amplitude analysis of a VLF radio signal on the occasion of the Kraljevo earthquake (Mw = 5.4). *Sci. Total Environ.* **2020**, *710*, 136406.
16. Kumar, S.; NaitAmor, S.; Chanrion, O.; Neubert, T. Perturbations to the lower ionosphere by tropical cyclone Evan in the South Pacific Region. *J. Geophys. Res. Space* **2017**, *122*, 8720–8732.
17. Nina, A.; Radovanović, M.; Milovanović, B.; Kovačević, A.; Bajčetić, J.; Č. Popović, L. Low ionospheric reactions on tropical depressions prior hurricanes. *Adv. Space Res.* **2017**, *60*, 1866–1877.
18. Biagi, P.F.; Maggipinto, T.; Righetti, F.; Loiacono, D.; Schiavulli, L.; Ligonzo, T.; Ermini, A.; Moldovan, I.A.; Moldovan, A.S.; Buyuksarac, A.; et al. The European VLF/LF radio network to search for earthquake precursors: Setting up and natural/man-made disturbances. *Nat. Hazards Earth Syst. Sci.* **2011**, *11*, 333–341.
19. Inan, U.S.; Lehtinen, N.G.; Moore, R.C.; Hurley, K.; Boggs, S.; Smith, D.M.; Fishman, G.J. Massive disturbance of the daytime lower ionosphere by the giant γ-ray flare from magnetar SGR 1806-20. *Geophys. Res. Lett.* **2007**, *34*, 8103.
20. Tanaka, Y.T.; Raulin, J.P.; Bertoni, F.C.P.; Fagundes, P.R.; Chau, J.; Schuch, N.J.; Hayakawa, M.; Hobara, Y.; Terasawa, T.; Takahashi, T. First Very Low Frequency Detection of Short Repeated Bursts from Magnetar SGR J1550-5418. *Astrophys. J. Lett.* **2010**, *721*, L24–L27.
21. Bajčetić, J.; Nina, A.; Čadež, V.M.; Todorović, B.M. Ionospheric D-Region Temperature Relaxation and Its Influences on Radio Signal Propagation After Solar X-Flares Occurrence. *Thermal Sci.* **2015**, *19*, S299–S309.
22. Ferguson, J.A. *Computer Programs for Assessment of Long-Wavelength Radio Communications, Version 2.0*; Space and Naval Warfare Systems Center: San Diego, CA, USA, 1998.
23. Marshall, R.A.; Wallace, T.; Turbe, M. Finite-Difference Modeling of Very-Low-Frequency Propagation in the Earth-Ionosphere Waveguide. *IEEE Trans. Antennas Propag.* **2017**, *65*, 7185–7197.
24. Rapoport, Y.; Grimalsky, V.; Fedun, V.; Agapitov, O.; Bonnell, J.; Grytsai, A.; Milinevsky, G.; Liashchuk, A.; Rozhnoi, A.; Solovieva, M.; et al. Model of the propagation of very low-frequency beams in the Earth–ionosphere waveguide: Principles of the tensor impedance method in multi-layered gyrotropic waveguides. *Ann. Geophys.* **2020**, *38*, 207–230.

25. Morfitt, D.G.; Shellman, C.H. *MODESRCH, an Improved Computer Program for Obtaining ELF/VLF Mode Constants in an EARTH-Ionosphere Waveguide*; Naval Electronics Laboratory Center: San Diego, CA, USA, 1976.
26. McRae, W.M.; Thomson, N.R. Solar flare induced ionospheric D-region enhancements from VLF phase and amplitude observations. *J. Atmos. Solar Terr. Phys.* **2004**, *66*, 77–87.
27. Thomson, N.R.; Rodger, C.J.; Clilverd, M.A. Large solar flares and their ionospheric D region enhancements. *J. Geophys. Res. Space* **2005**, *110*, A06306.
28. Žigman, V.; Grubor, D.; Šulić, D. D-region electron density evaluated from VLF amplitude time delay during X-ray solar flares. *J. Atmos. Solar Terr. Phys.* **2007**, *69*, 775–792.
29. Grubor, D.P.; Šulić, D.M.; Žigman, V. Classification of X-ray solar flares regarding their effects on the lower ionosphere electron density profile. *Ann. Geophys.* **2008**, *26*, 1731–1740.
30. Basak, T.; Chakrabarti, S.K. Effective recombination coefficient and solar zenith angle effects on low-latitude D-region ionosphere evaluated from VLF signal amplitude and its time delay during X-ray solar flares. *Astrophys. Space Sci.* **2013**, *348*, 315–326.
31. Nina, A.; Čadež, V. Electron production by solar Ly-α line radiation in the ionospheric D-region. *Adv. Space Res.* **2014**, *54*, 1276–1284.
32. Poulsen, W.L.; Bell, T.F.; Inan, U.S. The scattering of VLF waves by localized ionospheric disturbances produced by lightning-induced electron precipitation. *J. Geophys. Res. Space* **1993**, *98*, 15553–15559.
33. Han, F.; Cummer, S.A.; Li, J.; Lu, G. Daytime ionospheric D region sharpness derived from VLF radio atmospherics. *J. Geophys. Res.-Space Phys.* **2011**, *116*, 5314.
34. Thomson, N.R. Experimental daytime VLF ionospheric parameters. *J. Atmos. Solar Terr. Phys.* **1993**, *55*, 173–184.
35. McRae, W.M.; Thomson, N.R. VLF phase and amplitude: Daytime ionospheric parameters. *J. Atmos. Solar Terr. Phys.* **2000**, *62*, 609–618.
36. Thomson, N.R.; Rodger, C.J.; Clilverd, M.A. Daytime D region parameters from long-path VLF phase and amplitude. *J. Geophys. Res.-Space* **2011**, *116*, 11305.
37. Gross, N.C.; Cohen, M.B. VLF Remote Sensing of the D Region Ionosphere Using Neural Networks. *J. Geophys. Res. Space* **2020**, *125*, e2019JA027135.
38. Davis, R.M.; Berry, L.A. *A Revised Model of the Electron Density in the Lower Ionosphere*; Technical Report TR III-77; Defense Communications Agency Command Control Technical Center: Washington, DC, USA, 1977.
39. Todorović Drakul, M.; Čadež, V.M.; Bajčetić, J.; L. C. Popović, D.B.; Nina, A. Behaviour of electron content in the ionospheric D-region during solar X-ray flares. *Serb. Astron. J.* **2016**, *193*, 11–18.
40. Srećković, V.; Šulić, D.; Vujičić, V.; Jevremović, D.; Vyklyuk, Y. The effects of solar activity: Electrons in the terrestrial lower ionosphere . *J. Geograph. Inst. Cvijic* **2017**, *67*, 221–233.
41. Morgan, R.R. *World-Wide VLF Effective Conductivity Map*; Westinghouse Electric: Cranberry Township, PA, USA, 1968.
42. Wait, J.R.; Spies, K.P. *Characteristics of the Earth-Ionosphere Waveguide for VLF Radio Waves*; NBS Technical Note: Boulder, CO, USA, 1964.
43. Belrose, J.S.; Burke, M.J. Study of the Lower Ionosphere using Partial Reflection: 1. Experimental Technique and Method of Analysis. *J. Geophys. Res.* **1964**, *69*, 2799–2818.
44. Kane, J. Re-evaluation of ionospheric electron densities and collision frequencies derived from rocket measurements of refractive index and attenuation. *J. Atmos. Terr. Phy.* **1961**, *23*, 338–347.
45. Mitra, A.P., Ed. *Ionospheric Effects of Solar Flares*. Astrophysics and Space Science Library; Springer Nature: Cham, Switzerland, 1974; Volume 46.
46. Ferguson, J.A. *Ionospheric Profiles for Predicting Nighttime VLF/LF Propagation*; Technical report; Naval Ocean Systems Center: San Diego, CA, USA, 1980.
47. Kumar, A.; Kumar, S. Solar flare effects on D-region ionosphere using VLF measurements during low- and high-solar activity phases of solar cycle 24. *Earth Planets Space* **2018**, *70*, 29.
48. Hayes, L.A.; Gallagher, P.T.; McCauley, J.; Dennis, B.R.; Ireland, J.; Inglis, A. Pulsations in the Earth's Lower Ionosphere Synchronized With Solar Flare Emission. *J. Geophys. Res.-Space* **2017**, *122*, 9841–9847.
49. Cohen, M.B.; Inan, U.S.; Paschal, E.W. Sensitive Broadband ELF/VLF Radio Reception With the AWESOME Instrument. *IEEE Trans. Geosci. Remote Sens.* **2010**, *48*, 3–17.
50. Nina, A.; Čadež, V.M.; Bajčetić, J.; Mitrović, S.T.; Popović, L.Č. Analysis of the Relationship Between the Solar X-ray Radiation Intensity and the D-Region Electron Density Using Satellite and Ground-Based Radio Data. *Solar Phys.* **2018**, *293*, 64.
51. Ammar, A.; Ghalila, H. Estimation of nighttime ionospheric D-region parameters using tweek atmospherics observed for the first time in the North African region. *Adv. Space Res.* **2020**, *66*, 2528–2536.
52. Bilitza, D. IRI the International Standard for the Ionosphere. *Adv. Radio Sci.* **2018**, *16*, 1–11.
53. Thomson, N.R.; Clilverd, M.A.; Rodger, C.J. Midlatitude ionospheric D region: Height, sharpness, and solar zenith angle. *J. Geophys. Res. Space* **2017**, *122*, 8933–8946.

Applied Surface Science 608 (2023) 155114

Contents lists available at ScienceDirect

Applied Surface Science

journal homepage: www.elsevier.com/locate/apsusc

Full length article

Natural two-dimensional pyrophyllite: Nanoscale lubricant, electrical insulator and easily-machinable material

Borislav Vasić [a,*], Radoš Gajić [a], Ivana Milošević [a], Žarko Medić [a], Marina Blagojev [b], Marko Opačić [a], Aleksandar Kremenović [c], Dejan Lazić [d]

[a] Institute of Physics Belgrade, University of Belgrade, Pregrevica 118, 11080 Belgrade, Serbia
[b] Faculty of Mining and Geology, University of Belgrade, Đušina 7, 11000 Belgrade, Serbia
[c] Laboratory of Crystallography, Faculty of Mining and Geology, University of Belgrade, Đušina 7, 11000 Belgrade, Serbia
[d] Biotech Engineering D.O.O, Golsvordijeva 32, 11000 Belgrade, Serbia

ARTICLE INFO

Keywords:
Natural two dimensional materials
Phyllosilicates
Pyrophyllite
Nanofriction and wear
Insulating properties
Atomic force microscopy

ABSTRACT

Pyrophyllite, with the chemical formula $Al_2Si_4O_{10}(OH)_2$, is a naturally occurring and abundant van der Waals mineral belonging to the group of phyllosilicates. It is very soft, layered crystal used for sculpting and an excellent electrical and thermal insulator aimed for the operation at high pressure and temperature. Here, for the first time, two-dimensional (2D) pyrophyllite obtained by both mechanical and liquid phase exfoliation is presented and investigated at the nanoscale. The layered structure provides low friction coefficient of around 0.1 as measured by friction force microscopy. The wear properties, studied by atomic force microscope (AFM) based scratching, are distinctly different from graphene. Since the wear is initiated at low normal forces, 2D pyrophyllite can be routinely carved by the AFM tip and it is suitable for scratching based nanolithography. According to our optical measurements, 2D pyrophillite is an insulator with a band gap of ~ 5.2 eV. Local current measurements by conductive AFM reveal that 2D pyrophyllite flakes behave as efficient electrical insulators with a breakdown voltage of around 6 MV/cm. Therefore, the obtained results indicate possible applications of 2D pyrophyllite as a low-cost electric insulator and lubricant, as well as an easily-machinable material at the nanoscale.

1. Introduction

Layered materials are usually defined as a special crystal class existing in the form of weakly stacked atomic layers, like graphene in graphite. General property of these materials are the strong in-plane bonds and very weak interactions perpendicular to the planes, typically of the van der Waals type. Therefore, layered materials that can be exfoliated into atomically thin layers are often called van der Waals materials. Two dimensional (2D) materials concerns crystalline solids consisting of a single or few atomic layers. Huge interest for them started when large graphene flakes were isolated for the first time in 2004 by Novoselov et al. using mechanical exfoliation [1]. Extraordinary properties of graphene [2] triggered the search for new 2D materials. Nowadays hundreds of different 2D materials beyond graphene have been devised and thoroughly investigated because of their extraordinary properties that are not present in corresponding counterpart bulk materials. As a result, 2D materials find numerous applications in nanoelectronics, nanophotonics and optoelectronics, spintronics, sensing and many other fields [3–5].

After the discovery of graphene, the second generation of 2D materials, which includes hexagonal boron nitride, 2D transition metal dichalcogenides (such as MoS_2, WS_2, $MoSe_2$, WSe_2, $MoTe_2$) and functionalized graphene, quickly appeared [6–11]. The third-generation of 2D materials includes elemental analogues of graphene such as silicene, germanene, stanene, phosphorene [12], as well as with 2D transition metal carbides and carbonitrides (MXenes) [13], 2D silicon dioxide [14], and minerals [15]. Interestingly, many of them were firstly discovered by numerical calculations, and afterwards, experimentally obtained [16].

The most of 2D materials are synthetic, for instance large-scale 2D materials are commonly prepared by chemical vapour deposition. On the other hand, natural van der Waals minerals exist in most classes of 2D materials like semi-metallic graphite and semiconducting molybdenite MoS_2 and tungstenite WS_2. In recent years, a new family of 2D materials has appeared. It is based on layered natural minerals as a source of 2D materials [15]. This family includes 2D insulating materials based on phyllosilicates such as talc [18–24], muscovite (mica) [25],

---

[*] Corresponding author.
E-mail address: bvasic@ipb.ac.rs (B. Vasić).

https://doi.org/10.1016/j.apsusc.2022.155114
Received 5 August 2022; Received in revised form 23 September 2022; Accepted 26 September 2022
Available online 29 September 2022

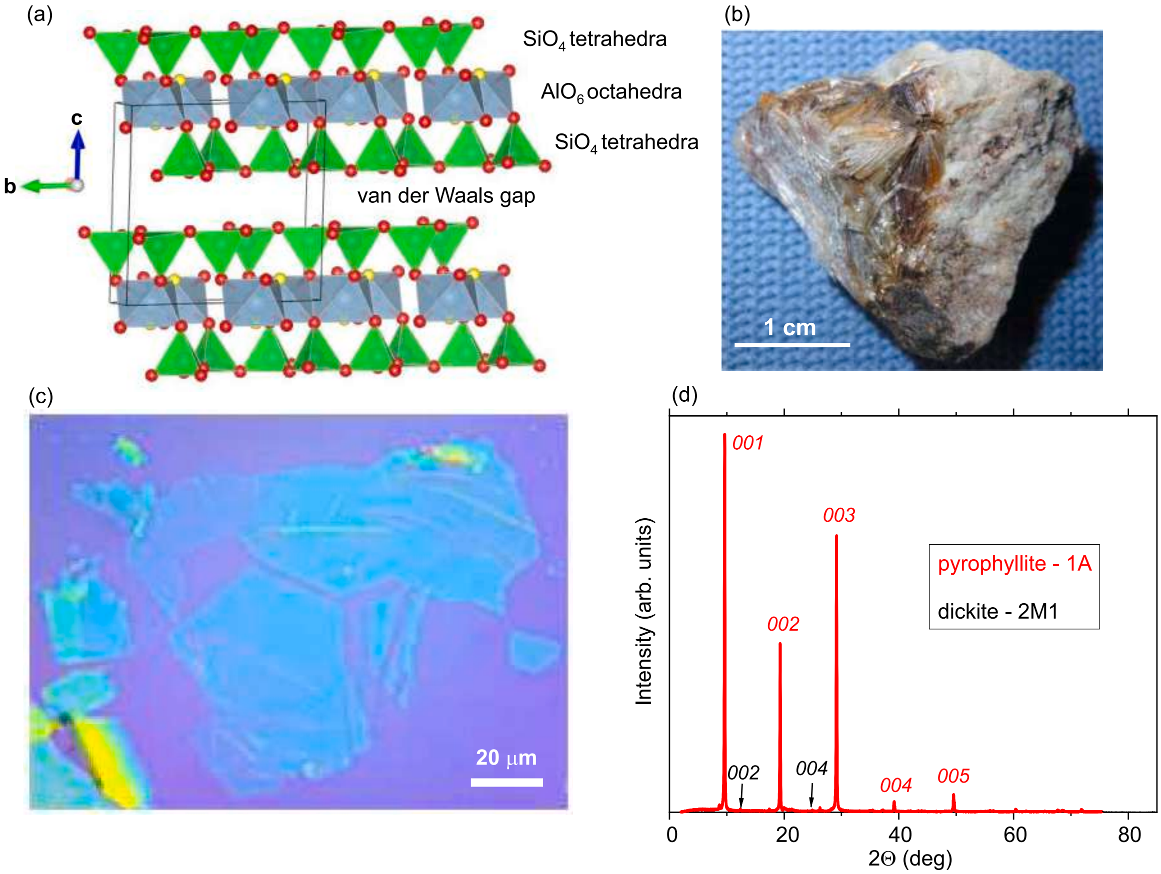

Fig. 1. (a) Polyhedral representation of pyrophyllite-1A structure: SiO_4 tetrahedra in green, AlO_6 octahedra in blue, oxygen atoms in red, OH group in yellow. The unit cell is outlined in black. VESTA program [17] was used for three-dimensional visualization of the crystal structure. (b) Optical image of the crystalline pyrophyllite used in this study. (c) Optical micrograph of mechanically exfoliated 2D pyrophillite flakes. (d) XRPD pattern of bulk pyrophyllite crystal which contains pyrophyllite-1A (PDF card # 01-075-0856) and small amount (near detection limit) of dickite-2M1 (PDF card # 00-058-2002). Most intense *hkl* reflections are marked.

biotite [26], vermiculite [27], clinochlore [28], and phlogopite [29], as well as 2D magnetic materials such as cylindrite [30] and iron-rich talc [31]. Furthermore, semiconducting van der Waals mineral franckeite has been used for the exfoliation of 2D van der Waals heterostructures [32–34]. Therefore, 2D materials can be obtained directly from natural minerals by just simple exfoliation and without complex synthetic procedures. As a result, search of 2D materials among natural minerals can be particularly interesting. Furthermore, clay minerals are abundant in Earth crust and therefore they serve as cost-effective sources of 2D materials. This mainly concerns phyllosilicates or layered silicates such as talc, pyrophyllte, kaolinite, gibbsite, etc., which are the most common and abundant clays.

Pyrophyllite (from Greek pyro—fire and phyllos—a leaf) is natural van der Waals mineral which belongs to the talc–pyrophyllite family of phyllosilicates. It is a hydrous aluminum silicate with the chemical formula $Al_2Si_4O_{10}(OH)_2$. Single layer of pyrophyllite consists of the AlO_6 octahedral sheet sandwiched between two SiO_4 tetrahedral layers (Fig. 1(a)). Pyrophyllite is a chemically inert material, good electrical and thermal insulator with a high melting point [35] and with a fairly high dielectric constant [36,37]. As a clay mineral, it is abundant and inexpensive. Therefore, it is widely used in refractories, high-grade ceramics, electric insulators, and as a filler in order to improve properties of paper, plastic, rubber, paint and other mixtures [35]. As a van der Waals material, pyrophyllite has a lamellar structure which indicates good frictional properties and its applications as a lubricant [38]. It is very soft mineral [35] which provides easy machining and making of various profiles, while at the same time, it can withstand large pressures. Therefore, bulk pyrophyllite mineral exhibits interesting properties with a broad range of potential applications. Still, its 2D form has not been studied so far, although small flakes of few layer pyrophyllite have been obtained by liquid phase exfoliation [39], whereas thermal exfoliation was investigated as well [40], but not in the context of 2D layers.

Here we present our report on 2D pyrophyllite with the focus on its properties related to potential applications as 2D electric insulator, lubricant and material suitable for nanolithography. Using mechanical and liquid phase exfoliation (LPE), we routinely fabricated few-layer pyrophyllite which can be exfoliated down to single-layer thickness. The initial characterization was done by X-ray powder diffraction (XRPD), Raman spectroscopy, UV–VIS spectroscopy, and optical microscopy. Afterwards, we focused on nanoscale mechanical and electrical properties of 2D pyrophyllite such as friction, wear, nanoscale machining, as well as insulating properties and dielectric breakdown, which were investigated by atomic force microscopy (AFM) based methods.

2. Experimental methods

2.1. Sample preparation

Here we used the crystalline pyrophyllite from Hillsborough, Orange County, North Carolina, USA (Fig. 1(b)). 2D pyrophyllite flakes were obtained by the mechanical exfoliation [41] onto SiO_2/Si substrate (with 300 nm thick SiO_2). Briefly, thick pyrophyllite flakes were separated from the bulk crystal by an adhesive tape. These flakes were further thinned by multiple peeling against two pieces of the tape, and finally transferred onto the substrate. The flakes of interest were selected by optical microscopy (typical optical micrograph depicted in Fig. 1(c)).

The starting material for LPE of pyrophyllite was ground pyrophyllite crystal (Hillsborough mine, Orange County, North Carolina, USA). Its dispersion was obtained in N-N-Dimethylformamide (DMF, Sigma Aldrich, product no. D4551), while the initial concentration of pyrophillite was 10 mg/mL (in 10 mL cylindrical vial). The solution was then sonicated in a low-power ultrasonic bath for 12 h. The resulting yellowish dispersion was centrifuged for 15 min at 1000 rpm. In order to fabricate pyrophyllite films from the obtained dispersion, Langmuir–Blodgett Assembly (LBA) technique at a water–air interface was used. This technique was previously employed for the preparation of graphene films as well [42,43]. In the first step, a small amount of pyrophyllite dispersion in DMF was added at the water–air interface. Then, after the pyrophyllite film was formed at the interface, it was slowly picked up by desired substrate. Three different substrates were used: SiO_2/Si for AFM measurements (morphological characterization), Au-coated SiO_2/Si for C-AFM measurements (current maps and breakdown voltage), and quartz for UV–VIS spectroscopy.

2.2. XRPD measurements, Raman and UV–VIS spectroscopy

The structural characterization was done by XRPD which was conducted at room temperature on Rigaku Smartlab X-ray Diffractometer in $\theta-\theta$ geometry (the sample in the horizontal position) in parafocusing Bragg–Brentano geometry using D/teX Ultra 250 strip detector in 1D standard mode with $\mathrm{CuK}\alpha_{1,2}$ radiation source (U = 40 kV and I = 30 mA). The XRPD pattern was collected in 2–90° 2θ range, with the step of 0.01°, and data collection speed of 6°/min. The pyrophyllite sample was spinning in the horizontal plane with the speed of 60 rounds per minute. The low background single crystal silicon sample holder was used to minimize the background. The PDXL2 integrated XRPD software (Version 2.8.30; Rigaku Corporation) was employed for XRPD data treatment.

Raman scattering measurements were performed on Tri Vista 557 Raman system, in backscattering micro-Raman configuration. The 514.5 nm line of an Ar^+/Kr^+ gas laser was used as an excitation source. Laser power was less than 1 mW on a sample in order to minimize its local heating. A microscope objective with the 50x magnification was used for focusing the laser beam. All measurements were performed at ambient conditions.

Optical transmittance of the pyrophyllite film (obtained by liquid phase exfoliation) was measured by ultraviolet–visible (UV–VIS) spectrophotometer Beckman Coulter DU 720 in the range from 200 to 900 nm.

2.3. AFM measurements

The morphological characterization of 2D pyrophillite was done by imaging in the tapping AFM mode. Friction was measured using friction force microscopy, by recording the lateral force which corresponds to the lateral torsion of the AFM cantilever during scanning in the contact AFM mode. The friction signal was calculated as a half difference between lateral forces measured in forward and backward scan direction. The measurements were done using NSG01 probes (nominal stiffness 5 N/m) from NT-MDT, while the applied normal load was up to ~300 nN, well below the threshold force needed to initiate wear. The wedge calibration of frictional forces was used in order to transform measured lateral signal into frictional forces [44].

Wear properties were studied by scratching the pyrophyllite flakes in the AFM contact mode. Square domains were scratched with an increased normal force (applied by the AFM tip) from the bottom to the top of the scan regions. The maximal normal load needed to initiate wear was around 1 μN. When a wear was initiated, the normal force was held constant. Mechanically robust and stiff, diamond coated probes DCP11 (nominal stiffness 11.5 N/m) from NT-MDT were used since they allowed high normal forces needed for scratching as well as subsequent imaging of scratched areas in the tapping AFM mode.

The AFM based nano-lithography was done using diamond coated probes HA_HR_DCP (nominal stiffness 35 N/m) from NT-MDT in three modes: nanoindentation and two lithographic modes, vector and raster. The nanoindentation mode is very similar to the measurement of force–displacement curves. The AFM scanner holding a sample was moved only vertically (without scanning in the horizontal plane) toward the AFM tip in order to induce a point-like deformation in pyrophyllite. For this purpose, the applied normal load was around 6 μN. In the lithographic modes, pyrophillite surface was scratched in the AFM contact mode according to predefined templates. In the case of the vector lithography, the templates were defined by discrete lines only, whereas in the case of the raster lithography, the square domains were taken for simplicity. During the nano-lithography, two force levels were applied. The low force level was applied along trajectories of the AFM tip which should stay intact (the movements between discrete line segments to be scratched, from the initial position to the first line segment, and from the last line segment back to the initial position). On the other hand, a high force level in the range ~2–6 μN was applied on segments which are to be scratched. The scratching velocity was around 0.2 μm/s. It was significantly decreased compared to the scanning speed in order to provide an efficient lithography.

The study of insulating properties and dielectric breakdown requires 2D pyrophyllite flakes placed between two metallic electrodes. In order to make possible study at the nanoscale, conductive AFM (C-AFM) was employed. For this purpose, the pyrophyllite flakes obtained by LPE method were deposited on a gold substrate. Then, a metallic AFM tip on the top of a pyrophyllite flake served as a top electrode, while the underlying gold was a bottom electrode. The bias voltage was applied on the gold, while the AFM tip in contact with the pyrophyllite flakes was (virtually) grounded. The current imaging was done by scanning in C-AFM mode, using highly doped and conductive, diamond coated probes DCP11, and simultaneously recording topography and local current. Dielectric breakdown was examined by measuring local I/V curves at single point, while the bias voltage was swept in a range ±10 V.

3. Results and discussion

3.1. Structural and vibrational properties

The results of XRPD measurements presented in Fig. 1(d) show that the specimen predominantly contains crystalline pyrophyllite-1A (PDF (Powder Diffraction File) card # 01-075-0856), whereas a small amount (near detection limit) of dickite-2M1 (PDF card # 00-058-2002) was also identified. The most intense reflections in the XRPD pattern of the dominant phase are $00l$ ($l = 1-5$) which is in accordance with the layered structure of pyrophyllite-1A. The XRPD results indicate that a crystalline pyrophyllite sample (Fig. 1(b)) has a triclinic lattice and 2:1 structure (two tetrahedral sheets and one octahedral sheet) depicted in Fig. 1(a). The refined unit cell parameters for pyrophyllite-1A are the following (estimated standard deviations in parenthesis): a = 5.14(2) Å, b = 8.99(4) Å, c = 9.28(4) Å, α = 91.88(8)°, β = 99.36(15)°, γ = 89.16(15)°, V = 423(3) $Å^3$. The refined values, within an experimental error, are in a very good agreement with the values obtained for pyrophyllite-1A (OH group in the structure) in both single crystal XRD experiment [45] and powder XRD experiment [46].

Raman spectra of the bulk crystalline pyrophyllite are presented in Fig. 2 in the spectral ranges from 50 to 1100 cm^{-1} and 3600 to 3750 cm^{-1}. The first range describes the fundamental vibrations of all phyllosilicates, whereas the second one displays the vibrations of the H_2O/OH group [47–49]. Our spectra are fully consistent with the previous published Raman spectra of crystalline pyrophyllite [47]. They contain all fundamental modes up to 1100 cm^{-1} as well as H_2O/OH peak at 3670 cm^{-1}. Details and the full assignment of all modes could be found elsewhere [47].

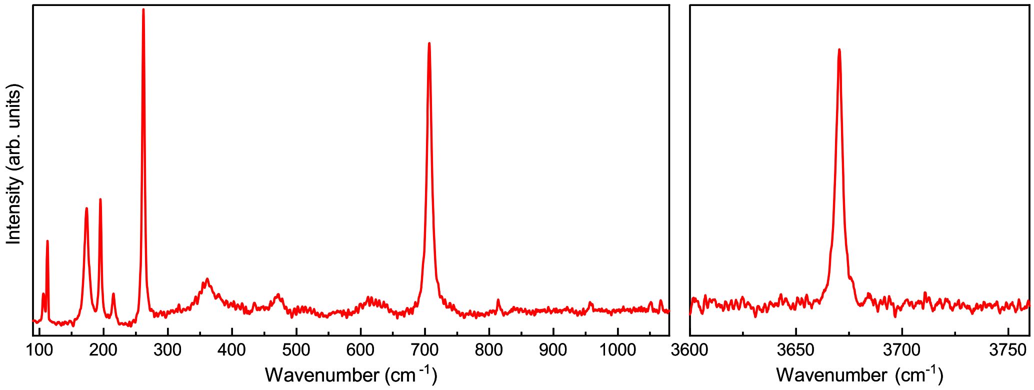

Fig. 2. Raman spectrum of a bulk pyrophyllite for two spectral ranges: the fundamental vibrations of phyllosilicates (left) and the H_2O/OH range (right).

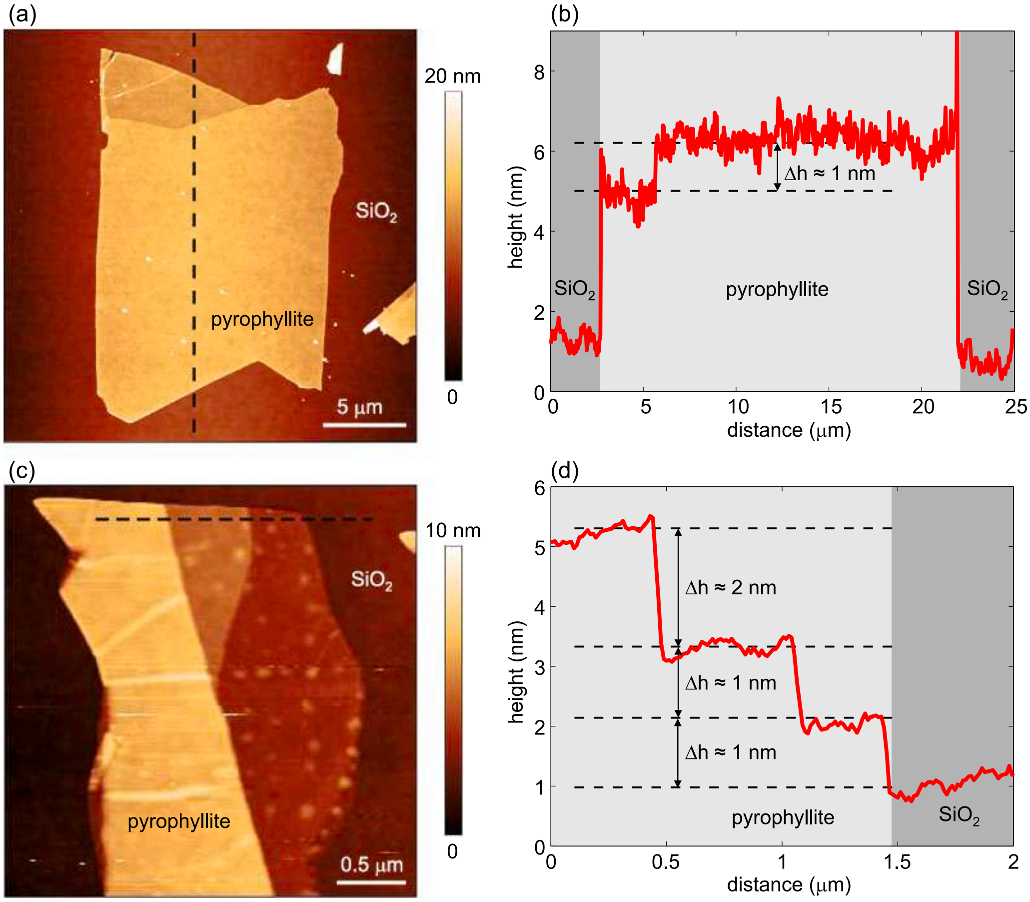

Fig. 3. (a), (c) Topographic images of pyrophillite flakes mechanically exfoliated on Si/SiO$_2$ with (b), (d) corresponding height profiles along dashed lines with indicated characteristic step heights.

3.2. Morphology

Fig. 3(a) depicts the topography of a typical flake obtained by mechanical exfoliation, with the height profile given in Fig. 3(b). It is a few-layer pyrophyllite with a thickness of ~5 nm and an area of ~15 × 20 μm^2. The root-mean-square roughness calculated on 5 × 5 μm^2 areas is only 0.6 nm indicating atomically flat surface free of residues. The height profile (Fig. 3(b)) reveals that a step height between two domains is only ~1 nm.

The trilayer structure of the pyrophyllite unit cell displayed in Fig. 1(a) consists of AlO$_6$ octahedral sheet sandwiched between two SiO$_4$ tetrahedral layers. According to XRPD results, the thickness of the neutral trilayer is 6.39 Å, whereas the thickness of van der Waals gap is 2.76 Å [45], measuring from the center of oxygen ions (O^{2-}). Accordingly, the effective thickness of the trilayer is around 9.2 Å, measuring from the top to bottom oxygen surfaces since we have to add two oxygen ion radii of 2.8 Å. Therefore, the thickness of single layer pyrophyllite measured by AFM should be around more or the same. The smallest thickness measured in our AFM experiments was always around 1 nm. The same minimal thickness was observed in AFM scratching based experiments as discussed below. Therefore, this value corresponds to the single layer of pyrophyllite. The small discrepancy between expected (around 9.2 Å) and measured thickness (around 1 nm) probably appears due to adsorbed water layer which is inevitable at ambient conditions and/or due to measurements done in

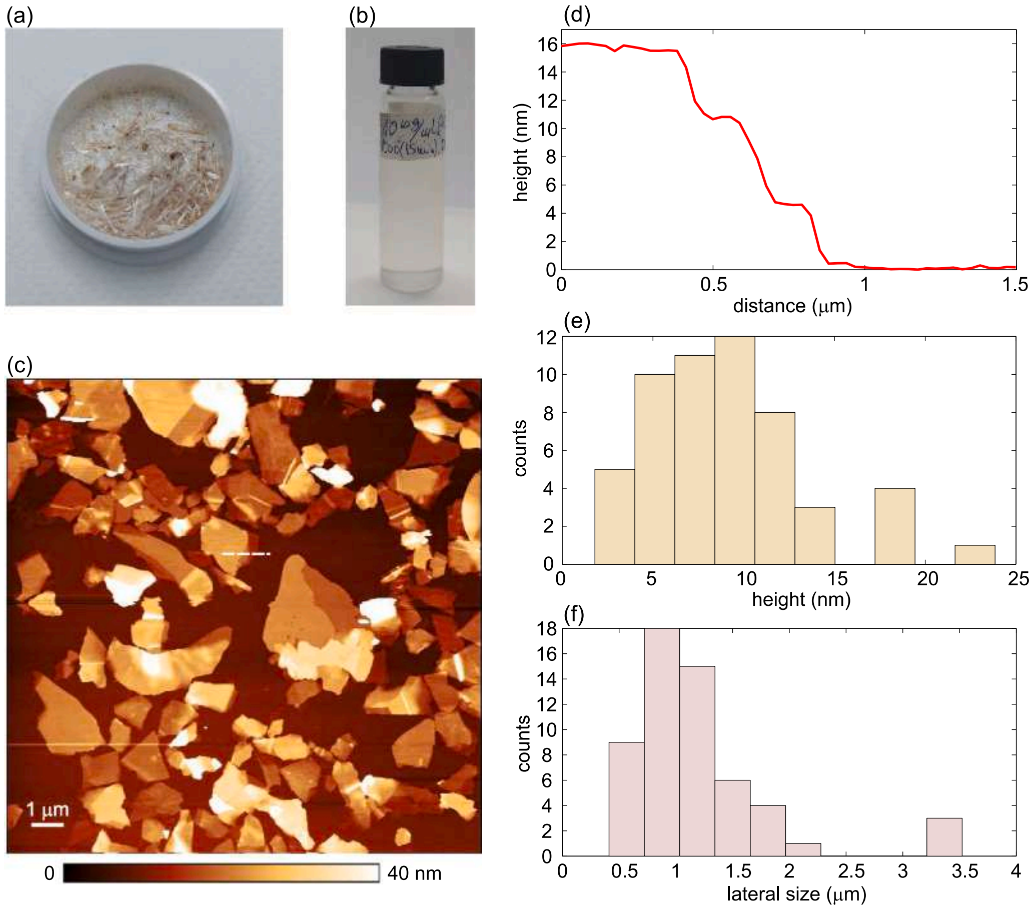

Fig. 4. (a) Ground pyrophyllite mineral used as a starting material for LPE and (b) the resulting dispersion employed for LBA. (c) Topographic image of pyrophillite flakes obtained by LPE and subsequent LBA on Si/SiO_2. (d) Height profile along the dashed line in (c). Histograms of (e) height and (f) lateral size of the flakes shown in (c).

tapping AFM mode, which commonly gives an increased step height on atomically thin layers [50].

Generally, we routinely exfoliated few layer pyrophillite flakes with the lateral size larger than 10 µm. On the other hand, yield of single layers was low, while their size was significantly smaller. One example is illustrated in Fig. 3(c). The corresponding height profile in Fig. 3(d) displays two single-layer step heights of ~1 nm, and the third step height of ~2 nm which corresponds to double-layer flake. As can be seen, the area of the single layer pyrophillite is only several square micrometers.

The ground pyrophyllite crystal and its yellowish dispersion used in LPE are depicted in Fig. 4(a) and (b), respectively. Topography of 2D pyrophyllite obtained by the LPE method is depicted in Fig. 4(c). The height profile in Fig. 4(d) displays three step heights of ~5 nm. Samples produced by the LPE method consist of a network of flakes with a typical height of 5–15 nm (Fig. 4(e)) and lateral dimensions of ~1 µm (Fig. 4(f)). The flakes have well defined shapes, flat surface and regular edges. Although they are thicker and smaller compared to those fabricated by the mechanical exfoliation, LPE method provides large scale production of 2D pyrophyllite. At the same time, the LPE method can be easily adapted to various substrates. This was employed below in the study of insulating properties and dielectric breakdown of 2D pyrophyllite, where the flakes were deposited on a gold substrate.

3.3. Friction

Friction properties are analyzed on a small segment of the pyrophyllite layer surrounded by SiO_2 as depicted in Fig. 5(a). In the friction force map displayed in Fig. 5(b), the pyrophyllite is represented by a dark contrast, thus indicating decreased friction compared to SiO_2. The height and friction force profiles from Fig. 5(c) reveal three times lower friction on the pyrophyllite. The same measurements were done for the normal force in the range ~30–330 nN. Average friction forces on both pyrophyllite and SiO_2 were calculated from the histograms of friction maps and the corresponding results are presented in Fig. 5(d). As can be seen, the friction force approximately linearly increases with the normal force in accordance with Amonton's law. The friction coefficients were calculated from the slopes of the linear fits (dashed lines in Fig. 5(d)). The obtained friction coefficient of the pyrophyllite flake $\mu_{pyr} = 0.12$ is more than four times lower than the friction coefficient of surrounding silicon-dioxide substrate ($\mu_{SiO_2} = 0.5$). At the same time, μ_{pyr} is very similar to the friction coefficient of graphene grown by chemical vapour deposition [51] and 2D talc [21]. Therefore, the presented results indicate good lubricating properties of few-layer thick pyrophyllite.

Generally, mechanical and liquid phase exfoliation give 2D layers with the same physical properties. The main difference between two methods is morphology of produced layers, the lateral size of the flakes before all. Therefore, we expect the same friction properties of pyrophyllite obtained by both methods. Additional friction measurements on LPE pyrophyllite prove this predictions. The results presented in figure S1 of Supplementary material show that pyrophyllite flakes obtained by LPE has a low friction coefficient of around 0.14, that is, very similar to pyrophyllite obtained by the mechanical exfoliation (0.12). Compared to the surrounding silicon-dioxide substrate, the friction is again decreased by around four times.

In our previous manuscript [21] we investigated friction as a function of talc thickness in detail. Talc friction reduces with number of layers (talc thickness), which is similar to other 2D materials, since so

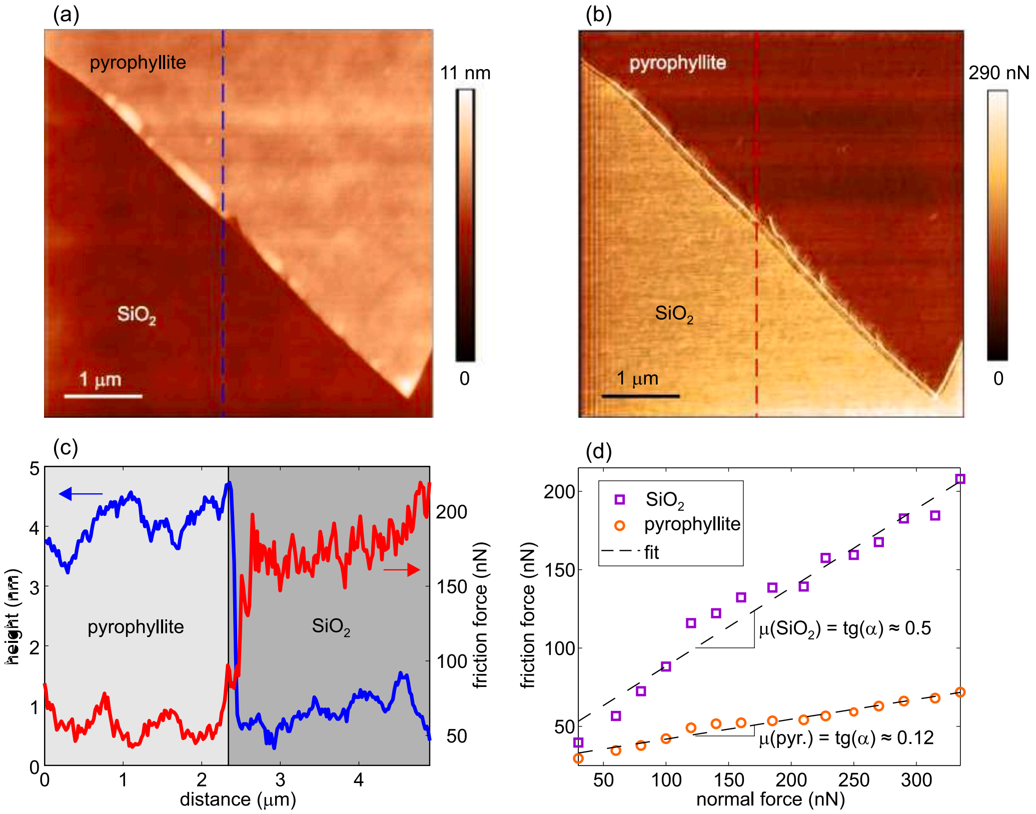

Fig. 5. (a) Topography and (b) friction force map of pyrophyllite flake on Si/SiO_2. (c) Height and force profiles along dashed lines in (a) and (b), respectively. (d) Average friction force (calculated from histograms of friction maps such as the one presented in (b)) as a function of the normal force applied by the AFM tip. Friction coefficients were calculated as slopes of the linear fits represented by dashed lines.

called puckering effect, responsible for the friction of 2D materials, is less pronounced for thicker layers due to larger bending rigidity. In the case of talc, this dependence is rather weak, since single layer is 1 nm thick and already consists of three atomic planes. Pyrophyllite and talc belong to the family of 2:1 phyllosilicates. Their chemical formulas are almost identical (pyrophyllite - $Al_2Si_4O_{10}(OH)_2$, talc - $Mg_3Si_4O_{10}(OH)_2$) and they have practically the same structure (octahedral plane with metallic (Al or Mg) ion sandwiched between two tetrahedral SiO layers). The thickness of the single layer (around 1 nm) is similar in both materials. Therefore, dependence of the friction as a function of pyrophyllite thickness should be the same as for talc. This conclusion is further confirmed in figure S1(b) of Supplementary material depicting friction map of pyrophyllite flakes produced by LPE. Although their thicknesses vary in a broad range from only several nanometers to several tens of nanometers, the friction force on the pyrophyllite is associated with a single peak in the corresponding histogram given in figure S1(c) (the observed dispersion (width of the histogram peak) is very similar to the dispersion of the friction force measured on SiO_2 substrate).

3.4. Wear

The next step was to analyze wear properties and behavior of 2D pyrophyllite for high normal load applied by the AFM tip during scanning in contact mode. Fig. 6(a) displays the topography recorded after the AFM scratching of the central square domain. From the right, left, and top side, the scratched domain is surrounded by walls (represented by a bright contrast) formed from the material deposited by the AFM tip. Enlarged topographic image of the scratched area is presented in Fig. 6(b) together with the characteristic height profile in Fig. 6(c). At the bottom of the figure, the pyrophyllite surface is flat and without visible wear scars due to low normal load. At the same time, the lateral force recorded during the AFM scratching is low and approximately constant as depicted in Fig. 6(d) and (e). Since there is no wear, the lateral force corresponds to the friction between the AFM tip and pyrophyllite.

In the experiment, the normal load was increasing as the AFM tip was moving from the bottom to the top. For high enough normal load of around 1.1 μN, the wear was initiated and afterwards, the normal load was held constant. As a result of the wear, pyrophyllite surface became crumpled with many local holes and bumps. The holes present local depressions made by peeling pyrophyllite layers, while bumps are local hills formed out of the material previously peeled off (Fig. 6(c)). The height profile in Fig. 6(c) reveals several step heights of ~1 nm. They correspond to single layer of pyrophyllite which therefore indicates that the AFM scratching leads to layer-by-layer peeling. The lateral force during the scratching (Fig. 6(d) and (e)) is increased compared to the bottom area without wear scars. Although this is expected due to higher normal load applied by the AFM tip, the lateral force profile is not flat anymore, but strongly oscillating. Obviously, bright puddles in the force map (Fig. 6(d)) and peaks in the force profile (Fig. 6(e)) correspond to strongly increased lateral force required for tearing and peeling of pyrophyllite layers.

According to the presented results, during the AFM scratching, pyrophyllite behaves in a different manner compared to well known 2D materials such as graphene and transition metal dichalcogenides (MoS_2, and WS_2) [52,53]. The scratching of these materials is associated with wrinkling at the initial stage, while at higher normal loads, it is followed by a sudden tearing along the direction of the AFM tip movement, and finally by a peeling of large segments and their folding. On the other hand, in the case of pyrophillite, exfoliated segments made by the AFM scratching are small, not folded, and they form local bumps of irregular shapes. Recently, similar results have been obtained for muscovite (mica), another phyllosilicate van der Waals mineral, and

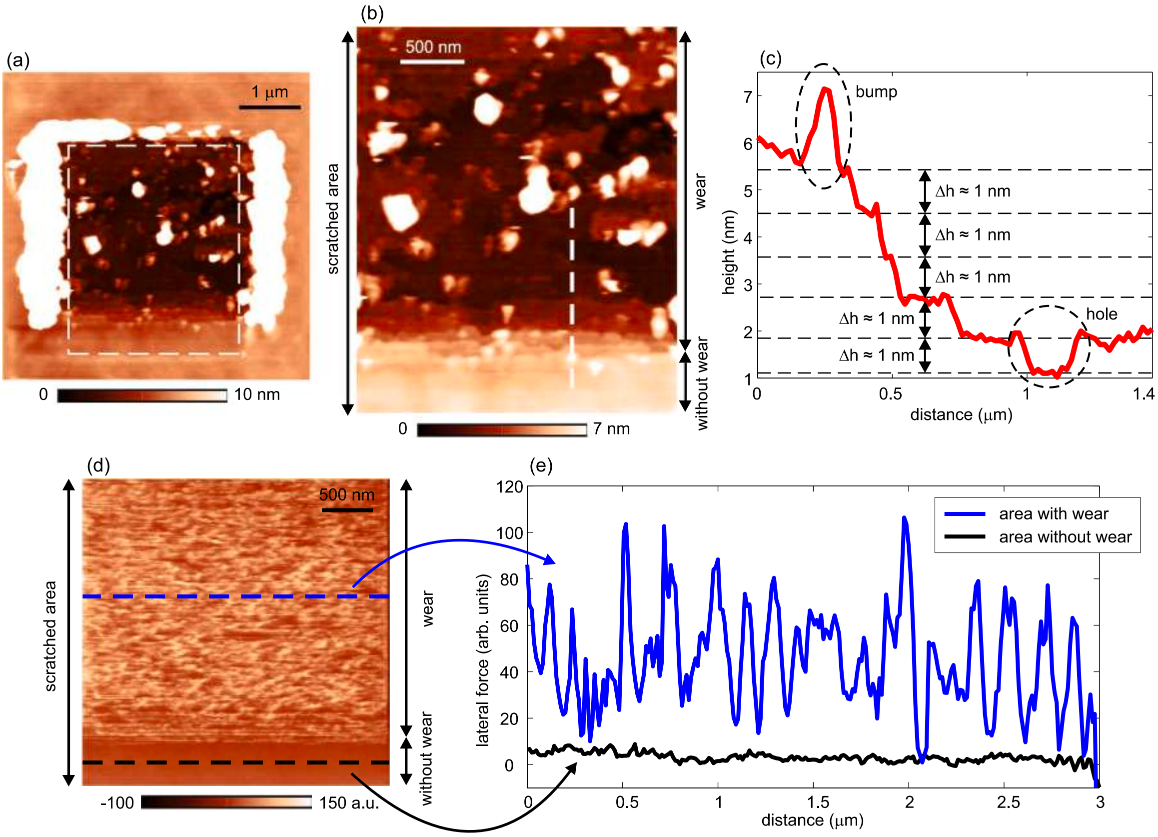

Fig. 6. (a) Topographic image of a pyrophyllite flake after the AFM scratching. (b) The topographic image of the domain encircled by the dashed line in (a) focusing on the scratched area only. (c) The height profile along the dashed line in (b) with indicated step heights of ~1 nm and local hole/bump (encircled by dashed lines). (d) The lateral force map recorded during the AFM scratching. (e) The lateral force profiles along two dashed lines in (d), standing for the area with and without wear.

the observed difference in wear properties were explained by different mechanical properties [53]. Accordingly, significant thickness of single layer of pyrophyllite (~1 nm) and large bending rigidity of ~70 eV [54] limit its flexibility and folding. At the same time, Young's modulus (modulus of elasticity) of ~100 GPa [55,56] and tensile strength less than 10 GPa [56,57] are much lower than in the case of graphene and transition metal dichalcogenides, which indicates much brittle structure of pyrophyllite. This can be indirectly confirmed by comparing threshold normal loads needed to initiate wear. In the case of graphene and transition metal dichalcogenides, the threshold load is at least several μN [52,53], while in the case of pyrophyllite, it is much lower, around 1 μN. As a result, pyrophillite layers are easily torn into small pieces during AFM scratching.

Wear of 2D materials is always started from their edges (these are weak points for wear), and not on homogeneous (flat) 2D flakes [58]. Since LPE 2D materials are associated with small flakes and huge number of exposed edges, their wear resistance is determined by their edges [59], and it is always lower that the wear resistivity of 2D material itself. For this reason, wear of LPE pyrophyllite was not studied here.

3.5. Nanoscale machining and nanolithography

As mentioned in the previous section, the AFM scratching of graphene and transition metal dichalcogenides generally leads to their peeling, but not to local cutting along directions defined by the movement of the AFM tip. On the other hand, lower elasticity and tensile strength of 2D pyrophyllite indicate that it could be suitable material for AFM scratching based nanolithography. The results of the nanolithography of 2D pyrophyllite are presented in Fig. 7. Three basic shapes and characteristic height profiles are presented for the following cases: the hole made by nanoindentation (Fig. 7(a–b)), the trench carved out by line scratching (Fig. 7(c–d)), and the square crater made by raster scratching (Fig. 7(e–f)). As can be seen, the AFM tip induces local carving of a pyrophyllite flake. This process is associated with the tearing of the pyrophyllite into small pieces, which are then deposited around the tip during its motion. The deposited material was then removed by several additional scans in contact AFM mode (not shown here). They were done at lower normal load, which was insufficient to cause pyrophyllite cutting and wear, but high enough to provide pushing of the deposited material by the AFM tip.

As can be seen, 2D pyrophyllite is efficiently carved by applying a local pressure at single point (Fig. 7(a)) as well as during AFM tip motion (Fig. 7(c)). Making of holes on wider areas is successfully achieved by AFM scratching along array of parallel lines (Fig. 7(e)). Depth of created objects was controlled by applied normal load as illustrated in Fig. 7(e–f) showing that a deeper crater was formed by a higher normal force. The width of the line trench in Fig. 7(c) is 150–300 nm. It is strongly influenced by the width of the diamond coated probes employed here, and it is reasonable to expect that a better resolution and more narrow features could be created with sharper AFM tips.

3.6. Electronic bandgap

Electronic bandgap was estimated from UV–VIS spectroscopic measurements. For that purpose, a large-area pyrophyllite film was obtained by LPE. The film thickness was around 20 nm as determined by AFM measurement. Transmittance through the pyrophyllite film for wavelengths in the range 200–900 nm is displayed in the inset of Fig. 8. As can be seen, the film is transparent with the transmittance in the visible region above 97%. The obtained transmittance spectrum allows the calculation of an intrinsic optical absorption coefficient

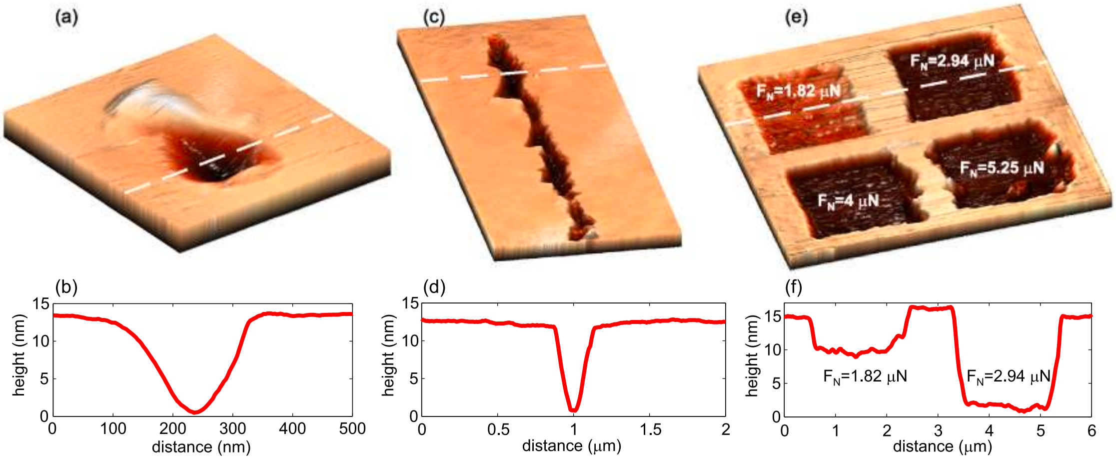

Fig. 7. The topographic images and the height profiles for three characteristic structures made by nanolithography of pyrophyllite: (a–b) single hole obtained by nanoindentation, (c–d) trench made by the AFM scratching along single line, (e–f) four square domains made by raster scratching.

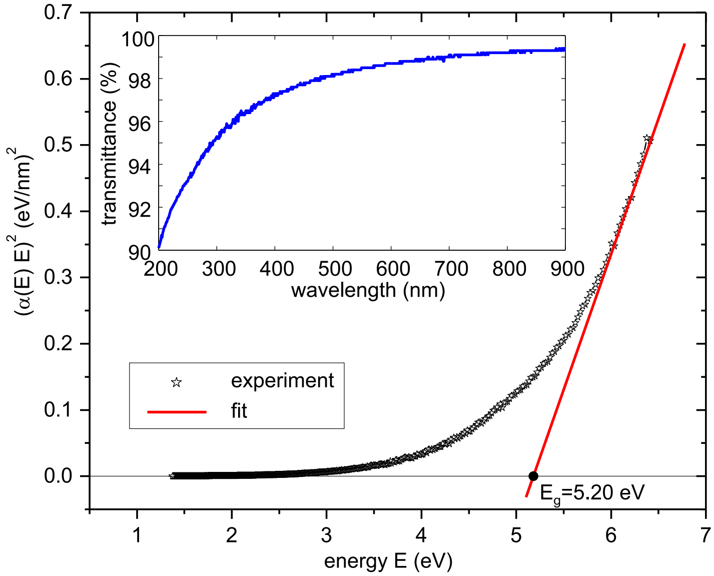

Fig. 8. The Tauc plot with estimated bandgap energy of ~5.20 eV obtained from the transmittance (plot in the inset) through ~20 nm thick pyrophyllite film obtained by LPE on a quartz substrate.

$\alpha(E)$. Namely, the well known Bourguer–Lambert–Beer (BLB) law gives the absorption coefficient as $\alpha_{\mathrm{BLB}}(E) = (1/d)\ln(1/T)$, where d is the film thickness and T the measured transmittance [60]. This is the simplest law representing the optical absorption in semiconductors, and in practice the BLB law turned out to be more than a good enough approximation.

For the estimation of a direct optical bandgap E_g, we used the Tauc method [61] and the standard fitting procedure of the linear part of $(\alpha(E)E)^2$ (Tauc plot), i.e. $(\alpha(E)E)^2 = \mathrm{const}\cdot(E - E_g)$. The Tauc plot displaying $(\alpha(E)E)^2$ as a function of the energy of incident light $E = h\nu$ (h is the Planck constant, ν is the frequency of incident photon) is given in Fig. 8. The plot indicates that the pyrophyllite film has a direct band gap of around 5.20 eV (the value obtained as the intersection point of the linear fit of the Tauc plot and x-axis). The obtained value is consistent with the theoretical value of 5.42 eV [55], whereas to best of our knowledge, this is the first experimentally obtained value of the pyrophyllite bandgap. The measured value is also close to the band gap of 2D hexagonal boron nitride (~6 eV) [62], which implies that pyrophyllite can be considered as efficient 2D insulator as well.

3.7. Insulating properties and dielectric breakdown

Hexagonal boron nitride has been a standard choice as insulator in 2D electronics [63–67]. Insulating properties and dielectric breakdown are usually explored by placing materials between two metallic electrodes in order to form a capacitor. Furthermore, C-AFM [68, 69] provides characterization at the nanoscale [63–65,70–72]. Recent studies have extended the family of 2D insulators to materials with improved properties, such as high-k van der Waals dielectrics [70].

In order to study dielectric properties, 2D pyrophyllite flakes obtained by LPE were deposited on a conductive substrate—thin gold film, which acted as a bottom electrode, while the AFM tip had a role of the top electrode. The topography image (Fig. 9(a)), corresponding current map (Fig. 9(b)), and characteristic profiles (Fig. 9(c)) reveal that pyrophyllite flakes with a thickness ranging from 3 nm to 22 nm are associated with a dark (black) contrast in the current map and zero current. The black color of pyrophyllite flakes in the current map in Fig. 9(b) is spatially homogeneous and therefore it does not contain current spikes which would indicate a possible dielectric breakdown. As a result, at the applied bias voltage $U = 2$ V, several nanometer thick pyrophyllite behaves as 2D insulator.

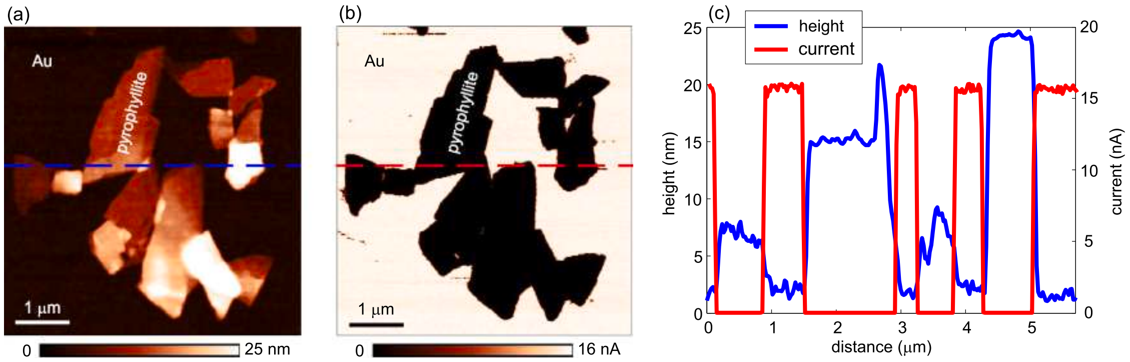

Fig. 9. (a) Topography and (b) the corresponding current maps of the pyrophillite flakes (obtained by LPE) deposited onto gold substrate. (c) The overlapped height and current profiles along the dashed lines in (a) and (b).

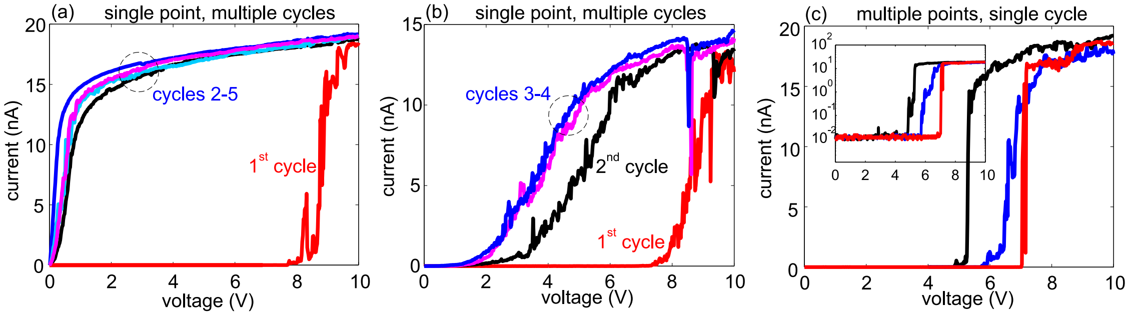

Fig. 10. (a) and (b) Successive cycles of the I/V curves measured at single point (but two different points). (c) The I/V curves (the first cycle only) measured at three different points of the same 10 nm thick pyrophyllite flake. The inset displays the I/V curves in semi-logarithmic scale.

In order to induce a dielectric breakdown, local I/V curves were measured in a wider voltage range. Typical results are given in Fig. 10(a) showing five successive cycles measured at the same point in the voltage range ±10 V. In the first cycle, the current is zero for voltages below ~8 V. After reaching this threshold voltage, the current rapidly grows indicating dielectric breakdown. In the next cycles (2–5), for small voltages below ~0.5 V, the current practically linearly increases with the applied bias voltage without any threshold (small nonlinearities around the zero voltage indicate possible Schottky barriers at the tip-sample contact, whereas the decreased slope of I/V curves for the voltages higher than ~0.5 V is due to limitations of the current amplifier). Therefore, pyrophyllite does not behave as an insulator anymore and the metallic AFM tip is practically short circuited by the bottom gold electrode. In another case presented in Fig. 10(b), after the first cycle and dielectric breakdown, the region with zero (or near to zero) current becomes narrower indicating gradually decreasing the electronic bandgap of pyrophyllite.

Fig. 10(c) displays the I/V curves (only the first cycles shown) measured at three different points on the same flake. Rapid increase of the current is observed for threshold voltage in the range 5–7 V. The semilogarithmic scale displayed in the inset reveals that below the threshold voltage, the current is at almost constant level in the order of 10^{-2} nA. Taking into account that the thickness of examined pyrophyllite flake was ~10 nm, the dielectric breakdown strength of 2D pyrophyllite is around 6 MV/cm. Although the obtained value is slightly below the strength of 2D hexagonal boron-nitride (~8 MV/cm) [63], the presented results indicate that 2D pyrophyllite has good insulating properties and could be considered as an efficient 2D dielectric and gate oxide. One of the main issue with applications of hexagonal boron-nitride as 2D insulator is its low dielectric constant (~3.9) responsible for high leakage currents. Although dielectric measurements of pyrophyllite are very rare [36,37], it is reasonable to expect lower leakage currents due to larger dielectric constant of pyrophyllite of around 10, which is also similar to the permittivity of the second member of 2:1 family of phyllosilicates—talc [73]. Still, this has to be confirmed in future studies since leakage currents are influenced by other factors, such as layers' quality (absence of structural defects) and the conduction/valence band discontinuity with respect to the substrate.

Morphological changes after the dielectric breakdown of phyrophyllite are illustrated in Fig. 11. Two- and three-dimensional images of the pyrophyllite flake (Fig. 11(a) and (b), respectively) are recorded in tapping mode after 30 I/V curves measured in the range ±10 V at the point marked by the arrow. As can be seen, a small hole appeared at the point where the I/V curves were measured, while protrusions appeared around the hole. Height profile in Fig. 11(c) reveals that the hole depth is around 1 nm which corresponds to the thickness of single layer of pyrophyllite. The presented results demonstrate that high local electric fields causing dielectric breakdown lead to local fracture of 2D pyrophyllite. The hole depth equal to the thickness of single layer of pyrophyllite indicates that in the considered case, only the most top pyrophyllite layer was locally cut, while the pyrophyllite thickness is reduced at this point. Although additional measurements should be done in future studies, these results suggest layer-by-layer breakdown of pyrophyllite which was previously confirmed in the case of hexagonal boron nitride [65].

Friction measurements done after the induced dielectric breakdown demonstrate that the point where I/V curves were previously measured is associated with increased friction compared to the rest of pyrophyllite flake. The increased friction indicates some chemical and/or structural changes on the pyrophyllite surface which should be further explored in future studies.

4. Conclusions

In a summary, we have thoroughly characterized pyrophyllite crystal and then successfully fabricated 2D flakes by using both mechanical exfoliation and LPE. Pyrophyllite was exfoliated down to single layer.

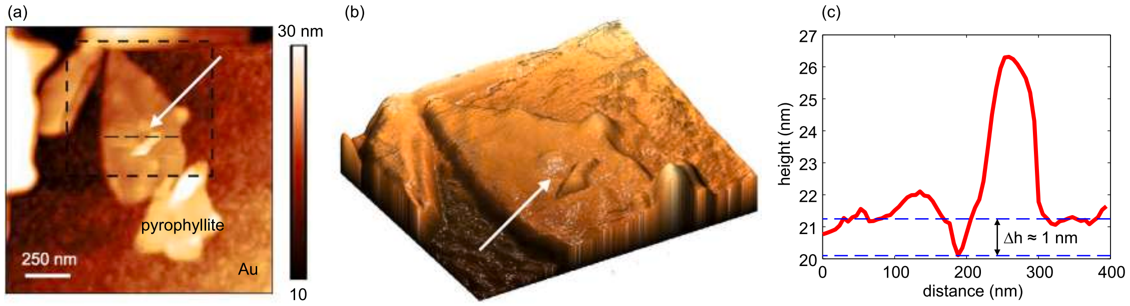

Fig. 11. (a) Two-dimensional topographic image of the pyrophyllite flake after 30 I/V curves measured in the range ±10 V at the point marked by the arrow. (b) Three-dimensional topographic image of the area marked by dashed square in (a). (c) Height profile along the dashed line marked in (a).

The lateral size of typical few-layer flakes was in the order of 10 μm in the case of the mechanical exfoliation, and 1 μm in the case of the LPE. 2D pyrophyllite has different wear properties compared to graphene and transition metal dichalcogenides. The wear is initiated at much lower normal loads while AFM based scratching leads to the tearing of pyrophyllite into small pieces, contrary to nano-exfoliation and folding, typically observed on graphene for example. Such wear properties provide easy machining at the nanoscale by the AFM tip which can be used as a tool for local carving and reshaping of pyrophyllite flakes. At the same time, 2D pyrophyllite has a low friction coefficient of ~0.1 and therefore, it joins the family of other van der Waals layered materials as a potential candidate for ultra-thin coatings aimed for solid lubrication in micro- and nano-mechanical devices. The optical measurements on thin (~20 nm) 2D pyrophyllite film obtained by the LPE reveal that it is transparent in the visible domain, with a large band gap of 5.2 eV. The local studies by C-AFM demonstrated that several nanometer thick pyrophyllite flakes behaves as 2D insulators with a high breakdown voltage of around 6 MV/cm, which is close to hexagonal boron-nitride. In addition, the larger dielectric permittivity of pyrophyllite compared to the boron nitride could provide lower leakage currents which needs to be confirmed in future studies.

CRediT authorship contribution statement

Borislav Vasić: Conceptualization, Investigation, Methodology, Formal analysis, Visualization, Writing – original draft. **Radoš Gajić:** Conceptualization, Investigation, Formal analysis, Resources, Supervision, Funding acquisition, Writing – review & editing. **Ivana Milošević:** Investigation, Visualization. **Žarko Medić:** Investigation, Visualization. **Marina Blagojev:** Investigation, Visualization. **Marko Opačić:** Investigation, Formal analysis, Visualization. **Aleksandar Kremenović:** Investigation, Formal analysis, Visualization, Writing – review & editing. **Dejan Lazić:** Investigation, Formal analysis.

Declaration of competing interest

The authors declare that they have no known competing financial interests or personal relationships that could have appeared to influence the work reported in this paper.

Data availability

Data will be made available on request.

Acknowledgments

We acknowledge funding provided by the Institute of Physics Belgrade, through the grant of the Ministry of Education, Science, and Technological Development of the Republic of Serbia. A. K. acknowledges funding provided by the Ministry of Education, Science and Technological Development of the Republic of Serbia (contract No. 451-03-68/2022-14/200126).

Appendix A. Supplementary data

Supplementary material related to this article can be found online at https://doi.org/10.1016/j.apsusc.2022.155114.

References

[1] K.S. Novoselov, A.K. Geim, S.V. Morozov, D. Jiang, Y. Zhang, S.V. Dubonos, I.V. Grigorieva, A.A. Firsov, Electric field effect in atomically thin carbon films, Science 306 (2004) 666–669.

[2] A.K. Geim, K.S. Novoselov, The rise of graphene, Nature Mater. 6 (2007) 183–191.

[3] T.F. Avouris, P. nad Heinz, T. Low, 2D Materials, Cambridge University Press, 2017.

[4] Y.M. Jhon, J.H. Lee, 2D Materials for Nanophotonics, Elsevier, 2021.

[5] M. Houssa, A. Dimoulas, A. Molle, 2D Materials for Nanoelectronics, CRC Press, 2016.

[6] B. Radisavljevic, A. Radenovic, J. Brivio, V. Giacometti, A. Kis, Single-layer MoS$_2$ transistors, Nat. Nanotechnol. 6 (2011) 147–150.

[7] M. Xu, T. Liang, M. Shi, H. Chen, Graphene-like two-dimensional materials, Chem. Rev. 113 (2013) 3766–3798.

[8] S.Z. Butler, S.M. Hollen, L. Cao, Y. Cui, J.A. Gupta, H.R. Gutiérrez, T.F. Heinz, S.S. Hong, J. Huang, A.F. Ismach, E. Johnston-Halperin, M. Kuno, V.V. Plashnitsa, R.D. Robinson, R.S. Ruoff, S. Salahuddin, J. Shan, L. Shi, M.G. Spencer, M. Terrones, W. Windl, J.E. Goldberger, Progress, challenges, and opportunities in two-dimensional materials beyond graphene, ACS Nano 7 (2013) 2898–2926.

[9] R. Ganatra, Q. Zhang, Few-layer MoS$_2$: A promising layered semiconductor, ACS Nano 8 (2014) 4074–4099.

[10] S. Manzeli, D. Ovchinnikov, D. Pasquier, O.V. Yazyev, A. Kis, 2D transition metal dichalcogenides, Nat. Rev. Mater. 2 (2017) 17033.

[11] K. Zhang, Y. Feng, F. Wang, Z. Yang, J. Wang, Two dimensional hexagonal boron nitride (2D-hBN): synthesis, properties and applications, J. Mater. Chem. C 5 (2017) 11992–12022.

[12] S. Balendhran, S. Walia, H. Nili, S. Sriram, M. Bhaskaran, Elemental analogues of graphene: Silicene, germanene, stanene, and phosphorene, Small 11 (2015) 640–652.

[13] M. Naguib, V.N. Mochalin, M.W. Barsoum, Y. Gogotsi, 25Th anniversary article: MXenes: A new family of two-dimensional materials, Adv. Mater. 26 (7) (2014) 992–1005.

[14] S. Shaikhutdinov, H.-J. Freund, Ultrathin silica films on metals: The long and winding road to understanding the atomic structure, Adv. Mater. 25 (2013) 49–67.

[15] R. Frisenda, Y. Niu, P. Gant, M. Muñoz, A. Castellanos-Gomez, Naturally occurring van der waals materials, npj 2D Mater. Appl. 4 (2020) 38.

[16] T. Gould, S. Lebègue, T. Björkman, J.F. Dobson, 2D structures beyond graphene: The brave new world of layered materials and how computers can help discover them, in: F. Iacopi, J. Boeckl, C. Jagadish (Eds.), 2D Materials, Academic Press, 2016, pp. 1–33, Ch. 1.

[17] K. Momma, F. Izumi, *VESTA3* for three-dimensional visualization of crystal, volumetric and morphology data, J. Appl. Crystallogr. 44 (2011) 1272–1276.

[18] A.B. Alencar, A.P.M. Barboza, B.S. Archanjo, H. Chacham, B.R.A. Neves, Experimental and theoretical investigations of monolayer and few-layer talc, 2D Mater. 2 (2015) 015004.

[19] A. Harvey, J.B. Boland, I. Godwin, A.G. Kelly, B.M. Szydłowska, G. Murtaza, A. Thomas, D.J. Lewis, P. O'Brien, J.N. Coleman, Exploring the versatility of liquid phase exfoliation: producing 2D nanosheets from talcum powder, cat litter and beach sand, 2D Mater. 4 (2017) 025054.

[20] A.R. Cadore, E. Mania, A.B. Alencar, N.P. Rezende, S. de Oliveira, K. Watanabe, T. Taniguchi, H. Chacham, L.C. Campos, R.G. Lacerda, Enhancing the response of NH$_3$ graphene-sensors by using devices with different graphene-substrate distances, Sensors Actuators B 266 (2018) 438–446.

[21] B. Vasić, C. Czibula, M. Kratzer, B.R.A. Neves, A. Matković, C. Teichert, Two-dimensional talc as a van der Waals material for solid lubrication at the nanoscale, Nanotechnology 32 (2021) 265701.

[22] D. Nutting, G.A. Prando, M. Severijnen, I.D. Barcelos, S. Guo, P.C.M. Christianen, U. Zeitler, Y. Galvão Gobato, F. Withers, Electrical and optical properties of transition metal dichalcogenides on talc dielectrics, Nanoscale 13 (2021) 15853–15858.

[23] G.A. Prando, M.E. Severijnen, I.D. Barcelos, U. Zeitler, P.C.M. Christianen, F. Withers, Y. Galvão Gobato, Revealing excitonic complexes in monolayer WS_2 on talc dielectric, Phys. Rev. Appl. 16 (2021) 064055.

[24] A.C. Gadelha, T.L. Vasconcelos, L.G. Cançado, A. Jorio, Nano-optical imaging of in-plane homojunctions in graphene and MoS_2 van der Waals heterostructures on talc and SiO_2, J. Phys. Chem. Lett. 12 (2021) 7625–7631.

[25] A. Castellanos-Gomez, M. Wojtaszek, N. Tombros, N. Agraït, B.J. van Wees, G. Rubio-Bollinger, Atomically thin mica flakes and their application as ultrathin insulating substrates for graphene, Small 7 (2011) 2491–2497.

[26] X. Ji, Y. Kang, J. Ouyang, Y. Chen, D. Artzi, X. Zeng, Y. Xiao, C. Feng, B. Qi, N.Y. Kim, P.E. Saw, N. Kong, O.C. Farokhzad, W. Tao, 2D black mica nanosheets: Synthesis of ultrathin biotite nanosheets as an intelligent theranostic platform for combination cancer therapy, Adv. Sci. 6 (2019) 1970118.

[27] Z. Huang, T. Lan, L. Dai, X. Zhao, Z. Wang, Z. Zhang, B. Li, J. Li, J. Liu, B. Ding, A.K. Geim, H.-M. Cheng, B. Liu, 2D functional minerals as sustainable materials for magneto-optics, Adv. Mater. 34, 2110464.

[28] R. de Oliveira, L.A.G. Guallichico, E. Policarpo, A.R. Cadore, R.O. Freitas, F.M.C. da Silva, V. d. C. Teixeira, R.M. Paniago, H. Chacham, M.J.S. Matos, A. Malachias, K. Krambrock, I.D. Barcelos, High throughput investigation of an emergent and naturally abundant 2D material: Clinochlore, Appl. Surf. Sci. 559 (2022) 153959.

[29] A.R. Cadore, R. de Oliveira, R. Longuinhos, V. de C. Teixeira, D.A. Nagaoka, V.T. Alvarenga, J. Ribeiro-Soares, K. Watanabe, T. Taniguchi, R.M. Paniago, A. Malachias, K. Krambrock, I.D. Barcelos, C.J.S. de Matos, Exploring the structural and optoelectronic properties of natural insulating phlogopite in van der waals heterostructures, 2D Mater. 9 (2022) 035007.

[30] Y. Niu, J. Villalva, R. Frisenda, G. Sanchez-Santolino, L. Ruiz-González, E.M. Pérez, M. García-Hernández, E. Burzurí, A. Castellanos-Gomez, Mechanical and liquid phase exfoliation of cylindrite: a natural van der Waals superlattice with intrinsic magnetic interactions, 2D Mater. 6 (2019) 035023.

[31] A. Matković, L. Ludescher, O.E. Peil, A. Sharma, K.-P. Gradwohl, M. Kratzer, M. Zimmermann, J. Genser, D. Knez, E. Fisslthaler, C. Gammer, A. Lugstein, R.J. Bakker, L. Romaner, D.R.T. Zahn, F. Hofer, G. Salvan, J.G. Raith, C. Teichert, Iron-rich talc as air-stable platform for magnetic two-dimensional materials, npj 2D Mater. Appl. 5 (2021) 94.

[32] A.J. Molina-Mendoza, E. Giovanelli, W.S. Paz, M.A. Niño, J.O. Island, C. Evangeli, L. Aballe, M. Foerster, H.S.J. van der Zant, G. Rubio-Bollinger, N. Agraït, J.J. Palacios, E.M. Pérez, A. Castellanos-Gomez, Franckeite as a naturally occurring van der Waals heterostructure, Nature Commun. 8 (2017) 14409.

[33] M. Velický, P.S. Toth, A.M. Rakowski, A.P. Rooney, A. Kozikov, C.R. Woods, A. Mishchenko, L. Fumagalli, J. Yin, V. Zólyomi, T. Georgiou, S.J. Haigh, K.S. Novoselov, R.A.W. Dryfe, Exfoliation of natural van der Waals heterostructures to a single unit cell thickness, Nature Commun. 8 (2017) 14410.

[34] K. Ray, A.E. Yore, T. Mou, S. Jha, K.K.H. Smithe, B. Wang, E. Pop, A.K.M. Newaz, Photoresponse of natural van der Waals heterostructures, ACS Nano 11 (2017) 6024–6030.

[35] M.A. Ali, H.A.M. Ahmed, H.M. Ahmed, M. Hefni, Pyrophyllite: An economic mineral for different industrial applications, Appl. Sci. 11 (2021) 11357.

[36] G.W. Timco, Z. Dvorak, H.H. Schloessin, Dielectric properties of pyrophyllite as a function of water vapor pressure, J. Appl. Phys. 47 (1976) 2232–2233.

[37] E. Izci, The investigation of dielectric properties of pyrophyllite, Key Eng. Mater. 264–268 (2004) 1361–1364.

[38] E.W. Bucholz, X. Zhao, S.B. Sinnott, S.S. Perry, Friction and wear of pyrophyllite on the atomic scale, Tribol. Lett. 46 (2012) 159–165.

[39] E.L. Brightbill, Design Rules for Discovering 2D Materials from 3D Crystals, University of North Carolina at Chapel Hill, 2016.

[40] M. Shamim, T.K. Mukhopadhyay, K. Dana, Kinetic pathway for thermal exfoliation of pyrophyllite, Appl. Clay Sci. 114 (2015) 40–47.

[41] K.S. Novoselov, D. Jiang, F. Schedin, T.J. Booth, V.V. Khotkevich, S.V. Morozov, A.K. Geim, Two-dimensional atomic crystals, Proc. Natl. Acad. Sci. USA 102 (2005) 10451–10453.

[42] A. Matković, I. Milošević, M. Milićević, T. Tomašević-Ilić, J. Pešić, M. Musić, M. Spasenović, D. Jovanović, B. Vasić, C. Deeks, R. Panajotović, M.R. Belić, R. Gajić, Enhanced sheet conductivity of Langmuir–Blodgett assembled graphene thin films by chemical doping, 2D Mater. 3 (2016) 015002.

[43] I.R. Milošević, B. Vasić, A. Matković, J. Vujin, S. Aškrabić, M. Kratzer, T. Griesser, C. Teichert, R. Gajić, Single-step fabrication and work function engineering of Langmuir–Blodgett assembled few-layer graphene films with Li and Au salts, Sci. Rep. 10 (2020) 8476.

[44] M. Varenberg, I. Etsion, G. Halperin, An improved wedge calibration method for lateral force in atomic force microscopy, Rev. Sci. Instrum. 74 (2003) 3362–3367.

[45] J.H. Lee, S. Guggenheim, Single crystal X-ray refinement of pyrophyllite-1Tc, Am. Mineral. 66 (1981) 350–357.

[46] R. Wardle, G.W. Brindley, The crystal structures of pyrophyllite, 1Te, and of its dehydroxylate, Am. Mineral. 57 (1972) 732–750.

[47] A. Wang, J.J. Freeman, B.L. Jolliff, Understanding the Raman spectral features of phyllosilicates, J. Raman Spectrosc. 46 (2015) 829–845.

[48] J. Kloprogge, Chapter 6 - Raman spectroscopy of clay minerals, in: W.P. Gates, J.T. Kloprogge, J. Madejová, F. Bergaya (Eds.), Infrared and Raman Spectroscopies of Clay Minerals, in: Developments in Clay Science, vol. 8, 2017, pp. 150–199.

[49] B. Lafuente, R.T. Downs, H. Yang, N. Stone, 1. The power of databases: The RRUFF project, 2015, pp. 1–30.

[50] P. Nemes-Incze, Z. Osváth, K. Kamarás, L.P. Biró, Anomalies in thickness measurements of graphene and few layer graphite crystals by tapping mode atomic force microscopy, Carbon 46 (2008) 1435–1442.

[51] K.-S. Kim, H.-J. Lee, C. Lee, S.-K. Lee, H. Jang, J.-H. Ahn, et al., Chemical vapor deposition-grown graphene: The thinnest solid lubricant, ACS Nano 5 (2011) 5107–5114.

[52] B. Vasić, A. Matković, U. Ralević, M. Belić, R. Gajić, Nanoscale wear of graphene and wear protection by graphene, Carbon 120 (2017) 137–144.

[53] A. Özoğul, E. Gnecco, M.Z. Baykara, Nanolithography-induced exfoliation of layered materials, Appl. Surf. Sci. Adv. 6 (2021) 100146.

[54] Y.-T. Fu, G.D. Zartman, M. Yoonessi, L.F. Drummy, H. Heinz, Bending of layered silicates on the nanometer scale: Mechanism, stored energy, and curvature limits, J. Phys. Chem. C 115 (2011) 22292–22300.

[55] X. Qin, J. Zhao, J. Wang, M. He, Atomic structure, electronic and mechanical properties of pyrophyllite under pressure: A first-principles study, Minerals 10 (2020) 778.

[56] A. Castellanos-Gomez, M. Poot, A. Amor-Amorós, G.A. Steele, H.S.J. van der Zant, N. Agraït, G. Rubio-Bollinger, Mechanical properties of freely suspended atomically thin dielectric layers of mica, Nano Res. 5 (2012) 550–557.

[57] G.D. Zartman, H. Liu, B. Akdim, R. Pachter, H. Heinz, Nanoscale tensile, shear, and failure properties of layered silicates as a function of cation density and stress, J. Phys. Chem. C 114 (2010) 1763–1772.

[58] B. Vasić, A. Matković, R. Gajić, I. Stanković, Wear properties of graphene edges probed by atomic force microscopy based lateral manipulation, Carbon 107 (2016) 723–732.

[59] R. Buzio, A. Gerbi, S. Uttiya, C. Bernini, A.E. Del Rio Castillo, F. Palazon, A.S. Siri, V. Pellegrini, L. Pellegrino, F. Bonaccorso, Ultralow friction of ink-jet printed graphene flakes, Nanoscale 9 (2017) 7612–7624.

[60] M. Fox, Optical Properties of Solids, Oxford University Press, 2010.

[61] P. Makuła, M. Pacia, W. Macyk, How to correctly determine the band gap energy of modified semiconductor photocatalysts based on UV–Vis spectra, J. Phys. Chem. Lett. 9 (2018) 6814–6817.

[62] G. Cassabois, P. Valvin, B. Gil, Hexagonal boron nitride is an indirect bandgap semiconductor, Nat. Photonics 10 (2016) 262–266.

[63] G.-H. Lee, Y.-J. Yu, C. Lee, C. Dean, K.L. Shepard, P. Kim, J. Hone, Electron tunneling through atomically flat and ultrathin hexagonal boron nitride, Appl. Phys. Lett. 99 (2011) 243114.

[64] L. Britnell, R.V. Gorbachev, R. Jalil, B.D. Belle, F. Schedin, M.I. Katsnelson, L. Eaves, S.V. Morozov, A.S. Mayorov, N.M.R. Peres, A.H. Castro Neto, J. Leist, A.K. Geim, L.A. Ponomarenko, K.S. Novoselov, Electron tunneling through ultrathin boron nitride crystalline barriers, Nano Lett. 12 (2012) 1707–1710.

[65] Y. Hattori, T. Taniguchi, K. Watanabe, K. Nagashio, Layer-by-layer dielectric breakdown of hexagonal boron nitride, ACS Nano 9 (2015) 916–921.

[66] Y.Y. Illarionov, T. Knobloch, M. Jech, M. Lanza, D. Akinwande, M.I. Vexler, T. Mueller, M.C. Lemme, G. Fiori, F. Schwierz, T. Grasser, Insulators for 2D nanoelectronics: the gap to bridge, Nature Commun. 11 (2020) 3385.

[67] K.K. Kim, H.S. Lee, Y.H. Lee, Synthesis of hexagonal boron nitride heterostructures for 2D van der Waals electronics, Chem. Soc. Rev. 47 (2018) 6342–6369.

[68] F. Giannazzo, G. Fisichella, G. Greco, P. Fiorenza, F. Roccaforte, Conductive atomic force microscopy of two-dimensional electron systems: From AlGaN/GaN heterostructures to graphene and MoS_2, in: M. Lanza (Ed.), Conductive Atomic Force Microscopy: Applications in Nanomaterials, WILEY-VCH Verlag, Weinheim, Germany, 2017, pp. 163–186, Ch. 7.

[69] F. Giannazzo, G. Greco, F. Roccaforte, C. Mahata, M. Lanza, Conductive AFM of 2D materials and heterostructures for nanoelectronics, in: U. Celano (Ed.), Electrical Atomic Force Microscopy for Nanoelectronics, Springer, Berlin, Germany, 2019, pp. 303–350, Ch. 10.

[70] C.-Y. Zhu, J.-K. Qin, P.-Y. Huang, H.-L. Sun, N.-F. Sun, Y.-L. Shi, L. Zhen, C.-Y. Xu, 2D indium phosphorus sulfide ($In_2P_3S_9$): An emerging van der Waals high-k dielectrics, Small 18 (2022) 2104401.

[71] Y. Ji, C. Pan, M. Zhang, S. Long, X. Lian, F. Miao, F. Hui, Y. Shi, L. Larcher, E. Wu, M. Lanza, Boron nitride as two dimensional dielectric: Reliability and dielectric breakdown, Appl. Phys. Lett. 108 (2016) 012905.

[72] A. Ranjan, N. Raghavan, M. Holwill, K. Watanabe, T. Taniguchi, K.S. Novoselov, K.L. Pey, S.J. O'Shea, Dielectric breakdown in single-crystal hexagonal boron nitride, ACS Appl. Electron. Mater. 3 (2021) 3547–3554.

[73] J.L. Rosenholtz, D.T. Smith, The dielectric constant of mineral powders, Am. Mineral. 21 (1936) 115–120.

Carbon 244 (2025) 120697

Contents lists available at ScienceDirect

Carbon

journal homepage: www.elsevier.com/locate/carbon

Research paper

Nanoscale structural superlubricity in solution-processed graphene films via tribo-induced transfer layers

Borislav Vasić [a],*, Ivana Milošević [a], Zorica Konstantinović [a], Miloš Ognjanović [b], Alberto Pomar [c]

[a] Institute of Physics Belgrade, University of Belgrade, Pregrevica 118, 11080 Belgrade, Serbia
[b] "Vinča" Institute of Nuclear Sciences-National Institute of the Republic of Serbia, University of Belgrade, Mike Petrovića Alasa 12-14, Belgrade, Serbia
[c] Instituto de Ciencia de Materiales de Barcelona, ICMAB-CSIC, Campus Universitario UAB, 08193 Bellaterra, Spain

ARTICLE INFO

Keywords:
Nanofriction
Superlubricity
Two dimensional materials
Graphene
Atomic force microscopy

ABSTRACT

So far, nanoscale superlubricity has been demonstrated in well-ordered van der Waals materials, such as graphite and mechanically exfoliated graphene. In contrast, this study demonstrates nanoscale superlubricity in structurally inhomogeneous systems such as solution-processed graphene films, which are promising for scalable and practical applications. The investigated graphene films were obtained via liquid-phase exfoliation (LPE) and deposited by Langmuir–Blodgett assembly technique at the water–air interface, while frictional measurements were performed using atomic force microscopy (AFM)-based techniques. To enable superlubricity in the system consisting of a silica AFM tip and an LPE graphene film, a tribo-induced, graphene-based conformal coating was first formed around the tip. Unlike previous studies that relied exclusively on pristine graphite, we easily transferred small and weakly adhered graphene flakes onto the AFM tip by rubbing it against the LPE graphene film in contact mode. Subsequent friction measurements were performed using these graphene-coated tips. The measurements on LPE films deposited onto silica and polyethylene terephthalate (PET) substrates revealed ultralow friction coefficients of approximately 0.005 on flat regions composed of large graphene flakes thereby confirming the emergence of the superlubric regime. However, the inherently non-uniform morphology of LPE films, with small flakes and numerous exposed edges, introduces localized high-friction regions and wear-prone sites that prevent superlubricity across extended areas. These findings highlight the importance of achieving large flake sizes with reduced density of exposed edges and improved flake adhesion in order to enable robust structural superlubricity in LPE graphene films.

1. Introduction

Structural superlubricity is a state of ultra-low friction, typically associated with a friction coefficient on the order of 0.001 or lower, arising when two crystalline surfaces slide over each other in incommensurate states [1–3]. This state is particularly relevant for applications because the low friction coefficient drastically reduces friction forces and the associated wear [4] and dissipation of mechanical energy [5]. Therefore, superlubricity is a highly desirable operating regime for the sliding components in various mechanical systems, as it improves energy efficiency and extends their durability. An ultra-low friction is also crucial in various electromechanical devices [6] such as electro-superlubric oscillators [7] and tribovoltaic generators [8,9].

Although some recent studies have demonstrated superlubricity in sliding contacts of van der Waals (vdW) and non-vdW materials [10,11], and even in the presence of surface contaminations [12], superlubricity has been typically achieved using layered vdW materials such as graphite [2,13–16], graphene [17], molybdenum disulfide [18,19], and vdW heterojunctions [20]. Weak vdW interactions between the layers in the vdW materials facilitate easy shearing and reorientation into incommensurate states thereby facilitating superlubric sliding of the layers.

Nevertheless, many practical systems contain sliding contacts involving both crystalline and non-crystalline material without a layered structure. A common strategy to achieve superlubricity in this case is to cover the non-crystalline surfaces by vdW materials, leading to the formation of a contact interface between two crystalline layers. Graphene, a typical representative of vdW materials, is commonly used for the covering the non-vdW materials due to its exceptional strength, flexibility, and light weight. It is used as a conformal coating that easily

---

* Corresponding author.
E-mail address: bvasic@ipb.ac.rs (B. Vasić).

https://doi.org/10.1016/j.carbon.2025.120697
Received 15 May 2025; Received in revised form 24 July 2025; Accepted 4 August 2025

wraps around various structures, as demonstrated in the cases of atomic force microscopy (AFM) tips [21], microsphere silica probes [22], and flat silica surfaces [23].

While AFM is a crucial experimental technique for studying friction at the nanoscale, AFM systems represent also practical examples of sliding contacts where one of the interacting materials may be non-crystalline and may lack a layered structure. In such cases, AFM tips are commonly coated with graphene to establish contact interface between two crystalline surfaces. Graphene-wrapped AFM tips have been fabricated using various methods, including direct growth of graphene on the AFM tips [24,25], dry [26–29] and wet [30,31] transfer, and dipping into a graphene solution [32–34].

A specific method for producing graphene-wrapped AFM tips involves tribo-induced transfer layers [35–42]. In this method, by rubbing a graphite surface with the AFM tip scanning in contact mode, small graphene flakes are transferred onto the tip. During subsequent sliding over the surface of a vdW material, the transferred graphene flakes on the AFM tip come into direct contact with the vdW material, enabling superlubric sliding [35–42]. This method is relatively simple yet highly efficient, making it well-suited for AFM-based friction studies, as the prepared graphene-wrapped AFM tips are ready for friction measurements.

The main challenge with superlubricity is maintaining the same and low friction level over extended periods of sliding [43]. A dominant factor which degrades superlubricity is the edge-pinning effect which arises due to enhanced friction across edges in vdW materials [44–46]. Therefore, so far, superlubricity at the nanoscale has been demonstrated only on well-ordered and single-crystalline vdW substrates such as graphite [2] or graphene fabricated by micromechanical exfoliation [17]. The objective of this study is to investigate whether and under which conditions, structural superlubricity arises in solution-processed graphene films. Generally, solution-processed vdW materials [47–50] are highly relevant for practical applications as large-area thin films can be fabricated using simple and cost-effective methods. Furthermore, the films can be deposited on virtually any technologically relevant surface using lab-scale techniques such as vacuum filtration [51] and Langmuir–Blodgett assembly [52], as well as using high-throughput industrial-scale fabrication methods including spray coating [53] and ink-jet printing [54]. These structurally inhomogeneous films exhibit a pronounced degree of disorder as they consist of a dense network of small and irregularly oriented flakes with many exposed edges [55]. Accordingly, it is reasonable to expect that the edge-pinning effect is particularly pronounced in films with this degree of structural inhomogeneity. Although previous experiments have demonstrated superlubricity in solution-processed 2D materials at the macroscale [56–61], the influence of their edges and other inhomogeneities on friction and superlubricity has remained unresolved.

In this manuscript, in contrast to the previous studies focused on well-ordered systems, we demonstrate nanoscale superlubricity in structurally inhomogeneous systems such as the solution-processed graphene films obtained by liquid phase exfoliation (LPE) and deposited using the Langmuir–Blodgett (LB) assembly technique. To clarify the microscopic mechanisms of superlubricity in these films and to investigate the influence of their structural inhomogeneities, we use AFM methods. We examine the effect of the normal force applied by the AFM tip on the superlubric regime and the onset of wear in the films as the normal force increases. We determine an approximate threshold for the maximum normal force under which LPE graphene films maintain superlubricity, and identify an optimal graphene flake size that facilitates stable superlubric behavior.

Furthermore, in contrast to the previous studies where only graphite has been employed as a substrate in the formation of tribo-induced transfer layers, we demonstrate that the LPE graphene films can serve as very efficient substrates for this purpose. The presented method used to transfer graphene flakes onto the AFM tip involves rubbing the LPE graphene films with the AFM tip in contact mode under gradually increasing normal loads.

The manuscript is organized as follows: Section 2 describes the experimental details; Section 3 provides a detailed analysis of the morphological properties of LPE graphene films; Section 4 discusses the formation of tribo-induced transfer layers on the AFM tip; Section 5 presents the demonstration of superlubricity in two LPE graphene films deposited on silica and polyethylene terephthalate (PET) substrates; and Section 6 analyzes the presented results and proposes optimal LPE graphene films that facilitate stable superlubricity.

2. Experimental

Solution-processed graphene films considered in this study were obtained by LPE. The graphene dispersion was prepared according to the protocol described in Refs. [62,63]. Graphite powder (Sigma Aldrich, product no. 332461) with an initial concentration of 18 mg/mL was dispersed in N-methyl-2-pyrrolidone (NMP, Sigma Aldrich, product no. 328634). The mixture was sonicated for 14 hours in a low-power ultrasonic bath, and then centrifuged at 3000 rpm for 60 minutes. The resulting graphene sheets dispersed in NMP were used to fabricate graphene films using the LB assembly technique at the water–air interface. A small amount of the as-prepared graphene dispersion was added to the water–air interface, and once the film had formed, it was carefully transferred onto the target substrates, SiO_2/Si wafers and PET. Owing to its high miscibility with water, NMP is expected to diffuse into the aqueous subphase during the LB assembly.

Hydrodynamic diameters of the graphene flakes (d_H), dispersed in NMP, were determined by dynamic light scattering (DLS) [64]. The measurements were performed using a Malvern Zetasizer Nano ZS90, equipped with a 4 mW He-Ne laser source (λ = 633 nm), in a 12 mm O.D. glass square cell with a cap (PCS8501), at 25±0.1°C. The graphene dispersion was sonicated for 10 min and equilibrated for the same time prior to the measurements.

Friction measurements of LPE graphene films were performed using friction force microscopy (FFM) under ambient conditions, employing an AFM system NTEGRA Prima with NSG01 probes (with a typical force constant of 5 N/m), both from NT-MDT. The measurements were performed in contact mode AFM, by simultaneously recording the topography of the films and the lateral forces exerted on the AFM tip during scanning. The measured lateral forces correspond to the lateral torsions of the AFM cantilever caused by the friction forces between the AFM tip and graphene films. The friction forces were calculated in the standard manner, as half the difference between the lateral forces recorded in the forward and backward scan direction. In order to convert the lateral forces measured in nanoamperes (as provided by our NT-MDT system) into actual values expressed in nanonewtons, the wedge calibration method was used [65]. The friction force values presented in Figs. 5(c), 8(d), and 9(c) were obtained by fitting each peak in the corresponding histograms with a Gaussian function. The mean values from the Gaussian fits were reported as friction forces, and the associated errors are given as standard deviations. In order to determine the friction coefficient of LPE graphene films, friction measurements were performed as a function of the normal force applied by the AFM tip. The friction coefficient was then calculated as the slope of a linear fit to the friction force plotted as a function of the normal force.

Tribo-induced transfer layers were formed prior to friction measurements, by transferring small graphene flakes from the LPE graphene film onto the AFM tip. This is discussed in detail in the next section, while here, we provide a brief description. The LPE graphene film was rubbed with the AFM tip, by scanning in contact mode AFM at increasing normal loads. As in the friction measurements, two signals were recorded simultaneously: topography and lateral (friction) forces. Tribo-induced transfer of graphene flakes onto the AFM tip is indicated

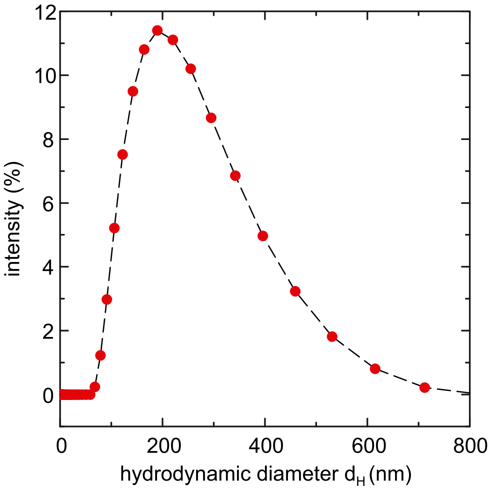

Fig. 1. DLS spectra of the graphene flakes dispersed in NMP.

by the following: 1. wear of the graphene film observed through topographic changes, including sudden cuts in some domains, their shift or rotation, thinning and peeling of flakes, and their deformation, and 2. a sudden increase in lateral forces which corresponds to an additional energy supplied by the AFM tip, required for the previously mentioned mechanical manipulations of the graphene flakes.

Scanning electron microscopy (SEM) was employed to measure morphology of LPE graphene films as well as to image the AFM tip before and after rubbing the graphene films. Therefore, SEM images were used to characterize morphological changes in the tip and to visualize and confirm the formation of tribo-induced transfer layers, consisting of graphene flakes adhered to the tip after rubbing. For this purpose, a QUANTA FEI 200 FEG-ESEM microscope was employed. The microscope was also equipped with an Energy Dispersive X-ray (EDX) system for chemical analysis, which was used for the quantitative analysis of elemental distribution on the AFM tips before and after rubbing.

3. Morphological properties of LPE graphene films

The initial size of graphene flakes was estimated using DLS measurements. Although this method is primarily intended for spherical nanoparticles, it can still provide a good approximate results for the lateral size of graphene flakes [64]. The hydrodynamic diameter of the graphene flakes in dispersion, calculated from the DLS spectra, is presented in Fig. 1. The measurement results indicate that the graphene flakes have an average size of approximately 192 nm. Additionally, the polydispersity index (PDI) was 0.239, suggesting a moderately broad size distribution.

Figs. 2(a)–(f) illustrate the morphology of the graphene film, characterized by optical microscopy, AFM and SEM. Each image highlights specific morphological features of the film. The presented results indicate that our LPE graphene films exhibit a quality comparable to those previously reported in the literature. The optical image in Fig. 2(a) indicates uniform coverage of the silica substrate by the graphene film. The film edge is characterized with a well-defined boundary as displayed in Fig. 2(b).

Large-scale AFM image in Fig. 2(c) reveals spatial variations in color contrast implying significant height fluctuations. The corresponding root-mean square surface roughness calculated from this image was 11 nm. The AFM image also reveals small holes in the film presented as regions with darker contrast. Typical example is indicated by the encircled region in Fig. 2(c). This region, together with several additional holes, are even more clearly visualized in the AFM amplitude signal map displayed in Fig. 2(d). The amplitude signal corresponds to the amplitude of the AFM cantilever oscillations during imaging in tapping mode which deviates from the specified set point due to tip-sample interactions.

SEM images in Figs. 2(e) and 2(f) reveal that the graphene films are composed of self-assembled nanoflakes with varied lateral sizes. Their orientation and stacking are governed by self-organization processes, which naturally introduce a degree of structural disorder. However, such disorder is a known and inherent feature of solution-processed 2D materials and represents a trade-off for the simplicity and scalability of producing large-area graphene films.

AFM images have been further analyzed to determine the film thickness and the lateral size of flakes. Fig. 3(a) displays the average height profile measured across the film edge (the boundary between the film and the bare silica substrate) within the narrow rectangular region marked in the topographic image in the inset. Significant height fluctuations of the graphene film prevented reliable thickness calculations directly from the height profile. Therefore, the profile was fitted with a step edge function as shown in Fig. 3(a). The resulting film thickness calculated from the step edge function was 12.9 ± 6.8 nm.

The lateral size of graphene flakes is illustrated by the height profiles in Fig. 3(b) (they were measured along the lines marked in the topographic image in the inset of Fig. 3(c)). The lateral size can be estimated as the distance between two successive local height minima. The upper profile reveals flakes with lateral dimensions in the range of approximately 50–200 nm, while the lower profile displays a single and large flake with a size on the order of several hundred nanometers.

The histogram of lateral flake sizes and corresponding Gaussian fit are shown in Fig. 3(b). The flake sizes were extracted from the topographic image depicted in the inset. The histogram exhibits a mode around 124 nm, whereas the average lateral size calculated from the Gaussian fit is 169 ± 71 nm. Both values are in good agreement with the average hydrodynamic diameter of graphene flakes calculated from DLS measurements. The observed difference is expected as the analysis of DLS measurements assumes spherical nanoparticles, whereas graphene flakes can be approximated as ultrathin 2D plates.

4. Formation of tribo-induced transfer layer and the onset of superlubricity

The lateral size of graphene flakes in the range of approximately 50–200 nm is well-matched to the utilized AFM probes (SEM image presented in Fig. 10(a)). Therefore, such graphene flakes are well-suited for wrapping around the AFM tips, as they can easily attach to the AFM tips without the need to tear the graphene. This could facilitate the formation of tribo-induced transfer layers compared to previous methods, which typically involved rubbing against highly oriented pyrolytic graphite (HOPG) [35–42]. Because HOPG consists of continuous graphene layers, in that case the AFM tip must first tear the top layers in order to form a graphene coating which will be transferred onto the tip.

In order to demonstrate superlubricity in systems consisting of silicon AFM probes and LPE graphene films, the first step was to create graphene-based, tribo-induced transfer layers on the silicon probes. This was achieved by rubbing the probes against the LPE graphene film (deposited onto the silica substrate) in contact mode AFM. Rubbing was conducted under three gradually increasing normal loads (68 nN, 112 nN, and 155 nN), and with ten cycles performed for each load. One cycle represents a complete scan of the considered square area. After completing ten cycles at one normal force, the load was increased for the next ten cycles on the same scan area. During rubbing, we monitored the topography and the lateral (friction) forces in order to identify the onset of wear, at which point the AFM tip began to scratch the graphene films. This may indicate the transfer of graphene flakes to the AFM tip. The resulting topographic images and friction maps are displayed in Fig. 4 presenting the result for the last, tenth cycle for

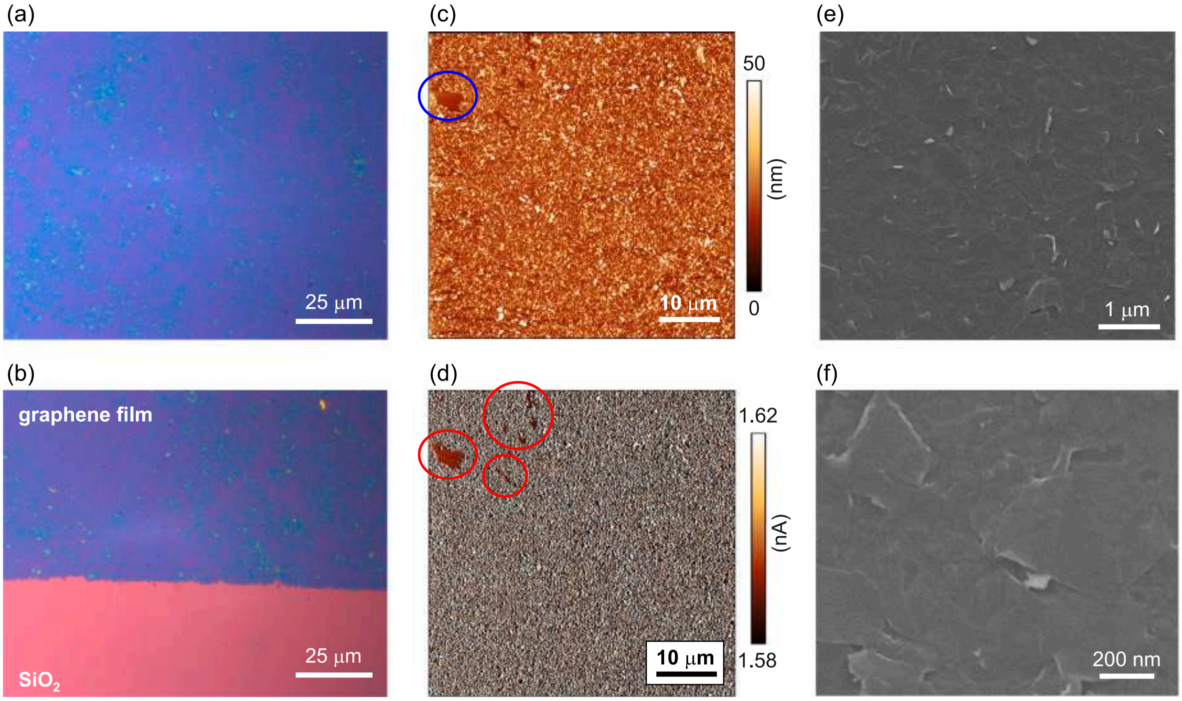

Fig. 2. Morphology of graphene films: (a) and (b) optical images, (c) AFM topographic image, (d) map of AFM amplitude signal (the amplitude of the AFM cantilever oscillations during imaging in tapping mode, in our AFM system expressed in nanoamperes (nA)), and (e) and (f) SEM images.

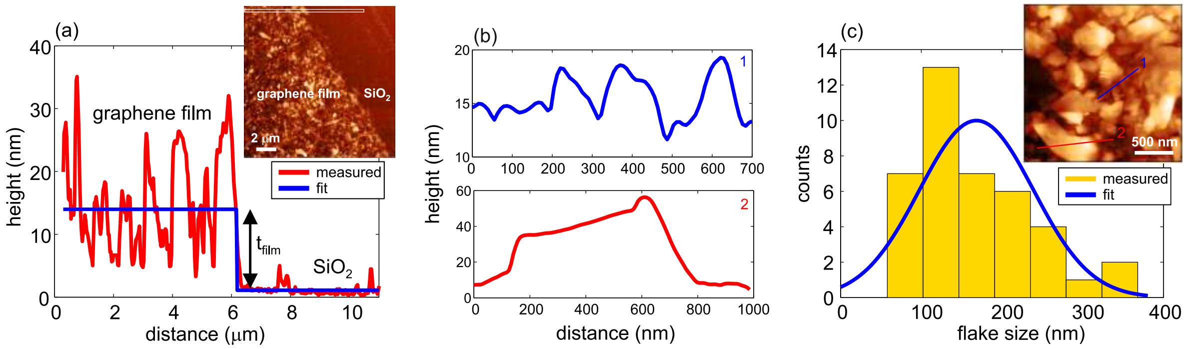

Fig. 3. (a) Average height profile measured across the edge of the graphene film whose topographic image is displayed in the inset. The averaging was performed within the narrow rectangular region highlighted in the topographic image. The fitting was done by a step function. (b) Height profiles acquired along the lines marked in the topographic image in part (c). (c) Histogram of graphene flake size acquired from the topographic image in the inset. Fitting was done by Gaussian function.

each load. The topographic image, recorded at the lowest normal load in Fig. 4(a), reveals no detectable wear of the film surface. Fig. 4(b) shows a topographic image recorded after ten cycles at an increased normal force of 112 nN, revealing clear morphological changes. After rubbing at a normal load of 155 nN, the graphene film was severely damaged, as shown in Fig. 4(c), indicating that most of the film was peeled away from the substrate.

The friction map in Fig. 4(d), recorded at the lowest normal force of 68 nN, displays a dark contrast representing low friction measured on the graphene film, and a small bright domain, encircled by the dashed line, that corresponds to high friction on the silica substrate. The graphene film also features a network of bright and narrow stripes which correspond to enhanced friction measured along the edges of graphene flakes. The three characteristic friction levels are further illustrated in the friction profile in Fig. 5(a) (taken along the dashed line in Fig. 4(d)). These include: large friction level on the silica substrate, low friction level on the graphene film (but spatially non-uniform, most likely due to the irregular morphology and curvature of the flakes, which result in a varying tip–sample contact area), and sharp friction peaks corresponding to the edges of graphene flakes. During scanning, the AFM tip perceives the graphene edges as additional potential barriers that have to be overcome in order to step from the substrate onto the graphene flakes. Therefore, crossing the graphene edges leads to additional torsion of the AFM cantilever, accompanied with increased friction force [55,66].

Friction map corresponding to a larger normal load of 112 nN is depicted in Fig. 4(e). As seen, the domains with brighter contrast corresponding to the substrate enlarge with increasing the normal load due to removal of the graphene film. A bright domain in Fig. 4(e), outlined by the dashed line, exhibits increased friction force, indicating enhanced mechanical interaction between the AFM tip and the graphene film. Under a normal load of 155 nN (Fig. 4(f)), most of the scan area displays a bright contrast, suggesting that much of the graphene film has been removed from the substrate. Nevertheless, the remaining graphene flakes (encircled by the dashed lines in Fig. 4(f)) appear dark, despite the increased normal load, indicating low friction.

Histograms of the friction maps in Figs. 4(d)–4(f) are presented in Fig. 5(b). Each histogram is associated with two peaks, where the lower (higher) peak corresponds to the graphene film (the silica substrate). The substrate peaks (the square markers in Fig. 5(b)) shift toward

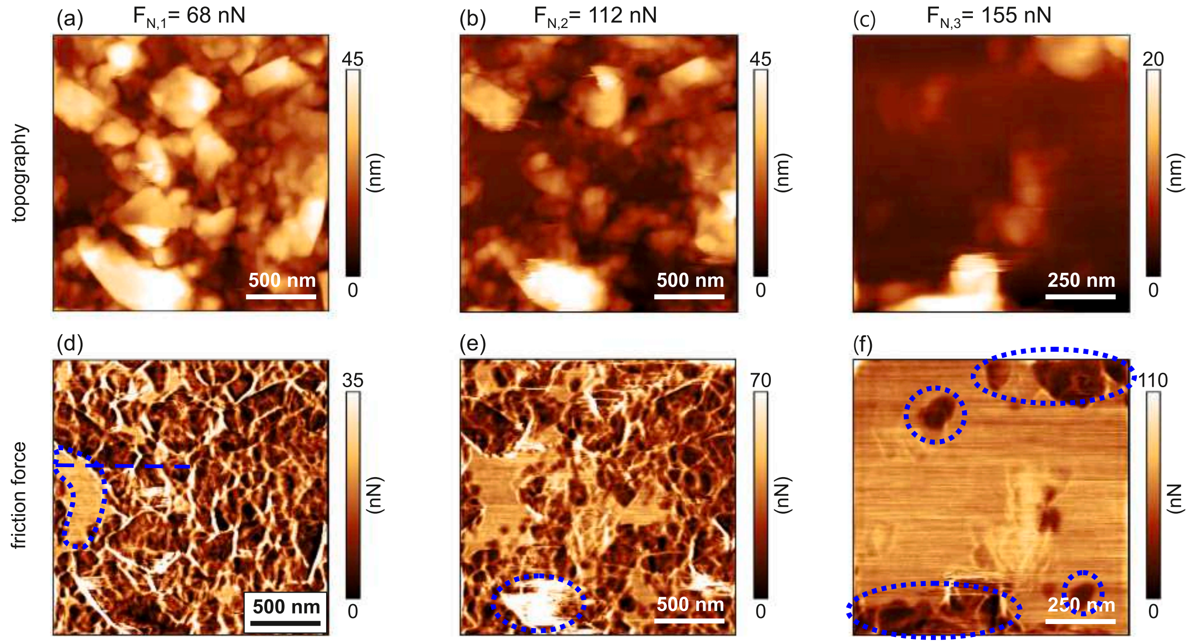

Fig. 4. Rubbing the LPE graphene film (deposited onto the silica substrate) in contact mode AFM under three gradually increasing normal loads (68 nN, 112 nN, and 155 nN): (a)–(c) topographic images, and (d)–(f) friction force maps. Ten cycles were performed for each load (one cycle represents a complete scan of the considered square area), whereas the results are presented for the last, tenth cycle for each load.

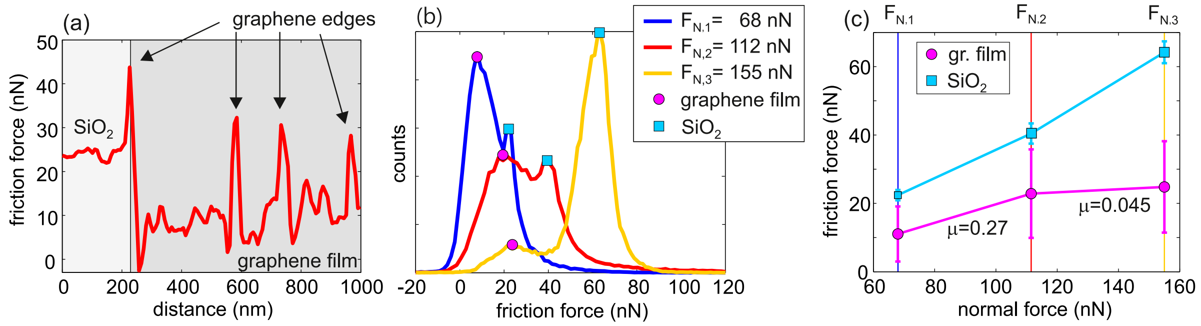

Fig. 5. Highlights of the friction measurement results in Fig. 4: (a) friction profile along the dashed line in Fig. 4(d) showing the friction along the silica substrate, graphene film, and graphene edges, (b) histograms of the friction maps in Figs. 4(d)–4(f), and (c) the evolution of the friction force as a function of the normal load with indicated friction coefficients of the graphene films for two distinct branches.

higher friction forces with increasing normal load, in accordance with Amontons's law. The graphene peaks (the circular markers in Fig. 5(b)) shift in the same manner only during the initial increase in the normal load from 68 nN to 112 nN. On the other hand, during the subsequent transition from 112 nN to 155 nN, the graphene peak exhibits only a very small shift toward higher values.

Based on the histogram results, the changes of measured friction forces as a function of the applied normal load are plotted in Fig. 5(c). The friction force measured on the substrate increases almost linearly. In contrast, the friction force measured on the graphene film exhibits two distinct branches with friction coefficients of 0.27 (during the transition from 68 nN to 112 nN) and 0.045 (during the transition from 112 nN to 155 nN), obtained as the slopes of these segments. The substantial decrease in the friction coefficient, along with the low value for the second branch, indicates that the system is approaching the superlubric regime.

The observed decrease in the friction coefficient suggests the transfer of graphene flakes onto the AFM tip, resulting in a sliding interface between two graphene layers. This transfer is associated with the peeling of graphene flakes from the substrate. In order to elucidate this process, we investigate the wear behavior of the graphene film in more detail. Topographic images of the LPE graphene film during four successive rubbing cycles at a normal force of 112 nN are depicted in Figs. 6(a)–6(d). Typical morphological changes of the film can be observed by following the sequence in the encircled region. Comparison between the first two cycles reveals distinct changes, as the encircled region in the second cycle (Fig. 6(b)) contains a narrow and short cut on the left side of the central graphene flake. During the third cycle (Fig. 6(c)), the bottom part of the graphene flake disappears, while in the fourth cycle (Fig. 6(d)), the entire graphene flake is completely peeled off. Next, we analyze in more detail the encircled region from Fig. 6(b) which is shown enlarged in Fig. 6(e). Two selected height profiles, the first one parallel to the cut and slightly shifted upward (profile 1), and the second one exactly along the cut (profile 2), are displayed in Fig. 6(f). The first profile shows a relatively flat and approximately 10 nm thick plateau between 200 nm and 550 nm, corresponding to the graphene flake. On the other hand, the profile taken along the cut comprises two distinct domains, the left one exhibiting decreased height and the right one increased height. The decreased height within the left domain indicates wear of the graphene layers that were partially peeled off. The peeled graphene layers were pushed by the AFM tip into the right domain thereby increasing its height.

The friction map for cycle 2 is displayed in Fig. 6(g), while the friction profiles along the graphene plateau and the cut are presented

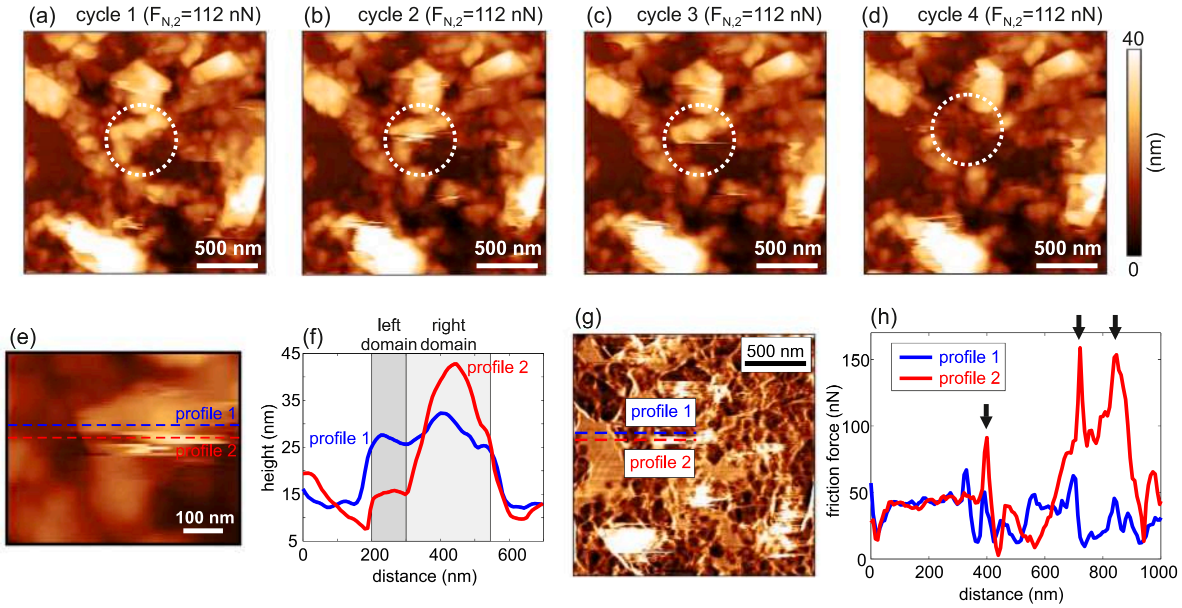

Fig. 6. The wear behavior of the graphene film: (a)–(d) topographic images of the LPE graphene film during four successive rubbing cycles at a normal load of 112 nN, (e) enlarged image of the encircled region from (b), (f) height profiles along the dashed lines in (e), (g) friction map for cycle 2, and (h) friction profiles along the dashed lines in (g) (the arrows mark pronounced friction peaks).

in Fig. 6(h). The friction profile along the cut (profile 2) displays pronounced friction peaks marked by the arrows. These friction peaks correspond to wear of the graphene layers, manifested through their cutting, tearing, and peeling. These mechanical deformations require an additional energy from the AFM tip, reflected by significantly increased lateral forces. From topographic images in Figs. 6(a)–(e), wear of the graphene flakes is initiated from the graphene edges due to their low wear resistance [55,66]. At sufficiently high normal loads, a transition occurs from mere imaging (without material modification) to tip-induced plastic deformations at the edges of the graphene flakes. Although wear is generally undesired, peeling of graphene flakes in this case provides strong evidence of their transfer onto the AFM tip.

The previous results can be summarized as follows. Wear of the graphene film was initiated at a normal load of 112 nN (Fig. 4(b)). A higher normal load of 155 nN resulted in pronounced peeling of the graphene film from the substrate (Fig. 4(c)). The lateral size of the graphene flakes (Fig. 5(a)) matched the size of the employed AFM tip, facilitating the formation of tribo-induced transfer layers and graphene-covered tips. During subsequent sliding, the investigated system consisted of the graphene film and graphene-covered AFM tip. As a result, sliding between two graphene layers resulted in decreased friction coefficient as observed in Fig. 5(d).

5. Superlubricity of LPE graphene films

In the next step, we investigated the sliding interaction between the previously prepared graphene-covered AFM tip and LPE graphene films. The aim was to confirm the superlubric regime through friction coefficient measurements. For this purpose, FFM measurements were conducted under varying normal forces on the graphene film deposited onto the silica substrate. Fig. 7 presents the measured topographic images (top row) and corresponding friction maps (bottom row). The topographic images (Figs. 7(a) and 7(b)) and friction maps (Figs. 7(e) and 7(f)), recorded at normal forces of 50 nN and 110 nN, respectively, show stable film morphology and no signs of wear. On the other hand, at an increased normal force of 195 nN, wear of the graphene film becomes clearly visible as displayed in Fig. 7(c). In the corresponding friction map in Fig. 7(g), the encircled regions reveal spatially extended bright domains with enhanced friction that are not localized along graphene edges only. These observations imply a prolonged and enhanced mechanical interaction between the AFM tip and the graphene flakes. By further increasing the normal force to 280 nN, most of the film was removed by the AFM tip, leaving behind a bare substrate, represented by the dark contrast in the topographic image in Fig. 7(d). At the same time, the friction map in Fig. 7(h) displays a very bright contrast, indicating increased friction resulting from pronounced wear. On the other hand, two larger graphene domains, encircled in Fig. 7(d), remain on the substrate. They exhibit dark contrast in all friction maps in Figs. 7(e)–7(h), which remains almost constant with the increasing normal force, indicating a very low friction coefficient.

The friction profiles along the dashed lines in Figs. 7(f) and 7(h) are depicted in Fig. 8(a). These profiles were measured across the graphene film containing large flakes and showing the dark contrast in the lower scan zone. They reveal two characteristic friction levels, the higher one corresponding to the silica substrate and the lower one to the graphene domains (the friction peaks associated with the graphene edge, particularly pronounced on the graphene film located on the right side, are omitted from the analysis). While the friction force on the silica substrate rises with increasing normal load (from 110 nN to 280 nN) in line with Amonton's law, the friction level on the graphene film domains stays nearly constant (particularly on the left side), regardless of the increasing normal load, thereby indicating an extremely low friction coefficient. The friction profiles along the dotted lines in Figs. 7(f) and 7(h) are depicted in Fig. 8(b). These profiles were obtained on the graphene film containing small flakes. At a higher normal load of 280 nN, the friction force increases significantly and simultaneously exhibits pronounced oscillations. The increased friction force corresponds to the wear of graphene flakes, whereas the observed oscillations and abrupt variations in the friction force originate from the stochastic nature of the wear process. Specifically, the AFM tip scratching induces cutting, tearing, and peeling of graphene flakes, as well as their pushing, rotation, and eventual crumpling. These processes typically occur together and in combination, making them inherently uncontrolled.

The histograms of the friction maps in Figs. 7(f) and 7(h) are presented in Fig. 8(c). Both histograms display three characteristic peaks. In the histogram obtained for 110 nN, the lower peak (the circular marker) corresponds to dark and large graphene flakes in the

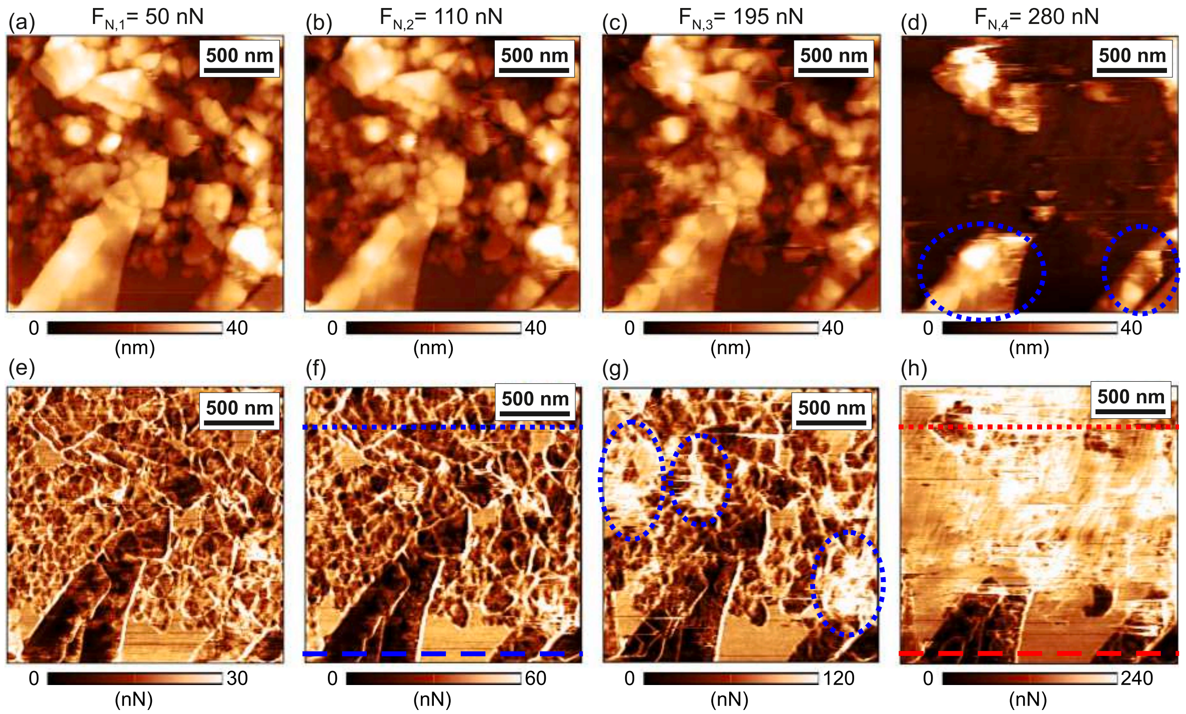

Fig. 7. Result of FFM measurements conducted on the LPE graphene film deposited onto the silica substrate: (a)–(d) topographic images and (e)–(h) corresponding friction maps recorded under gradually increasing normal force from 50 nN to 280 nN.

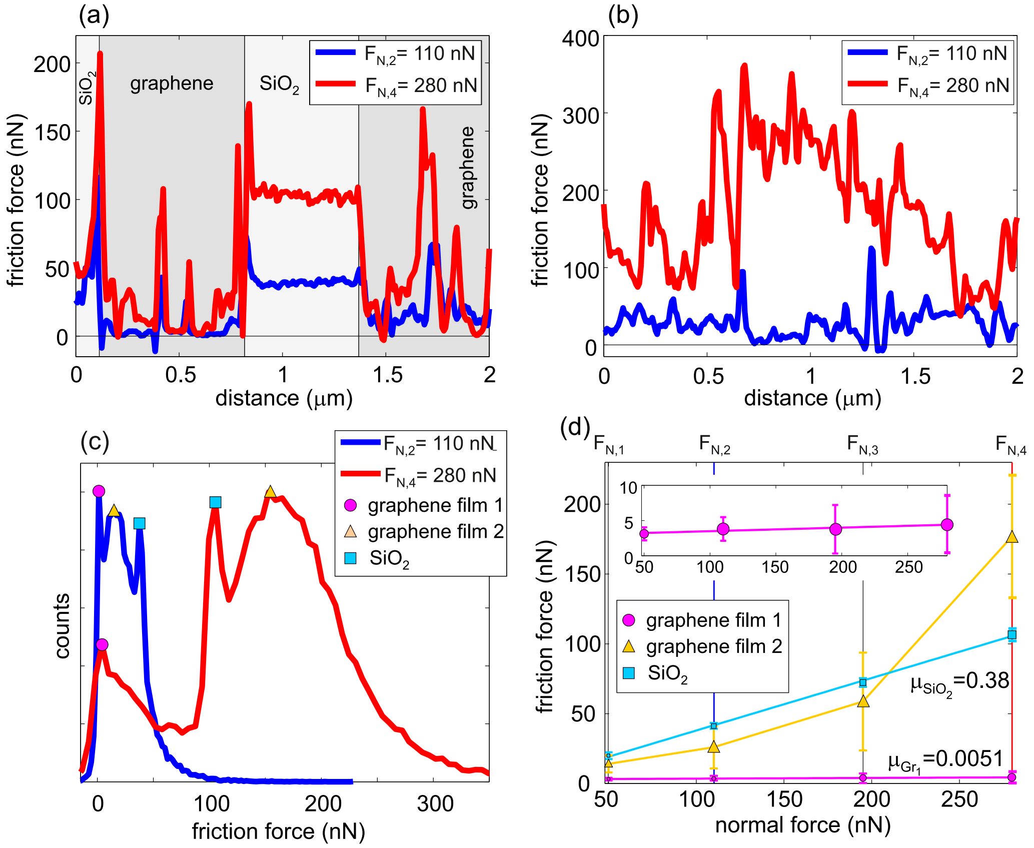

Fig. 8. (a) Friction profiles measured along the dashed lines in Figs. 7(f) and 7(h). (b) Friction profiles measured along the dotted lines in Figs. 7(f) and 7(h). (c) Histograms of the friction maps in Figs. 7(f) and 7(h). (d) Friction force as a function of the normal force with indicated friction coefficient for the graphene film and silica substrate.

lower part of the scan area (graphene film 1), the middle peak (the triangular marker) represents the remaining graphene film containing smaller flakes in the upper part of the scan area (graphene film 2), whereas the highest histogram peak (the square marker) corresponds to the silica substrate. In the histogram obtained for 280 nN, all peaks shift toward higher friction forces, though each in a distinct manner. While the lowest peak, corresponding to the large graphene flakes (graphene film 1), shifts only slightly, the peak corresponding to the rest of the graphene film (graphene film 2) shifts drastically toward values exceeding the friction forces measured on the substrate. Histograms for the friction maps presented in Figs. 7(e) and 7(g) were calculated and analyzed in the same manner.

By tracking the corresponding histogram peaks, we were able to plot the dependence of friction force as a function of normal load. The results are presented in Fig. 8(d). The friction force measured on the large graphene flakes (graphene film 1) fits well to an almost horizontal line, with the slope yielding a friction coefficient of only 0.0051. This low friction coefficient confirms the superlubric sliding of the AFM tip over the large graphene flakes. The friction force on the silica substrate fits well to a linear curve, resulting in a friction coefficient of 0.38. On the other hand, the friction force on the rest of the graphene film (graphene film 2) is non-linear consisting of three branches. Only the first branch (for a normal force from 50 nN to 110 nN) shows a friction coefficient lower than that of the silica substrate. However, with increasing normal load, the wear of the graphene film becomes more pronounced, leading to a gradual increase in the friction force.

To further support the previous results, similar FFM measurements under increasing normal load were performed on the LPE graphene film supported by the PET substrate. Topographic images at the initial (53 nN) and final normal load (310 nN) are presented in Figs. 9(a) and 9(b), respectively. Compared to the initial configuration, the final topographic image displays significant morphological changes on the right-hand side of the scan area. Here, the film morphology appears irregular, the image is blurred, and the edges of the graphene flakes are ill-defined, indicating severe film damage. In contrast, the large graphene flake on the left-hand side remained adhered to the substrate, exhibiting only minor morphological changes.

Friction maps for selected normal loads are presented in the top panel of Fig. 9(c). The large flake on the left-hand side displays a dark contrast that changes only slightly with increasing normal load, indicating a superlubric regime in this area. In contrast, the right-hand side of the friction maps shows a transition from dark contrast at lower normal loads to a very bright contrast at the highest normal load. The dark contrast and low friction observed at lower loads stem from the presence of graphene flakes, whereas at higher loads, the flakes are either peeled off from the substrate or severely damaged, resulting in the bright contrast and a significant increase in friction.

Histograms of the friction maps for all applied normal loads are presented in Fig. 9(d). They exhibit a pronounced and narrow peak near zero, corresponding to the friction of the large graphene flake on the left-hand side of the scan area (graphene film 1). This peak exhibits the minimal shift with increasing normal force. The second peak in each histogram, observed at higher friction forces, is broad and it represents the friction force measured on both the PET substrate and the small graphene flakes on the right-hand side of the scan area (graphene film 2). In contrast to the first peak, the second peak shifts significantly toward higher friction forces with increasing normal load.

The shift of the first peak was used to determine the evolution of the friction force measured on the large graphene flake as a function of the applied normal load. The corresponding results are presented in the bottom panel of Fig. 9(c). As in the previous case of the LPE graphene film on the silica substrate, the experimental data are well fitted by a linear curve yielding a friction coefficient of 0.0053, thereby confirming the superlubric regime.

Finally, in order to confirm tribo-induced transfer of graphene flakes onto the AFM tip, SEM imaging was performed on the tip before and after all friction experiments. Results are presented in Figs. 10(a) and 10(b), respectively. Fig. 10(a) reveals that the AFM tip exhibited a slightly rounded apex due to prior use in imaging. Fig. 10(b) displays a graphene flake surrounding the tip, which is highlighted by the dashed line. Due to intensive tip-sample interaction, the AFM tip became blunt after all rubbing and friction experiments, while the attached graphene flakes exhibit lateral dimensions on the order of hundreds of nanometers, thereby matching the broadened apex of the AFM tip. EDX spectroscopy was employed for chemical analysis to examine how this envelope changes the chemical composition. The analyses focused on the carbon peak to confirm an increased concentration of carbon atoms. The results in Fig. 10(c) show that the carbon peak measured on the AFM tip after rubbing increases by approximately a factor of two. The significantly increased concentration of carbon atoms confirms that graphene flakes have formed a coating around the AFM tip.

The presence of the graphene coating on the AFM tip after numerous friction experiments illustrated in Fig. 10(b) indicates its mechanical stability and strong adhesion between the graphene coating and the AFM tip surface. In this study, we utilized silicon AFM tips which are inherently covered by a thin layer of native silicon-oxide due to spontaneous oxidation in air. Therefore, in the considered system, the graphene coating is in direct contact with the silica layer. The dominant interaction between these two materials is vdW attraction which ensures strong adhesion between them [67]. The mechanical stability of graphene on silica is further enhanced by its flexibility. As a result, the graphene can easily wrap around nanoscale surface corrugations of the silica substrate thereby increasing effective contact area [68]. In the present case of graphene wrapped around the AFM tip, this implies that it conforms to the nanoscale tip asperities [36,69], which improves its mechanical stability and adhesion to the tip.

6. Discussion

Our results showed that investigated LPE graphene films were well suited both for the formation of tribo-induced transfer layers on AFM tips and for demonstrating the superlubric effect. Generally, LPE films of 2D materials consist of flakes with a broad distribution of lateral sizes, typically ranging from several tens of nanometers to a few micrometers. In our study, superlubricity was observed on large and flat graphene flakes, with reduced density of exposed edges, that exhibit characteristics of crystalline surfaces. Therefore, LPE graphene films that facilitate superlubricity should consist of flakes with the largest possible lateral dimensions. These films can be prepared by selectively removing smaller flakes via high-speed centrifugation of the initial dispersion [70–72]. The resulting lateral size of the graphene flakes obtained through controlled centrifugation ranged from several micrometers to over ten micrometers. Similar approaches for producing LPE films with large flakes have been demonstrated for other 2D materials, including MoS_2 [73], $Ti_3C_2T_x$ MXene [74], and graphene oxide [75]. Since these materials can also be employed as solid lubricants, they further expand the library of low-friction and potentially superlubric 2D materials accessible through LPE. Nevertheless, it is worth noting that LPE films with large flakes present challenges in terms of substrate coverage, as larger flakes tend to leave gaps that expose the underlying substrate.

While superlubricity was observed only on larger graphene flakes, tribo-induced transfer layers were formed from smaller flakes that are comparable to the size of the AFM tips used. The smaller flakes have less contact area with the substrate, resulting in lower total adhesion energy. As a result, they can be easily dragged by the AFM tip and subsequently transferred onto it. Additionally, smaller flakes do not need to be cut by the AFM tip, as they fit its size and can be directly transferred. Since the LPE graphene films contain many small flakes, they are well suited for fabricating graphene-coated AFM probes via tribo-induced transfer. These findings highlight that the optimal film morphology highly depends on applications. Namely, larger flakes

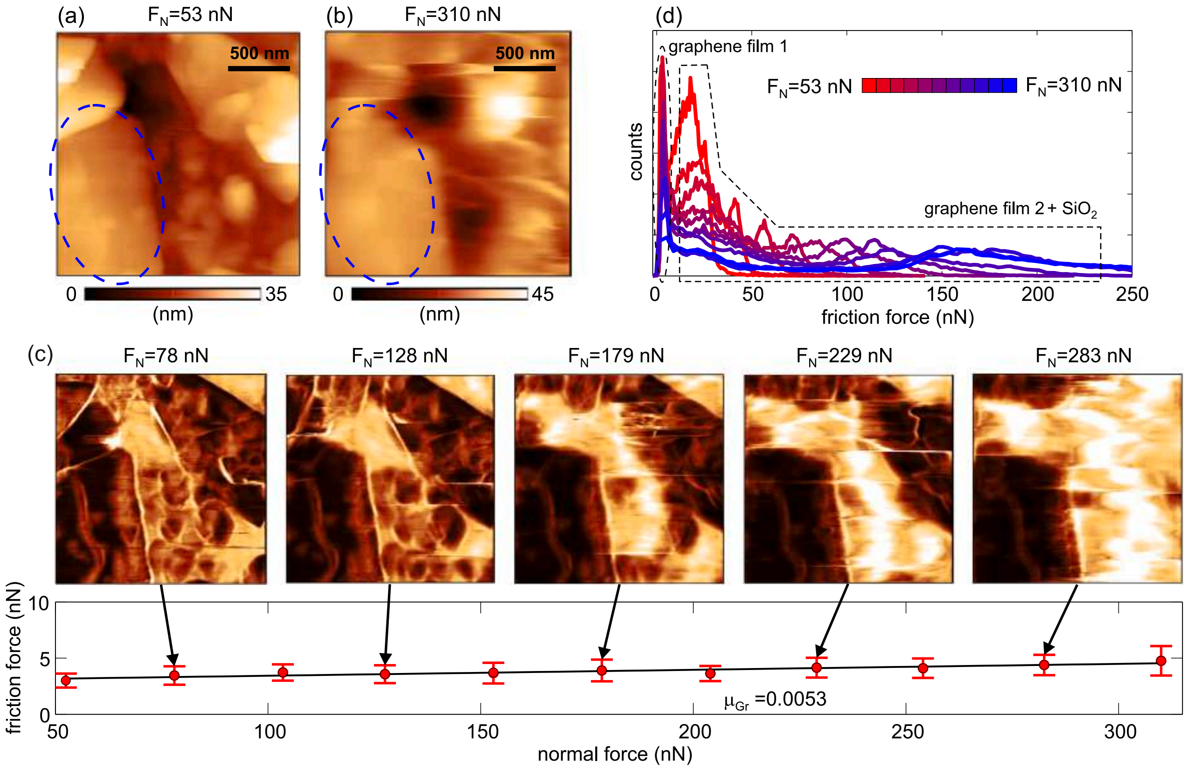

Fig. 9. Result of FFM measurements conducted on the LPE graphene film deposited onto the PET substrate: topographic images recorded (a) at the initial normal load of 53 nN, and (b) at the final normal load of 310 nN. (c) Top panel displays friction force maps with indicted normal loads, while the bottom panel shows the evolution of the friction force as a function of the normal load with indicated friction coefficient in the superlubric regime of the graphene film. (d) Histograms of the friction maps.

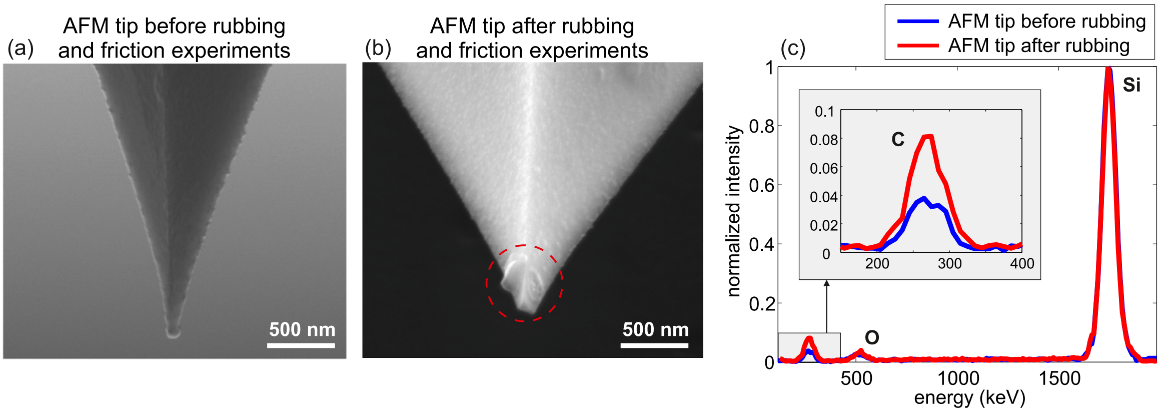

Fig. 10. SEM images of the AFM tip (a) before and (b) after rubbing and friction experiments. (c) EDX spectra of the AFM tip. The inset in (c) highlights the change in the carbon peak after the rubbing and friction experiments.

facilitate superlubricity, while smaller flakes serve a dual function as they improve film continuity and, at the same time, they are more suitable for the formation of a transfer layer.

The lateral size and dimensional matching between two graphene flakes are important factors influencing resulting friction. Namely, two twisted graphene flakes form characteristic Moiré patterns which strongly influence the frictional behavior. For a graphene flake of radius R sliding over a graphene substrate, the friction increases with $R^{0.5}$ and R^2 in the case of incommensurate and commensurate twist angles, respectively [76]. Therefore, the friction generally increases with the flake size, while the scaling exponent depends on twisting angle. This results explains why superlubricity is more readily achieved at the nanoscale.

In our case, the effective size of the graphene flake on the AFM tip is determined by the tip size and the tip–sample contact area, rather than by the overall lateral dimensions of the transferred flake. The NSG01 probes used in this study have a tip curvature radius of less than 10 nm, which is significantly smaller than the lateral dimensions of the graphene flakes comprising the LPE graphene film, presented in Fig. 3(c). According to the SEM image in Fig. 10(b), the AFM tip became blunted after the friction experiments, implying a slight increase in both the tip radius and the contact area. Nevertheless, the actual contact area is determined by the nanoscale asperities of the AFM tip, which are wrapped by the transferred graphene flakes [36]. Due to the nanoscale nature of these asperities, the effective size of the graphene flakes on the AFM tip is several orders of magnitude smaller than the lateral dimensions of the flakes comprising the LPE graphene film. According to Ref. [76], a geometry in which the lateral dimensions of one flake are significantly smaller than those of the other promotes low friction forces between the two flakes and facilitates superlubricity.

In addition, graphene flakes in LPE graphene films are self-assembled into turbostratic (disordered) stacks, characterized by misaligned and randomly oriented flakes. While such stacking is considered as a limitation for nanoelectronic applications, where well-ordered structures are preferred, it can be advantageous for tribological applications, such as lubrication. In turbostratic stacking, the flakes are removed from their commensurate states (typically AB stacking), allowing them to freely translate and slide over one another. This behavior has been demonstrated both experimentally [17] and theoretically [77].

The interaction between the AFM tip and the LPE graphene films was primarily influenced by the applied normal load, which was varied to reveal different operational regimes of the system. The first operational regime was characterized by stable and wear-free scanning, which was maintained for normal forces up to approximately 100 nN. In this regime, superlubricity was achieved on large and flat graphene flakes during scanning with graphene-covered probes. Wear was initiated in the second operational regime for normal loads exceeding ~ 150 nN. While most graphene flakes remained stable on the substrate without observable morphological changes, wear was evident through scratching of some flake edges, followed by the displacement, rotation, and deformation of the flakes. This is the regime in which transfer of graphene flakes from the substrate to the AFM tip typically occurred. The third operational regime was characterized by extensive wear of the graphene films at normal loads exceeding ~ 200 nN. This regime was characterized by extensive peeling of graphene flakes from the substrate across nearly the entire scanning area. Although some large graphene flakes exhibited superlubric behavior in the second and third regimes, stable superlubricity is expected to be achieved in the first regime during wear-free scanning.

In order to broaden the operational regime of LPE graphene films to accommodate higher normal loads, it is essential to use films composed of graphene flakes with improved adhesion. The first strategy to achieve this goal is to fabricate films composed of laterally large flakes. Due to their increased contact area with the substrate, large graphene flakes exhibit higher total adhesion energy. Stronger adhesion suggests that greater normal forces are needed to initiate wear. In addition, films composed of larger graphene flakes have a reduced density of exposed edges, which also contributes to increased wear resistance. As previously mentioned, LPE films with large graphene flakes can be fabricated by high-speed centrifugation of the initial dispersion [70–72]. The second strategy focuses on selecting an appropriate substrate and modifying its surface properties. Several approaches have been proposed in this context, including substrate cleaning via oxygen plasma treatment [78,79], selection of atomically flat surfaces [80,81], control of substrate roughness and chemistry [82], and adjustment of the oxidation degree of metallic substrates [83].

The friction coefficient achieved in the superlubric regime of LPE graphene films deposited on silica and PET substrates was on the order of 10^{-3}. To further reduce the friction coefficient, one approach is to use substrates that provide better adhesion of graphene flakes. For this purpose, the most natural choices are atomically flat substrates, such as mica and hexagonal boron nitride. FFM measurements of mechanically exfoliated 2D materials on such substrates demonstrated reduced friction coefficients due to the absence of the puckering effect [80]. Namely, due to improved adhesion, the out-of-plane deformations of 2D materials induced by the AFM tip are less pronounced, resulting in a reduced tip-sample contact area and, consequently, lower friction. In an analogous way, we believe that atomically flat substrates could further decrease the friction coefficient in the superlubric regime of LPE graphene films.

The potential presence of residual NMP in LPE graphene films can significantly influence their frictional properties. In contrast, our films were prepared using the LB method, in which graphene is assembled at the air–water interface rather than deposited directly from dispersion. Owing to its high miscibility with water, NMP rapidly diffuses into the aqueous subphase during this process, substantially reducing its concentration at the interface and in the final film. X-ray photoelectron spectroscopy (XPS) data for similar LPE graphene films, provided in the supplementary information of our previous study [63], show only a weak N 1s signal near 400.0 eV, characteristic of C–N bonding. These results indicate that only trace amounts of NMP remain in the final films. Therefore, we consider the influence of residual NMP on the measured friction forces to be negligible.

7. Conclusions

In summary, our results show that nanoscale superlubricity is attainable even in structurally inhomogeneous LPE graphene films deposited by LB technique on silica and PET substrate. Using AFM-based measurements, we demonstrated the superlubric regime on large graphene flakes with reduced density of exposed edges and with lateral dimensions on the order of a micron. This regime, characterized by a friction coefficient of ~ 0.005, was sustained during wear-free scanning under normal loads up to $\sim$ 100 nN. At higher loads, gradual wear was observed, initiated at the flake edges and followed by their peeling from the substrate.

We also showed that smaller flakes within the LPE films, having lateral dimensions up to several hundred nanometers (comparable to the tip size), promote the formation of tribo-induced transfer layers on AFM tips during contact-mode scanning. Owing to their abundance of small and weakly adhered flakes which can easily attach to the AFM tips, the LPE films can serve as efficient sources for the formation of tribo-induced transfer layers on AFM tips. Therefore, unlike graphite, which was previously employed for this purpose, where the AFM tip must first tear the top layers in order to form a graphene coating which will be transferred onto the tip, the LPE films offer a versatile alternative and broaden the range of materials available for tip coating.

Our results offer strategies for the rational design of LPE graphene films for tribological applications. Superlubricity requires films composed of flakes with large lateral dimensions and reduced density of exposed edges. To sustain the superlubricity under higher loads, improved adhesion of graphene flakes to the substrate is essential. This could be achieved by using large-area flakes or atomically flat substrates. Finally, the approach for achieving superlubricity in graphene based LPE films demonstrated here could be extended to other LPE 2D materials suitable for solid lubrication, including transition metal dichalcogenides [18,19], MXenes [60,61], phyllosilicates [84,85], etc.

CRediT authorship contribution statement

Borislav Vasić: Writing – original draft, Visualization, Methodology, Investigation, Formal analysis, Conceptualization. **Ivana Milošević:** Writing – original draft, Investigation, Formal analysis. **Zorica Konstantinović:** Writing – original draft, Investigation, Formal analysis. **Miloš Ognjanović:** Writing – original draft, Investigation, Formal analysis. **Alberto Pomar:** Writing – original draft, Supervision, Resources, Funding acquisition.

Declaration of Generative AI and AI-assisted technologies in the writing process

During the preparation of this work the authors used ChatGPT in order to enhance readability of the manuscript and language. After using this tool, the authors reviewed and edited the content as needed and take full responsibility for the content of the publication.

Declaration of competing interest

The authors declare that they have no known competing financial interests or personal relationships that could have appeared to influence the work reported in this paper.

Acknowledgments

BV, IM, and ZK acknowledge funding provided by the Institute of Physics Belgrade, through the grant of the Ministry of Education, Science, and Technological Development of the Republic of Serbia. AP and ZK acknowledge funding from the State Investigation Agency from "OXISOT" (PID2021-128410OB-I00) and the Severo Ochoa Programme for Centres of Excellence in R&D (CEX2023– 001263-S)

References

[1] M. Hirano, K. Shinjo, Superlubricity and frictional anisotropy, Wear 168 (1993) 121–125.
[2] M. Dienwiebel, G.S. Verhoeven, N. Pradeep, J.W.M. Frenken, J.A. Heimberg, H.W. Zandbergen, Superlubricity of graphite, Phys. Rev. Lett. 92 (2004) 126101.
[3] M.Z. Baykara, M.R. Vazirisereshk, A. Martini, Emerging superlubricity: A review of the state of the art and perspectives on future research, Appl. Phys. Rev. 5 (2018) 041102.
[4] J.A. Williams, Friction and wear of rotating pivots in MEMS and other small scale devices, Wear 251 (2001) 965–972.
[5] K. Holmberg, A. Erdemir, Influence of tribology on global energy consumption, costs and emissions, Friction 5 (2017) 263–284.
[6] D. Peng, Y. Wang, H. Li, Z. Wu, X. Yang, X. Huang, et al., Structural superlubric slidevices, Device 3 (2025) 100745.
[7] Z. Wu, X. Huang, X. Xiang, Q. Zheng, Electro-superlubric springs for continuously tunable resonators and oscillators, Commun. Mater. 2 (2021) 104.
[8] X. Huang, X. Xiang, J. Nie, D. Peng, F. Yang, Z. Wu, et al., Microscale schottky superlubric generator with high direct-current density and ultralong life, Nat. Commun. 12 (2021) 2268.
[9] L. Zhang, H. Cai, L. Xu, L. Ji, D. Wang, Y. Zheng, et al., Macro-superlubric triboelectric nanogenerator based on tribovoltaic effect, Matter 5 (2022) 1532–1546.
[10] D. Peng, J. Wang, H. Jiang, S. Zhao, Z. Wu, K. Tian, et al., 100 km wear-free sliding achieved by microscale superlubric graphite/DLC heterojunctions under ambient conditions, Nat. Sci. Rev. 9 (2021) nwab109.
[11] X. Huang, T. Li, J. Wang, K. Xia, Z. Tan, D. Peng, et al., Robust microscale structural superlubricity between graphite and nanostructured surface, Nat. Commun. 14 (2023) 2931.
[12] W.H. Oo, H. Gao, M.H. Müser, M.Z. Baykara, Persistence of structural lubricity on contaminated graphite: Rejuvenation, aging, and friction switches, Nano Lett. 24 (2024) 12118–12124.
[13] Z. Liu, J. Yang, F. Grey, J.Z. Liu, Y. Liu, Y. Wang, et al., Observation of microscale superlubricity in graphite, Phys. Rev. Lett. 108 (2012) 205503.
[14] J. Yang, Z. Liu, F. Grey, Z. Xu, X. Li, Y. Liu, et al., Observation of high-speed microscale superlubricity in graphite, Phys. Rev. Lett. 110 (2013) 255504.
[15] Y. Liu, K. Wang, Q. Xu, J. Zhang, Y. Hu, T. Ma, et al., Superlubricity between graphite layers in ultrahigh vacuum, ACS Appl. Mater. Interfaces 12 (2020) 43167–43172.
[16] T. Sun, E. Gao, X. Jia, J. Bian, Z. Wang, M. Ma, et al., Robust structural superlubricity under gigapascal pressures, Nat. Commun. 15 (2024) 5952.
[17] X. Feng, S. Kwon, J.Y. Park, M. Salmeron, Superlubric sliding of graphene nanoflakes on graphene, ACS Nano 7 (2013) 1718–1724.
[18] J.M. Martin, C. Donnet, T. Le Mogne, T. Epicier, Superlubricity of molybdenum disulphide, Phys. Rev. B 48 (1993) 10583–10586.
[19] H. Li, J. Wang, S. Gao, Q. Chen, L. Peng, K. Liu, et al., Superlubricity between MoS_2 monolayers, Adv. Mater. 29 (2017) 1701474.
[20] Y. Song, D. Mandelli, O. Hod, M. Urbakh, M. Ma, Q. Zheng, Robust microscale superlubricity in graphite/hexagonal boron nitride layered heterojunctions, Nat. Mater. 17 (2018) 894–899.
[21] F. Hui, S. Chen, X. Liang, B. Yuan, X. Jing, Y. Shi, et al., Graphene coated nanoprobes: A review, Crystals 7 (2017) 269.
[22] S.-W. Liu, H.-P. Wang, Q. Xu, T.-B. Ma, G. Yu, C. Zhang, et al., Robust microscale superlubricity under high contact pressure enabled by graphene-coated microsphere, Nat. Commun. 8 (2017) 14029.
[23] Z. Zhang, Y. Du, S. Huang, F. Meng, L. Chen, W. Xie, et al., Macroscale superlubricity enabled by graphene-coated surfaces, Adv. Sci. 7 (2020) 1903239.
[24] Y. Wen, J. Chen, Y. Guo, B. Wu, G. Yu, Y. Liu, Multilayer graphene-coated atomic force microscopy tips for molecular junctions, Adv. Mater. 24 (2012) 3482–3485.
[25] M. Pacios, P. Hosseini, Y. Fan, Z. He, O. Krause, J. Hutchison, et al., Direct manufacturing of ultrathin graphite on three-dimensional nanoscale features, Sci. Rep. 6 (2016) 22700.
[26] C. Martin-Olmos, H.I. Rasool, B.H. Weiller, J.K. Gimzewski, Graphene MEMS: AFM probe performance improvement, ACS Nano 7 (2013) 4164–4170.
[27] M. Lanza, A. Bayerl, T. Gao, M. Porti, M. Nafria, G.Y. Jing, et al., Graphene-coated atomic force microscope tips for reliable nanoscale electrical characterization, Adv. Mater. 25 (2013) 1440–1444.
[28] B. Li, J. Yin, X. Liu, H. Wu, J. Li, X. Li, et al., Probing van der Waals interactions at two-dimensional heterointerfaces, Nat. Nanotechnol. 14 (2019) 567–572.
[29] J. Li, J. Li, L. Jiang, J. Luo, Fabrication of a graphene layer probe to measure force interactions in layered heterojunctions, Nanoscale 12 (2020) 5435–5443.
[30] W. Shim, K.A. Brown, X. Zhou, B. Rasin, X. Liao, C.A. Mirkin, Multifunctional cantilever-free scanning probe arrays coated with multilayer graphene, PNAS 109 (2012) 18312–18317.
[31] G. Zhang, A.G. Güell, P.M. Kirkman, R.A. Lazenby, T.S. Miller, P.R. Unwin, Versatile polymer-free graphene transfer method and applications, ACS Appl. Mater. Interfaces 8 (2016) 8008–8016.
[32] F. Hui, P. Vajha, Y. Shi, Y. Ji, H. Duan, A. Padovani, et al., Moving graphene devices from lab to market: advanced graphene-coated nanoprobes, Nanoscale 8 (2016) 8466–8473.
[33] L. Cao, R. Liu, W. Zhang, Y. Wang, G. Wang, Z. Song, et al., High-reliability graphene-wrapped nanoprobes for scanning probe microscopy, Nanotechnology 33 (2021) 055704.
[34] R. Buzio, A. Gerbi, C. Bernini, L. Repetto, A. Silva, A. Vanossi, Dissipation mechanisms and superlubricity in solid lubrication by wet-transferred solution-processed graphene flakes: Implications for micro electromechanical devices, ACS Appl. Nano Mater. 6 (2023) 11443–11454.
[35] J. Li, J. Li, J. Luo, Superlubricity of graphite sliding against graphene nanoflake under ultrahigh contact pressure, Adv. Sci. 5 (2018) 1800810.
[36] J. Li, T. Gao, J. Luo, Superlubricity of graphite induced by multiple transferred graphene nanoflakes, Adv. Sci. 5 (2018) 1700616.
[37] Y. Liu, A. Song, Z. Xu, R. Zong, J. Zhang, W. Yang, et al., Interlayer friction and superlubricity in single-crystalline contact enabled by two-dimensional flake-wrapped atomic force microscope tips, ACS Nano 12 (2018) 7638–7646.
[38] J. Tian, X. Yin, J. Li, W. Qi, P. Huang, X. Chen, et al., Tribo-induced interfacial material transfer of an atomic force microscopy probe assisting superlubricity in a WS_2/graphene heterojunction, ACS Appl. Mater. Interfaces 12 (2020) 4031–4040.
[39] T.-D. Sha, H. Pang, L. Fang, H.-X. Liu, X.-C. Chen, D.-M. Liu, et al., Superlubricity between a silicon tip and graphite enabled by the nanolithography-assisted nanoflakes tribo-transfer, Nanotechnology 31 (2020) 205703.
[40] R. Buzio, A. Gerbi, C. Bernini, L. Repetto, A. Vanossi, Graphite superlubricity enabled by triboinduced nanocontacts, Carbon 184 (2021) 875–890.
[41] R. Buzio, A. Gerbi, C. Bernini, L. Repetto, A. Vanossi, Sliding friction and superlubricity of colloidal AFM probes coated by tribo-induced graphitic transfer layers, Langmuir 38 (2022) 12570–12580.
[42] K. Yu, Y. Peng, H. Lang, S. Ding, Y. Huang, Material transfer mechanism for fabrication of superlubricity interface by reciprocating rubbing on graphite under high contact stress, Carbon 188 (2022) 420–430.
[43] J. Li, X. Ge, J. Luo, Random occurrence of macroscale superlubricity of graphite enabled by tribo-transfer of multilayer graphene nanoflakes, Carbon 138 (2018) 154–160.
[44] M. Liao, P. Nicolini, L. Du, J. Yuan, S. Wang, H. Yu, et al., Uitra-low friction and edge-pinning effect in large-lattice-mismatch van der Waals heterostructures, Nat. Mater. 21 (2022) 47–53.
[45] C. Qu, K. Wang, J. Wang, Y. Gongyang, R.W. Carpick, M. Urbakh, et al., Origin of friction in superlubric graphite contacts, Phys. Rev. Lett. 125 (2020) 126102.
[46] H. Hu, J. Wang, K. Tian, Q. Zheng, M. Ma, The effects of disordered edge and vanishing friction in microscale structural superlubric graphite contact, Nat. Commun. 15 (2024) 10830.
[47] Y. Hernandez, V. Nicolosi, M. Lotya, F.M. Blighe, Z. Sun, S. De, et al., High-yield production of graphene by liquid-phase exfoliation of graphite, Nat. Nanotechn. 3 (2008) 563–568.
[48] J.N. Coleman, M. Lotya, A. O'Neill, S.D. Bergin, P.J. King, U. Khan, et al., Two-dimensional nanosheets produced by liquid exfoliation of layered materials, Science 331 (2011) 568–571.
[49] F. Bonaccorso, A. Lombardo, T. Hasan, Z. Sun, L. Colombo, A.C. Ferrari, Production and processing of graphene and 2d crystals, Mater. Today 15 (2012) 564–589.
[50] F. Withers, H. Yang, L. Britnell, A.P. Rooney, E. Lewis, A. Felten, et al., Heterostructures produced from nanosheet-based inks, Nano Lett. 14 (7) (2014) 3987–3992.
[51] G. Eda, G. Fanchini, M. Chhowalla, Large-area ultrathin films of reduced graphene oxide as a transparent and flexible electronic material, Nat. Nanotechn. 3 (2008) 270–274.
[52] X. Li, G. Zhang, X. Bai, X. Sun, X. Wang, E. Wang, et al., Highly conducting graphene sheets and Langmuir–Blodgett films, Nat. Nanotechn. 3 (2008) 538–542.

[53] P. Blake, P.D. Brimicombe, R.R. Nair, T.J. Booth, D. Jiang, F. Schedin, et al., Graphene-based liquid crystal device, Nano Lett. 8 (2008) 1704–1708.

[54] F. Torrisi, T. Hasan, W. Wu, Z. Sun, A. Lombardo, T.S. Kulmala, et al., Inkjet-printed graphene electronics, ACS Nano 6 (2012) 2992–3006.

[55] R. Buzio, A. Gerbi, S. Uttiya, C. Bernini, A.E. Del Rio Castillo, F. Palazon, et al., Ultralow friction of ink-jet printed graphene flakes, Nanoscale 9 (2017) 7612–7624.

[56] D. Berman, S.A. Deshmukh, S.K.R.S. Sankaranarayanan, A. Erdemir, A.V. Sumant, Macroscale superlubricity enabled by graphene nanoscroll formation, Science 348 (2015) 1118–1122.

[57] P. Wu, X. Li, C. Zhang, X. Chen, S. Lin, H. Sun, et al., Self-assembled graphene film as low friction solid lubricant in macroscale contact, ACS Appl. Mater. Interfaces 9 (2017) 21554–21562.

[58] P. Li, P. Ju, L. Ji, H. Li, X. Liu, L. Chen, et al., Toward robust macroscale superlubricity on engineering steel substrate, Adv. Mater. 32 (2020) 2002039.

[59] G. Tang, Z. Wu, F. Su, H. Wang, X. Xu, Q. Li, et al., Macroscale superlubricity on engineering steel in the presence of black phosphorus, Nano Lett. 21 (2021) 5308–5315.

[60] S. Huang, K.C. Mutyala, A.V. Sumant, V.N. Mochalin, Achieving superlubricity with 2D transition metal carbides (MXenes) and MXene/graphene coatings, Mater. Today Adv. 9 (2021) 100133.

[61] A. Macknojia, A. Ayyagari, D. Zambrano, A. Rosenkranz, E.V. Shevchenko, D. Berman, Macroscale superlubricity induced by MXene/$\mathrm{MoS_2}$ nanocomposites on rough steel surfaces under high contact stresses, ACS Nano 17 (2023) 2421–2430.

[62] A. Matković, I. Milošević, M. Milićević, T. Tomašević-Ilić, J. Pešić, M. Musić, et al., Enhanced sheet conductivity of Langmuir – Blodgett assembled graphene thin films by chemical doping, 2D Mater. 3 (2016) 015002.

[63] I.R. Milošević, B. Vasić, A. Matković, J. Vujin, S. Aškrabić, M. Kratzer, et al., Single-step fabrication and work function engineering of Langmuir–Blodgett assembled few-layer graphene films with Li and Au salts, Sci. Rep. 10 (2020) 8476.

[64] M. Lotya, A. Rakovich, J.F. Donegan, J.N. Coleman, Measuring the lateral size of liquid-exfoliated nanosheets with dynamic light scattering, Nanotechnology 24 (2013) 265703.

[65] M. Varenberg, I. Etsion, G. Halperin, An improved wedge calibration method for lateral force in atomic force microscopy, Rev. Sci. Instrum. 74 (2003) 3362–3367.

[66] A. Vasić, B. Matković, R. Gajić, I. Stanković, Wear properties of graphene edges probed by atomic force microscopy based lateral manipulation, Carbon 107 (2016) 723–732.

[67] S.P. Koenig, N.G. Boddeti, M.L. Dunn, J.S. Bunch, Ultrastrong adhesion of graphene membranes, Nat. Nanotechnol. 6 (2011) 543–546.

[68] M. Ishigami, J.H. Chen, W.G. Cullen, M.S. Fuhrer, E.D. Williams, Atomic structure of graphene on $\mathrm{SiO_2}$, Nano Lett. 7 (2007) 1643–1648.

[69] J. Li, J. Li, X. Chen, Y. Liu, J. Luo, Microscale superlubricity at multiple gold-graphite heterointerfaces under ambient conditions, Carbon 161 (2020) 827–833.

[70] U. Khan, A. O'Neill, H. Porwal, P. May, K. Nawaz, J.N. Coleman, Size selection of dispersed, exfoliated graphene flakes by controlled centrifugation, Carbon 50 (2012) 470–475.

[71] A.V. Alaferdov, A. Gholamipour-Shirazi, M.A. Canesqui, Y.A. Danilov, S.A. Moshkalev, Size-controlled synthesis of graphite nanoflakes and multi-layer graphene by liquid phase exfoliation of natural graphite, Carbon 69 (2014) 525–535.

[72] M. Telkhozhayeva, E. Teblum, R. Konar, O. Girshevitz, I. Perelshtein, H. Aviv, et al., Higher ultrasonic frequency liquid phase exfoliation leads to larger and monolayer to few-layer flakes of 2D layered materials, Langmuir 37 (2021) 4504–4514.

[73] A. O'Neill, U. Khan, J.N. Coleman, Preparation of high concentration dispersions of exfoliated $\mathrm{MoS_2}$ with increased flake size, Chem. Mater. 24 (2012) 2414–2421.

[74] K. Hantanasirisakul, T. Chantaurai, A. Limsukhon, P. Chomkhuntod, P. Poprom, M. Sawangphruk, Size selection and size-dependent optoelectronic and electrochemical properties of 2D titanium carbide ($\mathrm{Ti_3C_2T}_x$) MXene, Adv. Mater. Interfaces 9 (2022) 2201457.

[75] X. Qi, T. Zhou, S. Deng, G. Zong, X. Yao, Q. Fu, Size-specified graphene oxide sheets: ultrasonication assisted preparation and characterization, J. Mater. Sci. 49 (2014) 1785–1793.

[76] E. Koren, U. Duerig, Moiré scaling of the sliding force in twisted bilayer graphene, Phys. Rev. B 94 (2016) 045401.

[77] Y. Shibuta, J.A. Elliott, Interaction between two graphene sheets with a turbostratic orientational relationship, Chem. Phys. Lett. 512 (2011) 146–150.

[78] Y. Huang, E. Sutter, N.N. Shi, J. Zheng, T. Yang, D. Englund, et al., Reliable exfoliation of large-area high-quality flakes of graphene and other two-dimensional materials, ACS Nano 9 (2015) 10612–10620.

[79] R. Lukose, M. Lisker, F. Akhtar, M. Fraschke, T. Grabolla, A. Mai, et al., Influence of plasma treatment on $\mathrm{SiO_2/Si}$ and $\mathrm{Si_3N_4/Si}$ substrates for large-scale transfer of graphene, Sci. Rep. 11 (2021) 13111.

[80] C. Lee, Q. Li, W. Kalb, X.-Z. Liu, H. Berger, R.W. Carpick, et al., Frictional characteristics of atomically thin sheets, Science 328 (2010) 76–80.

[81] D.-H. Cho, L. Wang, J.-S. Kim, G.-H. Lee, E.S. Kim, S. Lee, et al., Effect of surface morphology on friction of graphene on various substrates, Nanoscale 5 (2013) 3063–3069.

[82] J.C. Spear, J.P. Custer, J.D. Batteas, The influence of nanoscale roughness and substrate chemistry on the frictional properties of single and few layer graphene, Nanoscale 7 (2015) 10021–10029.

[83] S. Zhao, Z. Zhang, Z. Wu, K. Liu, Q. Zheng, M. Ma, The impacts of adhesion on the wear property of graphene, Adv. Mater. Interfaces 6 (2019) 1900721.

[84] B. Vasić, C. Czibula, M. Kratzer, B.R.A. Neves, A. Matković, C. Teichert, Two-dimensional talc as a van der Waals material for solid lubrication at the nanoscale, Nanotechnology 32 (2021) 265701.

[85] B. Vasić, R. Gajić, I. Milošević, Ž. Medić, M. Blagojev, M. Opačić, et al., Natural two-dimensional pyrophyllite: Nanoscale lubricant, electrical insulator and easily-machinable material, Appl. Surf. Sci. 608 (2023) 155114.

Journal of the Serbian Chemical Society
JSCS@tmf.bg.ac.rs • www.shd.org.rs/JSCS

J. Serb. Chem. Soc. 90 (6) 823–836 (2025)
JSCS–5423

Original scientific paper
Published 24 June, 2025

Field experiment on the uptake of lead, strontium, cobalt and nickel in the wood and bark of spruce (*Picea abies* L.) and Douglas-fir (*Pseudotsuga menziesii* Mirb.)

IVANA R. MILOŠEVIĆ[1]*, SANJA ŽIVKOVIĆ[2], MILOŠ MOMČILOVIĆ[2],
ŽELJKA VIŠNJIĆ-JEFTIĆ[3], MILORAD VESELINOVIĆ[4], IVANA D. MARKOVIĆ[5]
and DRAGAN M. MARKOVIĆ[1]

[1]*Institute of Physics Belgrade, University of Belgrade, Pregrevica 118, 11080 Belgrade, Serbia,* [2]*Institute of Nuclear Sciences Vinča, University of Belgrade, Mike Petrovića Alasa 12–14, 11351 Belgrade, Serbia,* [3]*Institute for Multidisciplinary Research, University of Belgrade, Kneza Višeslava 1, 11090 Belgrade, Serbia,* [4]*Institute of Forestry, Kneza Višeslava 3, 11090 Belgrade, Serbia and* [5]*Worldwild Clinical Trials, Omladinskih brigada 90b, 11070 Belgrade, Serbia*

(Received 25 September, revised 13 December 2024, accepted 12 January 2025)

Abstract: Human activities have significantly altered the availability and circulation of pollutants, impacting their concentrations in the environment. This pollution notably affects trees. In this study, we conducted two separate experiments (I and II) to investigate the uptake of lead, strontium, cobalt, and nickel in spruce (*Picea abies* L.) and Douglas-fir (*Pseudotsuga menziesii* Mirb.) seedlings. These seedlings were exposed to elevated levels of these metals by adding them to the soil. Our field experiments provide insights into metal accumulation in natural environments. We measured concentrations of these elements, along with manganese and zinc, in the soil, wood, and bark using inductively coupled plasma-optical emission spectrometry (ICP-OES). The results showed increased levels of the added metals in the wood and bark of both tree species. Notably, there was a significant increase in lead and nickel concentrations in Douglas-fir wood. The lead concentration in Douglas-fir wood was 7 and 4 times higher in experiments I and II, respectively, compared to the control group of seedlings, while the nickel concentration was 18 and 10 times higher. These findings suggest that Douglas-fir wood has potential for phytostabilization of lead and nickel based on trace element concentrations and transfer factors.

Keywords: accumulation; trace elements; tree seedlings; phytostabilization; transfer factors.

---

* Corresponding author. E-mail: novovic@ipb.ac.rs
https://doi.org/10.2298/JSC240925009M

INTRODUCTION

Modern development and urbanization have led to the production of various pollutants, including trace elements, organic and inorganic compounds and pesticides, which can persist in the soil and harm the environment and human health. Trace elements are particularly disturbing due to their toxicity and resistance to natural degradation, accumulating in plants, animals and the environment over time.[1] Vascular plants serve as valuable indicators of environmental pollution. Different tree parts, such as leaves/needles, seeds, bark, and tree-rings, are used to monitor trace element contamination.[2–6] Trees, with their high biomass production, long vegetation periods, strong root systems and ability to tolerate and remediate pollutants, are effective in extracting trace elements.[7] This process, known as phytoextraction, helps prevent these elements from leaching into deeper soil layers and groundwater.

The bioavailability of metals to plants is influenced by their micronutrient demand and their ability to exude and eliminate toxic elements. Metal accumulation in plants is affected by the distribution of elements in different tissues, the presence of elements with similar physiochemical properties in the soil, the availability of elements in the soil, site conditions and tree species.[1] Metals with similar properties, such as ion size and charge, compete for binding sites in plants, affecting their uptake, translocation and accumulation.[8] Tree species also influence soil pH, impacting trace element availability. The release of organic acids and hydrogen ions from tree roots increases metal ion solubility and uptake.[8] Plants absorb trace elements through their roots and above-ground parts, like leaves and bark, with root uptake being the primary pathway for metals to enter trees.

Metal uptake generally increases as the concentration of metal ions in the external solution increases.[9] However, excessive concentrations of trace element in the soil can trigger protective mechanisms in plants that inhibit the absorption.[10] Therefore, the migration and accumulation of each metal within a tree involve individual and sophisticated biochemical processes and various transportation systems.[11] While the biological function of elements like Pb and Sr in higher plants is unknown and likely toxic, Ni is a part of the enzyme urease.[12] and Co is essential for several enzymes and coenzymes in higher plant systems.[13] The accumulation of trace elements in wood and bark has not been extensively studied, especially through field experiments. Donnelly *et al*. (1990) investigated lead mobility in red spruce seedlings, focusing on whether Pb ions remained in the xylem during uptake.[14] Numerous studies have focused on the uptake and translocation of radionuclides in plants, with a majority of them focused on the bark and foliar surfaces.[15,16] Metal mobility in plants depends on their metabolic function, background metal levels, and the dosage applied to foliar surfaces. Some studies have examined the toxic effects of trace element salts on tree growth and their potential for phytoextraction and phytostabilization.[10,17–20]

However, there is a significant research gap in studying trace element accumulation in wood and bark through field experiments. Furthermore, diverse trace elements accumulate at varying degrees within distinct plant species and parts, emphasizing the significance of understanding the levels of trace elements in plants. The investigation of Douglas-fir plant species in this regard remains insufficient. Studies that are based on collecting data about the accumulation of specific trace element in plants and their distribution among plant parts must be continued and diversified.[21]

The study aimed to investigate how elevated levels of Pb, Sr, Co, and Ni in soil affect their accumulation in spruce and Douglas-fir trees under natural conditions. This field experiment focused on trace element accumulation in wood and bark, with soil metal concentrations as the only variable. The research sought to understand how these metals are absorbed by the trees and to compare the sensitivity of spruce and Douglas-fir to Pb, Sr, Co and Ni, evaluating their potential for trace element accumulation.

EXPERIMENTAL

Study site and experimental design

Details about the study site and experimental design are given in the Supplementary material to this paper.

Amount of added metals

In experiment I, spruce and Douglas-fir seedlings were watered monthly with a solution containing 2 g L^{-1} of Pb and Sr, as well as 0.5 g $L^{-1}$of Co and Ni. In experiment II, the solution contained half of these concentrations. Seedlings were watered with tap water during the experiment. Metal solutions were prepared monthly using nitrate salts (all purchased from Merck: lead(II) nitrate $Pb(NO_3)_2$; strontium(II) nitrate $Sr(NO_3)_2$; cobalt(II) nitrate hexahydrate $Co(NO_3)_2{\cdot}6H_2O$ and nickel(II) nitrate hexahydrate $Ni(NO_3)_2{\cdot}6H_2O$) dissolved in tap water. Seedlings were watered for five months with solutions achieving concentrations of 2 g L^{-1} Pb and Sr and 0.5 g L^{-1} Co and Ni for the first experiment, and 1 g L^{-1} Pb and Sr, and 0.25 g L^{-1} Co and Ni for the second experiment. Total metal added was 10 mg $g^{-1}$of Pb and Sr and 2.5 mg g^{-1} of Co and Ni for experiment I, and half of that for experiment II, and those concentrations are total amounts to which plants were exposed in this experiment. All trees survived with normal growth and no signs of metal toxicity.

Sample preparation and experiment

To simplify the results, spruce and Douglas-fir trees from the first experiment are labelled "SI" and "DI", and from the second experiment, "SII" and "DII". Control groups are labeled "SC" and "DC".

Four seedlings of each species were cut, and 1 cm stem disks were sampled from 10 cm above the base (Fig. S-1d of the Supplementary material), along with bark and soil samples taken from 0–20 cm depth. Most of the fine roots of trees are found in the surface soil layer at this depth.[22] Soil before plantation was also collected to obtain the amount of the metal content in the soil before the field experiment. Tree wood, bark and soil were digested using an advanced microwave digestion system (Ethos 1, Milestone, Italy). Sample digestion in the Ethos 1 followed standard manufacturer-recommended programs, with the official software optimizing chemical volumes, temperature and pressure based on sample type and mass. About 0.5 g of powdered oven-dried samples, of spruce and Douglas-fir, were precisely weighed and mixed in the clean vessel with a mixture of 3 mL 30 % H_2O_2 (Suprapur®, Germany) and 5 mL 65 % HNO_3 (Suprapur®, Germany) and then heated with microwave energy, (with parameters t = 200 °C, KW = 1800 W, τ = 15 min and p = 90 bar). The soil was first dried at room temperature and then in order to ensure the homogeneity of soil samples, each of the samples was divided into six equal parts from which the same amount of soil was taken. This amount of soil was sieved through a plastic sieve, and then ground in a mortar to a powdery particle size. The sample was then dried in an oven to constant weight at a temperature of 60 °C. Soil samples (0.5 g) from each part of the experiment were thoroughly mixed before analysis to ensure a homogenous concentration, accurately measured, and placed in clean microwave preparation vessels with 8 mL 65 % HNO_3 (Suprapur®, Germany) and 2 mL 36 % HCl (Suprapur®, Germany). The parameters of the soil preparation program were the same as for the preparation of plant tissues. The temperature was controlled with a predetermined power program. After cooling and without filtration, the solution was diluted to a fixed volume of 25 mL. Quality control was assured by the use of procedural blanks. Precision and accuracy were confirmed by repeated analysis of NIST pine needles (1575a) as standard reference material.

The content of elements (Pb, Sr, Co, Ni, Mn and Zn) in each sample, prepared as diluted aqueous solutions, was quantified by inductively coupled plasma optical emission spectrometry-ICP-OES using a Thermo Scientific iCAP 7400 duo analyzer (Thermo Fisher Scientific Inc.). The calibration standard solutions were prepared from a Multi-element ICP IV standard stock solution (Merck). For each element determined, calibration curves were constructed and used to determine the analyte concentrations. The data acquisition and processing were performed by the Thermo Scientific Qtegra platform software. All measurements were carried out in triplicates. The pH of the soil was determined using a glass electrode (1741, La Motte Tracer-PockeTester) in a 1:5 (volume fraction) suspension of soil in deionized water. 2 g was precisely weighted, and 10 mL of deionized water was added. The suspension was stirred on a stirrer for 30 min and left for another 30 min to stand before pH measuring. The chemical analysis results were evaluated using One-Way ANOVA to compare the three groups (experiments I and II and control) for both tree species, followed by Tukey's test to identify specific group differences. Differences were considered statistically significant at the 0.05 level.

Transfer factor

The capacity of trees to extract trace elements from soil and their translocation to aboveground tissues can be evaluated by calculating the transfer factor, *TF*. Different calculations for transfer factors can be seen in the literature and most of them divide the average trace element concentration in the plant part by the concentration in soil.[23,24] Most of them showed only elevated concentrations of specific metals compared to soil or biogeochemical comparison of metals in different media (plant and soil) that occur under the same circumstances.[25] It does not show how the metal transfer from soil to plant changed on the treated site compared to the control site.[25] Including the control site (where natural processes affect metal transfer from soil to plant) in the calculations, we can get information about changes in transfer processes.[25] To investigate the transfer of externally added metals-to-soil (TF_{soil}); soil-to-wood transfer (TF_{wood}) and soil-to-bark transfer (TF_{bark}), for this experiment, *TF* was calculated (in %) by the following equations:

$$TF_{\text{soil}} = 100(I–C)_{\text{soil}}/EA \tag{1}$$

$$TF_{\text{wood}} = (I–C)_{\text{wood}}/(I–C)_{\text{soil}} \quad (2)$$

$$TF_{\text{bark}} = (I–C)_{\text{bark}}/(I–C)_{\text{soil}} \quad (3)$$

where I and C represent the mean Pb, Sr, Co and Ni concentrations obtained in the first experiment and control for two examined coniferous species (S and D), while EA is externally added concentration of metals examined. The same equations were used for the experiment II.

RESULTS AND DISCUSSION

Concentration of Pb, Sr, Co, Ni, Mn and Zn in soil, wood and bark of spruce and Douglas-fir seedlings

Mean Pb, Sr, Co and Ni concentrations in soil, wood, and bark of spruce and Douglas-fir seedlings are presented in Table I which were externally added in this field experiment. Also, mean Mn and Zn concentrations in soil, wood and bark and the measured pH of the spruce and Douglas-fir corresponding soils can be seen in Table I. Soil concentrations measured before plantation and performed field experiment were 21±1 μg g^{-1} for Pb, 78±4 μg g^{-1} for Sr, 22±1 μg g^{-1} for Co, 87±5 μg g^{-1} for Ni, 822±42 μg g^{-1} for Mn, and 118±5 μg g^{-1} for Zn. Maximally allowed concentrations in the soil for Pb, Co, Ni and Zn in the Republic of Serbia are 85, 9, 35 and 140 μg g^{-1}.[26] Soil concentrations of Co and Ni, both before planting and in the control samples, exceed the maximum levels permitted by the Regulation, likely reflecting the geochemical conditions of the experimental area. Additionally, air pollution cannot be ruled out, given the moderate traffic, residential heating, and the proximity to the largest waste dump in Vinča, which is the only landfill in the Belgrade city area.

Soil concentrations before plantation were as control concentrations (SC and DC) measured after metal addition in experiments I and II (Table I). Thus, levels of the metals of interest in the soil before additional metal watering were as in control, excluding the possibility of metal transfer from one experiment to another. Elevated concentrations in the soil (Table I) externally added did not affect plant growth during this 2-year experiment. Higher mean Pb, Sr, Co and Ni concentrations for bark can be seen for both examined tree species, than in their wood compartments (Table I).

Mean differences of Pb, Sr, Co and Ni for soil and bark of both examined species were significant, at the 0.05 level, between parallel experiments and control (one-way ANOVA), except for the Pb concentration in SII for bark. In the case of wood, mean differences were significant for Pb, Sr and Ni, except between Ni SII concentration and control. For some soil, wood, and bark mean differences between the I and II experiments weren't significant (Tukey test). For the pH, mean differences were significant, at the 0.05 level, between the II experiment and control for both tree species. Mean differences of Mn and Zn for soil, wood and bark of both examined species were significant, at the 0.05 level, between parallel experiments and control (one-way ANOVA, Tukey test), except for the Douglas-fir DII and DC and spruce SI and SII soil Zn concentration. In some cases, for soil, wood and bark the mean differences weren't significant between the I and II experiment.

TABLE I. Mean Pb, Sr, Co, Ni, Mn and Zn (n = 4) concentrations (μg g^{-1}) in soil, wood and bark seedlings of spruce first experiment-SI; second experiment-SII; control-SC; Douglas-fir first experiment-DI; second experiment-DII and control-DC, as well as corresponding soil pH

Experiment	Pb			Sr		
	Soil	Wood	Bark	Soil	Wood	Bark
SI	827±56	0.41±0.05	4.73±0.55	680±51	101±7	256±13
SII	505±30	<0.15	1.87±0.09	325±19	54.39±3.45	246±13
SC	21±1	<0.15	1.67±0.10	75±4	31.53±1.89	81±5
DI	634±30	1.06±0,10	2.44±0.13	371±21	46.37±3.68	197±13
DII	369±19	0.61±0,08	1.28±0.06	301±15	44.32±2.72	154±9
DC	23±1	<0.15	0.68±0.05	77±4	15.85±1.07	26±2
	Co			Ni		
	Soil	Wood	Bark	Soil	Wood	Bark
SI	97±6	<0.04	0.44±0.04	278±16	0.34±0.03	2.71±0.16
SII	73±4	<0.04	0.32±0.02	199±9	0.29±0.04	1.78±0.09
SC	20±1	<0.04	0.12±0.02	88±4	0.24±0.03	1.09±0.09
DI	84±6	<0.04	0.27±0.04	226±11	0.73±0.06	1.13±0.06
DII	63±3	<0.04	0.23±0.04	182±9	0.40±0.03	1.03±0.06
DC	21±2	<0.04	<0.04	89±4	<0.04	0.36±0.04
	Mn			Zn		
	Soil	Wood	Bark	Soil	Wood	Bark
SI	950±43	8.23±0.46	18.7±1.4	128±6	18.0±0.9	67.9±3.9
SII	923±42	8.41±0.49	23.4±1.9	125±5	21.5±1.0	73.4±4.4
SC	823±42	9.22±0.57	28.9±1.9	118±7	28.4±1.6	100±5
DI	951±43	3.38±0.23	13.7±0.9	131±7	5.36±0.37	22.0±1.9
DII	954±43	2.63±0.20	12.0±0.6	122±5	3.52±0.19	25.0±1.4
DC	852±46	5.00±0.27	8.71±0.44	113±5	7.66±0.38	30.4±1.6
	SI	SII	SC	DI	DII	DC
Soil pH	6.7±0.05	6.6±0.05	6.8±0.05	6.9±0.05	6.7±0.05	7.0±0.05

Pb and Sr concentration

From Fig. 1a, it can be seen, for spruce, that the Pb content in the soil increases, and the increase is about 40 (SI) and 24 (SII) times, compared to the control soil sample. This implies an elevation of Pb concentration in the SI wood and barks for SI and SII, compared to the control (Table I). The increase was 2.8 times for SI wood and 2.8 and 1.1 times for SI and SII in the bark, respectively (Fig. 1a). Comparing the concentrations of SI and SII (Fig. 1b) for Pb in soil, wood, and bark we obtain an increased concentration in the SI experiment of about 1.6, 2.8, and 2.5 times, respectively. Increased Sr content in the soil from 75 to SI-680 μg g^{-1} and SII-325 μg g^{-1} (9 and 4 times higher compared to control) directly influences the increase of Sr concentration in the spruce wood and bark (Table I; Fig. 1a). The concentration of Sr in the soil was about twice as high if we observe the ratio between the I and II experiment (Fig. 1b). Also, the concentration of Sr in wood is almost twice as high, ie. about 1.9 times (86 %). In the bark, this increase between the I and II experiment is about 4 % (Fig. 1b).

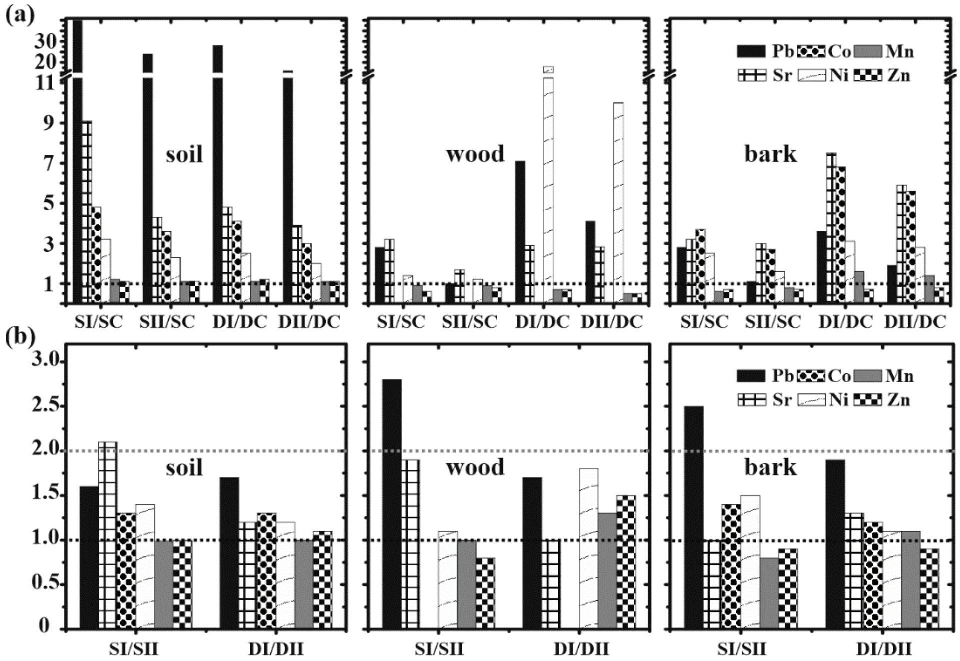

Fig. 1. Concentration ratios in soil, wood and bark: a) between the I and II experiment compared to the control and b) between the first-I and second-II experiment, for spruce-S and Douglas-fir-D. (Black line indicates a ratio of 1, representing no change in concentration, gray line represents a ratio of 2, suggesting that accumulation aligns with the two times higher externally added concentration for the I experiment; concentration ratios for cases where the detection limit was measured in the control-C were calculated using the value of the detection limit.).

In the case of Douglas-fir, it was noticed that with the increase of Pb concentration in the soil of 28 (DI) and 16 (DII) times, compared to control, the content in wood (7 and 4 times) and bark (4 and 2 times) also increases (Fig. 1a), Table I). An increase in the soil Pb content of 72 % between parallel experiments contributes to the increase of Pb in the wood of about 74 %, and the bark of about 91 %. The higher content of Sr in the soil (Table I) parallel experiments (5 and 4 times compared to control), as well as in the case of spruce, implies the higher content in Douglas-fir wood (3 times for both experiments) and bark (8 and 6 times). An increase of the Sr concentration in the soil for the I experiment of about 23 % (1.2 times) compared to the II experiment indicates that Sr content in wood is increased by about 5 % and in the bark by 28 %.

Co and Ni concentration

Elevated Co content in soil samples (5 and 4 times higher compared to control in the case of spruce, and 4 and 3 times for Douglas-fir) had an effect on increasing the concentration in the bark (4 and 3 times compared to control for spruce, and 7 and 6 times in the case of Douglas-fir) but not on wood where Co concentration was below the detection limit (Fig. 1a, Table I). Therefore, based on this experiment, the wood of spruce and Douglas-fir are not a good choice for Co. Increased Ni concentration in soil samples (3 – SI and 2 – SII times; 2.5 – DI and 2 – DII times compared to control) also have a direct effect on increasing the concentration (Fig. 1a, Table I) in both wood (1.4 – SI and 1.2 – SII times; 18 – DI and 10 – DII times compared to control) and bark (2.5 – SI and 2 – SII times; 3 – DI and 3 – DII times compared to control). About 40 % higher content of Ni in the soil was detected and about 14 % higher concentration for wood and about 52 % for the bark compared to the II experiment in the case of spruce. For Douglas-fir, it was 24 % for soil, 83 % for wood and 10 % for bark.

Mn and Zn concentration

Mn and Zn were examined because they are, among other elements, essential for higher plants and have several functions in plants.[13] As these elements weren't added in this experiment, differences compared to control are minimal, with most ratios near 1 (Fig. 1a). Some phenomena can be seen in this experiment for the examined tree species. Their concentrations in wood and bark compared to control (Table I; Fig. 1a) which slightly decreased (except for the Mn concentration in Douglas-fir bark, which increased), despite slightly higher soil concentrations (Table I).

Slight soil concentration increases for Mn (15, 12 %) and Zn (9, 6 %) in spruce and Mn (12, 12 %) and Zn (15, 7 %) in Douglas-fir soil in I and II experiments compared to control that was observed could be the consequence of the soil pH change.[2] Other factors, such as the impact of specific tree species on soil pH and the addition of heavy metals to the soil, can also influence the adsorption dynamics of essential elements by competing with or altering the total organic content (*TOC*) during root uptake. Externally added heavy metals can interact with *TOC*, affecting the behavior and availability of Mn and Zn. The effect of *TOC* on Mn and Zn uptake may differ between tree species due to variations in root systems, uptake mechanisms, and tolerance to nutrient imbalances. However, these aspects were not measured in this study. In SI and SII the pH decrease was 0.1 and 0.2; and in DI and DII it was 0.1 and 0.3, respectively, compared to the control pH value. The decrease of Mn for spruce in parallel experiments (SI and SII) expressed as a percentage compared to control was 11, 9 % for wood and 35, 19 % for bark, respectively. In the case of Zn, it was 37, 24 and 32 %, 27 %, respectively. For Douglas-fir wood, the decrease of Mn concentration was 32, 48 %, and the decrease of Zn concentration was 30, 54 % for wood and 27, 18 % for bark, respectively.

Studies indicate that trace elements move differently between tree organs across different tree species,[5,20,27–29] and plants retain trace elements at varying levels.[6] Traffic is a significant source of Pb, Ni and Zn pollution,[21,30] with Ni entering the atmosphere through fuel combustion, mining and urban waste burning, while Co is mainly used in rechargeable batteries for electronics.[31] The elevated Ni levels at the control site in our experiment may be due to these factors. Pb concentration in the control soil were below regulatory limits in Serbia and similar to road dust levels in areas with moderate traffic and residential heating contributing to pollution.[30] Thus, observed elevated Pb and Ni in wood and bark from both species are direct outcome of our experiments suggesting that bark and wood, especially of Douglas-fir, can collect and remediate these metals. The wood samples examined came from seedlings (with stem disks of 1 cm height and a volume of about 3.14 cm^3). If we scale this to mature trees (with 10 times the volume), we estimate that about 4.1 and 3.4 μg g^{-1} of Pb and Ni could be collected by spruce and 10.6 and 7.3 μg g^{-1} by Douglas-fir, with higher values possible when considering the full trunk. Several studies have shown elevated levels of trace elements in plants and soil in areas affected by air pollution,[5,6,31] but there is limited information on the trace element accumulation potential of many plant species. Research on Scots pines in Finland showed that Ni accumulates in wood,[29] while most elements are stored in roots.[17,18,20] Although roots were not examined, trace elements clearly moved from soil to wood and bark. Given the toxicity of Pb, Ni and Co, and their detrimental health effects with prolonged exposure,[31] it is crucial to extract these elements from the environment. Spruce and Douglas-fir could be used to phytostabilize trace elements in soil, reducing their mobility and leaching. An indication is that the addition of other metals to the soil and their accumulation in the body of wood and bark influence essential elements, and lead to a decrease in their plant parts. Higher Mn concentrations in background trees compared to those grown on sludge were found in tree seedlings.[32] Similarly, in beech roots a decrease in mineral cations (K, Ca, Mg, and Mn) was observed with increasing Pb and Cd in soil.[33] Prolonged exposure to elevated heavy metal levels, as suggested by our findings, could further reduce nutrient levels in plants and potentially lead to plant death over time. However, this conclusion requires further research beyond this experiment. The observed decrease in Mn and Zn may also result from competition between metals during root uptake, as Ni^{2+} and Zn^{2+} have similar physical and chemical properties,[12] leading to reduced Zn levels in wood and bark due to elevated Ni in the soil.

The impact of tree species on soil pH is important, as it influences trace elements availability to plants. The effect of different tree species on soil pH is most significant in the first 10 cm of the topsoil.[34] Topsoil pH was lower under *P. abies*, while *P. menziesii* appeared to be intermediate.[34] In this study, spruce (*P. abies*) had lower pH values than Douglas-fir (*P. menziesi*) in both control and parallel experiments (Table I). As a result, higher soil metal concentrations were observed for spruce (Fig. 1a). However, this did not translate into higher metal accumulation in wood and bark, as Douglas-fir showed greater accumulation, particularly for Ni and Pb (Fig. 1a).

Transfer factors

The capacity of trees to extract trace elements from soil and their translocation to aboveground tissues can be evaluated by calculating the transfer factor, *TF*. Three calculated ratios are presented in Fig. 2.

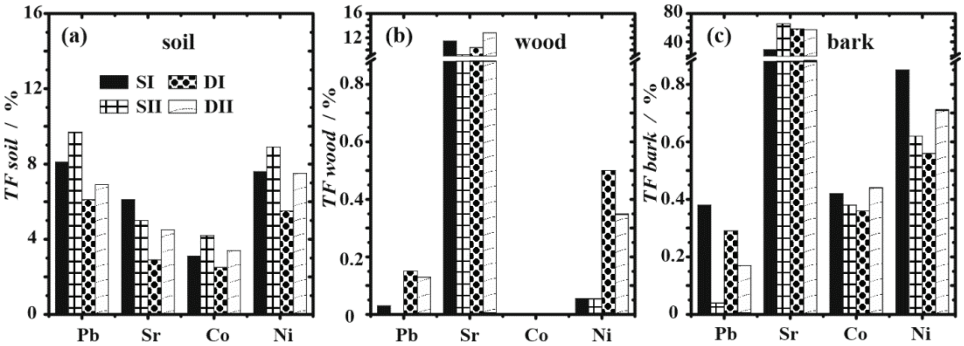

Fig. 3. Calculated transfer factors for spruce (S) and Douglas-fir (D), *TF*; a) for soil-TF_{soil}, b) wood-TF_{wood} and c) bark-TF_{bark}, expressed as a percentage.

Only a small amount (less than 10 %) of the externally added elements (EA) in the soil were in a form that is available and can be absorbed by roots and translocated throughout the plant (Fig. 2a) in these experiments. The smallest percentage of TF_{soil} was for DI Co concentration and the highest was in the case of SII Pb concentration (Fig. 2a). Generally looking, the second experiment had greater TF_{soil} probably due to the greater change in soil pH for both species. Lower pH increases the metal availability due to competition between hydrogen ions and metal ions at the uptake sites in the roots.[9] In wood and bark (Fig. 2 b and c), *TF*'s are less than 1 % (except for Sr) and the highest *TF*s are for Sr, in both species. The Sr is chemically related to Ca and plant roots normally do not discriminate between absorption of Ca^{2+} and Sr^{2+} from nutrient solutions.[23] This could be the reason for elevated *TF* in wood and bark for Sr (Fig. 2b and c).

Higher available Sr concentration in the soil in these experiments probably competes with the Ca concentration (a very important macronutrient for higher plants). Calculated TF_{wood} are greater in Douglas-fir than in spruce wood for examined elements and Ni and Pb in Douglas-fir stand out. Nickel is attributed to mobile elements,[25,32] and Ni uptake in our experiments confirms its high mobility. Pine, birch and black alder most efficiently took up Zn and Ni.[24] Although available soil concentrations of Pb compared to control (Fig. 1a) are higher than for Ni, transfer factors in wood for Ni are greater. In the case of bark, transfer factors are more pronounced than in wood. The highest TF_{bark} is for Sr, then Ni, Co and Pb. Also, small differences between spruce and Douglas-fir transfer factors for bark can be seen (Fig. 2c). The bark is intensively used as a bioindicator of atmospheric pollution but uptake of Pb, Sr, Co and Ni by tree root in these experiments indicate to their translocation from the soil to the bark. This pathway has to be taken into consideration in the highly polluted areas like the one where the elements are incorporated into the bark, especially in the case of Co which couldn’t be traced in spruce and Douglas-fir wood.

These experiments showed that metals added to natural soils were absorbed by tree roots and transferred to wood and bark within two years under normal conditions. Despite the soil concentration in the first experiment being double that of the second, the increase in metal content in soil, wood, and bark was not proportional. The second experiment had higher soil transfer factors (TF_{soil}) than the first, leading to a ratio of less than 2 between the experiments. Such studies provide valuable insights into heavy metal accumulation and distribution in tree species. Since plants can significantly reduce air pollution, expanding green spaces, this method provides a highly effective solution.

CONCLUSIONS

All spruce and Douglas-fir trees survived and grew normally during the two--year experiment. The general response of the two coniferous species was an increase of elements in wood and bark compared to controls, with only a slight decrease in Mn and Zn. Sr and Ni were absorbed most efficiently. While uptake wasn't directly proportional to soil metal concentrations, both species responded to elevated levels, indicating environmental pollution. Bark was also influenced by the added concentrations in the soil which has to be taken into consideration in highly polluted areas as the significant pathway. Bark, especially for Co, also acted as a useful indicator, unlike wood where Co was not detected. Thus, Douglas-fir wood can serve as a better bioindicator of Pb and Ni than spruce. Despite higher soil metal levels in spruce, Douglas-fir accumulated more Ni (18 and 10 times higher) and Pb (7 and 4 times higher), making it a better bioindicator for these metals. Expanding green spaces is a highly effective way to reduce air pollution, as plants play a significant role.

SUPPLEMENTARY MATERIAL

Additional data and information are available electronically at the pages of journal website: https://www.shd-pub.org.rs/index.php/JSCS/article/view/13064, or from the corresponding author on request.

Acknowledgments. The authors acknowledge funding provided by the Institute of Physics Belgrade, Institute of Nuclear Sciences Vinča and Institute for Multidisciplinary Research, through the grants by the Ministry of Science, Technological Development and Innovation of the Republic of Serbia.

ИЗВОД

ТЕРЕНСКИ ЕКСПЕРИМЕНТ О УСВАЈАЊУ ОЛОВА, СТРОНЦИЈУМА, КОБАЛТА И НИКЛА У ДРВЕТУ И КОРИ СМРЧЕ (*Picea abies* L.) И ДУГЛАЗИЈЕ (*Pseudotsuga menziesii* MIRB.)

ИВАНА Р. МИЛОШЕВИЋ[1], САЊА ЖИВКОВИЋ[2], МИЛОШ МОМЧИЛОВИЋ[2], ЖЕЉКА ВИШЊИЋ-ЈЕФТИЋ[3], МИЛОРАД ВЕСЕЛИНОВИЋ[4], ИВАНА Д. МАРКОВИЋ[5] и ДРАГАН М. МАРКОВИЋ[1]

[1]Инсшишуш за физику у Беоīраду, Универзишеш у Беоīраду, Преīревица 118, 11080 Беоīрад, [2]Инсшишуш за нуклеарне науке „Винча“, Универзишеш у Беоīраду, Мике Пешровића Аласа 12–14, 11351 Беоīрад, [3]Инсшишуш за мулшидисциūлинарна исшраживања, Универзишеш у Беоīраду, Кнеза Вишеслава 1, 11090 Беоīрад, [4]Инсшишуш за шумарсшво, Кнеза Вишеслава 3, 11090 Беоīрад и [5]Worldwild Clinical Trials, Omladinskih brigada 90b, 11070 Беоīрад

Људске активности су значајно промениле доступност и циркулацију загађујућих материја, утичући на њихове концентрације у животној средини, а загађење посебно утиче на дрвеће. У овој студији, спровели смо два одвојена експеримента (I и II) да бисмо испитали акумулацију олова, стронцијума, кобалта и никла у садницама смрче (*Picea abies* L.) и дуглазије (*Pseudotsuga menziesii* Mirb.). Ове саднице су биле изложене повишеном нивоу наведених метала, додавањем у земљу. Наши теренски експерименти пружају увид у акумулацију метала у природном окружењу. Мерили смо концентрације ових елемената, заједно са манганом и цинком, у земљишту, дрвету и кори користећи индуктивно спрегнуту плазма-оптичку емисиону спектрометрију (ICP-OES). Резултати су показали повећане нивое додатих метала у дрвету и кори обе врсте дрвећа. Приметно је да је дошло до значајног повећања концентрације олова и никла у дрвету дуглазије. Концентрација олова у дрвету дуглазије је била 7 и 4 пута већа у огледима I и II у односу на контролу, док је концентрација никла била 18 и 10 пута већа. Ови резултати, на основу концентрација елемената у траговима и трансфер фактора, сугеришу да дрво дуглазије има потенцијал ка фитостабилизацији олова и никла.

(Примљено 25. септембра, ревидирано 13. децембра 2024, прихваћено 12. јануара 2025)

REFERENCES

1. W. Liu, J. Ni, Q. Zhou, *Mater. Sci. Forum* **743–744** (2013) 768 (https://dx.doi.org/10.4028/www.scientific.net/MSF.743-744.768)
2. D. M. Marković, I. R. Milošević, D. Vilotić, *Environ. Sci. Pollut. Res.* **20** (2013) 136 (https://dx.doi.org/10.1007/s11356-012-1024-8)
3. M. Yousaf, K. L. Mandiwana, K. S. Baig, J. Lu, *Water Air Soil Poll.* **231** (2020) 382 (https://dx.doi.org/10.1007/s11270-020-04758-w)
4. W. Kusiak, J. Majka, I. Ratajczak, M. Górska, M. Zborowska, *Forests* **11** (2020) 746 (https://dx.doi.org/10.3390/F11070746)

5. H. Sevik, M. Cetin, A. Ozturk, H. B. Ozel, B. Pinar, *Appl. Ecol. Env. Res.* **17** (2019) 12843 (https://dx.doi.org/10.15666/aeer/1706_1284312857)
6. A. Turkyilmaz, H. Sevik, K. Isinkaralar, M. Cetin, *Environ. Sci. Pollut. R.* **26** (2019) 5122 (https://dx.doi.org/10.1007/s11356-018-3962-2)
7. L. Gómez, A. Contreras, D. Bolonio, J. Quintana, L. Oñate-Sánchez, I. Merino, *Adv. Bot. Res.*, **89** (2019) 281 (https://doi.org/10.1016/bs.abr.2018.11.010)
8. H. Marschner, *Mineral nutrition of higher plants*, Academic Press, London, 1995, p. 313 (https://doi.org/10.1016/C2009-0-02402-7)
9. M. N. V. Prasad, J. Hagemeyer, *Heavy metal stress in plants: From molecules to ecosystems*, Springer-Verlag, Berlin, 1999, p. 1 (ISBN: 3662077450)
10. M. Praspaliauskas, N. Pedisius, A. Gradeckas, *J. For. Res.* **29** (2018) 347 (https://doi.org/10.1007/s11676-017-0455-y)
11. N. Rascio, F. Navari-Izzo, *Plant Sci.* **180** (2011) 169 (https://doi.org/10.1016/j.plantsci.2010.08.016)
12. I. V. Seregin, A. D. Kozhevnikova, *Russ. J. Plant Phys.* **53** (2006) 257 (https://doi.org/10.1134/S1021443706020178)
13. B. J. Alloway, *Heavy metals in soils*, Springer Science & Business Media, Berlin, 2013, p. 196 (https://doi.org/10.1007/978-94-007-4470-7)
14. J. R. Donnelly, J. B. Shane, P. G. Schaberg, *J. Environ. Qual.* **19** (1990) 268 (https://doi.org/10.2134/jeq1990.00472425001900020012x)
15. Z. Q. Lin, N. N. Barthakur, P. H. Schuepp, G. G. Kennedy, *Environ. Exp. Bot.* **35** (1995) 475 (https://doi.org/10.1016/0098-8472(95)00039-9)
16. S. A. Watmough, T. C. Hutchinson, *Environ. Pollut.* **121** (2003) 39 (https://doi.org/10.1016/S0269-7491(02)00208-7)
17. A. Bonet, G. Pascaud, C. Faugeron, M. Soubrand, E. Joussein, V. Gloaguen, G. Saladin, *Int. J. Phytoremediat.* **18** (2016) 559 (https://doi.org/10.1080/15226514.2015.1086297)
18. C. Astier, V. Gloaguen, C. Faugeron, *Int. J. Phytoremediat.* **16** (2014) 790 (https://doi.org/10.1080/15226514.2013.856849)
19. M. S. Günthardt-Goerg, P. Vollenweider, R. Schulin, *Plants* **11** (2022) 523 (https://doi.org/10.3390/plants11040523)
20. O. P. Zhivotovsky, Y. A. Kuzovkina, C. P. Schulthess, T. Morris, D. Pettinelli, *Int. J. Phytoremediat.* **13** (2011) 731 (https://doi.org/10.1080/15226514.2010.525555)
21. H. Cobanoglu, H. Sevik, İ. Koç, *Water Air Soil Poll.* **234** (2023) 65 (https://doi.org/10.1007/s11270-023-06086-1)
22. S.-O. Borgegard, H. Rydin, *J. Appl. Ecol.* **26** (1989) 585 (https://doi.org/10.2307/2404084)
23. D. Butkus, E. Baltrėnaitė, *Ekologija* **53** (2007) 29 (ISSN: 0235-7224)
24. N. Mirecki, R. Agič, L. Šunić, L. Milenković, Z. S. Ilić, *Fresen. Environ. Bull.* **24** (2015) 4212 (ISSN: 1018-4619)
25. E. Baltrėnaitė, A. Lietuvninkas, P. Baltrėnas, *Water Air Soil Pollut.* **223** (2012) 4297 (https://doi.org/10.1007/s11270-012-1192-7)
26. *Official Gazette of the Republic of Serbia*, **64** (2019) 1
27. H. Sevik, M. Cetin, H. Ucun Ozel, H. B. Ozel, M. M. M. Mossi, I. Zeren Cetin, *Environ. Sci. Pollut. R.* **27** (2020) 2423 (https://doi.org/10.1007/s11356-019-06895-0)
28. G. Saladin, in *Soil Biology,* Vol. 44, Springer Science & Business Media, Berlin, 2015, p. 333 (https://doi.org/10.1007/978-3-319-14526-6_18)
29. K. Saarela, L. Harju, J. Rajander, J. Lill, S. Heselius, *Sci. Total Environ.* **343** (2005) 231 (https://doi.org/10.1016/j.scitotenv.2004.09.043)

30. S. N. Istanbullu, H. Sevik, K. Isinkaralar, O. Isinkaralar, *B. Environ. Contam. Tox.* **110** (2023) 1 (https://doi.org/10.1007/s00128-023-03720-w)
31. M. Cetin, A. M. O. Aljama, O. B. M. Alrabiti, F. Adiguzel, H. Sevik, I. Zeren Cetin, *Water Air Soil Pollut.* **233** (2022) 1 (https://doi.org/10.1007/s11270-022-05638-1)
32. D. Butkus, E. Baltrėnaitė, *Ekologija* **53** (2007) 68 (ISSN: 0235-7224)
33. S. W. Breckle, H. Kahle, *Vegetatio* **101** (1992) 43 (https://doi.org/10.1007/BF00031914)
34. L. Augusto, J. Ranger, D. Binkly, A. Rothe, *Ann. Forest. Sci.* **59** (2002) 233 (https://doi.org/10.1051/forest:2002020)
35. K. Isermann, *Handbook of Stable Strontium*, Springer-Verlag, Berlin, 1981, p. 65 (https://doi.org/10.1007/978-1-4684-3698-3_5).

Journal of the Serbian Chemical Society
JSCS@tmf.bg.ac.rs • www.shd.org.rs/JSCS

J. Serb. Chem. Soc. 90 (6) S229–S230 (2025) *Supplementary material*

SUPPLEMENTARY MATERIAL TO

Field experiment on the uptake of lead, strontium, cobalt and nickel in the wood and bark of spruce (*Picea abies* L.) and Douglas-fir (*Pseudotsuga menziesii* Mirb.)

IVANA R. MILOŠEVIĆ[1]*, SANJA ŽIVKOVIĆ[2], MILOŠ MOMČILOVIĆ[2],
ŽELJKA VIŠNJIĆ-JEFTIĆ[3], MILORAD VESELINOVIĆ[4], IVANA D. MARKOVIĆ[5]
and DRAGAN M. MARKOVIĆ[1]

[1]Institute of Physics Belgrade, University of Belgrade, Pregrevica 118, 11080 Belgrade, Serbia, [2]Institute of Nuclear Sciences Vinča, University of Belgrade, Mike Petrovića Alasa 12–14, 11351 Belgrade, Serbia, [3]Institute for Multidisciplinary Research, University of Belgrade, Kneza Višeslava 1, 11090 Belgrade, Serbia, [4]Institute of Forestry, Kneza Višeslava 3, 11090 Belgrade, Serbia and [5]Worldwild Clinical Trials, Omladinskih brigada 90b, 11070 Belgrade, Serbia

J. Serb. Chem. Soc. 90 (6) (2025) 823–836

STUDY SITE AND EXPERIMENTAL DESIGN

Details about the study site and experimental design are given in the Supplementary material to this paper.

The field experiment was carried out in Kaluđerica, Belgrade, Serbia, on Livada 1 Street as depicted in Fig. S-1 (a) and (b). Five-year-old spruce (*Picea abies* L.) and Douglas-fir (*Pseudotsuga menziesii* Mirb.) seedlings were obtained from the Institute of Forestry, Belgrade. In May 2017, 24 seedlings were planted across 48 m², divided into six groups, with four seedlings per group (Figure 1c). To prevent metal transfer, seedlings were spaced 1 meter apart. After rooting until January 2018, they were watered five times between January and May 2018 with Pb, Sr, Co, and Ni in two experiments, with the I experiment having double the concentrations of the II experiment. The third group of seedlings served as the control group. In May 2019, the seedlings were harvested.

---

* Corresponding author. E-mail: novovic@ipb.ac.rs

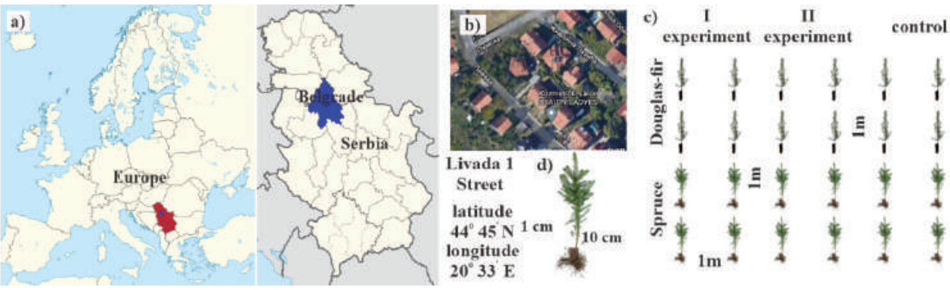

Fig. S-1. a) Sampling location of the performed field experiment, b) Google map of the location with the arrow showing the planted area, c) display of the planted seedlings with two parallel field experiments and control and d) display of the wood sampling.

PHOTONICA2015.

V International School and Conference on Photonics
& COST actions: MP1204 and BM1205
& the Second international workshop "Control of light and matter waves propagation and localization in photonic lattices“
www.vin.bg.ac.rs/photonica 2015

Book of Abstracts

Editors
Suzana Petrović, Goran Gligorić and Milutin Stepić

Belgrade, 2015.

Book of abstracts

PHOTONICA2015

the Fifth international school and conference on photonics

& COST actions: MP1204 and BM1205

& the Second international workshop "Control of light and matter waves propagation and localization in photonic lattices"

24 August – 28 August 2015

Belgrade, Serbia

Editors

Suzana Petrović, Goran Gligorić and Milutin Stepić

Vinča Institute of Nuclear Sciences, Belgrade, Serbia

Belgrade, 2015

ABSTRACTS OF TUTORIAL, KEYNOTE AND INVITED LECTURES AND CONTRIBUTED PAPERS

of

the Fifth international school and conference on photonics
PHOTONICA2015

and
COST actions MP1204 and BM1205

and
the Second international workshop
"Control of light and matter waves propagation and localization in photonic lattices"

24 August – 28 August 2015
Belgrade Serbia

Editors
Suzana Petrović, Goran Gligorić, Milutin Stepić

Technical assistance
Petra Beličev, Marijana Petković

Publisher
Vinča Institute of Nuclear Sciences
Mike Petrovića Alasa 12-14, P.O. Box 522
11001 Belgrade, Serbia

Printed by
Serbian Academy of Sciences and Arts

Number of copies
300

ISBN 978-86-7306-131-3

The PHOTONICA2015 (The Fifth International School and Conference on Photonics) is organized by the Vinča Institute of Nuclear Sciences, University of Belgrade (www.vinca.rs), the Serbian Academy of Sciences and Arts, the Optical Society of Serbia and Aston University, Birmingham, UK. Co-organizers of this meeting are: the Institute of Physics Belgrade, University of Belgrade (www.phy.bg.ac.rs), Faculty of Electrical Engineering, University of Belgrade (www.etf.bg.ac.rs), Institute of Chemistry, Technology and Metallurgy, University of Belgrade (www.ihtm.bg.ac.rs), Faculty of Technical Sciences, University of Novi Sad (www.ftn.uns.ac.rs), Faculty of physics, University of Belgrade (www.ff.bg.ac.rs), and Faculty of biology, University of Belgrade (www.bio.bg.ac.rs), under auspices and with support of the Ministry of Education, Science and Technological Development, Serbia.

The support of the sponsors of the Conference is gratefully acknowledged:

Sponsored by OSA
EPS
AMERICAN ELEMENTS
THE MATERIALS SCIENCE COMPANY ®
THORLABS
JDSU
Macval Tea
Macval
EXTREME D.O.O.
COHERENT®
GILDEN pλotonics
Ocean Optics
fianium ultrafast fiber lasers
Quantel

Committees

Scientific Committee

Aleksandar Krmpot, Serbia
Antun Balaž, Serbia
Arlene D. Wilson-Gordon, Israel
Boris Malomed, Israel
Branislav Jelenković, Serbia
Dejan Gvozdić, Serbia
Dejan Milošević, Bosnia and Herzegovina
Detlef Kip, Germany
Dragan Indjin, UK
Feng Chen, China
Giorgos Tsironis, Greece
Goran Isić, Serbia
Goran Pichler, Croatia
Jelena Radovanović, Serbia
Jovana Petrović, Serbia
Kurt Hingerl, Austria
Laurentius Windholz, Austria
Ljupčo Hadžievski, Serbia
Milutin Stepić, Serbia
Milivoj Belić, Qatar
Misha Sumetsky, UK
Nikola Burić, Serbia
Pavle Anđus, Serbia
Paul Harrison, UK
Radoš Gajić, Serbia
Sergei Turitsyn, UK
Slobodan Vuković, Serbia
Stefka Cartaleva, Bulgaria
Vladimir Škarka, France
Željko Šljivančanin, Serbia

Organizing Committee

Milutin Stepić, (Chair)
Misha Sumetsky, (Co-Chair)
Suzana Petrović, (Secretary)
Ljupčo Hadžievski
Jovana Petrović
Aleksandra Maluckov
Goran Gligorić
Petra Beličev
Aleksandar Daničić
Marija Ivanović
Nevena Raičević
Ana Radosavljević
Milan Trtica
Slobodan Zdravković
Biljana Gaković
Dalibor Čevizović
Branislav Jelenković
Zoran Grujić
Jelena Radovanović
Peđa Mihailović
Jovan Elazar
Bratislav Obradović
Milorad Kuraica
Zoran Jakšić
Slobodan Vuković
Miloš Živanov

COST actions BM1205 and MP1204 Training School Steering Committee

Mauro Pereira, UK
Anna Wojcik-Jedlinska, Poland
Dragan Indjin, UK
Jelena Radovanovic, Serbia
Antoine Muller, Switzerland
Andreas Wacker, Sweden
Ivan Bucharov, Bulgaria
Johan Stiens, Belgium
Florin Mihallescu, Romania
Czeslaw Skierbiszewski, Poland
Shumin Wang, Sweden
Igor Meglinski, Finland

Conference Topics

1. Quantum optics
2. Nonlinear optics
3. Ultrafast phenomena
4. Laser spectroscopy
5. Devices and components
6. Biophotonics
7. Optical communications
8. Sensing: plasmonics, fiber optics and interferometers
9. Holography and adaptive optics
10. Optical materials

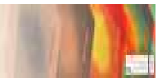

BMBS COST Action BM1205
European Network for Skin Cancer Detection using Laser Imaging
(24-28 August)

MPNS COST Action MP1204
TERA-MIR Radiation: Materials, Generation, Detection and Applications
(24-28 August)

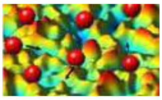

WORKSHOP
Control of light and matter waves propagation and localization in photonic lattices
(28-29 August)

The **International School and Conference on Photonics- PHOTONICA**, is a biennial event held in Belgrade since 2007. The first meeting in the series was called ISCOM (International School and Conference on Optics and Optical Materials), but it was later renamed to Photonica to reflect more clearly the aims of the event as a forum for education of young scientists, exchanging new knowledge and ideas, and fostering collaboration between scientists working within emerging areas of photonic science and technology.

A particular educational feature of the program is to enable students and young researchers to benefit from the event, by providing introductory lectures preceding most recent results in many topics covered by the regular talks. In other words, apart from the regular lectures, the plenary speakers will also give tutorial lectures specifically designed for students and scientists starting in this field.

The Conference consists of oral presentations and vibrant poster sessions. The wish of the organizers is to provide a platform for discussing new developments and concepts within various disciplines of photonics, by bringing together researchers from academia, government and industrial laboratories for scientific interaction, the showcasing of new results in the relevant fields and debate on future trends. This year our conference will contribute celebration of the International Year of Light as a global initiative which will highlight to the citizens of the world the importance of light and optical technologies. This PHOTONICA 2015 will include two COST Action meetings and one workshop with the main objective to promote knowledge in various disciplines of photonics. In additional to the lectures and seminars, a Round Table "Scientific publishing: Editors et altera" will be organized where the editors will present editorial and publishing policies of their journals and share their experiences. Following the official program, the participants will also have plenty of opportunity to mix and network outside of the lecture theatre with planned free time and social events.

This book contains 219 abstracts of all presentations at the **5th International School and Conference on Photonics, PHOTONICA2015**. Authors from 50 countries from all continents will present their work at the conference. There will be six tutorial and seven keynote lectures to the benefits of students and young researches. Twenty four invited lectures, five progress reports of young Serbian researchers and thirty one contributed talks will present most recent results in their research fields. Within the two poster sessions, students and young researches will present 146 poster presentations on their new results in a cozy atmosphere of the Serbian academy of science and arts.

Belgrade, July 2015
Editors

Transparent and conductive films from liquid phase exfoliated graphene

T. Tomašević-Ilić[1], J. Pešić[1], I. Milošević[1], J. Vujin[1], A. Matković[1], M. Spasenović[1] and R. Gajić[1]
[1]*Center for Solid State Physics and New Materials, Institute of Physics, University of Belgrade, Pregrevica 118, 11080 Belgrade, Serbia*
e-mail: ttijana@ipb.ac.rs

Liquid phase exfoliation of graphite presents a promising route for large-scale graphene production [1]. We describe basic advantages and disadvantages of the controlled deposition of few-layer graphene using the Langmuir-Blodgett (LB) method, which is compatible with usage in transparent conductors [2,3]. The graphene sheets (GS) were exfoliated from graphite by ultrasonic treatment in N-Methyl-2-pyrrolidone (NMP) and dimethylacetamide (DMA) solvents. For comparison, graphene sheets were also exfoliated in a water solution of surfactants. We confirm a higher exfoliation rate for surfactant-based processing compared to NMP and DMA. Furthermore, we demonstrate that our films exfoliated in NMP and DMA and deposited with LB have a higher optical transmittance compared to films obtained with vacuum filtration, which is a necessary step for GS exfoliated in water solutions [4]. The structural, optical and electrical properties of graphene layers were characterized with scanning electron microscopy, atomic force microscopy, ellipsometry, UV/VIS spectrophotometry and sheet resistance measurements. Our facile and reproducible method results in high-quality transparent conductive films with potential applications in flexible and printed electronics and coating technology.

This work is supported by the Serbian MPNTR through Projects OI 171005 and Innovation Project 451-03-2802-IP/1/167 and by Qatar National Research Foundation through Projects NPRP 7-665-1-125.

REFERENCES

[1] K. R. Paton et al., Nat. Mater. 13, 624 (2014).
[2] H. K. Kim et al., Nanoscale 5, 12365 (2013).
[3] F. Bonaccorso et al., Nat. Photon. 4, 611 (2010).
[4] M. Lotya et al., J. Am. Chem. Soc. 131, 3611 (2009).

XIX Symposium on Condensed Matter Physics
SFKM 2015

Book of Abstracts

---

7 – 11 September 2015
Belgrade, Serbia

Conference Chair

Leonardo Golubović, *West Virginia University*

Co-Chairs

Antun Balaž, *Institute of Physics Belgrade*
Igor Herbut, *Simon Fraser University*
Mihajlo Vanević, *Faculty of Physics Belgrade*
Nenad Vukmirović, *Institute of Physics Belgrade*

Organizing Committee

Antun Balaž, *Institute of Physics Belgrade*
Edib Dobardžić, *Faculty of Physics Belgrade*
Marko Mladenović, *Institute of Physics Belgrade*
Jovana Petrović, *Vinča Institute of Nuclear Sciences*
Mihajlo Vanević, *Faculty of Physics Belgrade*
Vladimir Veljić, *Institute of Physics Belgrade*
Nenad Vukmirović, *Institute of Physics Belgrade*

Organized by

Institute of Physics Belgrade
Faculty of Physics Belgrade
Vinča Institute of Nuclear Sciences
Serbian Academy of Sciences and Arts

Program Committee

Nataša Bibić, *Vinča Institute of Nuclear Sciences*
Ivan Božović, *Brookhaven National Laboratory*
Milan Damnjanović, *Faculty of Physics Belgrade*
Vladimir Dobrosavljević, *Florida State University*
Laszlo Forro, *EPFL Lausanne*
Gyula Eres, *Oak Ridge National Laboratory*
Radoš Gajić, *Institute of Physics Belgrade*
Zoran Hadžibabić, *Cambridge University*
Igor Herbut, *Simon Fraser University*
Zoran Ikonić, *University of Leeds*
Darko Kapor, *Dept. of Physics, University of Novi Sad*
Irena Knežević, *University of Wisconsin Madison*
Milan Knežević, *Faculty of Physics Belgrade*
Miodrag Kulić, *Goethe-Universität Frankfurt*
Milica Milovanović, *Institute of Physics Belgrade*
Ivanka Milošević, *Faculty of Physics Belgrade*
Branislav Nikolić, *University of Delaware*
Čedomir Petrović, *Brookhaven National Laboratory*
Zoran Popović, *Institute of Physics Belgrade*
Velimir Radmilović, *Faculty of Technology and Metallurgy Belgrade*
Zoran Radović, *Faculty of Physics Belgrade*
Miljko Satarić, *Faculty of Technical Sciences Novi Sad*
Vojislav Spasojević, *Vinča Institute of Nuclear Sciences*
Bosiljka Tadić, *Jožef Štefan Institute Ljubljana*
Milan Tadić, *School of Electrical Engineering Belgrade*
Filip Vukajlović, *Vinča Institute of Nuclear Sciences*

Ministry of Education, Science and Technological Development of Republic of Serbia has financially supported the organization of SFKM 2015.

XIX Symposium on Condensed Matter Physics
SFKM 2015

Conference Topics

Conference presentations cover a wide range of research topics within the experimental, theoretical, and computational condensed matter physics, including but not limited to the following:

Semiconductor physics: Electronic structure, Quantum dots and wires, Photonic crystals, High magnetic fields phenomena, Ultra-fast phenomena

Surface, interface, and low-dimensional physics: Graphene, Carbon and other nanotubes, Topological insulators, Complex oxide interfaces, Transport in nanostructures

Magnetism: Magnetic materials and phase transitions, Magneto-electronics and spintronics, Magnetic nanoparticles

Superconductivity: Conventional, high T_c, and heavy-fermion superconductors: Materials and mechanisms, Heterostructures: Proximity effect and transport phenomena

Strongly correlated and disordered systems: Materials with strong correlations and disorder, Dynamical properties from time-resolved experiments, Quantum fluids, Cold atoms and BEC

Phase transitions, phase ordering, and structural ordering of condensed matter: Equilibrium and dynamic phenomena, Ferroelectricity, Multiferroics, Quasi-Crystals, Crystal surface morphology and dynamics, Crystal growth

Soft and biological matter: Polymers, Liquids and gels, Liquid crystals, Elastomers, Membranes, Living cells and living matter

Statistical physics of complex systems: Networks and other structures

Conference venue:
Serbian Academy of Sciences and Arts, Knez Mihailova 35, Belgrade

Conference website: http://www.sfkm.ac.rs

Spectroscopic And Scanning Probe Microscopic Investigations And Characterization Of Graphene

A. Matković[a], I. Milošević[a], M. Milićević[a], A. Beltaos[a], T. Tomašević-Ilić[a], J. Pešić[a], M. M. Jakovljević[a], M. Musić[a], U. Ralević[a], M. Spasenović[a], Dj. Jovanović[a], B. Vasić[a], G. Isić[a] and R. Gajić[a]

[a] *Center for Solid State Physics and New Materials, Institute of Physics, University of Belgrade, Pregrevica 118, 11080 Belgrade, Serbia*

Abstract. Graphene synthesized by various techniques has different properties. Here we give an overview of several graphene synthesis techniques and device fabrication processes; as micromechanical exfoliation, fabrication of free standing membranes, chemical vapor deposition, liquid phase exfoliation, Langmuir-Blodgett assembly, wet transfer, shadow mask and UV photolithography. We employ various scanning probe and optical spectroscopy techniques to determine how these different fabrication processes affect properties of graphene, and present advantages and drawbacks for various applications.

In particular we focus on optical properties of graphene obtained using spectroscopic ellipsometry, and how these are altered by the interaction with an ambient [1], or various dielectric and metallic substrates [2], or by different fabrication processes [3]. We highlight how transfer residue and sample annealing affect optical properties of graphene [3], as well as how the interaction between graphene and a gold substrate can be observed through spectroscopic ellipsometry and Kelvin probe force microscopy [2]. In addition, we demonstrate how graphene can be manipulated by an atomic force microscope, using dynamic plow lithography [4].

Acknowledgement: This work is supported by the Serbian MPNTR through Projects OI 171005, III 45018, 451-03-2802-IP/1/167, by the EU FP7 project NIM_NIL (gr. a. No 228637 NIM_NIL: www.nimnil.org), and by the Qatar National Research Foundation through Project NPRP 7-665-1-125.

REFERENCES

1. Matković, A., Beltaos, A., Milićević, M., Ralević, U., Vasić, B., Jovanović, Dj., and Gajić, R., *Journal of Applied Physics* **112**, 123523 (2012).
2. Matković, A., Milićević, M., Chhikara, M., Ralević, U., Vasić, B., Jovanović, Dj., Belić, M., Bratina, G., and Gajić, R., *Journal of Applied Physics* **117**, 015305 (2015).
3. Matković, A., Ralević, U., Chhikara, M., Jakovljević, M. M., Jovanović, Dj., Bratina, G., and Gajić, R., *Journal of Applied Physics* **114**, 093505 (2013).
4. Vasić, B., Kratzer, M., Matković, A., Nevosad, A., Ralević, U., Jovanović, Dj., Ganser, C., Teichert, C., and Gajić, R., *Nanotechnology* **24**, 015303 (2013).

Chemical Doping Of Langmuir-Blodgett Assembled Graphene Films For Flexible Transparent Conductive Electrodes

A. Matković[a], I. Milošević[a], M. Milićević[a], T. Tomašević-Ilić[a], J. Pešić[a], M. Musić[a], M. Spasenović[a], Dj. Jovanović[a], B. Vasić[a], M. R. Belić[b] and R. Gajić[a]

[a]*Center for Solid State Physics and New Materials, Institute of Physics, University of Belgrade, Pregrevica 118, 11080 Belgrade, Serbia*
[b]*TeJas A&M University at Qatar, P.O. BoJ 23874 Doha, Qatar*

Abstract. We demonstrate how chemical doping can be used to enhance properties of liquid-phase exfoliated (LPE) graphene films. Langmuir-Blodgett assembly (LBA) on a water-air interface was used to fabricate multi-layer graphene films several square centimeters in size (Fig. 1(a)). Sheet conductivity of these films is enhanced through doping with nitric acid, leading to a fivefold improvement while retaining the same transparency as un-doped films (Fig. 1(b)). In addition, chemical doping increases the work function by 0.75 eV, to a value of 4.95 eV, making these films a promising candidate for anode electrodes in hybrid solar cells and organic electronics.

Acknowledgement: This work is supported by the Serbian MPNTR through Projects OI 171005, III 45018, 451-03-2802-IP/1/167 and by the Qatar National Research Foundation through Project NPRP 7-665-1-125.

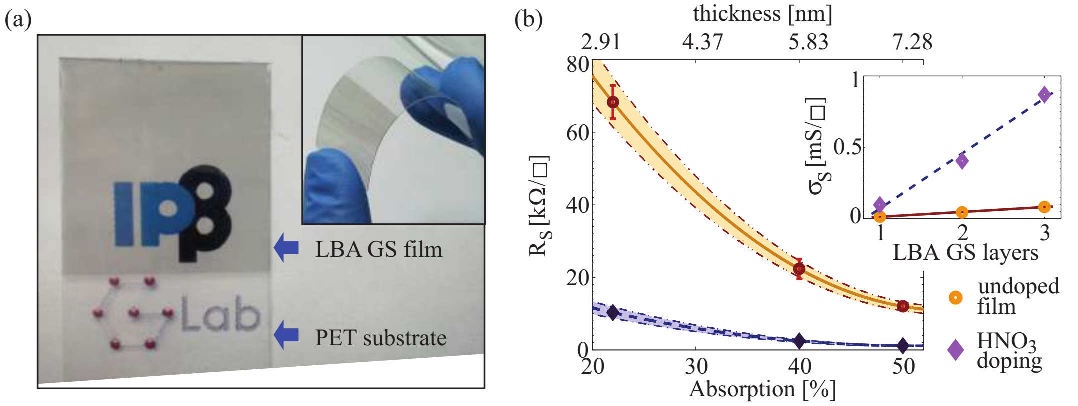

FIGURE 1. (a) 2×2 cm^2 LBA graphene sheet (GS) film on a polyethylene terephthalate (PET) substrate. (b) The sheet resistance (R_S) and sheet conductivity (σ_S) (inset) of stacked LBA GS layers, prior and after chemical doping.

PHYSICAL CHEMISTRY 2016

13th International Conference on Fundamental and Applied Aspects of Physical Chemistry

Proceedings
Volume II

B E L G R A D E
September 26-30, 2016

PHYSICAL CHEMISTRY 2016

13th International Conference on
Fundamental and Applied Aspects of
Physical Chemistry

Proceedings
Volume II

BELGRADE
September 26-30, 2016

ISBN 978-86-82475-33-0
Title: Physical Chemistry 2016 (Proceedings)
Editors: Željko Čupić and Slobodan Anić
Published by: Society of Physical Chemists of Serbia, Studentski trg 12-16,
11158, Belgrade, Serbia.
Publisher: Society of Physical Chemists of Serbia
For Publisher: Slobodan Anić, President of Society of Physical Chemists of Serbia
Printed by: "Jovan", Printing and Publishing Company; 200 Copies
Number of pages: 3+434; Format B5; printing finished in September 2016

Text and Layout: "Jovan"

200 - *Copy printing*

VARIATIONS IN LARCH TREE-RINGS METAL CONCENTRATIONS OF FOUR FORESTRY LOCATIONS

I. R. Milošević [1], D.M. Marković [2], D. Manojlović [3] and G. Roglić [3]

[1] *University of Belgrade, Institute of Physics, Pregrevica 118, 11070 Belgrade, Serbia. (novovic@ipb.ac.rs)*
[2] *Singidunum University, The Faculty of Applied Ecology, Požeška 83a, 11030 Belgrade, Serbia.*
[3] *University of Belgrade, Faculty of Chemistry, Studentski trg 12-16, 11000 Belgrade, Serbia.*

ABSTRACT

Cd, Fe, Mn, Pb, Sr and Zn were measured in larch (*Larix europaea* Lam.) tree-rings and corresponding soil samples collected at four forestry sites to investigate the variations in their concentrations from 1980. Concentrations were generally lowest at background sites. Elemental concentrations in soil samples were substantially higher than those measured in tree-rings. Among investigated elements the highest tree-ring concentration were measured for Mn while the Cd had the lowest concentration. The highest average tree-ring concentrations for Cd, Fe, Mn, Pb and Zn can be seen at the Avala location.

INTRODUCTION

The occurrence of trace elements in the environment is of particular concern due their environmental persistence, biogeochemical recycling and adverse effects. Several trace elements currently found in the environment are originated from anthropogenic impacts [1]. It has long been recognized that the tree-ring archive can capture changes in the chemical environment related to atmospheric chemistry, biogeochemical cycling and climate influences. Choosing tree-rings as potential bioindicators was due to trees large geographic distribution, long living and the fact that each year tree forms a new tree-ring that can be easily dated. Dendrochemistry relies on the basic assumption that the pollutant content of tree-rings reflects to some degree the chemical signal from the environment during the year of ring formation [2].

EXPERIMENTAL

The field studies were conducted in the three woodland locations in Serbia and one in Montenegro. Tree-rings of larch (*Larix europaea* Lam.) were collected together with corresponding soil (0-20 cm in depth). The first location is Avala (AA), a mountain located 16 km south-east of Belgrade. The Belgrade-Niš highway, Kruni put and regional road to Mladenovac runs east, north and west from the mountain. The second location is REIK Kolubara (AK). Larch at the Kolubara location has been applied for the rehabilitation by aforestation of the mechanically damaged land. Background locations were management unit Donji Pek in Kučevo (AKC) and village Trepča in Andrijevica municipality in the north-east part of Montenegro (ACG).

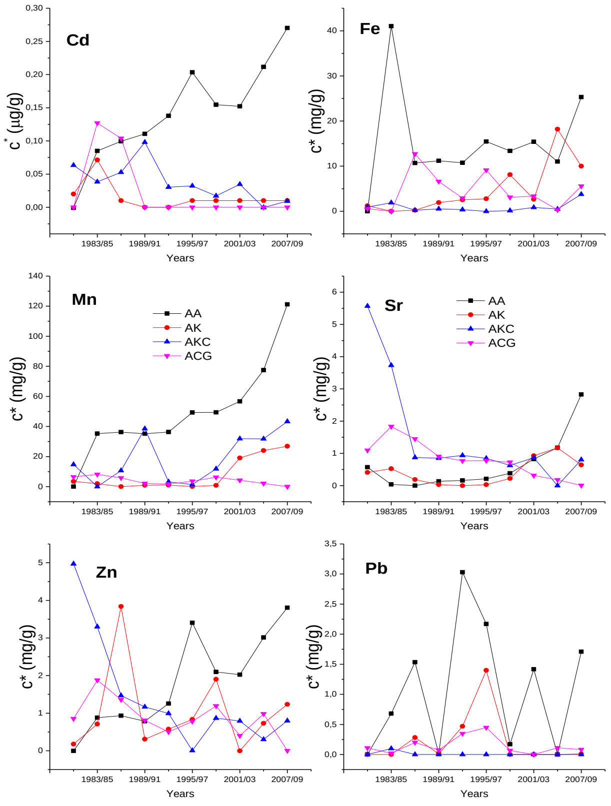

Figure 1. Mean Cd, Fe, Mn, Sr, Zn and Pb concentrations, c* (μg/g), in larch tree-rings at four forestry locations

At each site three larch trees of similar size were selected and their stem disks were taken at breast height (1.3 m). For further analysis the disks were cut into 3 year segments starting from 1980 with a stainless steel knife. Inductively coupled plasma atomic emission spectrometry (ICP-OES) was used to determine element content in solution samples. ICP-OES measurement was performed using Thermo Scientific iCAP 6500 Duo ICP spectrometer equipped with CID86 detector, standard glass concentric type nebulizer, quartz torch, and alumina injector and purged with argon. The digestion of tree-rings was performed on an Advanced Microwave Digestion System ETHOS 1, using HPR-1000/10S high pressure segmented rotor. In the digestion, about 0.5 g of powdered tree-ring sample precisely weighed was mixed in each clean vessel with a mixture of 3 ml H_2SO_4 and 5 ml HNO_3 for tree-ring sample and then heated with microwave energy for 30 min. After cooling and without filtration, the solution was diluted to a fixed volume of 25 ml. The sequential extraction using the Tessier procedure [3] was used for the examination of soil samples. The method involves five fractions (exchangeable, carbonate, Fe/Mn oxides, organic and residual), in which the mobility and bioavailability of elements decrease with increasing extraction phase. The extraction was carried out progressively based on an initial amount of about 1.0 g of soil, accurately weighed. The first three fractions form "mobile content", i.e. the part of the total concentration which under certain conditions can be mobilized and thus enter biogeochemical cycles. Soil pH was measured as follows: 5.0 g of soil was precisely weighed and 5ml of 1M KCl added. The suspension was then subjected to continuous agitation for 10 min and left to stand before pH was determined.

RESULTS AND DISCUSSION

Element concentrations measured in tree-rings and soil are summarized in Figure 1 and Table 1. The variation in tree-ring concentrations due to different local conditions (the variation of the background levels) was minimize by subtracting the minimum value from the actual concentration. Element tree-ring concentrations, c*, shown in Figure 1 do not refer to actual concentration in wood, but to the level of this content relative to the lowest level recorded for that tree. Subtracting the minimum value from the actual concentration reduces

Table 1. Average concentrations in larch tree-rings, mobile and total content in soil as well as pH values at four forestry locations.

Locations		AA	AK	AKC	ACG
Cd	Tree-ring	0.14	0.02	0.04	0.02
	Mobile content	0.36	<0.10	<0.10	<0.10
	Total content	0.46	0.23	0.94	0.90
Fe	Tree-ring	15.42	4.77	0.92	4.42
	Mobile content	1243	496	12409	10117
	Total content	8176	6723	66835	54436
Mn	Tree-ring	49.73	7.83	18.74	4.06
	Mobile content	603	141	1246	1607
	Total content	662	191	1949	1897
Pb	Tree-ring	1.07	0.22	0.01	0.15
	Mobile content	7.21	5.55	33.76	38.06
	Total content	16.50	13.04	51.14	55.53
Sr	Tree-ring	0.63	0.41	1.51	0.80
	Mobile content	15.59	7.33	16.38	30.00
	Total content	18.90	10.04	52.93	46.75
Zn	Tree-ring	1.82	1.03	1.47	0.88
	Mobile content	11.30	3.97	45.54	30.71
	Total content	33.35	23.08	147.58	151.11
	pH	5.80	6.00	4.50	5.30

differences between trees that are due to different local conditions, and concentrate on the trends over time. From Figure 1 it can be seen that concentrations were generally lowest at background sites. The highest average tree-ring concentrations for Cd, Fe, Mn, Pb and Zn (Table 1) can be seen at the Avala location. Among investigated elements the highest tree-ring concentration were measured for Mn while the Cd had the lowest concentration. Highest Pb concentration fluctuations in tree-rings can be seen at the Avala location. Similar Pb fluctuations were observed in our investigation in linden tree-rings [4]. Expected trends in tree-ring concentrations for the majority of trace elements is that on locations where anthropogenic influence is low there is no trend [5-6]. At the Avala location growing trend of Cd, Mn, Zn and Sr was observed while at other locations, depending of the element, the weaker trend or a decline in the concentration can be seen. Elemental concentrations in soil samples (Table 1) were substantially higher than those measured in tree-rings. This could be attributed to the relatively longer exposure of the soil to the atmospheric pollutants. Soil act as final sink for the elements deposited from air and also transferred by falling needles. Mobile content, relative to the total content, is for the majority of investigated elements highest at the Avala location.

CONCLUSION

At the Avala location during the last 12 years (1998-2009) the increase of Cd, Fe, Mn, Sr and Zn in larch tree-rings, relative to the entire period of study, expressed in percentage is 30%, 4%, 43%, 85% i 40%. At this location the highest fluctuations in Pb concentration can be seen, the highest average Pb tree-ring concentrations, as well as decrease in Pb concentration for 18%. Traffic activity at this site appears to be the main reason. Other investigated location has lower tree-ring trace element concentrations.

Acknowledgement

This work was partially supported by the Ministry of Education and Science of the Republic of Serbia (Grants no. III 43007 and OI 171005).

REFERENCES

[1] G. Blackmore, Science of the Total Environment, 1998, **214**, 21-48.

[2] H.C. MacDonald, C.P. Laroque, D. E. B. Fleming, M. R. Gherase, Dendrochronologia, 2011, **29**, 9-15.

[3] A. Tessier, P.G.C. Campbell, M. Bisson, Analytical Chemistry, 1979, **51**, 844-851.

[4] D.M. Marković, I.R. Milošević, D. Vilotić, 2013, Environmental Science and Pollution Research, **20**, 136-145.

[5] S.A. Watmough, 1999, Environmental Pollution, **106**, 391-403.

[6] C. Liang, H. Huang, 1992, Trees, **6**, 103-108.

Book of abstracts

PHOTONICA2019

The Seventh International School and Conference on Photonics, 26 August – 30 August 2019, Belgrade, Serbia

& Machine Learning with Photonics Symposium (ML-Photonica 2019)

AiPT MULTIPLY CARDIALLY FONTE

& ESUO Regional Workshop

ESUO
EUROPEAN
SYNCHROTRON
AND FEL USER
ORGANISATION

& COST action CA16221

AtomQT cost

Editors: Milica Matijević, Marko Krstić and Petra Beličev

Belgrade, 2019

ABSTRACTS OF TUTORIAL, KEYNOTE, INVITED LECTURES, PROGRESS REPORTS AND CONTRIBUTED PAPERS

of

The Seventh International School and Conference on Photonics
PHOTONICA2019, 26 August – 30 August 2019, Belgrade, Serbia

and
Machine Learning with Photonics Symposium

and
ESUO Regional Workshop

Editors
Milica Matijević, Marko Krstić and Petra Beličev

Technical Assistance
Danka Stojanović and Goran Gligorić

Publisher
Vinča Institute of Nuclear Sciences
Mike Petrovića Alasa 12-14, P.O. Box 522
11000 Belgrade, Serbia

Printed by
Serbian Academy of Sciences and Arts

Number of copies
300

ISBN 978-86-7306-153-5

PHOTONICA2019 (The Seventh International School and Conference on Photonica- www.photonica.ac.rs) is organized by Vinča Institute of Nuclear Sciences, University of Belgrade (www.vinca.ac.rs), Serbian Academy of Sciences and Arts (www.sanu.ac.rs), and Optical Society of Serbia (www.ods.org.rs).

Institute of Nuclear Sciences Vinča

Serbian Academy of Sciences and Arts

Optical Society of Serbia

Other institutions that helped the organization of this event are: Institute of Physics Belgrade, University of Belgrade (www.ipb.ac.rs), School of Electrical Engineering, University of Belgrade (www.etf.bg.ac.rs), Institute of Chemistry, Technology and Metallurgy, University of Belgrade (www.ihtm.bg.ac.rs), Faculty of Technical Sciences, University of Novi Sad (www.ftn.uns.ac.rs), Faculty of Physics, University of Belgrade (www.ff.bg.ac.rs), and Faculty of Biology, University of Belgrade (www.bio.bg.ac.rs). Joint event "Machine learning with Photonics Symposium" has been co-organized with programme partners H2020-RISE-CARDIALLY, H2020 – MULTIPLY and H2020-EID-FONTE.

PHOTONICA2019 is organized under auspices and with support of the Ministry of Education, Science and Technological Development, Republic of Serbia (www.mpn.gov.rs). PHOTONICA2019 is supported and recognized by OSA - The Optical Society (www.osa.org), Integrated Initiative of European Laser Research Infrastructures Laser Lab-Europe (www.laserlab-europe.eu) and European Physical Society (www.eps.org).

Ministry of Education, Science and Technological Development of the Republic of Serbia

The support of the sponsors of PHOTONICA2019 is gratefully acknowledged:

Self-organization of soliton-tweezers in suspensions of nanocomposites and graphens

M. Lekić[1], I. Milosević[1] , S. Rokotoarimalala[2] and V. Skarka[1,2,3]
[1]*Institute of Physics, University of Belgrade, Pregrevica 118, Belgrade, Serbia*
[2]*Laboratoire de Photonique d'Angers, EA 4464, University of Angers,*
2 Boulevard Lavoisier, 49045 Angers, France
[3]*Science Program, Texas A&M University at Qatar, P.O. Box 23874, Doha, Qatar*
e-mail: lekic@ipb.ac.rs

Laser beams and pulses are powerful tools for tweezing, photobiomodulation, and manipulation of soft matter including colloidal nanosuspensions, emulsions, foams, as well as all kinds of biomedia like myosin, kinesin, ribosomes, liposomes, bacterias, viruses, blood, and a variety of living cells in body water [1]. The laser modifies the nonlinear mater passing through. Simultaneously, the modified mater acts to the light altering it by a feedback mechanism. Therefore, light is controlled by light through interaction with nonlinear mater. Laser stability and precision are of crucial importance not only for brain surgery but also for nondestructive diagnostics using this feedback mechanism. In order to achieve the necessary dynamical stability, the promising mechanism is the self-structuring of the light into localized solitons via nonlinear interaction inside the colloidal nanosuspensions and other varieties of soft matter. Tweezing solitons stable propagation is self-organized by the balance of antagonist effects, *i.e.*, beam self-focusing and self-defocusing [2]. The high frequency pressure force of the laser field either attracts or repels the nanoparticles from the field region, depending if their optical index of refraction is larger or smaller than the background one [3]. In both cases, the nanoparticles density modification results in the nonlinear increase of effective index of refraction inside the beam making it self-focusing. We use this self-focusing effect to establish theoretically, numerically and experimentally the self-organization of soliton-tweezers as a novel kind of dynamically reconfigurable self-collimated tweezing facilities. Such soliton-tweezers will be able to photobiomodulate and manipulate, in a noninvasive way, micro and nanoparticles in body water and other soft mater of interest for medical and biological applications. Based on the synergy between theory and experiment via numerical simulations, other nanocomposites and colloidal nanosuspensions involving graphene and various two-dimensional materials will be tweezed using spatiotemporal dissipative solitons and multidimensional vortex solitons [4, 5].

REFERENCES

[1] A. Ashkin, J. M. Dziedzic, T. Yamane, Nature 330, 769 (1987).
[2] V. Skarka, N. B. Aleksic, Phys. Rev. Lett. 96, 013903 (2006).
[3] V. Skarka et al., Opt. Express 25, 10090 (2017).
[4] V. Skarka et al., Opt. Quant. Electron. 50, 37 (2018).
[5] V. Skarka et al., Phys. Rev. A 90, 023845 (2014).

Chemical doping of Langmuir-Blodgett assembled few-layer graphene films with Au and Li salts aimed for optoelectronic applications

I. R. Milošević[1], B. Vasić[1], A. Matković[2], J. Vujin[1], S. Aškrabić[3], C. Teichert[2] and R. Gajić[1]
[1] *Laboratory for Graphene, other 2D materials and Ordered Nanostructures of Center for Solid State Physics and New Materials, Institute of Physics, University of Belgrade, Belgrade, Serbia*
[2]*Institute of Physics, Montanuniversität Leoben, Leoben, Austria*
[3]*Nanostructured Matter Laboratory of Center for Solid State Physics and New Materials, Institute of Physics, University of Belgrade, Belgrade, Serbia*
e-mail: novovic@ipb.ac.rs

For mass production of graphene, simple and low-cost methods are needed especially in the cases where high-quality films are not crucial for the desired purposes. Thus, liquid-phase exfoliation (LPE) is a perspective way of obtaining stable dispersion of few-layer graphene sheets (GS) in the solvent [1]. A promising pathway to achieve high degree of ordering of graphene sheets prepared via LPE-process is to utilize Langmuir-Blodgett assembly (LBA) technique. Thin-films are self-assembled from LPE dispersion by LBA technique at the water-air interface. LBA method is a suitable method for production of large-scale, transparent, thin solution-processed graphene films [2, 3]. Chemical doping of graphene films allows to tune its work function (WF) and therefore gives LPE GS films the ability to serve two different roles in electronic and optoelectronic applications, both as an anode and as a cathode.

Here, we demonstrate the method for the forming and doping of LPE graphene sheet films (LPE GS) in one-step by metal standard solutions. Doping of the graphene film occurs at the moment of its formation from the LPE graphene dispersion by LBA method at the air-metal standard solution interface. n-doping is achieved by Li standard solutions (LiCl, $LiNO_3$, Li_2CO_3), while Au standard solution ($H(AuCl_4)$) leads to p-doping. WF of the film was decreased with Li based salts, while Au based salts increase the WF of the film. The maximal doping in both directions allow a significant range of around 0.7 eV for the WF modulation. The results were obtained for 0.1 mol/dm^3 concentration of dopants. Roughness of the LPE GS films does not change by the doping, except that doped films contain occasional agglomerates. FT-IR measurements point out that the charge transfer process is enabled by physical adsorption of the metal salts and that the graphene basal planes stay chemically unchanged by metal doping. No significant shifts of any characteristic Raman peaks of graphene were detected after chemical doping. Calculated values of the intensity ratio between D and D' peak indicate that the edges are the dominant type of defects in the undoped and metal salt doped LPE GS films. Electrical properties of the films were significantly influenced by changing the dopant (Au or Li). A significant suppression of the field-effect mobility and the increase of the sheet resistivity were observed in the case of the Li standard solution doping of the film. This indicates that adsorbed Li anions act as scattering centers for the charges. Lithium nitrate provides the largest work function modulation (by 400 meV) and the least influence on the sheet resistance of the film. Therefore, it was selected as the best choice for n-type doping.

Since, the proposed one-step method for chemical doping of graphene films allows to tune WF in a large range, it extends the potential use of these materials in low-cost optoelectronic applications, as in low-power lighting, sensors, transparent heating, and de-icing applications.

REFERENCES

[1] C. Backes et al., Chem. Mater. 29, 243 (2017).
[2] Q. Zheng et al., ACS Nano. 5, 6039 (2011).
[3] A. Matković et al., 2D Mater. 3, 015002 (2016).

7-11th October 2019
Belgrade, Serbia

http://www.sfkm.ac.rs/

The 20th Symposium on Condensed Matter Physics

BOOK OF ABSTRACTS

University of Belgrade,
Faculty of Physics

Institute of Physics Belgrade

Vinca Institute
of Nuclear Sciences

Serbian Academy
of Sciences and Arts

Ministry of Education, Science and
Technological Development,
Republic of Serbia

Conference Chair

Cedomir Petrovic, *Brookhaven National Laboratory, USA*

Željko Šljivančanin, *Vinča Institute of Nuclear Sciences Serbia*

Organizing Committee

Jelena Pešić, *Institute of Physics Belgrade*
Andrijana Šolajić, *Institute of Physics Belgrade*
Petar Mali, *Faculty of Sciences, University of Novi Sad*
Jelena Pajović, *Faculty of Physics, University of Belgrade, Serbia*
Srđan Stavrić, *Vinča Institute of Nuclear Sciences*
Svetislav Mijatović, *Faculty of Physics, University of Belgrade, Serbia*
Božidar Nikolić, *Faculty of Physics, University of Belgrade, Serbia* – chair

Organized by

Institute of Physics Belgrade

Faculty of Physics, University of Belgrade

Vinča Institute of Nuclear Sciences

Serbian Academy of Sciences and Arts

Program Committee

Ivan Božović, *Brookhaven National Laboratory, USA*
Vladimir Dobrosavljević, *Florida State University, USA*
Milan Damnjanović, *Faculty of Physics, University of Belgrade, Serbia*
Vladimir Djoković, *Vinča Institute, University of Belgrade, Serbia*
Gyula Eres, *Oak Ridge National Laboratory, USA*
Laszló Forró, *Ecole Polytechnique Fédérale de Lausanne, Switzerland*
Radoš Gajić, *Institute of Physics Belgrade, University of Belgrade, Serbia*
Igor Herbut, *Simon Fraser University, Canada*
Zoran Ikonić, *University of Leeds, UK*
Ivanka Milošević, *Faculty of Physics, University of Belgrade, Serbia*
Branislav Nikolić, *University of Delaware, USA*
Cedomir Petrovic, *Brookhaven National Laboratory, USA*
Dragana Popović, *National High Magnetic Field Laboratory USA*
Zoran S. Popović, *Vinča Institute, University of Belgrade, Serbia*
Zoran V. Popović, *Institute of Physics, University of Belgrade, Serbia*
Zoran Radović, *Faculty of Physics, University of Belgrade, Serbia*
Miljko Satarić, *Faculty of Technical Sciences, University of Novi Sad, Serbia*
Vojislav Stamenković, *Argonne National Laboratory, USA*
Željko Šljivančanin, *Vinča Institute, University of Belgrade, Serbia*
Bosiljka Tadić, *Jožef Štefan Institute, Slovenia*
Milan Tadić, *School of Electrical Engineering, University of Belgrade, Serbia*
Darko Tanasković, *Institute of Physics, University of Belgrade, Serbia*

XX SYMPOSIUM ON CONDENSED MATTER PHYSICS SFKM 2019

Conference presentations cover full range of research topics within the experimental, theoretical and computational condensed matter physics, including but not limited to the following:

Semiconductor physics. Electronic structure, Quantum dots and wires, Photonic crystals, High magnetic fields phenomena, Ultra-fast phenomena.

Surface, interface and low-dimensional physics. Graphene, Carbon and other nanotubes, Topological insulators, Complex oxide interfaces, Transport in nanostructures.

Magnetism. Magnetic materials and phase transitions, Magneto-electronics and spintronics, Magnetic nanoparticles.

Superconductivity. Conventional, high Tc, and heavy-fermion superconductors: Materials and mechanisms, Heterostructures: Proximity effect and transport phenomena.

Strongly correlated and disordered systems. Materials with strong correlations and disorder, Dynamical properties from time-resolved experiments, Quantum fluids, Cold atoms and BEC.

Phase transitions, phase ordering and structural ordering of condensed matter. Equilibrium and dynamic phenomena, Ferroelectricity, Multiferroics, Quasi-Crystals, Crystal surface morphology and dynamics, Crystal growth.

Soft and biological matter. Polymers, Liquids and gels, Liquid crystals, Elastomers, Membranes, Living cells and living matter.

Statistical physics of complex systems. Networks and other structures.

Conference venue:
Serbian Academy of Sciences and Arts, Knez Mihailova 35, Belgrade

Conference website: http://www.sfkm.ac.rs

LIST OF INVITED SPEAKERS

- Marco Aprili, PS-CNRS Université Paris-Sud, France
- Stefano Baroni, Scuola Internazionale Superiore di Studi Avanzati, Italy
- Wolfgang Belzig, University of Konstanz, Germany
- Emil Božin, Brookhaven National Laboratory, USA
- Harald Brune, Ecole Polytechnique Fédérale de Lausanne, Switzerland
- Liviu Chioncel, University of Augsburg, Germany
- Gyula Eres, Oak Ridge National Laboratory, USA
- Laszlo Forro, Ecole Polytechnique Fédérale de Lausanne, Switzerland
- Rudolf Gross, Walther Meissner Institute, Germany
- Rudi Hackl, Walther Meissner Institute, Germany,
- Igor Herbut, Simon Fraser University, Canada
- Kurt Hingerl, Johannes Kepler University, Linz, Austria
- Liv Hornekaer, Aarhus University, Denmark
- Zoran Ikonić, Univsity of Leeds, UK
- Vladimir Juričić, Nordita, KTH Royal Institute of Technology and Stockholm University, Sweden
- Milos Knezevic, Berlin Institute of Technology, Germany
- Hechang Lei, Renmin University
- Marjana Ležaić, Forschungszentrum J**ü**lich, Germany
- Zoran Mišković, University of Waterloo, Canada
- Francois Peeters, University of Antwerp, Belgium
- Axel Pelster, Technical University of Kaiserslautern, Germany
- Maria Peressi, University of Trieste, Italy
- Cedomir Petrovic, Brookhaven National Laboratory, USA
- Hyejin Ryu, Korea Institute of Science and Technology
- Milan Radović, Paul Scherrer Institute, Switzerland
- Nicolas Regnault, Ecole Normale Supérieure Paris, France
- Rastko Sknepnek, University of Dundee, UK
- Frank Steglich, MPICPfS Dresden and Zhejiang University
- Bosiljka Tadić, Jožef Štefan Institute, Slovenia
- Jack Tuszynski, University of Alberta, Canada
- Dieter Vollhardt, University of Augsburg, Germany
- Rok Zitko, Jožef Štefan Institute, Slovenia
- Qingming Zhang, Lanzhou University and Institute of Physics, Chinese Academy of Sciences

Liquid-phase Exfoliation of Graphene and Chemical Doping of Langmuir-Blodgett Assembled Graphene Films

Ivana R. Milošević[a], Borislav Vasić[a], Aleksandar Matković[b], Jasna Vujin[a] and Radoš Gajić[a]

[a]*Laboratory for Graphene, Other 2D Materials and Ordered Nanostructures of Center for Solid State Physics and New Materials, Institute of Physics, University of Belgrade, Serbia*
[b]*Institute of Physics, Montanuniversität Leoben, Austria*

Abstract. In current optoelectronic devices transparent conductive (TC) electrodes are widely used [1]. Graphene films as new TC material can be used to overcome shortcomings of the exited TC electrodes especially using graphene films as an active electrode. They offer advantages such as higher transparency over a broad range of light wavelengths, higher flexibility, excellent electrical conductivity and chemical stability. Using graphene films as an active electrode, band-structure alignment at the interface can be achieved with an appropriate work function (WF). Therefore, appropriate WF can enhance the charge injection and improve device performances. Chemical doping is an effective method for tuning of the WF by charge transfer between the graphene sheet films and dopants [2, 3]. Liquid-phase exfoliation (LPE) via sonication was the method for the preparation of graphene sheet (GS) dispersion. The films were self-assembled from LPE few-layer GS dispersion by Langmuir-Blodgett (LBA) technique at the water-air interface. Chemical doping of the films was performed in two ways. In the first approach, chemical doping with nitric acid is introduced after the film was formed. Fivefold improvement of sheet conductivity was achieved, with no change in transparency [4]. In the second approach, chemical doping of the film was happening at the moment of its formation. To achieve doping, metal standard solutions were introduced instead of water. Au based salts increase the WF of the films (p-doping), while Li based salts decrease it (n-doping). A span of 0.7 eV in both directions was obtained. Formation of the graphene films and both procedures of their chemical doping are very simple, low-cost and extend their potential use in low-cost optoelectronic applications as well as using them as an active electrode.

REFERENCES

1. Syu, J-Y., Chen, Y-M., Xu, K-X., He, S-M., Hung, W-C., Chang, C-L. and Su, C-Y., *RSC Adv.* **6**, 32746-32756 (2016).
2. Park, J., Lee, W. H., Huh, S., Sim, S. H., Bin Kim, S., Cho, K., Hong, B. H. and Kim, K. S., *J. Phys. Chem. Lett.* **2**, 841-845 (2011).
3. Kwon, K. C., Choi, K. S., Kim, B. J., Lee, J. L., and Kim, S. Y., *J. Phys. Chem. C.* **118**, 8187-8193 (2014).
4. Matković, A., Milošević, I., Milićević, M., Tomašević-Ilić, T., Pešić, J., Musić, et al. *2D Mater.* **3**, 015002 (2016).

PHYSICAL CHEMISTRY 2021

15th International Conference
on Fundamental and Applied Aspects of
Physical Chemistry

Proceedings
Volume II

September 20-24, 2021
Belgrade, Serbia

PHYSICAL CHEMISTRY 2021

15th International Conference
on Fundamental and Applied Aspects of
Physical Chemistry

Proceedings
Volume II

The Conference is dedicated to the

30th Anniversary of the founding of the Society of Physical Chemists of Serbia

and

100th Anniversary of Bray-Liebhafsky reaction

September 20-24, 2021
Belgrade, Serbia

Title: Physical Chemistry 2021 (Proceedings) **ISBN** 978-86-82475-40-8
Volume II: ISBN 978-86-82475-39-2
Editors: Željko Čupić and Slobodan Anić
Published by: Society of Physical Chemists of Serbia, Studentski Trg 12-16, 11158, Belgrade, Serbia
Publisher: Society of Physical Chemists of Serbia
For Publisher: S. Anić, President of Society of Physical Chemists of Serbia
Printed by: ″Jovan″, <Printing and Publishing Company, 200 Copies
Number of pages: 6+388, Format A4, printing finished in December 2021

Text and Layout: ″Jovan″

200 - *Copy printing*

CHEMICAL DOPING OF LANGMUIR-BLODGETT ASSEMBLED FEW-LAYER GRAPHENE FILMS WITH Li AND Au SALTS

I.R. Milošević [1], B. Vasić [1], A. Matković [2], J.Vujin [1]

[1] *University of Belgrade, Institute of Physics Belgrade, Laboratory for 2D materials of Center for Solid State Physics and New Materials, Pregrevica 118, 11080 Belgrade, Serbia.*
(novovic@ipb.ac.rs)
[2] *Institute of Physics, Montanuniversität Leoben, Austria*

ABSTRACT

To implement large-area solution-processed graphene films in low-cost transparent conductor applications, it is necessary to have control over the work function (WF) of the film. In this study we demonstrate a straightforward single-step chemical approach for modulating the WF of graphene films with Li and Au salts. Li-based salts decrease the work function, while Au-based salts increase the work function of the entire film. As a result, this method allowed to tune the WF of graphene electrodes in a range of 0.7 eV.

INTRODUCTION

Graphene has been identified as a promising material in electronics, especially as an electrode with the appropriate work function (WF). It can have two different roles as an electrode (as an anode and a cathode). The chemical vapor deposition (CVD) method has become the most common method for the production of large-area graphene films [1]. Still, simple and low-cost methods are needed for mass production. Liquid-phase exfoliation (LPE) is a promising way of obtaining large quantities of few-layer graphene sheets (GSs) in the solvent. In order to convert the dispersed GS into graphene thin films, the Langmuir-Blodgett assembly (LBA) technique could be used. Based on surface-tension induced self-assembly of nanoplatelets at the liquid-air interface or the interface of two liquids, LBA is a simple method for the production of large-scale, highly transparent, thin solution-processed graphene films [2-3].

To achieve the desired performance of the devices, tuning the electrodes' WF is very important. By modulating the WF, band-structure alignment at the interface can enhance the efficiency of carrier transport and lower contact resistance, thus improving the performance of the devices [4]. Chemical doping represents the effective method for tunning the WF by charge transfer between the GS films and dopants [5].

METHODS

Fabrication and doping of LPE GS films: GS dispersion was prepared from graphite powder of initial concentration 18 mg/mL and solvent (N-methyl-2-pyrrolidone, NMP). The solution was sonicated in a low-power ultrasonic bath for 14 h. The resulting dispersion was centrifuged for 60 min at 3000 rpm immediately after the sonication. Stock standard solutions used for n-doping are 1 mg/mL LiCl, $LiNO_3$ and Li_2CO_3 and for p-doping is the gold standard solution-$H(AuCl_4)$. By appropriate dilution of the stock solution with deionized water we obtained 0.1 mg/mL metal water solution which is then used in the doping process.

GS dispersion in NMP was used to fabricate transparent and conductive films by the LBA technique at a water-air interface [6]. A small amount of GS dispersion was added to the water-air interface and after the film was formed it was slowly scooped onto the target substrate (Figure 1). Applying the same process of fabricating the GS films and using the appropriate metal standard solution instead of water, chemical doping was achieved (Figure 1). For WF measurements SiO_2/Si wafer were used, as substrates.

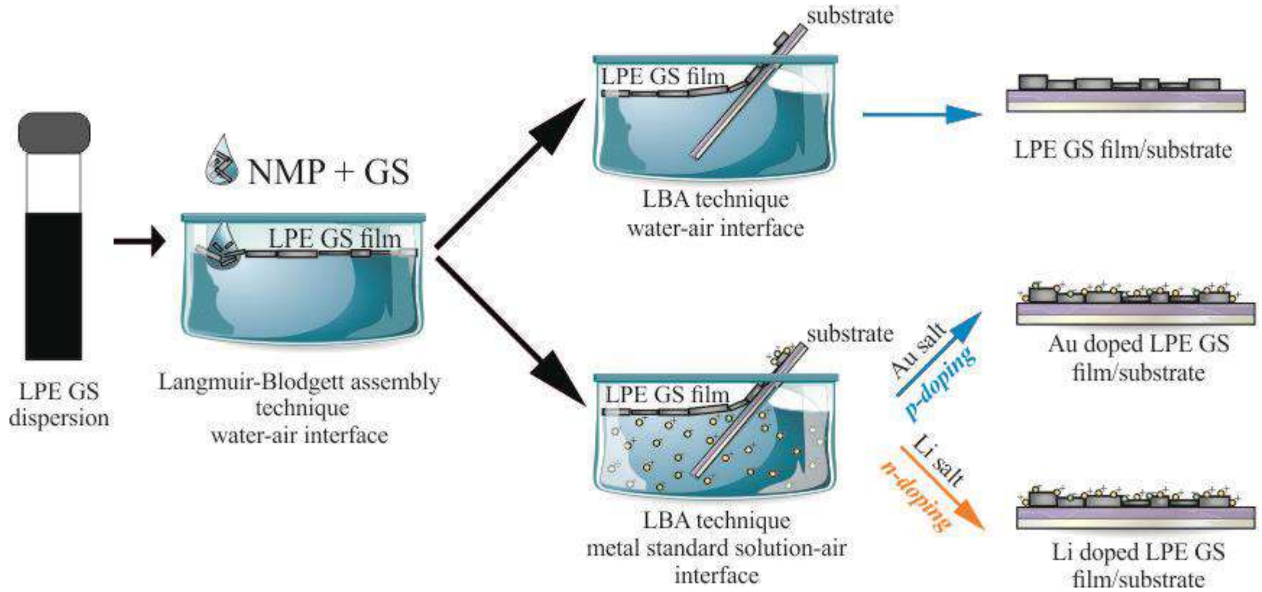

Figure 1. Schematic representation of the LPE GS film formation and its doping in the single-step process

WF measurements for undoped and doped LPE GS films: Kelvin probe force microscopy (KPFM), was employed in order to characterize changes in the electrical surface potential and corresponding Fermi level shifts due to doping. For this purpose, we measured the contact potential difference (CPD) between the AFM tip and the sample surface by using Pt covered NSG01/Pt probes with a typical tip curvature radius of 35 nm. For all samples, the CPD was measured on five 5x5 μm^2 areas, and then averaged. The CPD is equal to the work function difference between AFM tip (WF_t) and sample (WF_s), $CPD=WF_t-WF_s$. The calibration of the WF_t was done by a standard procedure consisting of KPFM measurements on a freshly cleaved HOPG with a well-known work function of 4.6 eV [7]. The absolute value of the WF was calculated as $WF_s = WF_t - CPD$, where CPD is measured by KPFM for all, undoped and doped LPE GS films and presented in Figure 2.

RESULTS AND DISCUSSION

Results for the values of the absolute WF are summarized in Figure 2. As can be seen, n-doping of graphene films is achieved by Li-based salts, whereas Au-based salt leads to p-doping.

According to Figure 2 (a), the maximal doping in both directions is similar, around 0.3-0.4 eV, finally providing a significant range of around 0.7 eV for the work function modulation of LPE GS films. The reported shift of the Fermi level is very similar to the other (comparable) systems in the literature. Compared with literature data of WF values changes [8] the same effect can be achieved, but advantages of our approach are fast and simple solution-based method for one-step fabrication and WF control of large-area graphene films.

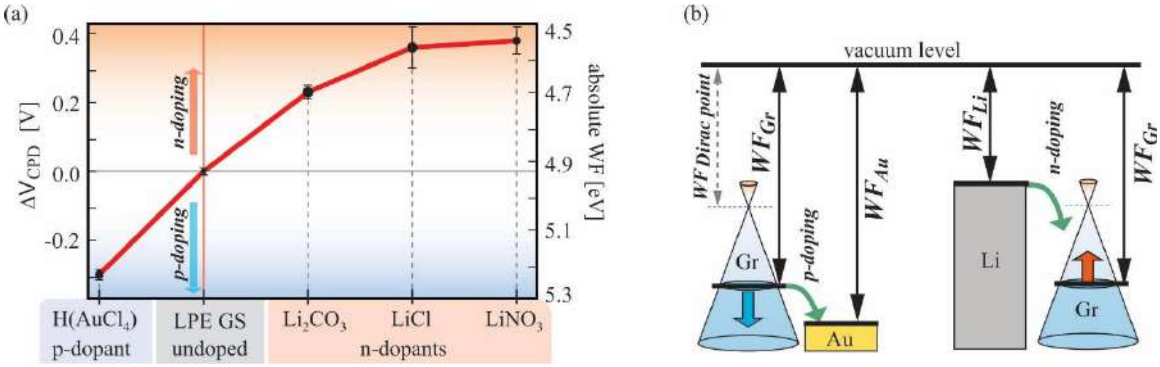

Figure 2. (**a**) Change in WF for doped LPE GS films for different dopants, in comparison to the undoped LPE GS film. (**b**) Schematic representation of the WF prior to the interaction (equal vacuum levels) for Au-based salt/graphene and Li-based salt/graphene.

The change of the WF due to the doping can be explained according to the schematic presentation in Figure 2 (b), illustrating Li (Au) as a lower (higher) work function material compared to GS films. Therefore, presence of Li-based salts results in a reduction of the WF of the entire film. This behavior can be interpreted as an increase in the Fermi level of GSs – compared to the value for the undoped films – indicating predominantly a charge transfer from Li-based salts to graphene (n-doping), as expected when considering that Li has lower WF than graphene (graphite). In contrast, the Au-based salt indicates charge transfer from graphene to Au-based salt and a relative reduction of the Fermi level in GSs (p-doping). It is also worth mentioning that the poly-crystalline nature of LPE based GS films, large amount of sheet edges and presence of the residual solvent (NMP) results in p-doped films [4]. Therefore, WF values are lower for the LPE-based films by at least 200 meV, than for the pristine exfoliated single-crystals [7]. p-type doping is also reflected on the WF of the reference samples (undoped LPE GS), and therefore on the whole accessible range for the WF modulation by this method. This was also highlighted in Figure 2 (b), where the $WF_{Dirac\ point}$ depicts the case of undoped graphene [7]

CONCLUSION

In our approach, we demonstrate a straightforward single-step method for forming and doping LPE GS films by metal standard solutions through charge transfer processes. Chemical doping of graphene allows to modulate its WF in a very large range (0.7 eV), and therefore potentially enables to use the same electrode material for both, the injection and the extraction of the electrons. Furthermore, solution-processed graphene films are in particular suited for the chemical modulations, since a large number of the sheet edges opens up many adsorption sites and enhances the doping effects when compared to many other types of graphene. Lithium nitrate (LiNO3) was selected as the best choice for n-type doping since it provides the largest WF modulation (by 400 meV).

Acknowledgement

The authors acknowledge funding provided by the Institute of Physics Belgrade, through the grant by the Ministry of Education, Science, and Technological Development of the Republic of Serbia.

REFERENCES

[1] Kwon, K.C. et al., J. Mater. Chem. C, 2013, **1**, 253–259.
[2] Li, X. et al., Nat. Nanotechnol. **3**, 538–542 (2008).
[3] Zheng, Q. et al., ACS Nano, 2011, **5**, 6039–6051.
[4] Syu, J.-Y., RSC Adv., 2016, **6**, 32746-32756.
[5] Milošević, I.R. et al., Sci. Report., 2020, **10:8476**, 1-12.
[6] Matković, A. et al., 2D Mater., 2016, **3**, 015002.
[7] Yu, Y. et al., Nano Lett., 2009, **9**, 3430–3434.
[8] Kwon, K. C., J. Phys. Chem. C, 2014, **118**, 8187–8193.

UPTAKE AND ACCUMULATION OF Pb AND Ni IN SPRUCE AND DOUGLAS-FIR TREE-RINGS AND BARK

I.R. Milošević [1], S. Živković [2], M. Momčilović [2], Ž. Višnjić-Jeftić [3], M. Veselinović [4], I. D. Marković [5] and D. M. Marković [1]

[1] *University of Belgrade, Institute of Physics Belgrade, Laboratory for 2D materials of Center for Solid State Physics and New Materials, Pregrevica 118, 11080 Belgrade, Serbia. (novovic@ipb.ac.rs)*
[2] *University of Belgrade, Institute of Nuclear Sciences Vinča, Mike Petrovića Alasa 12-14, 11351 Belgrade, Serbia.*
[3] *Institute for Multidisciplinary Research, University of Belgrade, Kneza Višeslava 1, 11090 Belgrade, Serbia.*
[4] *Institute of Forestry, Kneza Višeslava 3, 11090 Belgrade, Serbia.*
[5] *Worldwild Clinical Trials, Omladinskih brigada 90b, 11070 Belgrade, Serbia.*

ABSTRACT

Modern development and increasing urbanisation, have production of a wide range of different pollutants, as a side effect. Trees in particular are emerging as an active factor receiving pollution. In a two-year study, we exposed spruce (*Picea abies* Karst.) and Douglas-fir (*Pseudotsuga menziesii* Mirb.) seedlings to elevated concentrations of Pb and Ni by adding these elements in the soil. Their concentrations as well as Mn and Zn concentrations in soil, tree-rings and bark were determined with Inductively Coupled Plasma- Optical Emission Spectrometry (ICP-OES). Analyses showed an increase of Pb and Ni in examined plant parts (tree-rings and bark) for both tree species, especially for Douglas-fir tree-ring.

INTRODUCTION

Among different types of pollutants, heavy metals are the most significant ones, because they are very toxic even at very low concentrations and could not be degraded naturally. Higher plants have emerged as a valuable tool enabling information about environmental pollution and different parts of trees have been used to monitor heavy metal contamination in the environment e.g. leaves/needles, bark, and tree-rings [1-4]. The bioavailability of metals for plants is controlled by plant's requests for micronutrients and their capacity to absorb and eliminate toxic elements. Generally, it is expected that the uptake increases, as the concentration of the metal ions in the external solution increases. The influence of heavy metals on the accumulation in tree-rings and bark is an area that is faintly investigated, especially in the form of a field experiment.

METHODS

The field experiment was conducted in Livada 1 Street in Kaluđerica, Belgrade, Serbia. The seedlings of spruce (*Picea abies* L.) and Douglas-fir (*Pseudotsuga menziesii* Mirb.), 5 years old, were obtained from the Institute of Forestry in Belgrade. They were planted in May 2017 and were arranged in six groups containing four seedlings in each group with a 1m distance. From January to May seedlings of spruce and Douglas-fir were watered (five times in total) with Pb and Ni in parallel experiments (I experiment- 2 g/L of Pb, 0.5 g/L of Ni and II experiment- 1 g/L of Pb, 0.25 g/L of Ni. Metal solutions were prepared from their nitrate salts and tap water was used for the metal solution preparation.). The third group of seedlings was taken as a control group. Spruce and Douglas-fir seedlings were cut in May 2019. Bark was taken as a separate sample. Soil samples were collected from the base of each tree at 0-20 cm depth. Tree disk, bark and soil were digested using an Advanced Microwave Digestion

System (ETHOS 1, Milestone, Italy). Also, the pH of the soil was determined. The content of elements (Pb, Ni, Mn and Zn) in each sample, prepared as diluted aqueous solutions, has been determined by using a Thermo Scientific iCAP 7400duo Series instrument for ICP-OES.

In order to simplify the display of the results, spruce sampled at this location for the first experiment will have the abbreviated name ’SI’ and Douglas-fir ’DI’, for the second experiment ’SII’ and ’DII’ and in the case of control ’SC’ and ’DC’, respectively.

RESULTS AND DISCUSSION

Mean Pb and Ni concentrations in soil, tree-rings and bark of spruce and Douglas-fir seedlings treated by metal solutions, were presented in Table 1. Also, mean Mn and Zn concentrations in plant parts and soil can be seen, as well as pH of the corresponding soil. Mn and Zn were examined because they are, among other elements, essential for higher plants and have several functions in plants. They weren’t externally added in this field experiment

Pb concentration: From Figure 1, it can be seen that the Pb content in the soil increases. Compared to the control sample, the increase is about 40 and 24 times for SI and SII, respectively. This implies an elevation of Pb concentration in tree-rings of SI (2.8 times) and bark for SI (2.8 times) and SII (1.1 times), compared to control.

In the case of Douglas-fir, it was noticed that with the increase of Pb concentration in the soil (28 and 16 times, compared to control), the content in tree-rings (7 and 4 times) and bark (4 and 2 times) also increases (Figure 1).

Ni concentration: Increased Ni concentration in soil samples (3 (SI) and 2 (SII) times; 2.5 (DI) and 2 (DII) times compared to control) also have a direct effect on increasing the concentration in both tree-rings and bark (Figure 1).

Mn and Zn concentration: Although the soil has not been treated with these elements a very small difference between experiments comparing to control. For both examined tree species some unusual behaviour can be seen in these experiments. Their concentrations in tree-rings and bark were slowly lowered (except for the Mn concentration in Douglas-fir bark, where an increase can be seen) for the concentrations of SI and SII compared to control despite their slightly increased concentration in the soil (Mn (15%, 12%) and Zn (9%, 6%); Mn (12%, 12%) and Zn (15%, 7%)). This soil concentration increase could be the consequence of the soil pH decrease (SI- 0.1; SII- 0.2; and in DI- 0.1; DII- 0.3) [2]. The decrease of Mn and Zn in plant parts could be explained as a consequence of the competition between various metals in the course of their uptake by roots and by a disturbance of uptake mechanism [5].

Table 1. Mean Pb, Ni, Mn and Zn (n=4) concentrations in soil, tree-rings and bark of spruce and Douglas-fir seedlings (ppm), as well as, corresponding soil pH.

	Pb			**Ni**		
	soil	**tree-rings**	**bark**	**soil**	**tree-rings**	**bark**
SI	827±56	0.41±0.05	4.73±0.55	278±16	0.34±0.03	2.71±0.16
SII	505±30	<0.15	1.87±0.09	199±9	0.29±0.04	1.78±0.09
SC	21±1	<0.15	1.67±0.10	88±4	0.24±0.03	1.09±0.09
DI	634±30	1.06±0.10	2.44±0.13	226±11	0.73±0.06	1.13±0.06
DII	369±19	0.61±0.08	1.28±0.06	182±9	0.40±0.03	1.03±0.06
DC	23±1	<0.15	0.68±0.05	89±4	<0.04	0.36±0.04
	Mn			**Zn**		
	soil	**tree-rings**	**Bark**	**soil**	**tree-rings**	**Bark**
SI	950±43	8.23±0.46	18.70±1.36	128±6	18.01±0.91	67.86±3.90
SII	923±42	8.41±0.49	23.41±1.88	125±5	21.53±0.96	73.36±4.44
SC	823±42	9.22±0.57	28.85±1.85	118±7	28.41±1.62	100±5
DI	951±43	3.38±0.23	13.69±0.92	131±7	5.36±0.37	22.02±1.85
DII	954±43	2.63±0.20	12.03±0.55	122±5	3.52±0.19	24.98±1.44
DC	852±46	5.00±0.27	8.71±0.44	113±5	7.66±0.38	30.35±1.62
	SI	**SII**	**SC**	**DI**	**DII**	**DC**
Soil pH	6.7±0.05	6.6±0.05	6.8±0.05	6.90±0.05	6.7±0.05	7.0±0.05

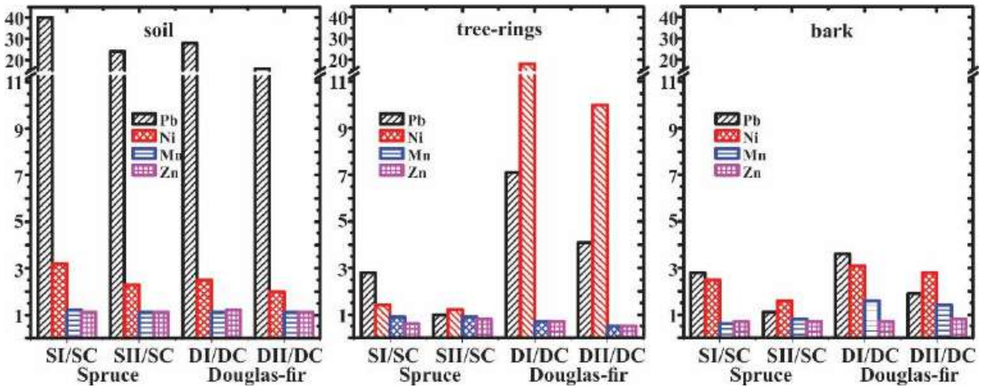

Figure 1. Concentration ratios between first-I and second-II experiment with control-C in soil, tree-rings and bark, for spruce and Douglas-fir.

CONCLUSION

All trees have survived the experiments (in these extreme conditions) and grew at a normal rate with no indications of metal toxicity. The addition of other metals (Pb and Ni) to soil leads to their increased accumulation in the body of tree-rings and bark, and the decrease of essential elements (Mn and Zn). Although every element uptake is a complex process, tree-rings of spruce and Douglas-fir react on elevated concentrations in the soil and can give information about environmental pollution. Bark was also influenced by the Pb and Ni elevated concentrations in the soil.

Acknowledgement

The authors acknowledge funding provided by the Institute of Physics Belgrade and Institute of Nuclear Sciences Vinča, through the grant by the Ministry of Education, Science, and Technological Development of the Republic of Serbia.

REFERENCES

[1] Aničić, M. et al., Ecological Indicators, 2011, **11**, 824–830.
[2] Marković, D.M. et al., Environ. Sci. Pollut. Res., 2013, **20**, 136-145.
[3] Turkyilmaz, A. et al. Environ. Sci. Pollut. Res., 2019, **26**, 5122–5130.
[4] Yousaf, M. et al., Water Air Soil Pollut., 2020, **231:382**, 1-9.
[5] Seregin, I. V., Kozhevnikova, A.D., Russ. J. Plant Physiol., 2006, **53**, 257–277.

Global Episteme Inc

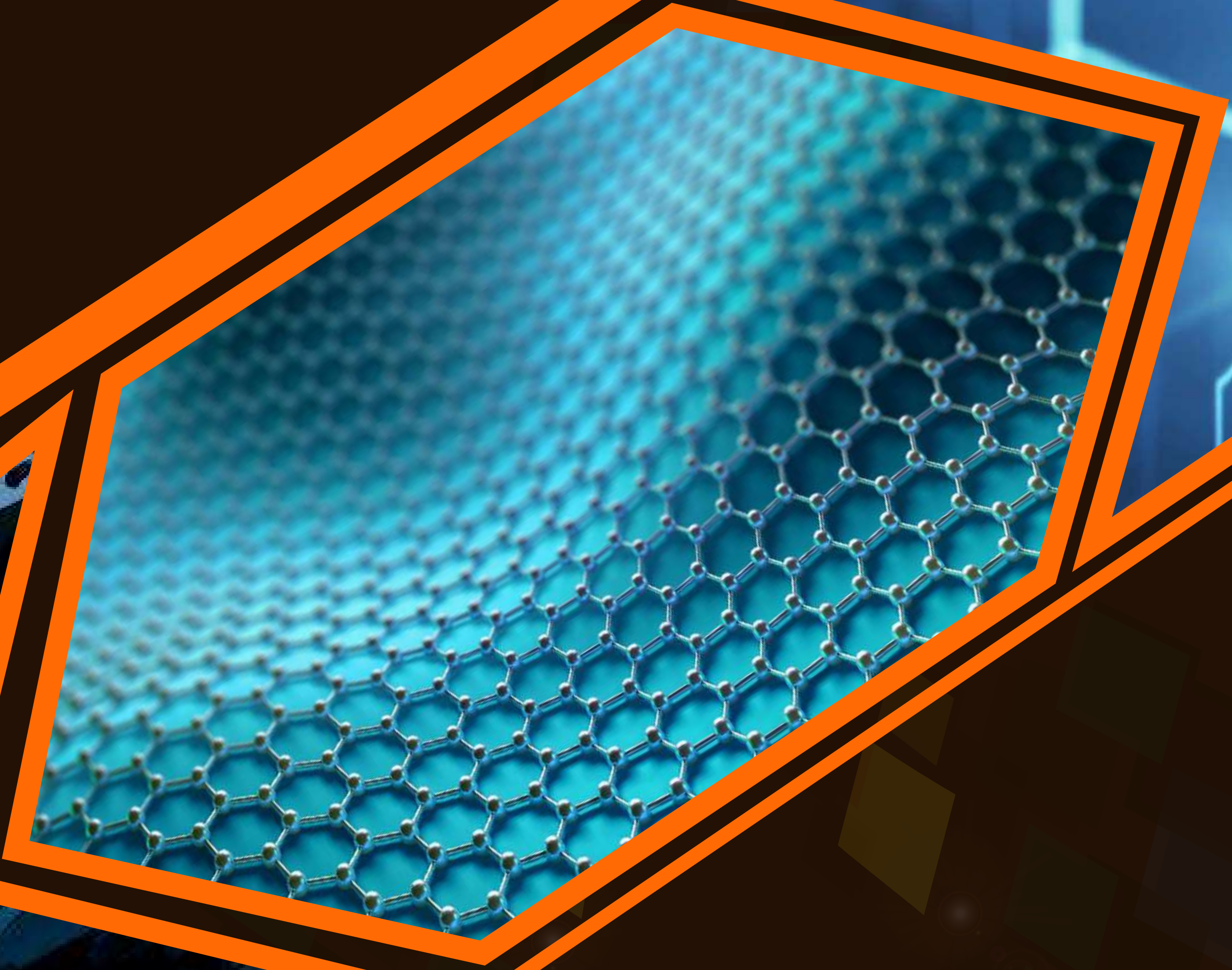

Webinar on

MATERIAL SCIENCE

31 March 2021

Chemical doping of Langmuir-Blodgett assembled graphene films

Ivana R Milošević[1]*, Borislav Vasić[1], Aleksandar Matković[2] and Jasna Vujin[1]

[1]University of Belgrade, Serbia
[2]Montanuniversität Leoben, Austria

Abstract

Graphene has been identified as a promising material in electronics, especially as an electrode with the appropriate Work Function (WF). Graphene displays ability to have two different roles as an electrode in electronic and optoelectronic devices (as an anode and a cathode). To achieve the desired performance of the devices, tuning the electrodes' WF is very important. By modulating the WF, band-structure alignment at the interface can enhance the efficiency of carrier transport and lower contact resistance, thus improving performance of the devices. Chemical doping represents the effective method for modulating the WF by charge transfer between the graphene sheet films and dopants, especially in the cases where graphene fabrication procedure results with many exposed basal-plane edges of graphene. Graphene Sheet (GS) dispersions were obtained from liquid-phase exfoliation of graphite and films were prepared using Langmuir-Blodgett Assembled (LBA) method. Such fabrication pathway is compatible with low cost and large scale fabrication. With the LBA method, GS self-assemble at the water-air interface forming a film. Different approaches for chemical doping can be applied to LBA graphene films. In the first approach, doping with nitric acid was done after film formation and a fivefold improvement of sheet conductivity was achieved (doi:10.1088/2053-1583/3/1/015002). This process does not affect electrodes' transparency. In the second approach doping with Li and Au salts was done during the film formation in the LBA process. Li and Au standard solutions were introduced instead of the water in the LBA technique. Au-based salts increase the WF of the films (p-doping), while Li-based salts decrease it (n-doping). As a result, this method allowed to tune the WF of graphene electrodes in a range of 0.7 eV (doi.org/10.1038/s41598-020-65379-1). Chemical doping of LBA graphene films is a simple and low-cost method for modulating WF, thus can widen their possible applications in low-cost optoelectronic devices.

Biography

Ivana R Milošević defended her PhD thesis (2014) at the Faculty of Physical Chemistry, University of Belgrade, Serbia. She is an assistant research professor at "Laboratory for 2D materials" at Centre for Solid State Physics and New Materials, Institute of Physics Belgrade. From 2020 she is Head of the Laboratory. Earlier, her experimental work was focused on environmental issues. Recently, the field of research has been expanded to synthesis of 2D materials, fabrication of thin and transparent films of 2D materials, chemical doping of 2D materials and their potential application in flexible and printed optoelectronics.

26 - 30 June 2023
Belgrade, Serbia

21. СИМПОЗИЈУМ ФИЗИКЕ КОНДЕНЗОВАНЕ МАТЕРИЈЕ

THE 21st SYMPOSIUM ON CONDENSED MATTER PHYSICS

BOOK OF ABSTRACTS

Institute of Physics Belgrade

Vinca Institute of Nuclear Sciences

University of Belgrade, Faculty of Physics

Serbian Academy of Sciences and Arts

Ministry of Science, Technological Development and Innovation

Conference Chairs

Vladimir Dobrosavljević, *Florida State University, USA*

Zorica Konstantinović, *Institute of Physics Belgrade*

Željko Šljivančanin, *Vinča Institute of Nuclear Sciences*

Organizing Committee

Jelena Pešić, *Institute of Physics Belgrade*- chair

Andrijana Šolajić, *Institute of Physics Belgrade*

Ivana Milošević, *Institute of Physics Belgrade*

Tijana Tomašević-Ilić, *Institute of Physics Belgrade*

Jelena Mitrić, *Institute of Physics Belgrade*

Bojana Višić, *Institute of Physics Belgrade*

Jovan Blagojević, *Institute of Physics Belgrade*

Marko Orozović, *Vinča Institute of Nuclear Sciences*

Mitra Stepić, *Vinča Institute of Nuclear Sciences*

Igor Popov, *Institute for Multidisciplinary Research, Belgrade*

Program Committee

Ivan Božović, *Brookhaven National Laboratory, USA*

Vladimir Dobrosavljević, *Florida State University, USA*

Milan Damnjanović, *Faculty of Physics, University of Belgrade, Serbia*

Vladimir Djoković, *Vinča Institute, University of Belgrade, Serbia*

Gyula Eres, *Oak Ridge National Laboratory, USA*

Laszló Forró, *University of Notre Dame, USA*

21. СИМПОЗИЈУМ ФИЗИКЕ КОНДЕНЗОВАНЕ МАТЕРИЈЕ

THE 21st SYMPOSIUM ON CONDENSED MATTER PHYSICS

26 - 30 June 2023, Belgrade, Serbia

https://www.sfkm2023.ipb.ac.rs/

Institute of Physics
Belgrade

Vinca Institute of
Nuclear Sciences

University of Belgrade,
Faculty of Physics

Serbian Academy of
Sciences and Arts

Ministry of Science, Technological
Development and Innovation

Fe-nanoparticle-modified Langmuir-Blodgett Graphene Films for Pb(II) Water Purification

Ivana R. Milošević[a], Jasna Vujin[a], Muhammad Zubair Khan[b], Thomas Griesser[c], Christian Teichert[b] and Tijana Tomašević-Ilić[a]

[a]*Institute of Physics Belgrade, University of Belgrade, 11080 Belgrade, Serbia*
[b]*Chair of Physics, Montanuniversität Leoben, Leoben, Austria*
[c]*Chair of Chemistry of Polymeric Materials, Montanuniversität Leoben, 8700 Leoben, Austria*

Abstract. The surface of nonmagnetic Langmuir-Blodgett self-assembled (LBSA) graphene films is modified through structure engineering by chemical functionalization with Fe nanoparticles in order to induce local magnetic domains and investigate the application of such films for heavy metal water purification. We prepared and modified our films by single-step Langmuir-Blodgett procedure [1]. The influence of Fe-based magnetic nanoparticles on the structure and magnetic properties of LBSA films was examined by Raman spectroscopy, X-ray photoelectron spectroscopy (XPS), and Magnetic Force Microscopy (MFM). Raman and XPS confirmed the surface modification of the graphene films. Compared to an unmodified graphene film, which has no detectable magnetic response, MFM phase images show a strong phase shift difference compared to the substrate (~0.2°), indicating the presence of a local magnetic moment. In addition, we examined the use of magnetized LBSA graphene films for the adsorption of Pb(II) ions by immersing the films into Pb(II) solution. Results from XPS measurements depict the ability of modified films to detect and adsorb Pb(II) ions from water-based solutions. The development of a new generation of magnetic self-assembled 2D material films for heavy metal sensing and water purification that can overcome the deficiencies such as low purification efficiency, short-term stability, and high cost is of great interest for various applications in green technology.

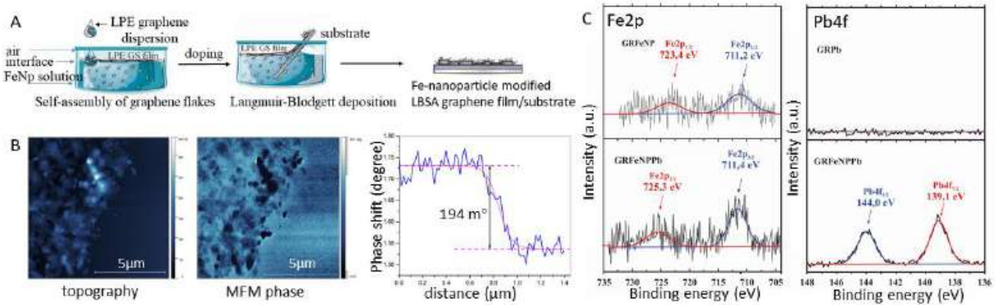

FIGURE 1. A) Fabrication of Fe-modified LBSA graphene films, B) AFM topography, MFM phase image, and representative MFM phase shift profile of Fe-modified LBSA films, C) XPS Fe2p spectra of modified films before and after interaction with Pb(II) ions, and Pb4f spectra of unmodified and modified films after interaction with Pb(II) ions.

REFERENCES

1. Milošević I. R. et al., *Sci. Rep.* **10**, 8476 (2020).

PHYSICAL CHEMISTRY 2024

17th International Conference
on Fundamental and Applied Aspects of
Physical Chemistry

Proceedings
Volume I

This conference is dedicated to the 100th anniversary of the birth of
Professor Slobodanka Caca Veljković

September 23-27, 2024
Belgrade, Serbia

Title: PHYSICAL CHEMISTRY 2024, 17th International Conference on Fundamental and Applied Aspects of Physical Chemistry (Proceedings) ISBN-978-86-82475-44-6
Volume I: ISBN-978-86-82475-45-3
Editors: Željko Čupić, Slobodan Anić and Ana Ivanović-Šašić
Published by: Society of Physical Chemists of Serbia, Studentski Trg 12-16, 11158, Belgrade, Serbia
Publisher: Society of Physical Chemists of Serbia
For Publisher: S. Anić, President of Society of Physical Chemists of Serbia
Printed by: ″Jovan″, <Printing and Publishing Company, Ilije Đuričića 19, Belgrade, 50 Copies
Number of pages: 12+402, Format A4, printing finished in December 2024.

Text and Layout: ″Jovan″

50- *Copy printing*

PHYSICAL CHEMISTRY 2024

17th International Conference on Fundamental and Applied Aspects of Physical Chemistry

Organized by

The Society of Physical Chemists of Serbia

in co-operation with

Institute of Catalysis, Bulgarian Academy of Sciences

and

Boreskov Institute of Catalysis, Siberian Branch of Russian Academy of Sciences

and

University of Belgrade, Serbia:

Faculty of Physical Chemistry
Institute of Chemistry, Technology and Metallurgy
Vinča Institute of Nuclear Sciences
Faculty of Pharmacy

and

Institute of General and Physical Chemistry, Belgrade, Serbia

EFFICIENT PRODUCTION OF TWO-DIMENSIONAL PYROPHYLLITE THROUGH LIQUID-PHASE EXFOLIATION

I.R. Milošević, T. Tomašević, J. Vujin, R. Panajotović, J. Pešić and T. Tomašević-Ilić

Institute of Physics Belgrade, University of Belgrade, Laboratory for 2D Materials, Center for Solid State Physics and New Materials, Pregrevica 118, 11080 Belgrade, Serbia.
(novovic@ipb.ac.rs)

DOI: https://doi.org/10.46793/Phys.Chem24I.361M

ABSTRACT

2D-Pyrophyllite, a layered material with notable physico-chemical properties, is suitable for various applications, such as electrical insulator, protective coating or lubricant. Liquid-phase exfoliation (LPE) has emerged as a promising, large-scale, low-cost method for obtaining substantial yields of high-quality, basal plane defect-free pyrophyllite flakes in dispersion. Optimizing exfoliation conditions is crucial for achieving these objectives. After adjusting experimental parameters (initial concentration of bulk material, sonication time, solvent type, and centrifugation rate), a stable pyrophyllite dispersion with a high concentration of 98.8 µg/mL was obtained. The LPE method enables the production of high-yield flakes with well-defined shapes, flat surfaces, and regular edges.

INTRODUCTION

Layered materials are compounds characterized by a structure in which atomic layers are bonded together by weak forces, making them easily separable to atomically thin layers. These materials exhibit strong in-plane and weak between layers bonds, typically of the van der Waals type. Some of them are graphene [1], transition metal dichalcogenides (TMDs) [2], elemental analogues to graphene like silicene, germanene etc. [3]. In recent years a new group of earth-abundant, low-cost nanomaterials has emerged. The new group, known as clay minerals, includes two-dimensional (2D) insulating materials based on phyllosilicates (talc, kaolinite, mica, pyrophyllite, vermiculite, etc.). Layered materials in 2D form exhibit unique electronic, mechanical, and chemical properties that differ from their bulk counterparts. To fully realize their potential, layered materials must be exfoliated.

The advancement of these materials has been limited by the absence of a straightforward method to exfoliate them into mono- or few-layer nanosheets in large quantities. One of the developed methods is liquid-phase exfoliation (LPE). This method is simpler and less costly than chemical vapor deposition and provides a higher yield than mechanical exfoliation. In this study, we present a method for obtaining 2D pyrophyllite nanosheet dispersions using ultrasound induced LPE. Optimization of exfoliation conditions (including the initial concentration of bulk material, sonication time, solvent type, and centrifugation rate) are key processes for enhancing the yield, stability, and quality of 2D pyrophyllite dispersions.

The pyrophyllite chemical formula is $Al_2Si_4O_{10}(OH)_2$. Pyrophyllite single layer consists of the $AlO_4(OH)_2$ octahedral sheet which is between two SiO_4 tetrahedral sheets [4]. Pyrophyllite is an abundant, inexpensive material, chemically inert, good electrical and thermal insulator with a high melting point, soft mineral which can withstand large pressures [5]. Pyrophyllite dispersions obtained by LPE method can be used to form films through various methods, such as spray coating, vacuum filtration, or Langmuir–Blodgett assembly (LBA).

METHODS

Liquid-phase exfoliation, a non-covalent exfoliation that uses solvents, is one of the most promising synthesis methods [1, 2, 6]. We have used sonication assisted LPE in ultrasonic bath (Figure 1) where ultrasound induces separation of 2D nanosheets from bulk material in appropriate solvent due to the propagation of ultrasound waves. The starting material for LPE of pyrophyllite was ground pyrophyllite crystal (Hillsborough mine, Orange County, North Carolina, USA). Sonication results in exfoliation of the initial flakes, where the largest were removed by centrifugation. Exfoliation conditions, such as the initial concentration of bulk material, sonication time, solvent type, and centrifugation rate were varied to enhance the yield, stability, and quality of pyrophyllite dispersions. When optimization was achieved, we had a stable dispersion of few-layer defect-free pyrophyllite nanosheets.

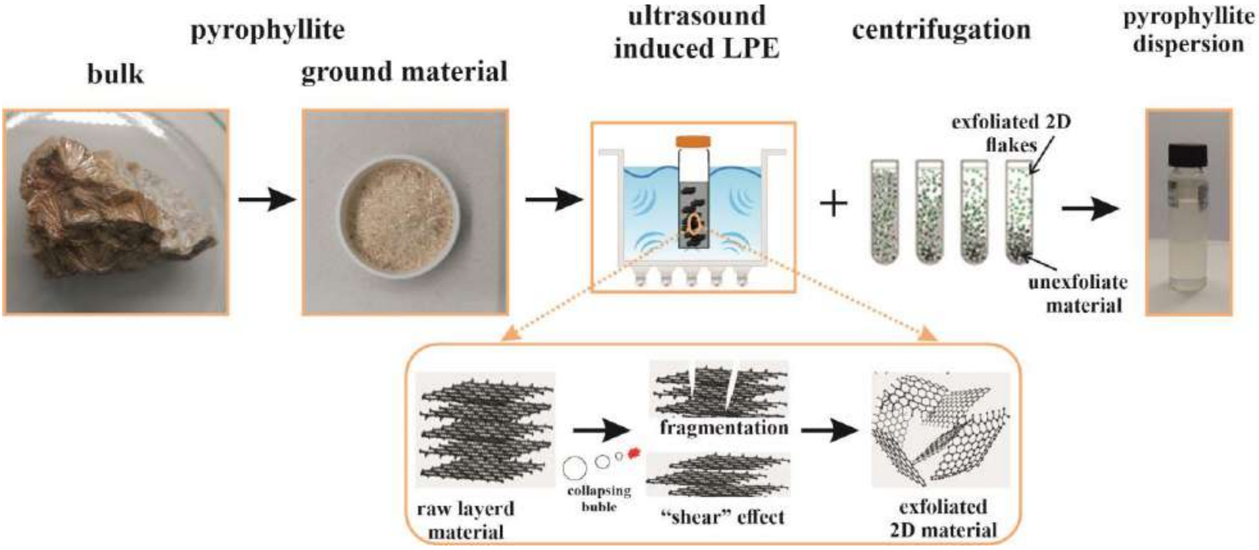

Figure 1. Schematic representation of pyrophyllite liquid-phase exfoliation (LPE).

For optical characterization of nanosheet dispersions, UV–VIS spectra were measured using a Shimadzu 2600i spectrophotometer with quartz cuvettes. Vacuum filtration was used to obtain the mass of exfoliated pyrophyllite flakes, a necessary parameter for calculating the absorption coefficient of pyrophyllite. For filtration of pyrophyllite dispersions Omnipore hydrophilic PTFE membrane filter (0.2 µm pore size) was used. The morphology characterization was done by imaging in the tapping AFM mode with an atomic force microscope, NTEGRA Spectra.

RESULTS AND DISCUSSION

The concentration of the dispersion can be calculated from the Lambert- Beer law ($A/l= \alpha c$, where l is the cell length, and c is the concentration) if the absorption coefficient (α) is known [1, 2, 7]. However, absorption coefficient is unknown for phyrophyllite dispersed in N-methylpyrrolidone (NMP) and Dimethylformamide (DMF). To determine the absorption coefficient firstly concentration after centrifugation must be determined, so we prepared pyrophyllite dispersions in NMP and DMF using ultrasound induced LPE method of initial concentration of 10 mg/mL. The dispersions were diluted two, five and ten times and the corresponding UV-VIS absorption spectra were recorded (Figure 2a) for both solvents. Precisely measured volume (V= 20mL) of both as-prepared (stock) and diluted pyrophyllite dispersions were passed through the PTFE membrane filters of known mass (Figure 2b, inset). Careful measurement of the filtered mass provided the concentration of as prepared-stock and diluted dispersions. The absorbance (660 nm) divided by the cell length was plotted versus concentration (Figure 2b) showing a linear relationship with measured concentrations, giving absorption coefficients of 15.6 mLmg^{-1}m^{-1} for DMF and 8.5 mLmg^{-1}m^{-1} for NMP. Using these absorption coefficients, we can determine the concentration for all subsequent samples.

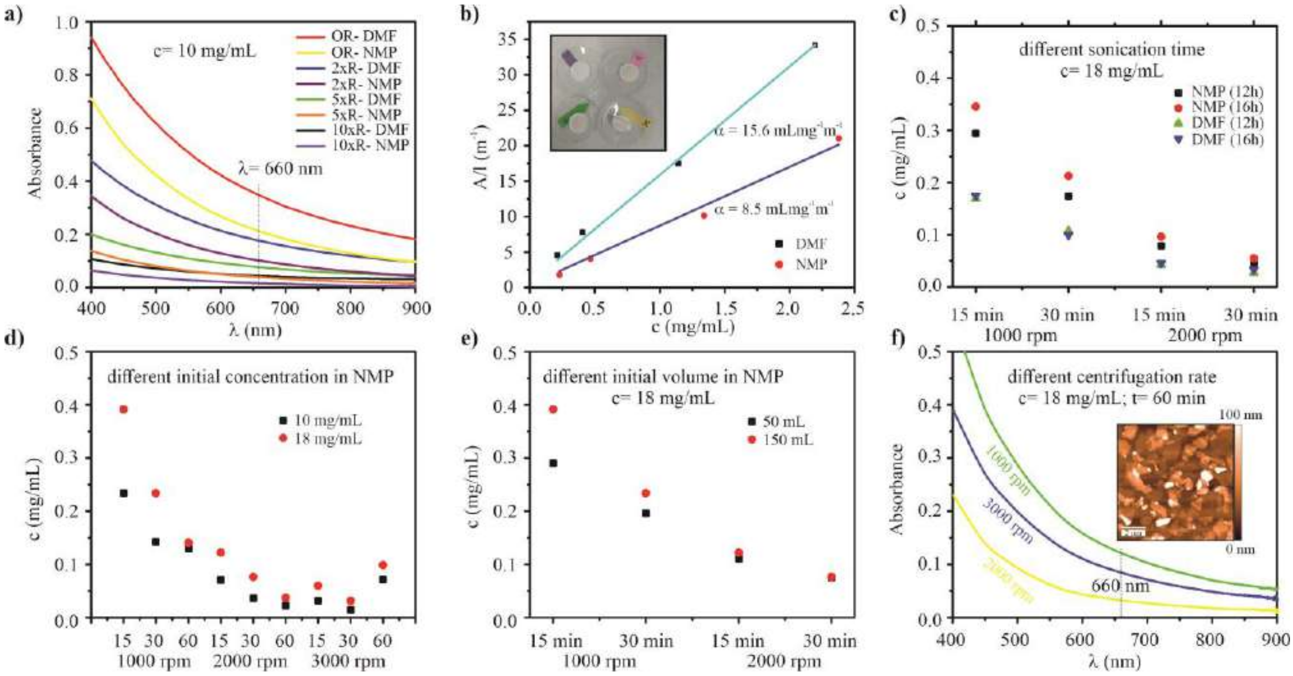

Figure 2. Optical characterization of pyrophyllite dispersions: a) Absorption spectra of pyrophyllite dispersions in NMP and DMF (initial concentration of 10 mg/mL): original stock dispersion after centrifugation (OR), and dispersions diluted 2, 5, and 10 times (2xR, 5xR, 10xR). b) Lambert-Beer plots: optical absorbance (λ= 660 nm) divided by cell length as a function of pyrophyllite concentration (inset: Filters showing the filtered dispersed material for the corresponding diluted dispersions). c) Pyrophyllite concentration calculated from the experimentally obtained absorption coefficient at 660 nm for different sonication times, starting with an initial concentration of 18 mg/mL in NMP and DMF. d) Pyrophyllite concentration calculated from the absorption coefficient at 660 nm for various initial concentrations in NMP. e) Pyrophyllite concentration calculated from the absorption coefficient at 660 nm for different initial volume with a concentration of 18 mg/mL in NMP; f) Absorption spectra for different centrifugation rates with a centrifugation time of 60 minutes (inset: Topography image of 2D pyrophyllite flakes obtained by LPE method on Si/SiO_2).

We varied exfoliation conditions, including the initial concentration of bulk material, sonication time, solvent type, and centrifugation rate, to optimize the yield, stability, and quality of pyrophyllite dispersions. Concentration was calculated using experimentally obtained absorption coefficients from absorbance (660 nm) for different sonication times with an initial concentration of 18 mg/mL in NMP and DMF (Figure 2c). Figure 2c shows that longer sonication times (16h) result in higher yields of dispersed pyrophyllite in both solvents. Also, for the 16h of sonication time NMP gives higher yields of pyrophyllite. Initial concentrations of 18 mg/mL yield higher concentrations across all centrifugation rates and times used. Similarly, larger initial volumes have the same effect, but at higher centrifugation rates, concentrations were equalized (Figure 2e). Dispersions centrifuged at lower rates were less stable, with pyrophyllite flakes aggregating after two weeks. Only about 20% of the dispersed flakes remained in the solvent, while the rest formed sediment. The least aggregation occurred at 3000 rpm compared to 1000 and 2000 rpm.

Additionally, 60 minutes was found to be the optimal centrifugation time for the best dispersion quality (Figure 2f). A stable pyrophyllite dispersion with a concentration of 98.8 µg/mL was obtained by using an initial concentration of 18 mg/mL ground pyrophyllite in NMP, sonicated for 16 hours in 150 mL, and centrifuged for 60 minutes at 3000 rpm.

The topography of the 2D pyrophyllite flakes obtained by the LPE method in NMP is shown in the inset of Figure 2f. The flakes exhibit well-defined shapes, flat surfaces, and regular edges, with varying lateral dimensions and heights. The samples produced by the LPE method consist of a network of flakes typically 5-15 nm in height and around 1 µm in lateral dimensions, as previously reported [8]. Although these flakes are thicker and smaller than those produced by mechanical exfoliation, the LPE method enables large-scale production and can be effectively used for various applications, particularly when combined with film formation techniques such as the Langmuir-Blodgett Assembly method.

CONCLUSION

We have demonstrated that by optimizing the exfoliation parameters in the LPE technique, it is possible to achieve a stable dispersion with a significant yield of high-quality pyrophyllite flakes, which have well-defined shapes, regular edges, and varying lateral dimensions and heights. By determining the absorption coefficient of pyrophyllite in different solvents and adjusting the initial concentration of bulk material, sonication time, and centrifugation rate, pyrophyllite can be dispersed at concentrations up to 98.8 µg/mL in NMP. This dispersion can be used to create thin films through vacuum filtration or the Langmuir-Blodgett Assembly methods, opening new perspectives for the application of pyrophyllite.

Acknowledgment

This research was supported by the Science Fund of the Republic of Serbia, Grant No 7456, 2D Material-based Tiled Network Films for Heritage Protection-2DHeriPro and by the Institute of Physics Belgrade through the grants by the Ministry of Science, Technological Development and Innovation of the Republic of Serbia.

REFERENCES

[1] Y. Hernandez, V. Nicolosi, M. Lotya et al., Nat. Nanotechnol., 3 (2008) 563.
[2] J.N. Colman, M. Lotya, A. O´Neill et al., Science, 331 (2011) 568.
[3] S. Balendhran, S. Walia, H. Nili et al., Small, 11 (2015) 640.
[4] A.I. Mitrović Rajić, Mechanochemical and thermal modification of pyrophyllite for use in electrochemical sensors and membranes, Doctoral Dissertation, Faculty of Physical Chemistry, 2023.
[5] M.A. Ali, H.A.M. Ahmed, H.M. Ahmed, M. Hefni, Appl. Sci., 11 (2021) 11357.
[6] A. Matković, I. Milošević, M. Milićević et al., 2D Mater., 3 (2016) 015002.
[7] M. Lotya, Y. Hernandez, P.J. King et al., J. Am. Chem. Soc., 131 (2009) 3611–3620.
[8] B. Vasić, R. Gajić, I. Milošević et al. Appl. Surf. Sci., 608 (2023) 155114.

PHYSICAL CHEMISTRY 2024

17th International Conference
on Fundamental and Applied Aspects of
Physical Chemistry

Proceedings
Volume II

This conference is dedicated to the 100th anniversary of the birth of Professor Slobodanka Caca Veljković

September 23-27, 2024
Belgrade, Serbia

Title: PHYSICAL CHEMISTRY 2024, 17th International Conference on Fundamental and Applied Aspects of Physical Chemistry (Proceedings) ISBN-978-86-82475-44-6
Volume II: ISBN-978-86-82475-46-0
Editors: Željko Čupić, Slobodan Anić and Ana Ivanović-Šašić
Published by: Society of Physical Chemists of Serbia, Studentski Trg 12-16, 11158, Belgrade, Serbia
Publisher: Society of Physical Chemists of Serbia
For Publisher: S. Anić, President of Society of Physical Chemists of Serbia
Printed by: ″Jovan″, <Printing and Publishing Company, Ilije Đuričića 19, Belgrade, 50 Copies
Number of pages: 6+368, Format A4, printing finished in December 2024

Text and Layout: ″Jovan″

50 - *Copy printing*

PHYSICAL CHEMISTRY 2024

17th International Conference on Fundamental and Applied Aspects of Physical Chemistry

Organized by

The Society of Physical Chemists of Serbia

in co-operation with

Institute of Catalysis, Bulgarian Academy of Sciences

and

Boreskov Institute of Catalysis, Siberian Branch of Russian Academy of Sciences

and

University of Belgrade, Serbia:

Faculty of Physical Chemistry
Institute of Chemistry, Technology and Metallurgy
Vinča Institute of Nuclear Sciences
Faculty of Pharmacy

and

Institute of General and Physical Chemistry, Belgrade, Serbia

PHYSICO-CHEMICAL INVESTIGATION OF XVI CENTURY FRESCO-PAINTINGS FROM MONASTERY CRNA REKA

B. Savić [1], J. Vujin [2], T. Tripković [3], J. Ciganović[4], I. R. Milošević[2], I. Živković[1] and T. Tomašević-Ilić [2]

[1] *Faculty of Applied Arts, University of Arts Belgrade of Belgrade, Kralja Petra 4, 11000 Belgrade, Serbia*
[2]*Institute of Physics Belgrade, University of Belgrade, Pregrevica 118, 11080 Belgrade, Serbia (ttijana@ipb.ac.rs)*
[3]*Institute for the Protection of Cultural Monuments of Serbia, Radoslava Grujica 11, 11118 Belgrade, Serbia*
[4]*Vinca Institute of Nuclear Sciences-National Institute of the Republic of Serbia, University of Belgrade, Mike Petrovića Alasa 12-14, 11351 Belgrade, Serbia*

DOI: https://doi.org/10.46793/Phys.Chem24II.695S

ABSTRACT

The 16th-century wall paintings of Monastery Crna Reka in Serbia are visibly deteriorating. Extensive wall degradation causes these frescoes to fall from their original positions and shatter into fragments. To address the proper restoration and conservation procedures, we examine the structure and morphology of the fragments. Micro-Raman spectroscopy and XRF revealed that the blue color on the wall paintings does not originate from blue pigments but results from the layer-by-layer technique of hematite and carbon black pigments by the artist, which, in combination with the mortar, gave a blue color sensation. Cross-sectional profiles and 3D maps obtained by profilometry show the surface morphology of these fragments, and can be consider as guidelines for further understanding of the various aspects of the painting's creation, monitoring future degradation process, and developing or applying protective coatings for Serbian frescoes.

INTRODUCTION

The 13th-century Monastery Crna Reka is located in southwestern Serbia, in the canyon of the Crna Reka river, on the rocky cliffs of mountain Mokra Gora. Its distinctive architecture renders it one of Serbia's most stunning cave-churches. The internal walls in Crna Reka were painted by the renowned artist Longin by al fresco-painting technique [1]. Despite having endured the passage of time without being demolished, exposure to various environmental factors upon natural aging has caused degradation of this unprotected monument, formation of micro and nanocracks, and eventually surface erosion. Such extensive degradation of the walls leads to the falling of fresco paintings. Preserving of this wall paintings which has been determined as the Heritage of the National Treasure category requires extensive restauration work. To ensure the long-term preservation of fresco paintings without altering their esthetics, it is essential to thoroughly understand their chemical structure and surface morphology [2]. Thus, conservators can make informed decisions on how to best maintain and protect frescoes against ongoing and future challenges. When Heritage samples must be analyzed, non-destructive techniques are the only option for obtaining information. The study by micro-Raman of cross sections is an effective tool capable of investigating the chemical structure of frescoes [3]. The use of cross sections can enable the identification of components in the artefacts from the support to the outermost layer. Combined with X-ray fluorescence (XRF), commonly used for the elemental characterization of heritage objects due to its ability to detect a wide range of painting materials, in a non-destructive, sensitive, and efficient way, it can reliably identify the pigment compositions [4]. In paintings, surface topography reveals unintended stylistic elements embedded in the surface of the painting that may include the deposition and drying of the paint, patterns in the brushwork, physiological factors, and other aspects of the painting's creation [5]. This work aims to interpret the painting technique used by the artist and characterize the paint compounds using XRF and Raman spectroscopy.

METHODS

Sampling sites of wall paintings are determined according to standard sampling of the Heritage of the National Treasure category determined by Republic Institute for the Protection of Cultural Monuments, Law on Cultural Heritage and Ethical Sampling Guidance of Icon Heritage Science Group. Sampling of fresco painting was carried out from places with an unstable connection, where a conservation-restoration intervention of consolidation would otherwise be carried out. **Figure 1**. shows extensive degradation of frescoes and sampling sites.

Figure 1. Photographs of two sampling sites (A and B) and selected places prior to collection.

NT-MDT NTEGRA Spectra System with a 100x microscope objective, and a TE cooled CCD (1,024×256 pixels) detector, was used to obtain the Raman spectra. The 532-nm laser line of a He/Ne laser was employed for Raman excitation. The laser power was kept below 2 mW using density filters, to avoid sample degradation. A Thermo Niton XL3t portable analyzer was used for non-destructive elemental analysis, featuring multiple primary filters on its 50 kV X-ray tube to enhance sample excitation. The instrument was mounted on a stand, and a camera inside the analyzer head allowed for the definition of the sample surface area for analysis. The analysis time was set to 90 seconds. Using Niton's TestAllGeo and Mining calibration modes, the concentrations of 30 elements on the sample surfaces were determined semi-quantitatively. NITON Data Transfer software (NDT_REL_8.2.1) was used for the instrument control via computer and reading and processing of the recorded spectra. For the surface topography characterization, the non-contact optical profilometer Zygo NewView 7100 (Middlefield, CT, USA) was used.

For all measurements the samples were analyzed without any previous mechanical or chemical treatment being undertaken.

RESULTS AND DISCUSSION

Optical microscopy of the cross-section of the Crna Reka (CR) fresco painting fragment reveals a black and red layered structure on the surface of the fresco painting support (**Figure 2A-inset**). The red layer is positioned as a layer between two black layers on the white painting support. **Figure 2A** depicts the Raman spectra of this untreated and unpolished cross-section sample. Bands at 227, 292, 405, 498, 611 and 657 cm^{-1}, characteristic for hematite (FeO3) [6], indicate that hematite was the main mineral used as a source of red pigments in these frescoes. The Raman spectra featured the origin of black layers on the support and on the surface. Broad bands at 1310 and 1591 cm^{-1} unequivocally indicate the presence of carbon-based compounds in this areas, attributed to carbon black. The band at 1310 cm-1 is due to sp^3-type C–C bonding, and the band at 1,597 cm^{-1} is due to sp^2-type C=C bonding. The absence of the symmetric stretching band of the phosphate group at 960 cm^{-1} excludes bone or ivory black pigments, suggesting that soot or powdered charcoal was the source of these black particles [7]. Strong bands at 285 cm^{-1} and 1081 cm^{-1}, and small band at 711 cm^{-1}, which was observed in the spectra, were attributed to calcite ($CaCO_3$) [8]. The Raman shift of bands related to black pigment and calcite indicate that the black paint could have been prepared by mixing the black pigment with lime or calcite. XRF spectra (**Figure 2B**) confirmed the results obtained by Raman spectroscopy. Although, the bluish is dominant color of the Monastery fresco paintings, XRF spectra indicates on the high presence of Ca and Fe of in all samples, without the presence of any element known to be used for blue pigments. Additionally, the presence of CaKα line in the XRF spectra and calcite in the Raman spectra indicates that the mortar on which it has been painted is a lime mortar, produced from limestone by heating calcium carbonate. This lime mortar has been used for millennia as pigments or primers, typically mixed with pigments in the fresco technique to bind the pigments.

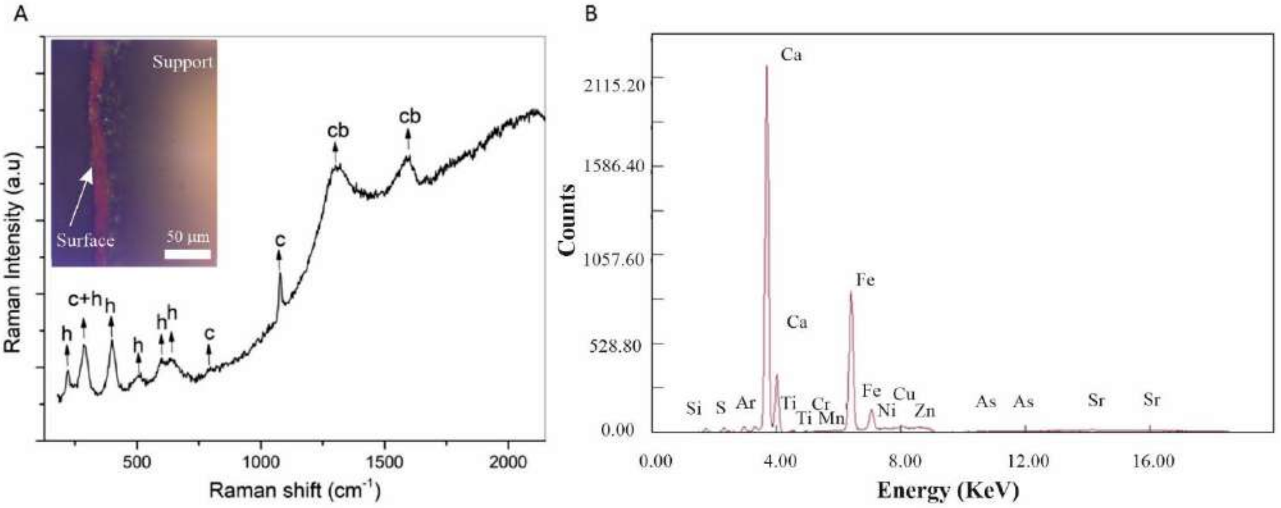

Figure 2. A) Representative Raman spectra of cross-section of the CR sample. Raman spectra featured the presence of hematite (h), calcite (c), and carbon black (cb) pigment; Optical Microscopy of unpolished and untreated cross-section of the CR sample. Scale bar is 50 µm. B) XRD spectra of the CR sample.

Figure 3 shows the surface morphology of the CR sample. High roughness is present across the entire surface. The areas with varying step heights, ranging from 4-10 µm, are likely the result of the deposition and drying of the paint during its creation. No patterns in the artist's brushwork were noticed. However, the surface inhomogeneity might result from degradation and requires further investigation. This should include examining other works by the artist and monitoring changes like cracking or flaking over time. Our findings provide a baseline record of the fresco's current condition. Conservators can use the established records to compare future observations, detect subtle changes and degradation progression, and determine the most suitable protective coating tailored to the specific needs of rough surfaces.

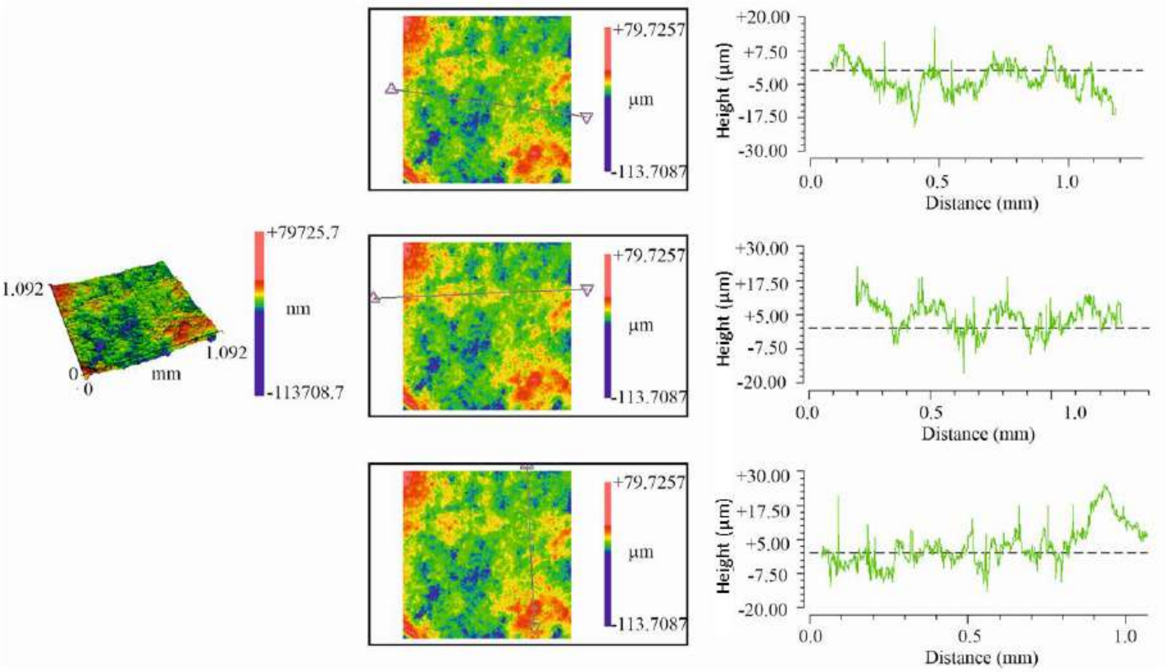

Figure 3. 3D and corresponding 2D maps with cross sectional profiles of CR sample.

CONCLUSION

The study of the cross sections indicates a layer-by-layer painting tecnique of fresco paintings from Crna Reka Monastery, and presents the characterisation of all layers (from the support to the most external) by micro-Raman spectroscopy. The following pigments were identified: hematite, carbon black, and calcite, and the composition was comfirmed by XRF measurements. Profilometry reveals the surface morphology of the paintings and provides information for future degradation monitoring of the frescoes.

Acknowledgment

This research was supported by the Science Fund of the Republic of Serbia, Grant No 7456, 2D Material-based Tiled Network Films for Heritage Protection-2DHeriPro, the Institute of Physics Belgrade through the Grant by the Ministry of Science, Technological Development and Innovations. Authors thank the Institute for the Protection of Cultural Monuments of Serbia for the collaboration. J. C. acknowledge Ministry of Science, Technological Development and Innovation of the Republic of Serbia through institutional funding (grant no: 451-03-66/2024-03/200017).

REFERENCES

[1] R. Stanić, Neka zapažanja o spomeničkim osobenostima Crnorečkog manastira i o programskim i stilskim odlikama zidnog slikarstva, u: Manastir Crna Rijeka i Sveti Petar Koriški, Naučni skup, Priština, Zubin Potok, Crna Rijeka, 25-26.V 1996, Priština, Beograd (1998) 163–179.
[2] P. Mora, Causes of deterioration of mural paintings, International Centre for the Study of the Preservation and the Restoration of Cultural Property, Rome (1974) 11–29.
[3] M.A. Ziemann et al., J. Raman Spectrosc. 52 (2020) 137–142.
[4] A. Harth, A. Herit Sci 12 (2024) 17.
[5] F. Ji et al., Herit Sci 9 (2021) 152.
[6] D. L. Argote et al., J. Archaeol. Sci. Rep. 32 (2020) 102375.
[7] A. Hernanz et al., J Raman Spectrosc 37 (2006) 492–497.
[8] S. Gunasekaran et al., J. Raman Spectrosc. 37 (2006) 892–899.

Ministry of
Research,
Innovation and
Digitization

Noblesse Optissima Style

NANOTEAM

Altium

7th International Conference on Emerging Technologies in Materials Engineering

EmergeMAT

PROGRAMME
and
Book of Abstracts

No. 7 / 2024

2024, 30th- 31th October

GARDEN MARSHAL Hotel,
Calea Dorobantilor 50B, Bucharest, Romania

IMNR
102 Biruinței Blvd, Pantelimon, ILFOV | OP 77145
Tel: +4021 3522046; +4021 3522048; +4021 3522050
Fax: +4021 3522049 | imnr@imnr.ro | www.imnr.ro

Avanmat

7th International Conference on Emerging Technologies in Materials Engineering EMERGEMAT

No.7 / 2024

30-31 October 2024
Bucharest, ROMANIA

www.imnr.ro

Format Hybrid

ISSN 2602-0424
ISSN-L 2602-0416

Print
ISSN 2602-0416
ISSN-L 2602-0416

Contact

MIRELA PETRICEANU
Specialist Proprietate Intelectuala CTT-AVANMAT
Centrul de Transfer Tehnologic
pentru Materiale Avansate,
Institutul National de Cercetare-Dezvoltare
pentru Metale Neferoase si Rare – IMNR
Bd. Biruintei nr. 102
Pantelimon, jud. Ilfov
T (+4021) 352 20 46 / 131
F (+4021) 352 20 49
mirela.petriceanu@imnr.ro

GRAPHENE ENHANCEMENT OF V_2O_5 AS CATHODE MATERIAL

Nataša Tomić[1*], Ivana R. Milošević[1], Jasna Vujin[1], Bojana Kuzmanović[2], Milica Vujković[3]

[1]Institute of Physics Belgrade, National Institute of the Republic of Serbia, University of Belgrade, Serbia
[2]Institute of Nuclear Sciences "Vinča", National Institute of the Republic of Serbia, University of Belgrade, Serbia
[3]Faculty of Physical Chemistry, University of Belgrade, Serbia
*Corresponding author: natasat@ipb.ac.rs

The pure V_2O_5 nanopowder, synthesized by acid-assisted hydrothermal method [1], was combined with water-based graphene dispersion in order to obtain the V_2O_5-graphene nanocomposite. Previously, the simple and low-cost method known as liquid phase exfoliation (LPE) [2] was used to get desired graphene dispersion. The influence of graphene coupling with the vanadium oxide was analysed from the structural, morphological, and electrochemical point of view. The structural properties of the nanomaterials, before and after graphene modification, was analysed by X-ray powder diffraction (XRPD). The morphological characteristics were investigated by Field Emission Scanning Electron Microscopy (FESEM). These nanostructures were tested as an electrode material for Li-ion batteries using Gamry Potentiostat/Galvanostat. The influence of graphene on the capacity and its stability was evaluated and discussed. The applied graphene-based modification approach was found to be successful in improving the cathode performance of V_2O_5.

References:

1. J. Liu, X.Wang, Q. Peng, Y. Li, *Advanced Materials* 17 (2005) 764.
2. T. Tomašević-Ilić, J. Pešić, I. Milošević, J. Vujin, A. Matković, M. Spasenović, R. Gajić, *Opt Quant Electron* 48 (2016) 319.

Acknowledgements:

The authors acknowledge funding provided by the Institute of Physics Belgrade, through the grant by the Ministry of Science, Technological Development and Innovation of the Republic of Serbia, as well as by the Innovation Fund of the Republic of Serbia - Proof of Concept (PoC) ID 5619, the Institute of Physics, University of Belgrade, Serbia.

BOOK OF ABSTRACTS

ADVANCES
IN SOLID STATE PHYSICS
AND NEW MATERIALS

ДОСТИГНУЋА У ФИЗИЦИ ЧВРСТОГ СТАЊА И НОВИХ МАТЕРИЈАЛА

30 година Центра за физику чврстог стања и нове материјале
Института за физику у Београду

ADVANCES IN SOLID STATE PHYSICS AND NEW MATERIALS

30 years of the Center for Solid State Physics and New Materials at the
Institute of Physics Belgrade

19 - 23 May 2025
Belgrade, Serbia

Conference Chairs

Nenad Lazarević, *Institute of Physics Belgrade, Serbia*
Emil S. Božin, *Institute of Physics Belgrade, Serbia*
Rudi Hackl, *IFW Dresden, Germany*
Zoran V. Popović, *Serbian Academy of Sciences and Arts (SANU), Serbia* – honorary chair

Organizing Committee

Jelena Pešić - chair
Bojana Višić – chair

Ana Kanjevac
Ana Milosavljević
Andrijana Šolajić
Barbara Bekić
Bojan Stojadinović
Branka Hadžić
Ivana Milošević
Jasmina Lazarević
Jelena Mitrić
Jelena Trajković
Jovan Blagojević
Lenka Filipović
Marko Opačić
Milica Petrović
Nataša Tomić
Novica Paunović
Tea Belojica
Tijana Tomašević Ilić

Advances in Solid State Physics and New Materials - May 19–23

Time	**Session A – Main Hall**	**May 20**	**Session B – Hall 1**	**Time**
12:20–14:15		**Lunch Break**		**12:20–14:15**
Chair	**Marko Kralj**		**Jelena Pešić**	**Chair**
14:15–14:45	**Matthias Opel** (Germany) *“Magnon Spin Transport in Antiferromagnetic Insulators”*		**Radmila Panajotovic** (Serbia) *“Graphene-based Composite Thin Films with Self Assembling Biomolecules as Active Elements in Sensors”*	**14:15–14:45**
			Ivana Milošević (Serbia) *“Tuning the Properties of Liquid-Phase Exfoliated Langmuir-Blodgett Assembled Graphene Films via Chemical Doping”*	**14:45–15:05**
14:45–15:15	**Bojana Višić** (Serbia), *“Inorganic Nanotubes and Nanowires in Polymer Matrices: Potential for Sensing Applications”*		**Nataša Tomić** (Serbia) *“The Morphological And Structural Changes Of* V_2O_5 *Cathode Film Upon Electrochemical Cycling”*	**15:05–15:25**
15:15–15:45	**Branislav Nikolić** (USA) *“How ultrafast demagnetization drives spin and charge currents and the ensuing THz radiation”*		**Bojan Stojadinović** (Serbia) *“Role of terbium dopant and oxygen vacancies on conductive properties of* $BiFeO_3$ *thin films”*	**15:25–15:45**
15:45–16:05		**Coffee Break**		**15:45–16:05**
Chair	**Andrijana Šolajić**		**Igor Pašti**	**Chair**
16:05–16:35	**Mazhar Ali** (Netherlands) *“The Josephson Diode Effect with 2D Kagome Mott Insulators* Nb_3X_8 *(X = Cl, Br, I)” (online)*		**Marko Spasenović** (Serbia) *“Laser-Induced Graphene on Polymer Substrates for Monitoring Physiological Parameters”*	**16:05–16:35**
16:35–17:05	**Nicola Poccia** (Italy and Germany) *“Exploring quantum complexity in artificially twisted superconducting heterostructures” (online)*		**Enrico Di Lucente** (Switzerland) *“Phonon Boltzmann transport equation beyond the semiclassical regime”*	**16:35–17:05**

30-minute talks: 25 min presentation + 5 min Q&A | 20-minute talks: 15 min presentation + 5 min Q&A

Tuning the Properties of Liquid-Phase Exfoliated Langmuir-Blodgett Assembled Graphene Films via Chemical Doping

Ivana R. Milošević[a], Tijana Tomašević-Ilić[a] and Jasna Vujin[a]

[a]*Institute of Physics Belgrade, University of Belgrade, 11080 Belgrade-Zemun, Serbia*

Abstract. The increasing interest in graphene and other 2D materials extends across scientific and technological fields, shifting from fundamental research to practical applications. Doping plays a crucial role in tailoring their electrical, optical, and magnetic properties, broadening their usability. Among various scalable synthesis methods, liquid-phase exfoliation (LPE) followed by Langmuir-Blodgett (LB) deposition enables the fabrication of thin graphene films with excellent substrate coverage, offering high reactivity and tunability. Chemical doping with nitric acid for p-doping significantly enhances the sheet conductivity (five times) of LPE LB graphene films, improving their potential for electronic applications [1]. Furthermore, we developed a single-step doping strategy, replacing water with metal standard solutions as the liquid subphase, that integrates film formation and doping at the liquid-air interface [2]. By employing Li-based salts for n-doping and Au-based salts for p-doping, we achieved a tunable work function spanning nearly 1 eV, making these films suitable for electron and hole injection interfaces in optoelectronics. Beyond electronic modifications, we used the single-step approach to introduce localized magnetic domains into nonmagnetic LPE LB films via Fe nanoparticle functionalization, exploring their potential for heavy metal water purification. Raman and XPS confirmed successful surface modification, while MFM revealed a strong phase shift (~0.2°), indicating localized magnetic moments absent in unmodified films.

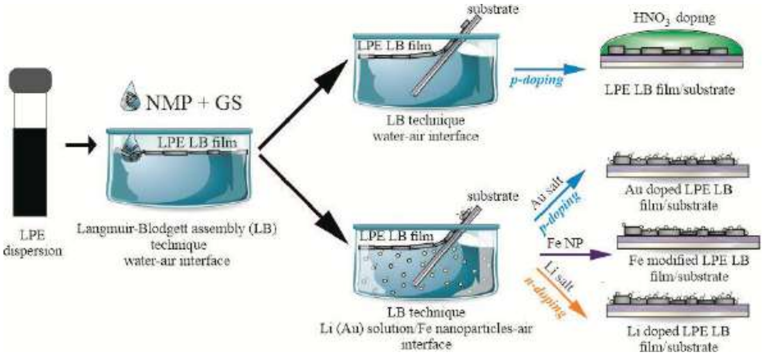

FIGURE 1. Fabrication and chemical doping of Liquid-Phase Exfoliated Langmuir-Blodgett Assembled Graphene Films (LPE LB) Graphene Films.

REFERENCES

1. Matković A. et al., *2D Mater.* **3**, 015002 (2016).
2. Milošević I. R. et al., *Sci. Rep.* **10**, 8476 (2020).

Tiled Network Films from Liquid Phase Exfoliated h-BN and Phyllosilicates: Properties and Perspectives for Heritage Protection

Tijana Tomašević-Ilić[a], Ivana Milošević[a], Jasna Vujin[a], Jelena Pešić[a], Radmila Panajotović[a], Bojana Savić[b] and Irena Živković[b]

[a]*Institute of Physics Belgrade, University of Belgrade, Pregrevica 118, 11080 Belgrade, Serbia*
[b]*Faculty of Applied Arts, University of Arts Belgrade, Kralja Petra 4, 11000 Belgrade, Serbia*

Abstract. Nanotechnology approaches in conservation and restoration practices have enabled the development of advanced materials, offering promising solutions to mitigate the degradation of various artefacts [1–3]. Nevertheless, addressing the main conservation challenges with universal, durable, and cost-effective coatings, suitable for large-scale production remains an ongoing issue. As part of the 2DHeriPro project, we focused on exploring nanostructures beyond graphene-based materials to develop durable 2D material-based protective coatings for a broad range of heritage artefacts. We developed thin films from liquid-phase exfoliated (LPE) hexagonal boron nitride (h-BN), talc, and pyrophyllite, and systematically evaluated their potential for Heritage preservation. Our investigation encompassed an analysis of their chemical structure, optical properties, morphology, wettability, reversibility, and stability under conditions of high relative humidity, an oxidative environment, and thermal stress. Furthermore, to assess the compatibility of the films with wall-painting artefacts, we fabricated replica-models of fresco-paintings using colorimetry, spectroscopy, and morphology data obtained from heritage samples collected at relevant sites. These models, serving as substrates for the Langmuir-Blodgett (LB) deposition of 2D material-based films and the investigation of their compatibility, were produced from lime fresco mortar and identified pigments in order to reproduce the same color perception as the original artefacts. Although LB films from LPE h-BN with nanometer thickness exhibited superior transparency, hydrophobicity, and resistance to relative humidity and oxidation, colorimetric analysis of our films deposited on the model samples indicated that LPE talc-based films show the highest potential for application as coatings across diverse artefacts. In this presentation, we will outline the motivation, innovative approaches, and key findings from the first year of the 2DHeriPro project.

This research was supported by the Science Fund of the Republic of Serbia, Grant No 7456, 2D Material-based Tiled Network Films for Heritage Protection-2DHeriPro.

REFERENCES

1. Baglioni et al. *Molecules* **26**, 3967 (2021).
2. Kotsidi M. et al., *Nat. Nanotechnol.* **16**, 1004–1010 (2021).
3. Galvagno e. et al., *Adv. Funct. Mater.* **34** 2313043 (2024).

Effects of Exfoliation Parameters and Relative Humidity on the Structure of Kaolinite Nanoplates

Barbara Bekić[a], Jelena Mitrić[a], Jasna Vujin[a], Radmila Panajotović[a], Ivana Milošević[a] and Tijana Tomašević-Ilić[a]

[a]*Institute of Physics Belgrade, University of Belgrade, Pregrevica 118, 11080 Belgrade, Serbia.*

Abstract. We investigated the influence of exfoliation parameters and exposure to relative humidity (RH) on the inner and external hydroxyl groups of kaolinite nanoplates obtained by liquid-phase exfoliation (LPE) and deposited onto the solid substrate using the Langmuir-Blodgett technique. Kaolinite, a naturally occurring layered aluminosilicate, is widely used in nanocomposites, environmental remediation, and biomedical applications [1]. Its hydroxyl-rich surface readily interacts with water molecules, particularly under varying humidity, thereby altering its physicochemical properties. While the exfoliation increases the surface area, introduces defects, exposes inner layers and may lead to reorientation or partial removal of hydroxyl groups, high RH conditions can affect the surface hydroxylation by promoting H-bonding, as well as the regeneration and rearrangement of hydroxyl groups [2, 3]. In our study, we demonstrate how both LPE parameters (water content of the solvent, exfoliation time, and the initial concentration of bulk material), and exposure to high RH (>70%) affected the structure of produced kaolinite nanoplates. UV-VIS spectroscopy, XRD, Raman Spectroscopy and AFM confirmed the successful exfoliation of the material, while FTIR indicated that exfoliation conditions could be effectively tuned to control and optimize the hygroscopic behavior of kaolinite nanoplates.

This research was supported by the Science Fund of the Republic of Serbia, Grant No 7456, 2D Material-based Tiled Network Films for Heritage Protection-2DHeriPro.

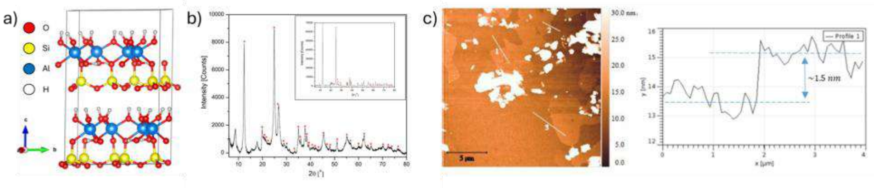

FIGURE 1. a) Crystal structure of kaolinite, b) XRD patterns of LPE and bulk kaolinite (inset), c) AFM image of kaolinite nanoplates (left) with height profile (right).

REFERENCES

1. Nisticò, R. Inorganics **10**, 40 (2022).
2. X. Huang et al., Langmuir **35** 13833–13843 (2019).
3. Kloprogge, J., Spectroscopic Methods in the Study of Kaolin Minerals and Their Modifications, Springer Mineralogy, Springer, Cham., 2019, pp. 41-96

Proceedings of the 10th World Congress on Recent Advances in Nanotechnology (RAN 2025)
Barcelona, Spain - April, 2025
Paper No. ICNNFC 110
DOI: 10.11159/icnnfc25.110

Optimization of Iron Nanoparticle Biosynthesis Using Bacterial Isolates from Natural Environments

Iva Rosić[1], Marina Anteljević[1], Ivana Marić[1], Ivana R. Milošević[1], Tijana Tomašević-Ilić[1], Tanja Berić[1,2]
[1]Institute of Physics Belgrade, University of Belgrade Pregrevica 118, 11080 Zemun, Belgrade
[2]Faculty of Biology, University of Belgrade, Studentski trg 16, 11000 Belgrade
riva@ipb.ac.rs; amarina@ipb.ac.rs; mivana@ipb.ac.rs; novovic@ipb.ac.rs; ttijana@ipb.ac.rs; tanjab@bio.bg.ac.rs

Iron nanoparticles (FeNPs) have a wide range of applications in various industries due to their unique properties, such as high surface area, superparamagnetism, and favorable surface-to-volume ratio [1]. Key applications include the electromagnetic industry (battery development), bioremediation, wastewater treatment, pharmaceuticals (as vesicles for targeted drug delivery), and nanomedicine for diagnostics like magnetic resonance imaging [2]. However, conventional physical and chemical synthesis methods are expensive, especially for biological applications requiring special biocompatible coatings [3]. These methods also consume significant energy and use toxic reagents, posing environmental risks [4]. Therefore, biological synthesis using bacteria that reduce iron extracellularly or intracellularly presents a sustainable alternative. This method aligns with global sustainability goals, as it relies on bacterial metabolic reactions. It is also simple and economical, given the widespread availability of bacteria in various environments, the ease of laboratory cultivation, and their short generation time. The FeNPs have an inherent biocompatible coating and reduced toxicity [5]. However, two major challenges hindering the industrial success of this approach are inconsistent size uniformity and low yield compared to conventional methods [6].

The main objective of our ongoing study is to optimize iron bionanoparticles production using bacteria from natural environments by comparing different conditions for FeNP synthesis. We aim to isolate and identify iron-reducing and magnetotactic bacteria, test various synthesis conditions (effects of strain selection, iron salt type and concentration, pH, and temperature), and isolate, purify, and characterize FeNPs using physical methods (UV-Vis, FTIR, SEM). The goal is to develop a protocol with yields and uniformity comparable to physicochemical methods at an industrial scale.

Here, we present results from the first step of optimization, focusing on the isolation and selection of bacteria that demonstrated intracellular and extracellular synthesis of FeNPs. Bacteria were isolated from samples collected from seven locations in Serbia, including river waters and mud, rusty surfaces, rocks, soil, and mining sites. Pure strains were identified via 16S rRNA sequencing and tested for FeNP synthesis.

A total of 62 isolates were obtained. Four isolates (two *Stenotrophomonas* sp. and two *Bacillus megaterium*) exhibited magnetosomes and synthesized intracellular magnetite nanoparticles, confirmed by movement towards a magnetic field under a microscope. Extracellular synthesis was observed in 36 isolates (22 from $FeCl_3 \times 6\ H_2O$ and 14 from $FeCl_2 \times 4\ H_2O$) from 11 genera, based on yellow-orange precipitates indicating iron reduction. Notably, two *B. megaterium* isolates exhibited both intracellular and extracellular synthesis, while eight isolates synthesized iron from both salts. The most common genera in FeNP synthesis were *Bacillus* and *Pseudomonas*.

This part of the study confirmed extracellular FeNP synthesis by known nanoparticle-producing genera, such as *Enterobacter* sp., *Achromobacter* sp., and *Stenotrophomonas* sp. It also demonstrated FeNP synthesis by strains from genera previously known for silver and gold nanoparticle synthesis, including *Lysinibacillus* sp., *Geobacillus* sp., *Serratia* sp., and *Arthrobacter* sp. Additionally, FeNP synthesis was observed in *Buttiauxella* sp. and *Pseudoarthrobacter* sp., for which nanoparticle synthesis had not been previously studied, opening new research opportunities.

In conclusion, this study presents a first step toward optimizing bacterial FeNP synthesis by selecting strains for both intracellular and extracellular production. The potential for FeNP synthesis in these bacteria is promising, especially for sustainable nanotechnology development.

References

[1] A. Ali, H. Zafar, M. Zia, I. Haq, A. R. Phull, J. S. Ali, A. Hussain, “Synthesis, characterization, applications, and challenges of iron oxide nanoparticles“, Nanotechnol Sci Appl., vol. 19, no. 9, pp. 49-67, 2016.

[2] K. A. Altammar, “A review on nanoparticles: characteristics, synthesis, applications, and challenges“, Front Microbiol., vol. 17, no. 14, 1155622, 2023.

[3] D. Sharma, S. Kanchi, K. Bisetty, “Biogenic synthesis of nanoparticles: A review“, Arab. J. Chem., vol. 12, no. 8, pp. 3576-3600, 2019.

[4] X. F. Zhang, Z. G. Liu, W. Shen, S. Gurunathan, “Silver Nanoparticles: Synthesis, Characterization, Properties, Applications, and Therapeutic Approaches”, Int. J. Mol. Sci., vol. 17, no. 9, 1534, 2016.

[5] S. Majeed, M. Danish, M. N. M. Ibrahum, S. H. Sekeri, M. T. Ansari, A. Nanda, G. Ahmad, “Bacteria Mediated Synthesis of Iron Oxide Nanoparticles and Their Antibacterial, Antioxidant, Cytocompatibility Properties”, J. Clust., vol. 32, pp. 1083–1094, 2021.

[6] N. Marooufpour, M. Alizadeh, M. Hatami, B. A. Lajayer, “Biological Synthesis of Nanoparticles by Different Groups of Bacteria” in Nanotechnology in the Life Sciences Springer, Cham, 2021, vol. 32, pp. 1083–1094.